RESIDUAL-BASED VARIATIONAL MULTISCALE MODELS FOR THE LARGE EDDY SIMULATION OF COMPRESSIBLE AND INCOMPRESSIBLE TURBULENT FLOWS

By

Jianfeng Liu

A Thesis Submitted to the Graduate

Faculty of Rensselaer Polytechnic Institute

in Partial Fulfillment of the

Requirements for the Degree of

DOCTOR OF PHILOSOPHY

Major Subject: MECHANICAL ENGINEERING

Approved by the
Examining Committee:

_____
Prof. Assad A. Oberai, Thesis Adviser

_____
Prof. Mark S. Shephard, Member

_____
Prof. Donald A. Drew, Member

_____
Prof. Onkar Sahni, Member

Rensselaer Polytechnic Institute
Troy, New York

July 2012
(For Graduation August 2012)

CONTENTS

LIST OF TABLES

LIST OF FIGURES

DEDICATION

I gratefully dedicate my dissertation to my family members. A special feeling of gratitude to my loving parents, Xiujun Liu and Lijuan Zhang, for their nurturing, endless love, support and encouragement. Thank you for always pushing me and guiding me.

I also dedicate my dissertation to my girl friend, Boyang Zhang, for her patience, tolerance and understanding.

Finally, I'd like to dedicate my dissertation and give special thanks to my dissertation advisor Professor Assad Oberai, who is also my friend, for his encouragement and patience throughout the entire doctorate program.

ACKNOWLEDGEMENT

This dissertation would not have been possible without the guidance and the help of many individuals who in one way or another contributed and extended their valuable assistance in the preparation and completion of this work.

Foremost, I would like to express my sincere gratitude to my advisor and friend Professor Assad Oberai for his constantly generous support of my Ph.D study and research. His patience, knowledge, motivation and enthusiasm guided me in all the time of research and writing of this thesis. His incredible dedication to my professional and technical growth has been the key factor in my completion of this thesis.

Special thanks to the rest of my committee: Professor Mark Shephard, Professor Donald Drew, and Professor Onkar Sahni, for their encouragement, instructive suggestions, insightful comments, and their willingness to serve on my committee. I would also like to thank Professor Lucy Zhang for her serving on my committee for a while.

I wish to extend my warmest thanks to my fellow groupmates in RPI for their support: Zhen Wang, Sevan Goenezen, Jayanth Jagular, Yixiao Zhang, David Sondak, Jingsen Ma, Elizabete Rodrigues Ferreira and Jean-Francois Dord. I would also like to thank my dear friends who share enjoyable times together: Boyang Zhang, Xingshi Wang, Chu Wang, Yi Chen, Qiukai Lu, Lijuan Zhang, Fan Zhang, Tie Xie, Zhi Li, Yanheng Li, Weijing Wang, Frank Yong, James Young, Chayut Napombejara, Michel Rasquin and James Jiang. I appreciate their help and friendship. These acknowledgements would not be complete without thanking the staffs at RPI, who have helped me in various aspects.

Last but not the least, I would like to thank my parents: Xiujun Liu and Lijuan Zhang, for giving birth to me and supporting me spiritually throughout my life.

ABSTRACT

In the large-eddy simulation (LES) for turbulent flows, the large scale unsteady turbulent motions which are affected by the flow geometry, are directly solved, while the effects of the small scale motions which have a universal character are modeled. Compared with direct numerical simulation (DNS), the huge computational cost for solving the small-scale motions in high Reynolds number flows is avoided in LES.

In the variational multiscale (VMS) formulation of LES, the starting point for deriving models is the weak or the variational statement of conservation laws, whereas in the traditional filter-based LES formulation it is the strong form of these equations. In the residual-based variational multiscale (RBVM) formulation, the basic idea is to split the solution and weighting function spaces into coarse and fine scale partitions. Splitting the weighting functions in this way yields two sets of coupled equations: one for the coarse, or the resolved, scales and another for the fine, or the unresolved, scales. The equations for the fine scales are observed to be driven by the residual of the coarse scale solution projected onto the fine scale space. These equations are solved approximately and the solution is substituted in the equations for the coarse scales. In this way the effect of the unresolved scales on the resolved scales is modeled.

In this thesis we develop and test several LES models that are based on the RBVM formulation. These include:

1. The RBVM model, which is extended to compressible flows for the first time.

2. A new mixed model for compressible flows comprised of the RBVM model and the traditional Smagorinsky-type eddy viscosity model. In this model the RBVM term is used to model the cross-stresses and the eddy viscosity is used to model the Reynolds stresses.

3. A new residual-based eddy viscosity (RBEV) model for incompressible and

compressible flows that displays a "dynamic" behavior without the need to evaluate any dynamic parameters, thus making it easy to implement.

4. A purely residual-based mixed model comprised of the RBVM model for the cross-stresses and the RBEV model for the Reynolds stresses, that is relatively easy to implement.

All these models are tested in modeling the decay of compressible homogeneous isotropic turbulence using a Fourier-spectral basis. The RBVM, the RBEV and the purely residual based mixed model are also tested in predicting the statistics of an incompressible turbulent channel flow using the finite element method. It is found that in general, the new residual-based models outperform the traditional eddy viscosity models.

CHAPTER 1
Introduction

1.1 Turbulent Flows

Turbulent flows are a common phenomena in nature. They are observed when a ship travels on the surface of the ocean, in the water coming out of a pipe, and in the wake of a racing car. The notion of a turbulent flow was recorded more than 500 years [1]. However it was not until about 100 years ago, the scientists and engineers begin to investigate and understand the turbulent flows in detail [2].

In 1883 Osborne Reynolds reported a very famous and important experiment in the history of turbulence [2]. In this experiment dye was steadily injected at the centerline of a long pipe carrying flowing water. Reynolds observed that, depending on the speed of the water, the dye in the pipe showed different behavior. When the speed was small, the dye appeared as a straight line at the center of the pipe. When the speed was increased, the straight line became curved line. When the speed was farther increased beyond a certain threshold value, the dye mixed with the water, and it was difficult to tell the dye from the surrounding water. Further it appeared that it would be impossible to predict the behavior of this flow. At this point the flow is said to be turbulent. By changing the speed of the water and the pipe diameter, or even replacing the water with an other fluid material, the transition to turbulence was always observed at a fixed parameter.

Later this experiment was summarized by the single non-dimensional parameter, which is called the Reynolds number Re. The Reynolds number is defined as

$$Re = UL/\nu, \tag{1.1}$$

where U is characteristic velocity and L is characteristic length scale of the flow, and ν is the kinematic viscosity of the fluid. The Reynolds number denotes the

ratio of inertial forces and viscous forces. Generally speaking, when the Reynolds number $Re < 2300$, the dye in the flow is a straight line, and this kind flow is called a *laminar flow*. When Reynolds number $Re > 4000$, the line is broken, and the dye is mixed with water and it becomes a *turbulent flows*. The region in between ($2300 < Re < 4000$) is called the *transition region*. However, it is necessary to point that, the values of 2300 and 4000 are not always the boundaries for the laminar flow and turbulent flow. In some situations, laminar flow is observed at $Re > 4000$. Comedy in some cases, with $Re < 2000$, turbulent can be observed. But generally speaking, when Re is high, the flow is more likely to be turbulent.

There is no rigid definition of turbulence. However, turbulence is characterized by the some important features, such as highly irregular motion, highly rotational structure, and enhanced dissipative and diffusive mechanisms. An essential feature of turbulent flows is that the fluid velocity field varies significantly and irregularly as a function position and time [3]. In turbulent flows, the irregular, unsteady motions transport momentum, heat and matter at a rate that are several orders of magnitude more than molecular motion. Consequently, turbulent flow is responsible for a large amount of the energy consumption (through turbulent drag) and most of the heat transfer and matter transport in engineering flows [4].

1.2 Approaches to Studying Turbulence

In the industrial application, turbulent flows are very important and play a role in the design of aircrafts, engines, high speed automobiles, or even nuclear power plants. After 100 years study, people learn some basic knowledge about turbulent flows. Unfortunately, we are still far away from accurately understanding and predicting the behavior of turbulent flows. As Nobel laureate Richard Feynman stated " turbulence is the most important unsolved problem of classical physics."

Nowadays, there are mainly three ways to study turbulent flows: a theoretical approach, an experimental approach and a numerical approach.

The theoretical study of turbulent flows is based on the Navier-Stokes (NS) equations. However, because of the unsteady, irregular, random and chaotic characteristic of turbulence, it is very difficult to solve these partial differential equations analytically for most practical situations. It is especially true when we know that these equations can lead to chaotic solutions. Currently, the theoretical understanding of turbulent flow is mostly based on statistical studies. The Russian mathematician Andrey Kolmogorov proposed the first statistical theory of turbulence, based on the hypothesis of energy cascade [5, 6, 7]. This theory is usually referred as the K41 theory and we will utilize this theory in Chapter 3. One important conclusion of the K41 theory is that, turbulent flows contain eddies of different length scales. Kinetic energy is transferred from larger eddies to smaller ones. Although the hypothesis leads to a simple expression for how energy is distributed among eddies of different sizes, it does not provide a tool which can be used to predict the behavior of complicated flows in an industrial setting.

Experimental study of turbulence is another approach to understanding turbulence. Wind tunnels provide useful information for aerodynamic studies. A lot of important experimental data has come from wind tunnels. On one hand, these results can be used to validate some theories, and on the other hand, they can be used to develop more accurate and higher fidelity models. However, experimental study of turbulence is not an easy task. For example, turbulence usually occurs at high speeds or large spatial scale. Often it is not easy or cheap to achieve these high speeds or large spatial scale. For example it is very difficult to realize experiments that study atmospheric boundary layers or supersonic flows. Even for some industrial applications such as the testing of new designs for cars and airplanes, such experiments can become very expensive, because the design process usually requires several cycles.

The numerical simulation of turbulent flows, which is a part of computational fluid dynamics (CFD), is the " third approach " in the study turbulent flows. The

numerical simulation is very new compared to the experimental approach which has been around from the seventeenth century, and theoretical approach which started in the eighteenth century. The numerical simulation requires two important ingredients: a high-speed digital computer and the development of accurate numerical algorithms. Numerical simulation can be thought of as a connection between experimental and theoretical studies of turbulent flows. By solving the NS equations numerically, we can develop an understanding of some behaviors observed in experiments. In addition to this, numerical simulation can replace experiments in cases where it is impossible to perform the experiment or it is too expensive.

1.3 Numerical Simulation of Turbulent Flows

According to the K41 theory, in turbulent flows kinetic energy is transferred from larger length scales to smaller length scales. Based on this idea, the eddies in turbulent flows can be divided into three categories based on their length scales. Integral length scales are the largest scales. These eddies obtain energy from the mean flow and also from each other. Kolmogorov length scales are the smallest scales. In this range, the energy input from nonlinear interactions and the energy lost from dissipation due to viscous effect balance each other. Eddies in the inertial subrange are between the largest and the smallest scales. They pass the energy from the largest to the smallest length scale without dissipating it.

There are several important numerical methods available to simulate turbulent flows. There are the direct numerical simulation (DNS), large-eddy simulation (LES), and Reynolds-averaged Navier-Stokes (RANS) equations. The research presented in this proposal is dedicated to LES. To assess the performance of LES models, their results will be compared to DNS results obtained on much finer grids. In the following paragraphs we present a brief introduction to DNS, LES and RANS.

1.3.1 Direct Numerical Simulation (DNS)

In DNS we solve the Navier-Stokes equations without any model term. All the scales of motion are resolved. It is the simplest approach and it could provide

unbeatable accuracy. The drawback of DNS is the very large computational cost. In order to simulate all the scales, the computational domain has to be large enough to contain the largest eddies, and the grid spacing has to be small enough to capture the smallest eddies. The cost increases rapidly with the Reynolds number (approximately as Re^3). The DNS approach was not widely used before 1970s because of the lack of computer power. Even now, DNS has been only applied to turbulent flows with low or moderate Reynolds numbers.

1.3.2 Large-Eddy Simulation (LES)

As discussed in previous subsection, the computational cost of DNS is high, and it increases rapidly with the Reynolds number, so that DNS is not usually applied to high Reynolds number flows. LES has be developed to tackle this problem. In turbulent flows, the larger-scale motions are affected by the flow geometry and are not universal, while the smaller scales have a universal character. Further, most of the energy is contained in the large scales but most of the computational cost is spent in solving the small scales. So the basic idea of LES is that the larger-scale motions are computed explicitly, and the influence of the smaller scales is represented by simple models. Thus, compared with DNS, the vast computational cost of explicitly representing the small-scale motions is avoided.

1.3.3 Reynolds-averaged Navier-Stokes (RANS) Equations

Besides DNS and LES, the Reynolds-averaged Navier-Stokes (RANS) equations are also used to model turbulent flows. These equations are the ensemble-averaged equations of motion for fluid flow. Reynolds decomposition is used for RANS, so an instantaneous quantity is decomposed into its ensemble-averaged and fluctuating values. The same averaging procedure is applied to the NS equations. RANS equations contains the averaged variables and terms that depend on the fluctuating variables. The terms containing the fluctuating variables must be modeled, and they must be expressed only in terms of the averaged quantities. This expressions is called model terms. Some models include the Spalart-Allmaras, $k-\omega$, $k-\epsilon$, and SST models which add additional equations to bring closure to the RANS equations. Compared to LES, the RANS have smaller computational cost, but they do

not provide instantaneous quantities and good estimation for fluctuation.

1.4 LES of Turbulent Flows

In this section, we will introduce large eddy simulation of turbulent flows with more details. LES of incompressible and compressible flows are described separately, but we should keep in mind that they share the same basic idea. In order to simulate the effect of the small scales, Smagorinsky model [8] is introduced for incompressible flows and Smagorinsky-Yoshizawa -eddy-diffusivity (SYE) model [9] for compressible flows. Smagorinsky model model is the simplest model [3] and is widely used for LES. Especially, we will use a dynamic version of SYE model in this thesis as a LES model for compressible flows in some sections. And the Smagorinsky model is used as comparison case in some other sections.

1.4.1 LES of Incompressible Flows

In DNS, the velocity field $\boldsymbol{u}(\boldsymbol{x}, t)$ contains all the length scales. In LES, in order to split the velocity field into a large scale (coarse scale) velocity field and a small scale (fine scale) velocity field, a low-pass filtering operation is introduced. The general filtering operation is defined by

$$\int G(\boldsymbol{r}, \boldsymbol{x}) d\boldsymbol{r} = 1, \tag{1.2}$$

the filtered velocity field $\boldsymbol{U}^h(\boldsymbol{x}, t)$ is determined by

$$\bar{\boldsymbol{u}}(\boldsymbol{x}, t) = \int G(\boldsymbol{r}, \boldsymbol{x}) \boldsymbol{u}(\boldsymbol{x} - \boldsymbol{r}, t) d\boldsymbol{r}, \tag{1.3}$$

and the residual field is defined by

$$\boldsymbol{u}'(\boldsymbol{x}, t) \equiv \boldsymbol{u}(\boldsymbol{x}, t) - \bar{\boldsymbol{u}}(\boldsymbol{x}, t), \tag{1.4}$$

The incompressible Navier-Stokes equations are

$$\frac{\partial u_i}{\partial x_i} = 0, \tag{1.5}$$

$$\frac{\partial u_i}{\partial t} + \frac{\partial}{\partial x_j}(u_i u_j) = -\frac{1}{\rho}\frac{\partial p}{\partial x_i} + \frac{\partial \sigma_{ij}}{\partial x_j}. \tag{1.6}$$

In the equations above u_i is the velocity field, p is the pressure, ρ is the fixed density, σ_{ij} is the viscous stress tensor. We apply the filtering operation to the Navier Stokes equations and arrive at

$$\frac{\partial \bar{u}_i}{\partial x_i} = 0, \tag{1.7}$$

$$\frac{\partial \bar{u}_i}{\partial t} + \frac{\partial}{\partial x_j}(\bar{u}_i \bar{u}_j) = -\frac{1}{\rho}\frac{\partial \bar{p}}{\partial x_i} + \frac{\partial \bar{\sigma}_{ij}}{\partial x_j} + \frac{\partial \tau_{ij}^{SGS}}{\partial x_j}, \tag{1.8}$$

where

$$\tau_{ij}^{SGS} = \bar{u}_i \bar{u}_j - \overline{u_i u_j}. \tag{1.9}$$

is the subgrid stress (SGS) tensor. In order to close the equations for the filtered velocity, a model for the subgrid stress tensor τ_{ij}^{SGS} is needed. The simplest model is the Smagorinsky model [8], which also forms the basis for several of the more advanced models, such as dynamic Smagorinsky model [10], the the mixed Bardina model [11], and the mixed Clark model [12].

The Smagorinsky model is expressed as a linear eddy-viscosity model

$$\tau_{ij}^{SGS} = -2\nu_t \bar{S}_{ij}, \tag{1.10}$$

It relates subgrid stress τ_{ij}^{SGS} to the filtered rate of strain $\bar{S}_{ij}$, through $\nu_r(x,t)$, which is the eddy viscosity, modeled as

$$\nu_t = (C_s \Delta)^2 |\bar{\boldsymbol{S}}|, \tag{1.11}$$

where $\bar{\boldsymbol{S}}$ is the characteristic filtered rate of strain, $\triangle$ is the filter width, and C_s is the Smagorinsky coefficient. We note that $C_s = 0.1$ is a preferred value for free-shear

flows and for channel flow.

1.4.2 LES of Compressible Flows

In compressible flows, it is convenient to use Favre filtering to avoid the introduction of subgrid-scale terms in the equation of conservation of mass. Favre (or density-averaged) quantities [13] are defined as $\widetilde{f} \equiv (\rho f)^h/\rho^h$. Applying this filter to the compressible Navier Stokes equations yields two subgrid quantities:

$$\tau_{kl}^{SGS} = \bar{\rho}\widetilde{u_k u_l} - \widetilde{u}_k\widetilde{u}_l), \tag{1.12}$$

$$q_k^{SGS} = \bar{\rho}(\widetilde{u_k T} - \widetilde{u}_k\widetilde{T}). \tag{1.13}$$

In the equations above T is the temperature, τ_{kl}^{SGS} is the subgrid scale stress tensor and q_k^{SGS} is the subgrid scale heat flux, which appears in the filtered energy equation. Both these terms need to modeled in terms of the filtered variables. The simplest model is based on eddy diffusivity concept and is due to Samgorinsky and Yoshizawa [9]. It is given by

$$\tau_{kl}^{SGS} = -2C_0\bar{\rho}\Delta^2|\widetilde{\boldsymbol{S}}|(\widetilde{S^h}_{kl} - \frac{1}{3}\widetilde{S^h}_{mm}\delta_{kl}) + \frac{2}{3}C_1\bar{\rho}\Delta^2|\widetilde{\boldsymbol{S}}|^2\delta_{kl}, \tag{1.14}$$

$$q_k^{SGS} = -\frac{\bar{\rho}C_s\Delta^2|\widetilde{\boldsymbol{S}}|}{Pr_T}\frac{\partial\widetilde{T}}{\partial x_k}. \tag{1.15}$$

In the equations above $\widetilde{\boldsymbol{S}}$ is the filtered rate of strain, C_0 is the Smagorinsky parameter that goes to model the deviatoric component of the subgrid stress, C_1 is the model attached to the dilatational component of subgrid stress, and Pr_T is the turbulent Prandtl number. All these three parameters need to be specified in order to use this model.

In contrast to all the models described in the previous page, the research in this thesis does not use spatial filters to derive LES equations. Rather it uses projection operators applied to the variational formulation of the Navier-Stokes equations. This approach is based on the Variational Multiscale formulation (VMS) [14] and is

described in the following section.

1.5 Residual based Variational Multiscale (RBVM) Formulation

In large eddy simulation (LES) the large scales of fluid motion are explicitly resolved while the effect of the fine scales on the large scales is modeled using terms that depend solely on the large scale variables. In filter-based LES this scale separation is achieved through the application of spatial filters that tend to smooth a given field variable. In contrast to this in the variational multiscale (VMS) formulation the scale separation is achieved through projection operators [14]. In addition in the VMS formulation the starting point for deriving LES models is the weak or the variational statement of conservation laws, whereas in the filter-based LES formulation it is the strong form of these equations.

In the residual-based variational multiscale (RBVM) formulation [15, 16] the basic idea is to split the solution and weighting function spaces into coarse and fine scale partitions. Splitting the weighting functions in this way yields two sets of coupled equations: one for the coarse scales and another for the fine, or the unresolved, scales. The equations for the fine scales are observed to be driven by the residual of the coarse scale solution projected onto the fine scale space. Hence the name the "residual-based" VMS formulation. These equations for the unresolved scales are solved approximately and the solution is substituted in the equations for the coarse scales. In this way the effect of the fine or the unresolved scales on the coarse scales is modeled.

Thus far the RBVM formulation has been applied to incompressible turbulent flows [15, 17]. In this context in [18, 19] it was observed that while the RBVM formulation accurately modeled the cross-stress terms ($\bar{u}u'$) it did not at all model the Reynolds stress terms ($u'u'$). To remedy this a mixed model was proposed that appended to the RBVM terms a Smagorinsky eddy viscosity model [8] in order to capture the effect of the Reynolds stresses. The value of the Smagorinsky parame-

ter in this model was determined dynamically, while accounting for the dissipation induced by the RBVM terms. In tests of the decay of incompressible homogeneous turbulence it was observed that the mixed model was more accurate than the RBVM and the dynamic Smagorinsky models.

In this thesis we aim to extend these ideas to compressible turbulent flows. First, we consider the extension of the RBVM formulation to compressible flows. Thereafter motivated by the shortcomings of this model in the incompressible case we consider a mixed version of this model (which is referred as the MM1 model) where we add the Smagorinsky, Yoshizawa [9], and eddy diffusivity terms to model the Reynolds components of the deviatoric subgrid stresses, the dilatational subgrid stresses and the subgrid heat flux vector, respectively [10]. Through a simple analysis of the subgrid mechanical energy and through the dynamic approach we conclude that out of these the RBVM formulation requires a model only for the deviatoric component of the Reynolds stresses. The other significant subgrid quantities are adequately represented within the RBVM formulation. Thus the mixed RBVM formulation for compressible flows contains only one additional term when compared with the RBVM formulation, which is the deviatroic Smagorinsky model.

1.6 Residual based Eddy Viscosity (RBEV) Model

In LES the large scale fluctuations are resolved and the effect of the fine scale fluctuations on the large scales is modeled through terms that depend only on the large scales. Over the years several LES models have been developed, and a majority of these, to some extent the commonly used ones, are based on the concept of an eddy viscosity. This idea is motivated by direct analogy with a molecular viscosity. Just as the molecular viscosity represents momentum transfer through fluctuations of the atomistic particles, the turbulent eddy viscosity represents momentum transfer through fluctuating continuum fluid velocity.

The Smagorinsky model is the most popular eddy viscosity based LES model.

In this model the eddy viscosity is taken to be proportional to a local rate of strain and a representative length scale, often set to a measure of the grid size. Despite its popularity, this model has its drawbacks. In particular, it has been recognized that it must be modified in space and time whenever the turbulence is decaying or damped in some spatial regions (close to a wall, for example). The most effective way to accomplish this is to employ the so-called dynamic approach based on the Germano identity. In this approach the subgrid stresses on the computational grid and on a test-filter scale are considered. The difference between these two, which can be explicitly determined once scale similarity is invoked, is used to estimate the magnitude of the Smagorinsky eddy viscosity. This approach, which has been widely used, has been successful in simulating complex flows. However, it is cumbersome in that (1) it requires the use of at least one additional filter and (2) it involves averaging, either in space, or time, or along material trajectories in order to achieve a smoothly varying eddy viscosity. The dynamic approach may be thought of as a way of repairing a glaring drawback of the Smagorinsky model. That is, it does not vanish when the flow field is devoid of any fluctuations. In that sense it is inconsistent.

In this thesis we present a new eddy viscosity model that is inherently consistent and circumvents the use of a dynamic approach. Our model is based on ideas derived from the variational multiscale (VMS) formulation. Within this approach an equation for the fine scales is derived from the original variational formulation for the Navier Stokes equations. This equation is then approximated to obtain an explicit, approximate expression for the fine scales. In this expression it is observed that the fine scales are driven by the residual of the coarse scales. Thus when the coarse scales are accurate, the residual vanishes, as do the fine scales. We recognize that once an expression for the fine scales is obtained (albeit an approximate one), it may be used to estimate the viscosity induced by these scales on the coarse scales. In analogy to the molecular viscosity we may assume that the turbulent, or eddy, viscosity is proportional to the magnitude of the fine scale velocity times a length scale which plays the role of the mean free path. In the context of LES it makes

sense to select this length scale to be proportional to the grid size. As a result we have $\nu_T \sim |u'|h$. We dub this model the residual-based eddy viscosity (RBEV) model.

Further, motivated by the mixed model (MM1) based on the RBVM model and the dynamics Smagorinsky model, a purely residual-based mixed model (MM2) based on the RBEV model and the RBVM model is also proposed.

1.7 Description of Chapters

The layout of this thesis is as follows. In Chapter 2, four residual-based models for large eddy simulation of turbulent flows are derived for both incompressible and compressible flows. They are the residual-based variational multiscale model (RBVM), the mixed model (MM1) based on the RBVM model and the dynamic Smagorinsky-Yoshizawa-eddy diffusivity (DSYE) model, the residual-based eddy viscosity model(RBEV), and the purely residual based mixed model (MM2) based on the RBVM and RBEV models. In Chapter 3, we test the performance of the new LES models in predicting the decay of compressible, homogeneous, isotropic turbulence (HIT) in regimes where shocklets are known to exist within Fourier-spectral method. In Chapter 4, we test the RBEV model and the MM2 model on the incompressible fully developed turbulent channel flows within finite element method. Conclusions will be drawn in Chapter 5.

CHAPTER 2
Residual Based Methods for Large Eddy Simulation of Turbulent Flows

In the residual-based variational multiscale (RBVM) formulation [15, 16] the basic idea is to split the solution and weighting function spaces into coarse and fine scale partitions. Splitting the weighting functions in this way yields two sets of coupled equations: one for the coarse scales and another for the fine, or the unresolved, scales. The equations for the fine scales are observed to be driven by the residual of the coarse scale solution projected onto the fine scale space. Hence the name the "residual-based" VMS formulation. These equations for the unresolved scales are solved approximately and the solution is substituted in the equations for the coarse scales. In this way the effect of the fine or the unresolved scales on the coarse scales is modeled.

Thus far the RBVM formulation has been applied to incompressible turbulent flows [15, 17]. In this context in [18, 19] it was observed that while the RBVM formulation accurately modeled the cross-stress terms ($\bar{u}u'$ terms) it did not at all model the Reynolds stress terms ($u'u'$). To remedy this a mixed model was proposed that appended to the RBVM terms a Smagorinsky eddy viscosity model [8] in order to capture the effect of the Reynolds stresses. The value of the Smagorinsky parameter in this model was determined dynamically, while accounting for the dissipation induced by the RBVM terms. In tests of the decay of incompressible homogeneous turbulence it was observed that the mixed model was more accurate than the RBVM and the dynamic Smagorinsky models.

In this chapter, we aim to extend the ideas of RBVM formulation to compressible turbulent flows. Thereafter motivated by the shortcomings of this model in the incompressible case we consider a mixed version of this model (MM1) where we add the Smagorinsky, Yoshizawa [9], and eddy diffusivity terms to model the Reynolds

components of the deviatoric subgrid stresses, the dilatational subgrid stresses and the subgrid heat flux vector, respectively [10]. Through a simple analysis of the subgrid mechanical energy and through the results of the dynamic approach we conclude that out of these the RBVM formulation requires a model only for the deviatoric component of the Reynolds stresses. The other significant subgrid quantities are adequately represented within the RBVM formulation. Thus the mixed RBVM formulation (MM1) for compressible flows contains only one additional term when compared with the RBVM formulation, which is the deviatroic Smagorinsky model.

Second, we present a new eddy viscosity model that is inherently consistent and circumvents the use of a dynamic approach. Our model is based on ideas derived from the variational multiscale (VMS) formulation. Within an explicit, approximate expression for the fine scales is derived. In this expression it is observed that the fine scales are driven by the residual of the coarse scales. Thus when the coarse scales are accurate, the residual vanishes, as do the fine scales. We recognize that once an expression for the fine scales is obtained (albeit an approximate one), it may be used to estimate the viscosity induced by these scales on the coarse scales. In analogy to the molecular viscosity we may assume that the turbulent, or eddy, viscosity is proportional to the magnitude of the fine scale velocity times a length scale which plays the role of the mean free path. In the context of LES it makes sense to select this length scale to be proportional to the grid size. As a result we have $\nu_T \sim |u'|h$. We dub this model *the residual-based eddy viscosity* (RBEV) model. This RBEV model can be applied to both incompressible and compressible flows.

Finally, a purely residual based mixed model (MM2) based on the RBVM and RBEV models for incompressible and compressible flows is introduced.

The layout of the remainder of this chapter is as follows. In Section 2.1, we provide a concise derivation of the RBVM method applied to a generic partial differential equation for both incompressible and compressible turbulent flows. In Section

2.2, a mixed model (MM1) based on the RBVM and the dynamic Smagorinsky-Yoshizawa-eddy diffusivity (DSYE) model is proposed for compressible turbulent flow. In Section 2.3, a residual based eddy viscosity model is proposed for both incompressible and compressible turbulent flows. In Section 2.4, purely residual based mixed model (MM2), that combines the RBVM and RBEV models, is proposed for both incompressible and compressible turbulent flows. This model is simpler to implement than MM1 in that it does not rely on a dynamic procedure to determine its parameters.

2.1 Residual-based variational multiscale formulation (RBVM)

In this section, the RBVM formulation of LES for the incompressible and compressible Navier-Stokes equations is developed. For a detailed derivation of the RBVM approach for the incompressible Navier-Stokes equations the reader is referred to [15].

The strong form of the incompressible Navier–Stokes equations in dimensionless variables is given by

$$\nabla \cdot \boldsymbol{u} = 0, \tag{2.1}$$

$$\rho \frac{\partial \boldsymbol{u}}{\partial t} + \rho \nabla \cdot (\boldsymbol{u} \otimes \boldsymbol{u}) = -\nabla p + \frac{1}{Re} \nabla^2 \boldsymbol{u} + \boldsymbol{f}, \tag{2.2}$$

where $\rho = 1$, Re is the Reynolds number.

The strong form of the compressible Navier–Stokes equations in dimensionless variables is given by

$$\frac{\partial \rho}{\partial t} + \nabla \cdot \boldsymbol{m} = 0, \tag{2.3}$$

$$\frac{\partial \boldsymbol{m}}{\partial t} + \nabla \cdot (\frac{\boldsymbol{m} \otimes \boldsymbol{m}}{\rho}) = -\nabla p + \frac{1}{Re} \nabla \cdot \boldsymbol{\sigma} + \boldsymbol{f}, \tag{2.4}$$

$$\frac{\partial p}{\partial t} + \nabla \cdot (\boldsymbol{u} p) + (\gamma - 1) p \nabla \cdot \boldsymbol{u} = \frac{(\gamma - 1)}{Re} \Phi + \frac{1}{M_\infty^2 Pr Re} \nabla \cdot (\mu \nabla T), \tag{2.5}$$

where the viscous stress tensor $\boldsymbol{\sigma}$ is given in terms of the rate of strain $\boldsymbol{S}$ by

$$\boldsymbol{\sigma} = 2\mu(\boldsymbol{S} - \frac{1}{3}tr(\boldsymbol{S})\boldsymbol{I}), \tag{2.6}$$

and the viscous dissipation Φ is given by

$$\Phi = \boldsymbol{\sigma} : \boldsymbol{S}. \tag{2.7}$$

The system is closed with an equation of state

$$\gamma M_\infty^2 p = \rho T. \tag{2.8}$$

Further, the dynamic viscosity is expressed in terms of the local temperature using,

$$\mu = T^{0.76}. \tag{2.9}$$

This problem is posed on a spatial domain Ω and in the time interval $]0, T[$ with given initial condition data and boundary conditions. In the above equations, ρ is the density, $\boldsymbol{u}$ is the velocity, $\boldsymbol{m} = \rho\boldsymbol{u}$ is the momentum, p is the thermal pressure, T is temperature, M_∞ is the free-stream Mach number, γ is the adiabatic index, Pr is the Prandtl number, Re is the Reynolds number and $\boldsymbol{f}$ is a forcing function. The density, velocity, temperature and viscosity are scaled by their reference values while the pressure is scaled by the product of the reference density and the square of the reference velocity. The Reynolds number is based on the reference values of the velocity, length, viscosity and density. For the homogeneous turbulence problem considered in this paper, the flow is assumed to be periodic with a period 2π in each coordinate direction. The values of the physical parameters are provided in Chapter 3.

Note that one can write Equations (2.1) and (2.2), Equations (2.3) – (2.5) concisely as

$$\mathcal{L}\boldsymbol{U} = \boldsymbol{F}, \tag{2.10}$$

where $\boldsymbol{U} = [\boldsymbol{u}, p]^T$ are the unknowns with $\boldsymbol{F} = [\boldsymbol{f},\ 0]^T$ for the incompressible case and $\boldsymbol{U} = [\rho, \boldsymbol{m}, p]^T$ are the unknowns with $\boldsymbol{F} = [0, \boldsymbol{f}, 0]^T$ for the compressible case. $\mathcal{L}$ represents the differential operator associated with the Navier-Stokes equations.

The weak form of Equation 2.10 is given by: Find $\boldsymbol{U} \in \mathcal{V}$ such that

$$A(\boldsymbol{W}, \boldsymbol{U}) = (\boldsymbol{W}, \boldsymbol{F}) \qquad \forall \boldsymbol{W} \in \mathcal{V}. \tag{2.11}$$

Here $A(\cdot, \cdot)$ is a semi-linear form that is linear in its first slot, $(\cdot, \cdot)$ denotes the L_2 inner product, and $\boldsymbol{W}$ is the weighting function. For the incompressible case it is given by $W = [\boldsymbol{w}, q]^T$ and for the compressible case it is given by $W = [r, \boldsymbol{w}, q]^T$. $\mathcal{V}$ is the space of trial solutions and weighting functions. In this presentation we have chosen the same space for both trial solutions and weighting functions in order to keep the presentation simple.

The semi-linear form of incompressible case is given by

$$\begin{aligned} A(\boldsymbol{W}, \boldsymbol{U}) \quad \equiv \quad & (\boldsymbol{w}, \boldsymbol{u}_{,t}) - (\nabla \boldsymbol{w}, \boldsymbol{u} \otimes \boldsymbol{u}) \\ & - (\nabla \cdot \boldsymbol{w}, p) + \frac{2}{Re}(\nabla^S \boldsymbol{w}, \nabla^S \boldsymbol{u}) + (q, \nabla \cdot \boldsymbol{u}). \end{aligned} \tag{2.12}$$

Here $\nabla^S = (\nabla + \nabla^T)/2$ is the symmetric gradient operator.

The semi-linear form of compressible case is given by

$$\begin{aligned} A(\boldsymbol{W}, \boldsymbol{U}) \quad \equiv \quad & (r, \rho_{,t}) - (\nabla r, \boldsymbol{m}) \\ & + (\boldsymbol{w}, \boldsymbol{m}_{,t}) - (\nabla \boldsymbol{w}, \frac{\boldsymbol{m} \otimes \boldsymbol{m}}{\rho}) \\ & - (\nabla \cdot \boldsymbol{w}, p) + \frac{1}{Re}(\nabla \boldsymbol{w}, \boldsymbol{\sigma}) \\ & + (q, p_{,t}) - (\nabla q, \boldsymbol{u} p) - (1 - \gamma)(q, p \nabla \cdot \boldsymbol{u}) \\ & - \frac{(\gamma - 1)}{Re}(q, \Phi) + \frac{1}{M_\infty^2 Pr Re}(\nabla q, \mu \nabla T). \end{aligned} \tag{2.13}$$

The weak form is posed using the infinite dimensional function space $\mathcal{V}$. In

practice this space is approximated by its finite-dimensional counterpart $\mathcal{V}^h \subset \mathcal{V}$. In the residual-based variational multiscale formulation the goal is to construct a finite dimensional problem whose solution is equal to $\mathbb{P}^h \boldsymbol{U}$, where $\mathbb{P}^h : \mathcal{V} \rightarrow \mathcal{V}^h$ is a projection operator that defines the desired or optimal solution. If the range of $\mathbb{P}^h$ is all of $\mathcal{V}^h$ then it is possible to split $\mathcal{V} = \mathcal{V}^h \oplus \mathcal{V}'$ which implies that for every $\boldsymbol{V} \in \mathcal{V}$ there is a unique decomposition $\boldsymbol{V} = \boldsymbol{V}^h + \boldsymbol{V}'$, where $\boldsymbol{V}^h = \mathbb{P}^h \boldsymbol{V} \in \mathcal{V}^h$ and $\boldsymbol{V}' = \mathbb{P}' \boldsymbol{V} \in \mathcal{V}'$. The space $\mathcal{V}' \equiv \{\boldsymbol{V} \in \mathcal{V} | \mathbb{P}^h \boldsymbol{V} = \boldsymbol{0}\}$, and $\mathbb{P}' = \mathbb{I} - \mathbb{P}^h$ where $\mathbb{I}$ is the identity operator. Using this decomposition in Equation (2.11) for both the weighting functions and the trial solutions we arrive at a set of coupled equations. Find $\boldsymbol{U}^h \in \mathcal{V}^h$ and $\boldsymbol{U}' \in \mathcal{V}'$, such that

$$A(\boldsymbol{W}^h, \boldsymbol{U}^h + \boldsymbol{U}') = (\boldsymbol{W}^h, \boldsymbol{F}) \qquad \forall \boldsymbol{W}^h \in \mathcal{V}^h, \tag{2.14}$$

$$A(\boldsymbol{W}', \boldsymbol{U}^h + \boldsymbol{U}') = (\boldsymbol{W}', \boldsymbol{F}) \qquad \forall \boldsymbol{W}' \in \mathcal{V}'. \tag{2.15}$$

The idea is to solve for $\boldsymbol{U}'$ in terms of $\boldsymbol{U}^h$ and $\boldsymbol{F}$ analytically using the fine scale equation (Equation (2.15)), and substitute the expression for $\boldsymbol{U}'$ into the coarse-scale equation (Equation (2.14)), which is to be solved numerically. By doing this one would have introduced in the coarse scale equation the effect of the fine or subgrid scales.

To derive an expression for $\boldsymbol{U}'$ we subtract $A(\boldsymbol{W}', \boldsymbol{U}^h)$ from both sides of Equation (2.15),

$$\begin{aligned} A(\boldsymbol{W}', \boldsymbol{U}^h + \boldsymbol{U}') - A(\boldsymbol{W}', \boldsymbol{U}^h) &= -A(\boldsymbol{W}', \boldsymbol{U}^h) + (\boldsymbol{W}', \boldsymbol{F}) \\ &= -(\boldsymbol{W}', \mathcal{L}\boldsymbol{U}^h - \boldsymbol{F}), \end{aligned} \tag{2.16}$$

where we have performed integration by parts on the first term on the right hand side of the first line of Equation (2.16). For general functions in $H^1(\Omega)$ the quantity $\mathcal{L}\boldsymbol{U}^h$ must be interpreted in the sense of distributions. Note that this equation for $\boldsymbol{U}'$ is driven by the coarse-scale residual $\mathcal{R}(\boldsymbol{U}^h) \equiv \mathcal{L}\boldsymbol{U}^h - \boldsymbol{F}$. Further, when the coarse-scale residual is zero its solution is given by $\boldsymbol{U}' = \boldsymbol{0}$. The formal solution of Equation (2.16) may be written as

$$\boldsymbol{U}' = \mathcal{F}'(\mathcal{R}(\boldsymbol{U}^h); \boldsymbol{U}^h). \tag{2.17}$$

This implies that the fine scales are a functional of the residual of the coarse scales and are parameterized by the coarse scales. Thus they depend on the entire history of the coarse scales and their residual. A short-time approximation that does away with all the history effects and replaces the differential operator in Equation (2.16) by an algebraic operator is given by

$$\boldsymbol{U}' \approx -\mathbb{P}'\boldsymbol{\tau}(\boldsymbol{U}^h)\, \mathbb{P}'^T \mathcal{R}(\boldsymbol{U}^h). \tag{2.18}$$

Here $\mathbb{P}'^T : \mathcal{V}^{h*} \rightarrow \mathcal{V}^*$ is the transpose of $\mathbb{P}'$, where the spaces $\mathcal{V}^{h*}$ and $\mathcal{V}^*$are dual of $\mathcal{V}^h$ and $\mathcal{V}$, respectively, with respect to the L_2 duality pairing [20]. Further, $\boldsymbol{\tau}$ is a matrix that depends on $\boldsymbol{U}^h$. The operator $\boldsymbol{\tau}$ is selected to approximate the Green's operator for the fine-scale problem, and can be thought of as a double integral of the Green's operator.

In moving from Equation (2.17) to Equation (2.18) instead of solving a very complicated equation for the fine scales, a gross approximation is made. In particular it is assumed that the fine scales are equal to the residual of the coarse scales, which represent the rate of unbalance for the coarse scale representation of a given conservation variable, times the characteristic time scale. In the advective limit this time scale is the time it takes to advect the fine scale scales across a typical grid size, and in the diffusive limit it is the time it takes for them to diffuse. The precise definition of $\boldsymbol{\tau}$ is presented in Chapter 3 and Chapter 4 when the models are implementd. For a discussion on this the reader is referred to [14, 15] . The approximation for $\boldsymbol{U}'$ above differs from that in [15] in the inclusion of the projectors $\mathbb{P}'$ and $\mathbb{P}'^T$. We believe that these projectors are necessary in order to maintain a formal consistency between the exaction equation for the fine scales Equation (2.16) and its approximation Equation (2.18). In particular the operator $\mathbb{P}'^T$ ensures that any component of the residual that is not "sensed" by a function in $\mathcal{V}'$ does not

contribute to the fine scales, and the operator $\mathbb{P}'$ ensures that the approximation for the fine scales belongs to $\mathcal{V}'$. In this regard the approximation above is closer to the orthogonal sub-scales method of Codina [16].

Using this expression in Equation (2.14) we arrive at the equation for the residual-based variational multiscale (RBVM) formulation: Find $\boldsymbol{U}^h \in \mathcal{V}^h$, such that

$$A(\boldsymbol{W}^h, \boldsymbol{U}^h - \mathbb{P}'\boldsymbol{\tau}\,\mathbb{P}'^T\mathcal{R}(\boldsymbol{U}^h)) = (\boldsymbol{W}^h, \boldsymbol{F}) \qquad \forall \boldsymbol{W}^h \in \mathcal{V}^h. \tag{2.19}$$

Remark: The space for $\boldsymbol{U}'$, that is $\mathcal{V}'$, is infinite dimensional. However, in practice this space must also be approximated with a finite dimensional space. Furthermore it must be selected such that the cost of computing $\boldsymbol{U}'$ in this space does not overwhelm the total computational costs. In our application, where we have used Fourier modes, the coarse scale space is comprised of all modes with wavenumber less than or equal to the cutoff wavenumber k^h, and *the fine scale space is comprised of all modes with wavenumber greater than* k^h *but less than or equal to* $3k^h/2$. This choice is motivated by tests (not shown here) that have shown that using a fine scale space that is larger than this does not significantly alter the results. Thus in order to minimize the computational effort we select the smallest possible space for $\boldsymbol{U}'$. We note that the ratio of memory costs for the RBVM model to the no-model case scales as α^3, where $\alpha > 1$ is the ratio of the cutoff wavenumber for the fine scales to the coarse scales. The ratio of flops per time-step also scales with the same power of α. Therefore it is imperative that α be kept small in order for the RBVM formulation to be competitive.

2.2 A mixed model based on residual based variational multiscale formulation (MM1)

In [19], for incompressible flows the authors demonstrated that while the RBVM model works well for the cross-stress term it does not introduce an adequate model for the Reynolds stress term. Subsequent analysis has revealed that the RBVM approximation for the fine scales produces a reasonable estimate for their

magnitude [21, 22]. Thus the reason why the Reynolds stresses are not accurately represented is not because their magnitude is underestimated, rather it is that they are uncorrelated with the large-scale rate of strain tensor. A likely explanation for this is the exclusion of the history effects in the approximation for the fine scales which prevents these correlations from evolving. With this in mind they appended to the RBVM model the dynamic Smagorinsky model in order to model the Reynolds stress.

2.2.1 Weak Form of MM1

We will first review the mixed model based on RBVM formulation for incompressible flows presented in [19]. Then we extend this model to compressible flows. We label this model as MM1, for mixed model 1, in anticipation of another mixed model that is proposed in Section 2.4.

Incompressible flows

In [19], based on the results of their a-priori analysis, the authors conclude that the RBVM model captures the cross-stresses reasonably well but does not accurately model the Reynolds stress term. On the other hand, it appears that the Reynolds stress term may be well represented by a simple eddy viscosity. Motivated by these observations they propose a mixed model where they append to the RBVM formulation the Smagorinsky eddy viscosity term. In this model the variational multiscale term models the cross-stress contribution, while the Smagorinsky term models the Reynolds stress contribution.

Thus the weak or variational formulation of the new mixed model of incompressible flows is given by: Find $\boldsymbol{U}^h \in \mathcal{V}^h$, such that

$$\begin{aligned} A\big(\boldsymbol{W}^h, \boldsymbol{U}^h + \boldsymbol{U}'\big) + \big(\nabla^S \boldsymbol{w}^h, \quad 2(c_s h)^2 |\boldsymbol{S}^h| \boldsymbol{S}^h\big) \\ = (\boldsymbol{W}^h, \boldsymbol{F}) \quad \forall \boldsymbol{W}^h \in \mathcal{V}^h, \end{aligned} \tag{2.20}$$

Here c_s is the Smagorinsky parameter and $\boldsymbol{S}^h$ is the rate of strain. When utilizing a Fourier-spectral discretization while specifying $\mathbb{P}^h$ to the H^1 projection

this expression simplifies to: Find $\boldsymbol{U}^h \in \mathcal{V}^h$, such that

$$\begin{aligned} &A\big(\boldsymbol{W}^h, \boldsymbol{U}^h\big) + \big(\nabla^S \boldsymbol{w}^h, \quad 2(c_s h)^2 |\boldsymbol{S}^h| \boldsymbol{S}^h\big) \\ &- \big(\nabla \boldsymbol{w}^h, \boldsymbol{u}^h \otimes \boldsymbol{u}' + \boldsymbol{u}' \otimes \boldsymbol{u}^h + \boldsymbol{u}' \otimes \boldsymbol{u}'\big) \\ &\qquad\qquad = (\boldsymbol{W}^h, \boldsymbol{F}) \quad \forall \boldsymbol{W}^h \in \mathcal{V}^h, \end{aligned} \tag{2.21}$$

where $\boldsymbol{u}^h \otimes \boldsymbol{u}'$ and $\boldsymbol{u}' \otimes \boldsymbol{u}^h$ are cross-stress term and $\boldsymbol{u}' \otimes \boldsymbol{u}'$ is the Reynolds stress term. A variant of the proposed mixed model is obtained by discarding the contribution from the RBVM model to the Reynolds stress. That is by neglecting the $\boldsymbol{u}' \otimes \boldsymbol{u}'$ term in Equation (2.21). This is a reasonable proposition since as shown in [19], the Reynolds stress term is not modeled accurately by this term. Instead it is well represented by the Smagorinsky term.

Compressible flows

We follow the same approach and propose, the following mixed model for compressible flows: Find $\boldsymbol{U}^h \in \mathcal{V}^h$, such that

$$\begin{aligned} &A\big(\boldsymbol{W}^h, \boldsymbol{U}^h + \boldsymbol{U}'\big) \\ &+ \big(\nabla \boldsymbol{w}^h, \quad 2C_0 h^2 \rho^h |\boldsymbol{S}^h| \boldsymbol{S}^h_{dev} - \frac{2}{3} C_1 h^2 \rho^h |\boldsymbol{S}^h|^2 \boldsymbol{I}\big) \\ &+ \big(\nabla q^h, \quad \frac{C_0}{Pr_t \gamma M_\infty^2} h^2 \rho^h |\boldsymbol{S}^h| \nabla T^h\big) \\ &\qquad\qquad = (\boldsymbol{W}^h, \boldsymbol{F}) \quad \forall \boldsymbol{W}^h \in \mathcal{V}^h, \end{aligned} \tag{2.22}$$

where $A(\cdot, \cdot)$ is defined in Equation (2.13), $\boldsymbol{S}^h$ is the rate of strain computed the velocity field $\boldsymbol{u}^h \equiv \boldsymbol{m}^h / \rho^h$, the subscript *dev* denotes its deviatoric component and $T^h \equiv \gamma M_\infty^2 p^h / \rho^h$. From the definitions of $\boldsymbol{u}^h$ and T^h we note that these correspond to the so-called Favre-averaged variables in traditional LES nomenclature.

Comparing with Equation (2.19), we note that two new terms have been added. The first term models the deviatoric and dilatational components of the subgrid scale stress tensor and the second term models the subgrid heat flux vector. For the

deviatoric component of the subgrid stress we have utilized the Smagorinsky eddy viscosity model [8], for the dilatational component we have utilized Yoshizawa's model [9], and for the subgrid heat flux vector we have utilized an eddy diffusivity type model. In a typical LES the first term is employed to represent both the cross and Reynolds stress components of the subgrid stress, whereas in our mixed model it is added to represent the missing Reynolds stress. In the following section we demonstrate that the RBVM model by itself introduces a reasonable expression for the dilatational Reynolds stress component. Based on this analysis we do not include an eddy viscosity model for the dilatational component of subgrid stress (that is $C_1 = 0$). Further in Section 4 we note that the dynamic procedure yields a negative value for Pr_t^{-1} which is clipped to zero. Thus in effect in the mixed model $C_1 = Pr_t^{-1} = 0$ and the only non-zero term corresponds to C_0, that is a model for the deviatoric subgrid stresses.

2.2.2 Analysis of mechanical energy for the RBVM formulation

In this section we derive a mechanical energy identity for the RBVM formulation for compressible flow. We split the total rate transfer of mechanical energy due to the subgrid scales into a dilatational and deviatoric component. For the deviatoric component, in earlier studies of incompressible flows it has been shown that the RBVM model is unable to model the Reynolds stress term, and for this purpose a mixed model is necessary. For the dilatational component, we demonstrate that the RBVM model introduces a cross and a Reynolds-stress term, where the latter is similar to the Yoshizawa model. As a result no additional model is required for the dilatational component of the stress tensor.

We begin by noting that Equation (2.22) contains all the models considered in the manuscript. In particular when $\boldsymbol{U}' = \mathbf{0}$ and $C_1 = C_0 = 0$, it represents the Galerkin method, or the DNS case; when only $\boldsymbol{U}' = \mathbf{0}$ it reduces to the Smagorinsky-Yoshizawa model; when $C_1 = C_0 = 0$, it reduces to the RBVM model; when all terms are active it represents the mixed model.

Setting $\boldsymbol{W}^h = [0, \boldsymbol{u}^h, 0]^T$ in this equation for the Galerkin method we arrive at mechanical energy identity:

$$\frac{d}{dt}\Big(\frac{1}{2}\int_\Omega \rho^h |\boldsymbol{u}^h|^2 dx\Big) = \overbrace{-\int_\Omega \frac{|\boldsymbol{u}^h|^2}{2}\big(\rho^h_{,t} + \nabla\cdot(\rho^h\boldsymbol{u}^h)\big)dx - \int_\Omega \boldsymbol{S}^h : \boldsymbol{\sigma}^h_t dx}^{\equiv \epsilon^h_{Gal}}, \quad (2.23)$$

where $\boldsymbol{\sigma}^h_t = -p^h\mathbf{1} + \frac{1}{Re}\boldsymbol{\sigma}^h$ is the total Cauchy stress tensor. This equation states that the rate of change of kinetic energy is determined by the dissipation induced by the molecular stresses and a term that depends on the residual of the continuity equation. We combine these two contributions into a term denoted by ϵ^h_{Gal}.

Next we consider Equation (2.22) written for the Smagorinsky-Yoshizawa model and set $\boldsymbol{W}^h = [0, \boldsymbol{u}^h, 0]^T$ to arrive at the mechanical energy identity for this model:

$$\begin{aligned}\frac{d}{dt}\Big(\frac{1}{2}\int_\Omega \rho^h |\boldsymbol{u}^h|^2 dx\Big) &= \epsilon^h_{Gal} \\ &\quad -2C_0h^2\int_\Omega \rho^h |\boldsymbol{S}^h||\boldsymbol{S}^h_{dev}|^2 dx \\ &\quad +\frac{2}{3}C_1h^2\int_\Omega \rho^h |\boldsymbol{S}^h|^2(\nabla\cdot\boldsymbol{u}^h)dx,\end{aligned} \quad (2.24)$$

where $\boldsymbol{S}^h_{dev}$ denotes the deviatoric part of $\boldsymbol{S}^h$. From this equation we conclude that the deviatoric contribution to the rate of change of kinetic energy is negative and thus this term always dissipates resolved kinetic energy. On the other hand, the dilatational contribution can either add or remove kinetic energy. When $\nabla\cdot\boldsymbol{u}^h < 0$, that is we have a flow where resolved scales are undergoing a compression, this term is negative and as a result the resolved scales loose kinetic energy. The situation is reversed in the case of an expansion.

Finally we consider Equation (2.22) written for the RBVM model and set

$\boldsymbol{W}^h = [0, \boldsymbol{u}^h, 0]^T$ to arrive at the mechanical energy identity:

$$\begin{aligned}\frac{d}{dt}\Big(\frac{1}{2}\int_\Omega \rho^h |\boldsymbol{u}^h|^2 dx\Big) \;\approx\; & \epsilon^h_{Gal} \\ & -\int_\Omega \rho^h \boldsymbol{S}^h_{dev} : (\boldsymbol{u}^h \otimes \boldsymbol{u}' + \boldsymbol{u}' \otimes \boldsymbol{u}^h + \boldsymbol{u}' \otimes \boldsymbol{u}')_{dev} dx \\ & +\frac{1}{3}\int_\Omega \rho^h (\nabla \cdot \boldsymbol{u}^h)(2\boldsymbol{u}^h \cdot \boldsymbol{u}' + |\boldsymbol{u}'|^2) dx. \end{aligned} \tag{2.25}$$

We have used the $\approx$ symbol above to indicate that we are only considering the dominant RBVM model terms in this equation. The second line of Equation (2.25) contains the RBVM contributions to the deviatoric portion of the subgrid stress, while the third line contains the contributions to the dilatational portion. Further, in both these lines the last term is the Reynolds stress term. We note that there is a significant difference in the structure of the Reynolds stress terms. In the deviatoric case this term is such that it must rely on correlations between $\boldsymbol{u}'$ and $\boldsymbol{u}^h$ to ensure that $\boldsymbol{S}^h_{dev} : (\boldsymbol{u}' \otimes \boldsymbol{u}')_{dev} > 0$ at most spatial locations so that the integral will be dissipative overall. As mentioned in Section 2.2 the approximation for $\boldsymbol{u}'$ calculated using the RBVM approximation does not achieve this. On the other hand, in the dilatational case, *regardless of the correlations between* $\boldsymbol{u}'$ *and* $\boldsymbol{u}^h$ *the Reynolds stress term is such that it always extracts energy from the the coarse scales when they are undergoing a compression, and adds energy when they expand.* In this regard it is exactly like the Smagorinsky-Yoshizawa model. This implies that the RBVM model for the dilatational component of the Reynolds stress will be effective as along as the magnitude of $\boldsymbol{u}'$ is evaluated accurately. Thus it would appear that in the mixed model it is not necessary to add the Smagorinsky component to the dilatational portion of subgrid stresses. So in our mixed model $C_1 = 0$, while C_0 and Pr_t are determined dynamically.

Summary All models described in this paper and tested in the following section are contained in Equation (2.22) (see also Table 2.1). For a direct numerical simulation there are no model terms, so in this equation $\boldsymbol{\tau} = \boldsymbol{0}$ and $C_0 = C_1 = 0$. For the dynamic Smagorinsky-Yoshizawa-eddy diffusivity model (DSYE) the fine scale solution is zero, so $\boldsymbol{\tau} = \boldsymbol{0}$ and C_0, C_1 and Pr_t are determined dynamically

Table 2.1: A concise description of all models based on the terms appearing in Equation (2.22).

Terms	No Model	Smagorinsky-Yoshizawa	RBVM	MM1
$\boldsymbol{\tau}$	$\mathbf{0}$	$\mathbf{0}$	✓	✓
C_0	0	✓	0	✓
C_1	0	✓	0	0
Pr_t^{-1}	0	✓	0	0

using the variational counterpart of the Germano identity [23, 24] (see Section 2.2.3 below). For the residual based variational multiscale model (RBVM) the fine scales are active, that is $\boldsymbol{\tau} \neq \mathbf{0}$ while $C_0 = C_1 = 0$. For the mixed model the fine scales are active $\boldsymbol{\tau} \neq \mathbf{0}$, $C_1 = 0$, while C_0 and Pr_t are determined dynamically. In our simulation of the decay of compressible turbulence using the mixed model we have found that dynamic procedure almost always yields negative values for Pr_t, indicating that RBVM model alone introduces adequate dissipation in the energy equation. In order to avoid unstable solutions we set $Pr_t^{-1} = 0$ whenever this happens. The net result is that in the mixed model the only active term is Smagorinsky model for the deviatoric component of the subgrid stress.

Remark We note that our mixed model is similar to other mixed models, including the scale-similarity model [11, 25, 26, 27] and the tensor-diffusivity model [28, 29] in that it contains distinct models for the cross-stress term and the Reynolds stress term. However, the form of the model term for the cross stress in our model is distinct from other mixed models.

2.2.3 Derivation of the dynamic calculation for C_0, C_1 and Pr_t.

In this section we describe the dynamic procedure we have used to determine the unknown parameters in the LES models. We have utilized the variational counterpart of the Germano identity described in [23, 24].

DSYE model

The equations for this model are given by Equation (2.22) with $\boldsymbol{U}' = 0$. In this equation, in order to focus on the momentum equations we select $\boldsymbol{W}^h = [0, \boldsymbol{w}^h, 0]$,

to arrive at

$$
\begin{aligned}
&(\boldsymbol{w}^h, \boldsymbol{m}^h_{,t}) - (\nabla \boldsymbol{w}^h, \frac{\boldsymbol{m}^h \otimes \boldsymbol{m}^h}{\rho^h}) - (\nabla \cdot \boldsymbol{w}^h, p^h) + \frac{1}{Re}(\nabla \boldsymbol{w}^h, \boldsymbol{\sigma}^h) \\
&+\left(\nabla \boldsymbol{w}^h, 2C_0 \rho^h h^2 |\boldsymbol{S}^h| \boldsymbol{S}^h_{dev} - \frac{2}{3} C_1 \rho^h h^2 |\boldsymbol{S}^h|^2 \boldsymbol{I} \right) = 0 \qquad \forall \boldsymbol{w}^h.
\end{aligned}
\tag{2.26}
$$

In the equations above $h = \pi/k^h$, where k^h is the cutoff wavenumber. The equations for the same model used in a coarser discretization with the finite dimensional space $\mathcal{V}^H \subset \mathcal{V}^h$ are given by

$$
\begin{aligned}
&(\boldsymbol{w}^H, \boldsymbol{m}^H_{,t}) - (\nabla \boldsymbol{w}^H, \frac{\boldsymbol{m}^H \otimes \boldsymbol{m}^H}{\rho^H}) - (\nabla \cdot \boldsymbol{w}^H, p^H) + \frac{1}{Re}(\nabla \boldsymbol{w}^H, \boldsymbol{\sigma}^H) \\
&+\left(\nabla \boldsymbol{w}^H, 2C_0 \rho^H H^2 |\boldsymbol{S}^H| \boldsymbol{S}^H_{dev} - \frac{2}{3} C_1 \rho^H H^2 |\boldsymbol{S}^H|^2 \boldsymbol{I} \right) = 0 \qquad \forall \boldsymbol{w}^H.
\end{aligned}
\tag{2.27}
$$

where $H = \pi/k^H$, where k^H is the cutoff wavenumber at the H-scale. In this study we have selected $k^H = k^h/2$. Since $\mathcal{V}^H \subset \mathcal{V}^h$, we replace $\boldsymbol{w}^h$ with $\boldsymbol{w}^H$ in Equation (2.26), and subtract the resulting equation from Equation (2.27) to arrive at

$$
\begin{aligned}
&\left(\nabla \boldsymbol{w}^H, \frac{\boldsymbol{m}^h \otimes \boldsymbol{m}^h}{\rho^h} - \frac{\boldsymbol{m}^H \otimes \boldsymbol{m}^H}{\rho^H} \right) = \\
&-2C_0 \left(\nabla \boldsymbol{w}^H, \rho^H H^2 |\boldsymbol{S}^H| \boldsymbol{S}^h_{dev} - \rho^h h^2 |\boldsymbol{S}^h| \boldsymbol{S}^h_{dev} \right) \\
&+\frac{2}{3} C_1 \left(\nabla \boldsymbol{w}^H, \rho^H H^2 |\boldsymbol{S}^H|^2 \boldsymbol{I} - \rho^h h^2 |\boldsymbol{S}^h|^2 \boldsymbol{I} \right) \qquad \forall \boldsymbol{w}^H.
\end{aligned}
\tag{2.28}
$$

In arriving the this equation we have set

$$
\begin{aligned}
(\boldsymbol{w}^H, \boldsymbol{m}^H_{,t} - \boldsymbol{m}^h_{,t}) &= 0, \\
(\nabla \cdot \boldsymbol{w}^H, p^H - p^h) &= 0, \\
(\nabla \boldsymbol{w}^H, \boldsymbol{\sigma}^H - \boldsymbol{\sigma}^h) &= 0,
\end{aligned}
\tag{2.29}
$$

the first two relations above hold exactly for a Fourier-spectral spatial discretization, while the last is an assumption.

In Equation (2.28) we select $\nabla \boldsymbol{w}^H = \boldsymbol{S}^H_{dev}$, and recognize that $(\boldsymbol{S}_{dev}, \boldsymbol{I}) = 0$,

to arrive at

$$\begin{aligned}\left(\boldsymbol{S}^H_{dev}, \frac{\boldsymbol{m}^h \otimes \boldsymbol{m}^h}{\rho^h} - \frac{\boldsymbol{m}^H \otimes \boldsymbol{m}^H}{\rho^H}\right) = \\ -2C_0(\boldsymbol{S}^H_{dev}, \rho^H H^2 |\boldsymbol{S}^H| \boldsymbol{S}^H_{dev} - \rho^h h^2 |\boldsymbol{S}^h| \boldsymbol{S}^h_{dev}),\end{aligned} \tag{2.30}$$

which yields the final expression for C_0,

$$C_0 = -\frac{1}{2} \frac{\left(\boldsymbol{S}^H_{dev}, \frac{\boldsymbol{m}^h \otimes \boldsymbol{m}^h}{\rho^h} - \frac{\boldsymbol{m}^H \otimes \boldsymbol{m}^H}{\rho^H}\right)}{\left(\boldsymbol{S}^H_{dev}, \rho^H H^2 |\boldsymbol{S}^H| \boldsymbol{S}^H_{dev} - \rho^h h^2 |\boldsymbol{S}^h| \boldsymbol{S}^h_{dev}\right)}. \tag{2.31}$$

In order to determine C_1 we select $\nabla \boldsymbol{w}^H = \boldsymbol{I}$ in Equation (2.28), to arrive at

$$\begin{aligned}\left(1, tr\big(\frac{\boldsymbol{m}^h \otimes \boldsymbol{m}^h}{\rho^h} - \frac{\boldsymbol{m}^H \otimes \boldsymbol{m}^H}{\rho^H}\big)\right) = \\ 2C_1(1, \rho^H H^2 |\boldsymbol{S}^H|^2 - \rho^h h^2 |\boldsymbol{S}^h|^2),\end{aligned} \tag{2.32}$$

which yields

$$C_1 = \frac{1}{2} \frac{\left(1, tr\big(\frac{\boldsymbol{m}^h \otimes \boldsymbol{m}^h}{\rho^h} - \frac{\boldsymbol{m}^H \otimes \boldsymbol{m}^H}{\rho^H}\big)\right)}{(1, \rho^H H^2 |\boldsymbol{S}^H|^2 - \rho^h h^2 |\boldsymbol{S}^h|^2)}. \tag{2.33}$$

In order to determine the turbulent Prandtl number in Equation (2.22), we choose $\boldsymbol{W}^h = [0, 0, q^h]$ to get

$$\begin{aligned}&(q^h, p^h_{,t}) - (\nabla q^h, \boldsymbol{u}^h p^h) - (1-\gamma)(q^h, p^h \nabla \cdot \boldsymbol{u}^h) \\ &- \frac{(\gamma - 1)}{Re}(q^h, \Phi^h) + \frac{1}{M^2_\infty Pr Re}(\nabla q^h, \mu^h \nabla T^h) \\ &+ \big(\nabla q^h, \quad \frac{C_0}{Pr_t \gamma M^2_\infty} h^2 \rho^h |\boldsymbol{S}^h| \nabla T^h\big) = 0 \qquad \forall q^h.\end{aligned} \tag{2.34}$$

Similarly at the $H-$scale we arrive at

$$\begin{aligned}
&(q^H, p^H_{,t}) - (\nabla q^H, \boldsymbol{u}^H p^H) - (1-\gamma)(q^H, p^H \nabla \cdot \boldsymbol{u}^H) \\
&- \frac{(\gamma-1)}{Re}(q^H, \Phi^H) + \frac{1}{M_\infty^2 Pr Re}(\nabla q^H, \mu^H \nabla T^H) \\
&+ \left(\nabla q^H, \quad \frac{C_0}{Pr_t \gamma M_\infty^2} H^2 \rho^H |\boldsymbol{S}^H| \nabla T^H\right) = 0 \qquad \forall q^H.
\end{aligned} \tag{2.35}$$

Since $\mathcal{V}^H \subset \mathcal{V}^h$, we may replace q^h with q^H in (2.34) and subtract the result from Equation (2.35) to arrive at

$$\begin{aligned}
&\left(\nabla q^H, \frac{\boldsymbol{m}^h p^h}{\rho^h} - \frac{\boldsymbol{m}^H p^H}{\rho^H}\right) = \\
&\frac{C_0}{Pr_t \gamma M_\infty^2}\left(\nabla q^H, h^2 \rho^h |\boldsymbol{S}^h| \nabla T^h - H^2 \rho^H |\boldsymbol{S}^H| \nabla T^H\right) \qquad \forall q^H.
\end{aligned} \tag{2.36}$$

Where we have made use of

$$\begin{aligned}
(q^H, p^H_{,t} - p^h_{,t}) &= 0, \\
(q^H, p^H \nabla \cdot \boldsymbol{u}^H - p^h \nabla \cdot \boldsymbol{u}^h) &= 0, \\
(q^H, \Phi^H - \Phi^h) &= 0, \\
(\nabla q^H, \mu^H \nabla T^H - \mu^h \nabla T^h) &= 0.
\end{aligned} \tag{2.37}$$

The first relation above holds exactly for a Fourier-spectral spatial discretization, while the others are assumed. We let $\nabla q^H = \nabla T^H$, in Equation (2.36) and arrive at

$$\begin{aligned}
&\left(\nabla T^H, \frac{\boldsymbol{m}^h p^h}{\rho^h} - \frac{\boldsymbol{m}^H p^H}{\rho^H}\right) = \\
&\frac{C_0}{Pr_t \gamma M_\infty^2}\left(\nabla T^H, h^2 \rho^h |\boldsymbol{S}^h| \nabla T^h - H^2 \rho^H |\boldsymbol{S}^H| \nabla T^H\right).
\end{aligned} \tag{2.38}$$

This equation yields

$$Pr_t = \frac{C_0}{\gamma M_\infty^2} \frac{\left(\nabla T^H, h^2 \rho^h |\boldsymbol{S}^h| \nabla T^h - H^2 \rho^H |\boldsymbol{S}^H| \nabla T^H\right)}{\left(\nabla T^H, \dfrac{\boldsymbol{m}^h p^h}{\rho^h} - \dfrac{\boldsymbol{m}^H p^H}{\rho^H}\right)}. \tag{2.39}$$

Mixed model

The procedure in this case is the same as for the DYSE model, except in Equation (2.22) $\boldsymbol{U}' \neq 0$. In particular we get

$$C_0 = -\frac{1}{2} \frac{\left(\boldsymbol{S}_{dev}^H, \frac{(\boldsymbol{m}^h + \boldsymbol{m}') \otimes (\boldsymbol{m}^h + \boldsymbol{m}')}{\rho^h + \rho'} - \frac{(\boldsymbol{m}^H + \boldsymbol{m}'') \otimes (\boldsymbol{m}^H + \boldsymbol{m}'')}{\rho^H + \rho''}\right)}{\left(\boldsymbol{S}_{dev}^H, \rho^H H^2 |\boldsymbol{S}^H| \boldsymbol{S}_{dev}^H - \rho^h h^2 |\boldsymbol{S}^h| \boldsymbol{S}_{dev}^h\right)}, \tag{2.40}$$

and

$$Pr_t = \frac{C_0}{\gamma M_\infty^2} \frac{\left(\nabla T^H, h^2 \rho^h |\boldsymbol{S}^h| \nabla T^h - H^2 \rho^H |\boldsymbol{S}^H| \nabla\ T^H\right)}{\left(\nabla T^H, \frac{(\boldsymbol{m}^h + \boldsymbol{m}')(\overline{p}^h + p')}{\rho^h + \rho'} - \frac{(\boldsymbol{m}^H + \boldsymbol{m}'')(p^H + p'')}{\rho^H + \rho''}\right)}. \tag{2.41}$$

Where ρ', $\boldsymbol{m}'$ and p' are the fine scale variables at the h-scale and ρ'', $\boldsymbol{m}''$ and p'' are the variables at the H-scale.

Remark: In the DSYE model, C_0, C_1 and Pr_t are calculated dynamically, while in the mixed model only C_0 and Pr_t are using dynamic valure and $C_1 = 0$ as it should has no contribution.

2.3 Residual based eddy viscosity model (RBEV)

2.3.1 Weak form of the RBEV model

An approximate solution to the weak form of Navier Stokes Equations (2.1) − (2.2) and Equations (2.3) − (2.5) is obtained by approximating the infinite dimensional space $\mathcal{V}$ with a finite dimensional $\mathcal{V}^h \subset \mathcal{V}$. The equation for the approximate

solution $\boldsymbol{U}^h$ is given by: find $\boldsymbol{U}^h \in \mathcal{V}^h$ such that

$$A(\boldsymbol{W}^h, \boldsymbol{U}^h) = (\boldsymbol{W}^h, \boldsymbol{F}) \quad \forall \boldsymbol{W}^h \in \mathcal{V}^h. \tag{2.42}$$

When $\mathcal{V}^h$ is sufficiently refined so as to resolve all scales of motion down to the Kolmogorov length scale, $\boldsymbol{U}^h$ represents the direct numerical simulation (DNS) solution. However, when this is not the case, and the fine scales are not represented, $\boldsymbol{U}^h$ is very inaccurate and represents the coarse DNS solution. The accuracy of this solution may be improved by adding to it terms that model the effect of the missing or unresolved scales on the resolved scales. In this case Equation (2.42) is replaced by: find $\boldsymbol{U}^h \in \mathcal{V}^h$ such that

$$A(\boldsymbol{W}^h, \boldsymbol{U}^h) + M(\boldsymbol{W}^h, \boldsymbol{U}^h) = (\boldsymbol{W}^h, \boldsymbol{F}) \quad \forall \boldsymbol{W}^h \in \mathcal{V}^h. \tag{2.43}$$

where $M(\boldsymbol{W}^h, \boldsymbol{U}^h)$ denotes the model term.

In the incompressible case the model term is often represented by an eddy viscosity in direct analogy with the viscous models for transfer of momentum through molecular motion. The assumption is that the subgrid turbulent eddies redistribute momentum among the coarse velocity scales just like the thermal fluctuations of particles redistribute momentum among the continuum velocity scales. It is therefore reasonable to assume, in direct analogy with molecular diffusion of momentum that the eddy viscosity $\nu_t = \bar{C}h|\boldsymbol{u}'|$, where $|\boldsymbol{u}'|$ plays the role of the thermal velocity fluctuations and the grid size h plays the role of mean free path of these eddies. As a result we have

$$M(\boldsymbol{W}^h, \boldsymbol{U}^h) = (\nabla^s \boldsymbol{w}^h, 2\bar{C}h|\boldsymbol{u}'|\boldsymbol{S}^h). \tag{2.44}$$

The constant $\bar{C}$ in the above equation may be determined by equating the dissipation induced by the model term to the total dissipation and is derived in Section 2.3.2. This yields $\bar{C} = 0.0740$.

For turbulent flows where compressibility is important, following Yoshizawa, the fine scale fluctuations introduce two other terms. As a result we propose

$$\begin{aligned} M(\boldsymbol{W}^h, \boldsymbol{U}^h) = \quad & 2\bar{C}(\nabla^s \boldsymbol{w}^h, \rho^h h|\boldsymbol{u}'|\boldsymbol{S}^h_{dev}) \\ & - \frac{1}{3}(\nabla \cdot \boldsymbol{w}^h, \rho^h |\boldsymbol{u}'|^2) + \frac{\bar{C}}{Pr_t \gamma M_\infty^2}(\nabla q^h, \rho^h h|\boldsymbol{u}'|\nabla T^h). \end{aligned} \tag{2.45}$$

In the equation above $Pr_t = 0.5$ is the turbulent Prandtl number assumed to be constant.

In the expressions above there is no undetermined parameter, however we have made use of $\boldsymbol{u}'$, the fine scale velocity field, which is obviously not known in a coarse scale simulation. However, tt may be evaluated using the VMS formulation as described in Section 2.1.

2.3.2 Estimate of the RBEV parameter $\bar{C}$

In this subsection, we determine the value of RBEV parameter $\bar{C}$. The constant $\bar{C}$ is determined by equating the dissipation induced by the model term to the total dissipation. The idea is similar as the derivation of static Smagorinsky parameter c_s [30]. The derivation presented in this section is based on homogeneous isotropic turbulence, and uses the knowledge of *Kolmogorov spectrum* described in Section 3.3.

The RBEV model can be viewed in two parts. First, the linear eddy-viscosity model

$$\tau_{ij} = -2\nu_t S^h_{ij}, \tag{2.46}$$

is used to relate the residual stress to the filtered rate of strain. The coefficient of proportionality ν_t is the eddy viscosity of the residual motions. Second, the eddy viscosity is modeled as

$$\nu_t = \bar{C} h |\boldsymbol{u}'|, \tag{2.47}$$

where the grid size is defined as $h = \pi/k^h$ and k^h is the cutoff wavenumber. According to the eddy-viscosity model, the rate of transfer of energy to the residual motions or the dissipation ε is

$$\varepsilon = -\tau_{ij} S_{ij}^h. \tag{2.48}$$

In addition, we need the Kolmogorov spectrum, it is shown as

$$E(k) = C_K \varepsilon^{2/3} k^{-5/3}, \tag{2.49}$$

where C_K is the Kolmogorov constant. Using Equations (2.46) and (2.49) in Equation (2.48), we get,

$$\varepsilon = 2\nu_t S_{ij}^h S_{ij}^h, \tag{2.50}$$

because

$$S_{ij}^h S_{ij}^h = \int_0^{k^h} k^2 E(k) dk, \tag{2.51}$$

so

$$\varepsilon = 2\nu_t \int_0^{k^h} k^2 E(k) dk, \tag{2.52}$$

with Equation (2.47), Equation (2.52) becomes

$$\varepsilon = 2\bar{C} h |\boldsymbol{u}'| \int_0^{k^h} k^2 E(k) dk, \tag{2.53}$$

with

$$|\boldsymbol{u}'| = |u_i' u_i'|^{1/2} = \big(2 \int_{k^h}^{\infty} E(k) dk\big)^{1/2}, \tag{2.54}$$

so

$$\varepsilon = 2\bar{C}h\big(2\int_{k^h}^{\infty} E(k)dk\big)^{1/2}\int_0^{k^h} k^2 E(k)dk. \tag{2.55}$$

Put Equation (2.49) into Equation (2.55)

$$\varepsilon = 2\bar{C}h(2\int_{k^h}^{\infty} C_K\varepsilon^{2/3}k^{-5/3}dk)^{1/2}\int_0^{k^h} k^2 C_K\varepsilon^{2/3}k^{-5/3}dk. \tag{2.56}$$

Finally we arrive at

$$\bar{C} = \frac{2}{3\sqrt{3}C_K^{3/2}\pi}. \tag{2.57}$$

With Kolmogorov constant $C_K = 1.4$, we get $\bar{C} = 0.0740$.

2.4 A purely residual based mixed model (MM2)

In Section 2.2, a mixed model based on the RBVM and dynamic Smagorinsky-Yoshizawa-eddy diffusivity (DSYE) model was proposed. It is motivated by the work [19] for incompressible flows. The authors demonstrated that while the RBVM model works well for the cross-stress term it does not introduce an adequate model for the Reynolds stress term. Our work in Section 2.2 fellows the same idea. We use the DSYE model to simulate the effect of Reynolds stress term while the RBVM for the cross-stress term. However, as it is shown in Section 2.2, in order to implement the dynamic Smagorinsky-Yoshizawa-eddy diffusivity components in the mixed model (MM1), the dynamic parameters C_0 and Pr_t must be evlauated. The procedure for calculating these parameters involves the variational counterpart of the Germano identity, which needs two different coarse scales and is cumbersome to implement. This is especially true when there is no homogeneous coordinate along which one might evaluate averages, and when solving problems with general unstructured grids.

In Section 2.1 we proposed a new RBEV model that is easy to implement and contains no undetermined dynamic parameters. However, the model is inherently

dynamic in that it automatically vanished when the residual of the coarse scales is small. Thus it presents in alternative model that may be used with the RBVM model in order to create a new mixed model. In comparison with the mixed proposed in Section 2.2 this model is purely residual based, and doe not rely on the dynamic evaluation of parameters. We refer to this mixed model as MM2.

MM2 for Incompressible flows:

For the incompressible flow, the purely residual based mixed model (MM2) is given by: Find $\boldsymbol{U}^h \in \mathcal{V}^h$, such that

$$A\big(\boldsymbol{W}^h, \boldsymbol{U}^h + b_1\boldsymbol{U}'\big) + \big(\nabla \boldsymbol{w}^h, 2\bar{C}\rho^h h|\boldsymbol{u}'|\boldsymbol{S}^h\big) = (\boldsymbol{W}^h, \boldsymbol{F}) \qquad \forall \boldsymbol{W}^h \in \mathcal{V}^h. \tag{2.58}$$

where $\boldsymbol{U} = [\boldsymbol{u}, p]^T$ are the unknowns with $\boldsymbol{F} = [\boldsymbol{f},\ 0]^T$, and $A(\cdot,\cdot)$ is defined in Equation (2.12), $\boldsymbol{S}^h$ is the rate of strain. We note that in comparison with the mixed model MM1 (see Equation (2.21)), in MM2 the Smagorinsky term is replaced by the RBEV term.

MM2 for Compressible flows:

For the compressible flow, the purely residual based mixed model (MM2) is given by: Find $\boldsymbol{U}^h \in \mathcal{V}^h$, such that

$$\begin{aligned} &A\big(\boldsymbol{W}^h, \boldsymbol{U}^h + \boldsymbol{U}'\big) \\ &+ \big(\nabla \boldsymbol{w}^h, 2\bar{C}\rho^h h|\boldsymbol{u}'|\boldsymbol{S}^h_{dev}\big) - \big(\nabla \cdot \boldsymbol{w}^h, \frac{1}{3}\rho^h|\boldsymbol{u}'|^2\big) \\ &+ \big(\nabla q^h, \frac{\bar{C}}{Pr_t\gamma M_\infty^2}\rho^h h|\boldsymbol{u}'|\nabla T^h\big) \\ &\qquad\qquad = (\boldsymbol{W}^h, \boldsymbol{F}) \qquad \forall \boldsymbol{W}^h \in \mathcal{V}^h, \end{aligned} \tag{2.59}$$

where $\boldsymbol{U} = [\rho, \boldsymbol{m}, p]^T$ are the unknowns with $\boldsymbol{F} = [0, \boldsymbol{f}, 0]^T$, and $A(\cdot,\cdot)$ is defined in Equation (2.13), $\boldsymbol{S}^h$ is the rate of strain computed the velocity field $\boldsymbol{u}^h \equiv \boldsymbol{m}^h/\rho^h$, the subscript dev denotes its deviatoric component and $T^h \equiv \gamma M_\infty^2 p^h/\rho^h$.

Compared with Equation (2.19), we note that three new terms have been

added. The first two term models the deviatoric and dilatational components of the subgrid scale stress tensor and the third term models the subgrid heat flux vector. In comparison with the mixed model MM1, we note that the Smagorinsky and the eddy diffusivity term have been replaced by their RBEV counterparts. We note that we do not need a RBEV term for the diltational component of the residual stresses because the RBVM formulation already provides this (see the discussion in Section 2.2.2).

Remark We note that our mixed model is similar to other mixed models, including the scale-similarity model [11, 25, 26, 27] and the tensor-diffusivity model [28, 29] in that it contains distinct models for the cross-stress term and the Reynolds stress term. However, the form of the model term for the cross stress in our model is distinct from other mixed models. In addition, this purely residual based mixed model (MM2) is much easier for the implementation than the mixed model based on dynamic Smagorinsky model (MM1).

CHAPTER 3
Large-Eddy Simulation of Compressible Homogeneous Isotropic Turbulent Flows

3.1 Introduction

In this chapter, we test the performance of the four LES models developed in Chapter 2 for compressible turbulent flows within a Fourier-spectral method method. They are

- the residual-based variational multiscale (RBVM) model
- the mixed model based on RBVM (MM1)
- the residual-based eddy viscosity (RBEV) model
- the purely-residual based mixed model (MM2)

We will test the performance of these LES models in predicting the decay of compressible, homogeneous, isotropic turbulence in regimes where shocklets are known to exist. The LES models will be tested with Taylor micro-scale Reynolds numbers of $Re_\lambda \approx 65$ and $Re_\lambda \approx 120$ on 32^3 and 64^3 grids.

The layout of this chapter is as follows. In Section 3.2, we specialize the weak form of the models developed in Chapter 2 to a spectral method that utilizes Fourier basis functions. The precise definition for the unresolved scales, and well as the parameters $\boldsymbol{\tau}$ is also provided. Homogeneous Isotropic Turbulence (HIT) is introduced in Section 3.3 to understand the behavior of turbulent flows. In Section 3.4, we apply the RBVM model and the MM1 model to decay of compressible

Portions of this chapter previously appeared as: J. Liu, and A. A. Oberai, "The residual-based variational multiscale formulation for the large eddy simulation of compressible flows, " *Comput. Methods Appl. Mech. Eng.*, accepted, 2012.

turbulent flows. In Section 3.5, the RBEV model and the MM2 model will be applied to to study the same flows. Conclusions are drawn in Section 3.6.

3.2 LES models

In Chapter 2, we have introduced and developed the residual based variational multiscale model (RBVM), a mixed model based on RBVM (MM1), the residual based eddy viscosity model (RBEV) and the purely residual based mixed model (MM2). In this chapter we will apply these LES models to study the decay of compressible homogeneous isotropic turbulent flows by using a Fourier-spectral method.

3.2.1 Weak form of LES models

RBVM and MM1 models:

The weak form of the RBVM and MM1 models is given by Equation (2.22) in Chapter 2. It is repeated here for convenience: Find $\boldsymbol{U}^h \in \mathcal{V}^h$, such that

$$\begin{aligned} & A\big(\boldsymbol{W}^h, \boldsymbol{U}^h + \boldsymbol{U}'\big) \\ & + \big(\nabla \boldsymbol{w}^h, 2C_0 h^2 \rho^h |\boldsymbol{S}^h| \boldsymbol{S}^h_{dev}\big) - \big(\nabla \boldsymbol{w}^h, \frac{2}{3} C_1 h^2 \rho^h |\boldsymbol{S}^h|^2 \boldsymbol{I}\big) \\ & + \big(\nabla q^h, \quad \frac{C_0}{Pr_t \gamma M_\infty^2} h^2 \rho^h |\boldsymbol{S}^h| \nabla T^h\big) \\ & \qquad\qquad = (\boldsymbol{W}^h, \boldsymbol{F}) \qquad \forall \boldsymbol{W}^h \in \mathcal{V}^h, \end{aligned} \tag{3.1}$$

In Equation (3.1), C_0, C_1 and ${Pr_t}^{-1}$ are three parameters and $\boldsymbol{U}'$ is given by Equation (2.18). This equation contains the following LES models within it:

- With $C_0 = C_1 = {Pr_t}^{-1} = 0$ and $\boldsymbol{\tau} = \boldsymbol{0}$, we arrive at the direct numerical simulation (DNS).
- With $C_0 = C_1 = {Pr_t}^{-1} = 0$, but $\boldsymbol{\tau} \neq \boldsymbol{0}$, we arrive at the residual based variational multiscale model (RBVM).
- With C_0, C_1 and ${Pr_t}^{-1}$ are determined dynamically, and $\boldsymbol{\tau} = \boldsymbol{0}$, we arrive at the dynamic Smagorinsky-Yoshizawa-eddy diffusivity model (DSYE).

- With C_0, C_1 and ${Pr_t}^{-1}$ are kept at a fixed value, and $\boldsymbol{\tau} = \mathbf{0}$, we arrive at the static Smagorinsky-Yoshizawa-eddy diffusivity model (SSYE).

- With C_0 and ${Pr_t}^{-1}$ are determined dynamically, $C_1 = 0$ and $\boldsymbol{\tau} \neq \mathbf{0}$ we arrive at mixed model based on RBVM and DSYE (MM1).

RBEV and MM2 models:

The weak from for the RBEV and the MM2 models is given by Equation (2.59) in Chapter 2. It is repeated here for convenience:
Find $\boldsymbol{U}^h \in \mathcal{V}^h$, such that

$$\begin{aligned} & A\big(\boldsymbol{W}^h, \boldsymbol{U}^h + b_1 \boldsymbol{U}'\big) \\ & + \big(\nabla \boldsymbol{w}^h, 2\bar{C}\rho^h h|\boldsymbol{u}'|\boldsymbol{S}^h_{dev}\big) - \big(\nabla \cdot \boldsymbol{w}^h, b_2 \frac{1}{3}\rho^h |\boldsymbol{u}'|^2\big) \\ & + \big(\nabla q^h, \frac{\bar{C}}{Pr_t \gamma M^2_\infty}\rho^h h|\boldsymbol{u}'|\nabla T^h\big) \\ & \qquad\qquad = (\boldsymbol{W}^h, \boldsymbol{F}) \qquad \forall \boldsymbol{W}^h \in \mathcal{V}^h, \end{aligned} \tag{3.2}$$

In Equation (3.2), b_1, b_2 are parameters. This equation contains the following LES models within it:

- With $b_1 = b_2 = \bar{C} = 0$, we arrive at the direct numerical simulation (DNS).

- With $b_2 = \bar{C} = 0$, but $b_1 \neq 0$, we arrive at the residual based variational multiscale model (RBVM).

- With $b_2 \neq 0$ and $\bar{C} \neq 0$ but $b_1 = 0$, we arrive at the residual based eddy viscosity model (RBEV).

- With $b_1 \neq 0$ and $\bar{C} \neq 0$ while $b_2 = 0$, we arrive at the purely residual based mixed model (MM2).

3.2.2 Unresolved scales and stabilization parameter $\boldsymbol{\tau}$

The unresolved scales $\boldsymbol{U}' = [\rho', \boldsymbol{m}', p']$ that appear in Equations (3.1) and (3.2) are determined by

$$\boldsymbol{U}' \approx -\mathbb{P}'\boldsymbol{\tau}(\boldsymbol{U}^h)\,\mathbb{P}'^T\mathcal{R}(\boldsymbol{U}^h), \tag{3.3}$$

where $\mathbb{P}'$ is a projection operator that maps an element of $\mathcal{V}$ to $\mathcal{V}'$ and $\mathcal{R}(\boldsymbol{U}^h) \equiv \mathcal{L}\boldsymbol{U}^h - \boldsymbol{F}$ is the coarse-scale residual. For other details, please refer to the discussion in Section 2.

The coarse-scale residual $\mathcal{R}(\boldsymbol{U}^h) = (\mathcal{R}_\rho, \mathcal{R}_{\boldsymbol{m}}, \mathcal{R}_p)^T$ is given by

$$\begin{aligned}
\mathcal{R}_\rho &= \frac{\partial \rho^h}{\partial t} + \nabla \cdot \boldsymbol{m}^h, && (3.4)\\
\mathcal{R}_{\boldsymbol{m}} &= \frac{\partial \boldsymbol{m}^h}{\partial t} + \nabla \cdot (\frac{\boldsymbol{m}^h \otimes \boldsymbol{m}^h}{\rho^h}) + \nabla p^h - \frac{1}{Re}\nabla \cdot \boldsymbol{\sigma}^h - \boldsymbol{f}, && (3.5)\\
\mathcal{R}_p &= \frac{\partial p^h}{\partial t} + \nabla \cdot (\boldsymbol{u}^h p^h) - (\gamma - 1)p^h \nabla \cdot \boldsymbol{u}^h - \frac{(\gamma-1)}{Re}\Phi^h \\
&\quad - \frac{1}{M_\infty^2 PrRe}\nabla \cdot (\mu^h \nabla T^h). && (3.6)
\end{aligned}$$

We assume a diagonal form for the matrix $\boldsymbol{\tau}$, that is $\boldsymbol{\tau} = diag(\tau_c, \tau_m, \tau_m, \tau_m, \tau_e)$. Each of τ_c, τ_m and τ_e represents a combination of an advective and a diffusive time-scale associated with differential operator for the fine scales. Our definition for $\boldsymbol{\tau}$ for the compressible Navier-Stokes equations is motivated by the work of [15, 31]. The τ's are given by

$$\begin{aligned}
\tau_c &= C_\tau \Big[\quad (\lambda)^2 \quad \Big]^{-1/2}, \\
\tau_m &= C_\tau \Big[\quad (\lambda)^2 + \left(\frac{4}{h^2}\frac{<\mu^h>}{<\rho^h> Re}\right)^2 \quad \Big]^{-1/2}, \\
\tau_e &= C_\tau \Big[\quad (\lambda)^2 + \left(\frac{4}{h^2}\frac{\gamma <\mu^h>}{<\rho^h> P_r Re}\right)^2 \quad \Big]^{-1/2},
\end{aligned} \tag{3.7}$$

with

$$\frac{1}{\lambda^e} = \frac{1-e^{-Ma}}{\lambda_1^e} + \frac{e^{-Ma}}{\lambda_2^e}, \tag{3.8}$$

$$(\lambda_1^e)^2 = \frac{4}{h^2} < |\boldsymbol{u}^h|^2 > (1 + 2Ma^{-2} + Ma^{-1}\sqrt{4 + Ma^{-2}}), \tag{3.9}$$

$$(\lambda_2^e)^2 = \frac{4}{h^2} < |\boldsymbol{u}^h|^2 >, \tag{3.10}$$

where $h = \frac{\pi}{k^h}$ is the grid size, $\boldsymbol{u} = \frac{\boldsymbol{m}^h}{\rho^h}$, $< \cdot >$ denotes the spatial average of a quantity, $Ma = \sqrt{< |\boldsymbol{u}^h|^2 >}/ < c^h >$ is the turbulent Mach number, and $c^h = (T^h)^{1/2}/M_\infty$ is the local speed of sound. C_τ is constant, which is either 1 or 1/2. In the equation above λ is the reciprocal of the characteristic advective time scale. It is a combination of a time scale that is appropriate for the low-Mach number limit λ_2 and another that is appropriate for the high Mach number limit, λ_1. In this case λ can be thought of as a doubly-asymptotic approximation of the two. We note that a similar approximation was proposed in [31], however it underestimated the value of λ in the compressible limit.

3.2.3 Specialization to a Fourier spectral basis

We will apply the RBVM model, the MM1 model, the RBEV model and the MM2 model to simulate the decay of homogeneous isotropic turbulence of compressible flows. We assume that $\Omega =]0, 2\pi[^3$ and the density, velocity and pressure fields satisfy periodic boundary conditions. We propose to simulate this problem using the Fourier-spectral method. In this case the space of functions $\mathcal{V}^h$ are approximated by a Fourier-spectral basis. Fourier modes with $|\boldsymbol{k}| < k^h$ are used to define $\mathcal{V}^h$. We note that these basis functions have the special property that they are orthogonal to each other in all H^m inner-products. In addition, we define the projector $\mathbb{P}^h$ to be the H^1 projection and due to the orthogonality of the Fourier modes this is the low-pass sharp cut-off filter in wavenumber space. Then $\mathbb{P}'$ is the high-pass, sharp cutoff filter in wavenumber space.

As a result of this, the expression for the fine scale variables $\boldsymbol{U}' = [\rho', \boldsymbol{m}, p']^T$

simplify to:

$$\begin{aligned}
\rho' &= 0, && (3.11)\\
\boldsymbol{m}' &= -\mathbb{P}'\tau_m\mathbb{P}'^T\big(\nabla\cdot(\frac{\boldsymbol{m}^h\otimes\boldsymbol{m}^h}{\rho^h})-\frac{1}{Re}\nabla\cdot\boldsymbol{\sigma}^h\big), && (3.12)\\
p' &= -\mathbb{P}'\tau_e\mathbb{P}'^T\big(\nabla\cdot(\boldsymbol{u}^hp^h)-(\gamma-1)p^h\nabla\cdot\boldsymbol{u}^h-\frac{(\gamma-1)}{Re}\Phi^h\\
&\quad -\frac{1}{M_\infty^2PrRe}\nabla\cdot(\mu^h\nabla T^h)\big). && (3.13)
\end{aligned}$$

Further, the equations for all the LES models derived in the previous section simplify to

$$\begin{aligned}
\frac{\partial\widehat{\rho}^h}{\partial t} &+ i\boldsymbol{k}\cdot\widehat{\boldsymbol{m}}^h=0, && (3.14)\\
\frac{\partial\widehat{\boldsymbol{m}}^h}{\partial t} &+ i\boldsymbol{k}\cdot\frac{\widehat{\boldsymbol{m}\otimes\boldsymbol{m}}}{\rho}+i\boldsymbol{k}\widehat{p}^h=\\
&\quad \frac{i\boldsymbol{k}\cdot\widehat{\boldsymbol{\sigma}}}{Re}+i\boldsymbol{k}\cdot2\widehat{\rho^h\nu_t\boldsymbol{S}^h_{dev}}-\frac{i\boldsymbol{k}}{3}\widehat{\rho^hu^2_{rms}}, && (3.15)\\
\frac{\partial\widehat{p}^h}{\partial t} &+ i\boldsymbol{k}\cdot\widehat{\boldsymbol{u}p}+(\gamma-1)\widehat{p\nabla\cdot\boldsymbol{u}}=\\
&\quad \frac{(\gamma-1)}{Re}\widehat{\boldsymbol{\sigma}:\boldsymbol{S}}+\frac{i\boldsymbol{k}}{M_\infty^2}\cdot\big(\frac{\widehat{\mu(T)\nabla T}}{PrRe}+\frac{\widehat{\rho^h\nu_t\nabla T^h}}{\gamma Pr_t}\big), && (3.16)
\end{aligned}$$

where the hat denotes the Fourier coefficient of a variable corresponding to a wavenumber $\boldsymbol{k}$. In addition $\rho=\rho^h+\rho'$, $\boldsymbol{m}=\boldsymbol{m}^h+\boldsymbol{m}'$, $p=p^h+p'$, $\boldsymbol{u}=\boldsymbol{m}/\rho$, $\boldsymbol{u}^h=\boldsymbol{m}^h/\rho^h$, $T=\gamma M_\infty^2p/\rho$, $T^h=\gamma M_\infty^2p^h/\rho^h$, $\boldsymbol{S}$ and $\boldsymbol{S}^h$ are the symmetric gradients of $\boldsymbol{u}$ and $\boldsymbol{u}^h$ respectively, and $\boldsymbol{\sigma}=\mu(T)\boldsymbol{S}_{dev}$.

All the models to be tested in this can be obtained by defining ν_t and u_{rms} as follows:

1. For no model (DNS), $\nu_t=u_{rms}=0$ and $\rho'=\boldsymbol{m}'=p'=0$.

2. For the static Smagorinsky-Yoshizawa eddy viscosity model (Static SYE), $\nu_t=C_0^2h^2|\boldsymbol{S}^h|$ and $u^2_{rms}=2C_1h^2|\boldsymbol{S}^h|^2$, where $C_0=0.1,0.16$, $C_1=0.020$ and $Pr_t=0.5$, and $\rho'=\boldsymbol{m}'=p'=0$.

3. For the dynamic Smagorinsky-Yoshizawa eddy viscosity model (DSYE), $\nu_t = C_0^2 h^2 |\boldsymbol{S}^h|$ and $u_{rms}^2 = 2C_1 h^2 |\boldsymbol{S}^h|^2$, where C_0, C_1 and Pr_t are determined dynamically, and $\rho' = \boldsymbol{m}' = p' = 0$.

4. For the residual based variational multiscale model (RBVM), $\nu_t = u_{rms} = 0$, ρ', $\boldsymbol{m}'$ and p' are given by Equations (3.11)-(3.13).

5. For the MM1 model, $\nu_t = C_0^2 h^2 |\boldsymbol{S}^h|$ and $u_{rms}^2 = 0$, where C_0 and Pr_t are determined dynamically, and ρ', $\boldsymbol{m}'$ and p' are given by Equations (3.11)-(3.13).

6. For the residual based eddy viscosity model (RBEV) $\nu_t = \bar{C} h |\boldsymbol{u}'|$ and $u_{rms} = |\boldsymbol{u}'|$, where $\boldsymbol{u}'$ is given by $\boldsymbol{u}' = \frac{\boldsymbol{m}'}{\rho^h}$ with $\boldsymbol{m}'$ given by Equation (3.12), $\bar{C} = 0.0740$ and $Pr_t = 0.5$. However, in all the other terms $\rho' = \boldsymbol{m}' = p' = 0$.

7. For the MM2 model, $\nu_t = \bar{C} h |\boldsymbol{u}'|$ and $u_{rms} = |\boldsymbol{u}'|$, where $\boldsymbol{u}'$ is given by $\boldsymbol{u}' = \frac{\boldsymbol{m}'}{\rho^h}$, $\bar{C} = 0.0740$ and $Pr_t = 0.5$. ρ', $\boldsymbol{m}'$ and p' are given by Equations (3.11)-(3.13).

3.3 Homogeneous Isotropic Turbulence (HIT)

The concept of using statistical methods for the analysis of turbulent flows was introduced by G. I. Taylor in the 1930s. These methods include using studying structure functions and their Fourier transforms in order to understand turbulent flows. As mentioned in Chapter 1, in 1941 the Russian statistician Kolmogorov published three papers [5, 6, 7] on the statistical theories of turbulence, which is known as the K41 theory. His theory provides a prediction of the structure functions and their Fourier transforms for of a homogeneous isotropic turbulent flow. Kolmogorov demonstrated that even though the velocity of a homogeneous isotropic turbulent flow fluctuates in an unpredictable manner, the energy spectrum (how much kinetic energy is present on average at a particular length scale) is predictable.

Homogeneous isotropic turbulence

Homogeneous isotropic turbulence is the simplest and most fundamental turbulent flow. If all the statistics of turbulence are invariant under a shift in position, the field $\boldsymbol{u}(\boldsymbol{x}, t)$ is *homogeneous*. If the field is also statistically invariant under rotations and reflections of the coordinate system, then it is *isotropic*. If the flow field is statistically invariant under all translations, rotations and reflections of the coordinate system, it is said to be *homogeneous isotropic turbulence* (HIT).

It should be pointed out that, the HIT is an idealization and never happens in nature. Fortunately, HIT can be realized in the lab to help study the theory of HIT. It can be approximately generated in a wind or water tunnel by let a uniform fluid stream that passes through a uniform metal grid. Once the fluid passes the metal grid, there is no production of turbulent kinetic energy, the turbulence decays downstream of the grid. The downstream distance to the grid can be interpreted as psuedo-time. In this way is the decay of homogeneous isotropic turbulence is experimentally realized. However, the turbulence from this method is relatively homogeneous in planes normal to the mean flow, and it is not fully isotropic. Another approach has been to use fans. In [32], eight synthetic jet actuators on the corners of a cubic chamber are used to create energetic turbulence, and HIT without a mean flow was realized in a small region at the center of the chamber.

Fourier modes

In order to show a clear picture of the energy cascade, we will examine the Navier-Stokes equations in wavenumber space. In this subsection we will apply Fourier modes to the Navier-Stokes equations for homogeneous turbulence in which the mean velocity is zero.

The Fourier series representation of the turbulent velocity field in 3D is

$$\boldsymbol{u}(\boldsymbol{x},t) = \sum_{\boldsymbol{k}} e^{i\boldsymbol{k}\cdot\boldsymbol{x}}\widehat{\boldsymbol{u}}(\boldsymbol{k},t), \tag{3.17}$$

where $\boldsymbol{k}$ is the wavenumber, $e^{i\boldsymbol{k}\cdot\boldsymbol{x}}$ is the Fourier modes and $\widehat{u}_j(\boldsymbol{k},t)$ are the Fourier coefficients of velocity, which are defined as

$$\widehat{u}_j(\boldsymbol{k},t) = \mathcal{F}_k\{u_j(\boldsymbol{x},t)\}, \tag{3.18}$$

the operator $\mathcal{F}_{\boldsymbol{k}}\{\quad\}$ determines the coefficient for the Fourier mode with wavenumber $\boldsymbol{k}$. It is defined as

$$\mathcal{F}_{\boldsymbol{k}}\{g(\boldsymbol{x})\} = \frac{1}{\mathcal{L}^3}\int_0^{\mathcal{L}}\int_0^{\mathcal{L}}\int_0^{\mathcal{L}} g(\boldsymbol{x})e^{-i\boldsymbol{k}\cdot\boldsymbol{x}}dx_1dx_2dx_3 = \widehat{g}(\boldsymbol{k}). \tag{3.19}$$

The Fourier operator transfers variables from spatial space $\boldsymbol{u}(\boldsymbol{x},t)$ to wavenumber space $\widehat{\boldsymbol{u}}(\boldsymbol{k},t)$.

Turbulent kinetic energy (TKE) in spectral space

The total kinetic energy E can be written with a spatial average,

$$E = \frac{1}{2} < u_i^2 >= \frac{1}{2}\frac{1}{V}\int\int\int u_i(\boldsymbol{x})u_i(\boldsymbol{x})d\boldsymbol{x}, \tag{3.20}$$

where V is the volume. The angle brackets represent an spatial average.

According to the mathematics of Fourier transform, the total kinetic energy can be written as

$$E = \frac{1}{2}\int\int\int \widehat{\boldsymbol{u}}(\boldsymbol{k})\cdot\widehat{\boldsymbol{u}}^*(\boldsymbol{k})\mathtt{d}\boldsymbol{k} = \int\int\int E(\boldsymbol{k})d\boldsymbol{k}, \tag{3.21}$$

where $E(\boldsymbol{k})$ is defined as the kinetic energy of the Fourier mode with wavenumber $\boldsymbol{k}$,

$$E(\boldsymbol{k}) = \frac{1}{2}\widehat{\boldsymbol{u}}(\boldsymbol{k}) \cdot \widehat{\boldsymbol{u}}^*(\boldsymbol{k}), \tag{3.22}$$

where $\widehat{\boldsymbol{u}}^*(\boldsymbol{k})$ is the conjugate of $\widehat{\boldsymbol{u}}(\boldsymbol{k})$. $E(\boldsymbol{k})$ contains directional information. In an isotropic velocity fields the spectrum does not depend on directions. Usually, we want to know the energy at a particular scale $k = |\boldsymbol{k}|$ without any interest in its direction. To find $E(k)$, we integrate over the spherical shell of radius k (in 3-dimensions),

$$E = \int\int\int E(\boldsymbol{k})\mathtt{d}\boldsymbol{k} = \int_0^\infty E(k)dk. \tag{3.23}$$

As the mean velocity is zero, so the kinetic energy E is equal to turbulent kinetic energy K. Then we get the turbulent kinetic energy K,

$$K = \int_0^\infty E(k)dk, \tag{3.24}$$

the dissipation ϵ can be defined based on the energy spectrum as,

$$\epsilon = \int_0^\infty 2\nu k^2 E(k)dk, \tag{3.25}$$

where ν is the kinematic viscosity.

The Taylor-scale Reynolds number Re_λ is often used to characterize HIT, which is defined based on K and ϵ as

$$Re_\lambda = \big(\frac{20}{3}\frac{K^2}{\epsilon\nu}\big). \tag{3.26}$$

Energy cascade

Turbulence can be considered to be composed of eddies of different sizes. Eddies with characteristic size ℓ have a characteristic velocity $u(\ell)$ and characteristic timescale $\tau(\ell) = \ell/u(\ell)$. The eddies in the largest size range are characterized by the lengthscale ℓ_0 which is comparable to the flow scale $\mathcal{L}$, and their characteristic velocity u_0 is on the order of the r.m.s. turbulence intensity which is comparable to

characteristic velocity $\mathcal{U}$ of the HIT.

The large eddies are usually unstable and they break up into smaller eddies. In this way kinetic energy contained in large eddies is transferred to smaller eddies. These smaller eddies have a similar break-up process, and transfer their energy to even smaller eddies. The procedure of kinetic energy transfer from large eddies to small eddies is the *energy cascade*. Energy cascade continues until the Reynolds number $Re(\ell) = u(\ell)/\ell$ is sufficiently small that the eddy motion is stable, and molecular viscosity is effective in dissipating the kinetic energy. Then kinetic energy is converted into heat, and lost to the environment. This procedure is called dissipation.

The Kolmogorov hypotheses and Characteristic scales of turbulence

The K41 theory contains three hypotheses, and among other things it can determine the size of the smallest eddies that are responsible for dissipating the energy in the energy cascade. First, it is useful to introduce a lengthscale $\ell_{EI} \approx \frac{1}{6}\ell_0$, which is used to separate the anisotropic large eddies $\ell > \ell_{EI}$ and the isotropic small eddies $\ell < \ell_{EI}$. The three Kolmogorov hypotheses are as following [3]:

Kolmogorov's hypothesis of local isotropy: At sufficiently high Reynolds number, the small-scale turbulent motions ($\ell \ll \ell_0$) are statistically isotropic.

Kolmogorov's first similarity hypothesis: In every turbulent flow at sufficiently high Reynolds number, the statistics of the small-scale motions ($\ell < \ell_{EI}$) have a universal form that is uniquely determined by ν and ϵ.

Given the two parameters ν and ϵ, the characteristic length, velocity, and time scales for the smallest eddies can be determined. These are the Kolmogorov scales:

$$\begin{aligned} \eta &= (\nu^3/\varepsilon)^{1/4}, \\ u_\eta &= (\varepsilon\nu)^{1/4}, \\ \tau_\eta &= (\nu/\varepsilon)^{1/2}. \end{aligned} \tag{3.27}$$

Kolmogorov's second similarity hypothesis: In every turbulent flow at sufficiently high Reynolds number, the statistics of the motions of scale ℓ in the range $\ell_0 \gg \ell \gg \eta$ have a universal form that is uniquely determined by ε, independent of ν.

According to the Kolmogorov's hypotheses, the eddy scales in the turbulent flows can be classified into three ranges: the integral length scales range, the inertial subrange scales range and the Kolmogorov scales (the dissipation range). Motions in the inertial subrange are determined by inertial effects, and viscous effects are negligible. Motions in the dissipation range have significant viscous effects, and they are responsible for essentially all of the dissipation. For the Energy cascade, the energy is usually injected into the system at the integral length scale range, then the kinetic energy is transferred by the inertial subrange to Kolmogorov scales as the large eddies are broken down to small eddies. At the Kolmogorov scales, the eddies are stable and the kinetic energy converted into heat due to dissipation.

Kolmogorov spectrum

Another important information obtained from K41 theory is the Kolmogorov energy spectrum, which demonstrates the energy spectrum $E(k)$ is predictable. According to Kolmogorov's first similarity hypothesis, in the inertial subrange the energy spectrum is only a function of the dissipation rate and the size of the eddies. that is

$$E(k) = f(\epsilon, k). \tag{3.28}$$

We use dimensional analysis: Kinetic energy $E \sim L^2/T^2$, wavenumber $k \sim 1/L)$, energy spectrum $E(k) \sim L^3/T^2$ and dissipation $\epsilon \sim L^2/T^3$. Using this in Equation (3.28), we arrive at,

$$E(k) = C_K \epsilon^{2/3} k^{-5/3}. \tag{3.29}$$

This is the famous Kolmogorov spectrum, one of the cornerstone of turbulence theory. C_K is a universal constant, the Kolmogorov constant, experimentally found to be approximately 1.5. Figure 3.1 is a schematic representation of this spectrum.

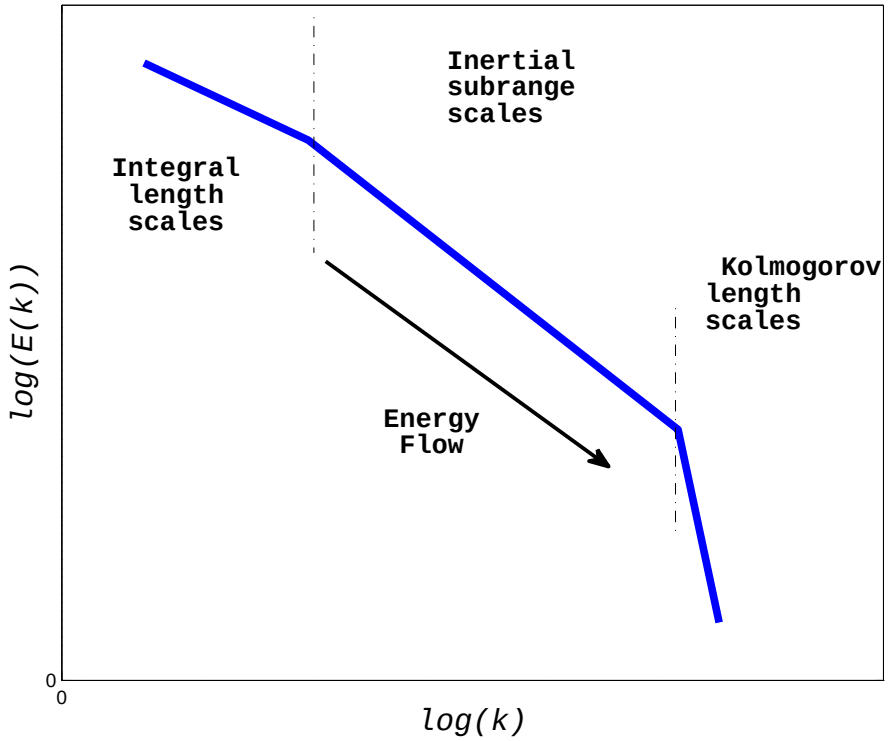

Figure 3.1: Sketch of energy spectrum.

3.4 Numerical Results for RBVM and MM1

In this section we present results using the RBVM, the mixed RBVM and the dynamic Smagorinsky-Yoshizawa-eddy diffusivity (DSYE) model with a spectral basis. All variables are represented using a Fourier basis with a cut-off wave number denoted by k^h. The test problem corresponds to a DNS simulation of the decay of homogeneous turbulence for a compressible fluid computed in [33]. In particular we focus on the D9 case described in that paper with $\Omega =]0, 2\pi[^3$. In order to validate our implementation of the compressible Navier-Stokes equations we compute our own DNS results and compare with the results presented in [33] and achieve good agreement. The physical parameters associated with the cases we have considered are listed in Table 3.1. They include the initial spectrum for the turbulent kinetic energy $E(k, 0)$, the initial total kinetic energy $q^2/2$, the free stream Mach number M_∞, the turbulent Mach number, Ma, the Reynolds number R_e and the ratio of initial compressible to total kinetic energy χ. We assume that there are no fluctuations in the initial values of the thermodynamic quantities, namely pressure, density and the temperature. We choose Prandtl number $Pr = 0.7$ and the adiabatic index for air to be $\gamma = 1.4$.

3.4.1 Low Reynolds Number Case

For compressible flows the velocity field is comprised of solenoidal (incompressible) and dilatational (compressible) components, $\boldsymbol{u}^s$ and $\boldsymbol{u}^c$ respectively. For the case of isotropic turbulence in Fourier space the Helmholtz decomposition is unique and is given by

$$\widehat{\boldsymbol{u}}^c = [(\boldsymbol{k} \cdot \widehat{\boldsymbol{u}})/k^2]\boldsymbol{k}, \tag{3.30}$$

$$\widehat{\boldsymbol{u}}^s = \widehat{\boldsymbol{u}} - \widehat{\boldsymbol{u}}^c \ . \tag{3.31}$$

Let K^s and K^c denote the turbulent kinetic energy from the solenoidal and dilatational velocity components, respectively. We define $\chi = K^c/(K^c + K^s)$ as the ratio of compressible kinetic energy to the total kinetic energy.

The turbulent Mach number $Ma = \sqrt{< |\boldsymbol{u}^h|^2 >}/ < c^h >$, where $< \cdot >$

Table 3.1: Parameters for the decay of homogeneous compressible turbulence.

$E(k,0)$	$\frac{q^2}{2}$	M_∞	Ma	Re	χ
$0.011k^4e^{-2\left(\frac{k}{4}\right)^2}$	1.3235	0.184 -0.430	0.300-0.700	376	0.2-0.6

represents the spatial average and c is the local speed of sound. We approximate the turbulent Mach number with the root-mean-square Mach number $Ma \approx \sqrt{< |\boldsymbol{u}^h|^2 > /c^{h2}}$, which is easier to evaluate.

These parameters lead to the development of local, weak shocks, referred to as shocklets close to the regions where the local Mach number exceeds unity. As pointed out in [33] this happens when $\nabla \cdot \boldsymbol{u}$ obtains a large negative value corresponding to the deceleration of a supersonic flow to a subsonic flow. During the decay of turbulence the local Mach number varies in the range $Ma \sim 0.1 - 0.7$, and the Taylor microscale Reynolds number, $Re_\lambda = \mathcal{O}(27 - 65)$. We refer this low Reynolds number test as Case $Re_\lambda = 65.5$.

We solve the Navier Stokes equations on a grid with N^3 points and compute all integrals on a $(3N/2)^3$ grid. We note that even for the DNS simulation this does not de-alias all the terms, but does guarantee the accurate computation of predominantly quadratic terms. For the DNS simulation $N = 256$ and for the LES simulations $N = 32$. For the LES calculations we use the truncated velocity field obtained from the DNS at $t/T_e = 1.2$, where $T_e = 0.667$ is the eddy turn-over time [33], as the initial condition. We compare the performance of the models from $t/T_e = 1.2 \sim 7.0$, which corresponds to a Taylor micro-scale Reynolds number of $Re_\lambda = 65.5 \sim 27.4$. For time integration we use the fourth-order Runge-Kutta algorithm, and we evaluate all terms explicitly. The details of the numerical algorithm can be found in [34]. For all the LES models in this section, $C_\tau = 0.5$. For more details, the readers are referred to [35].

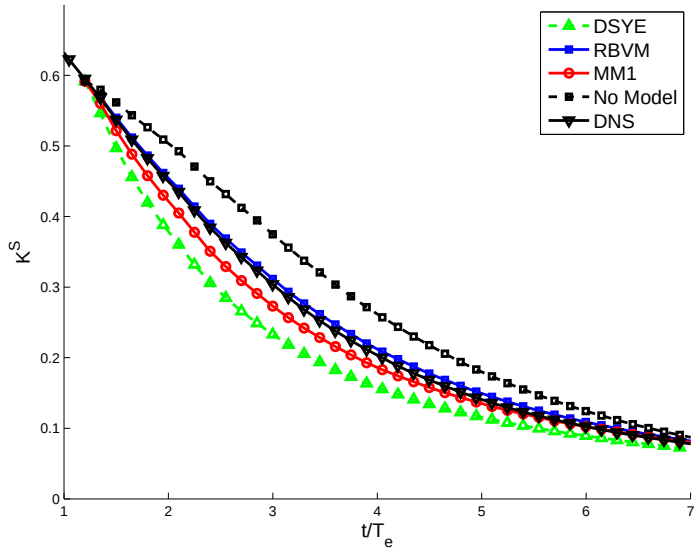

Figure 3.2: Time history of turbulent kinetic energy of the incompressible velocity component for the $Re_\lambda = 65.5$ case on a 32^3 grid with $\chi = 0.4$ and $Ma = 0.488$. A comparison of the DSYE, RBVM, MM1, and no model cases.

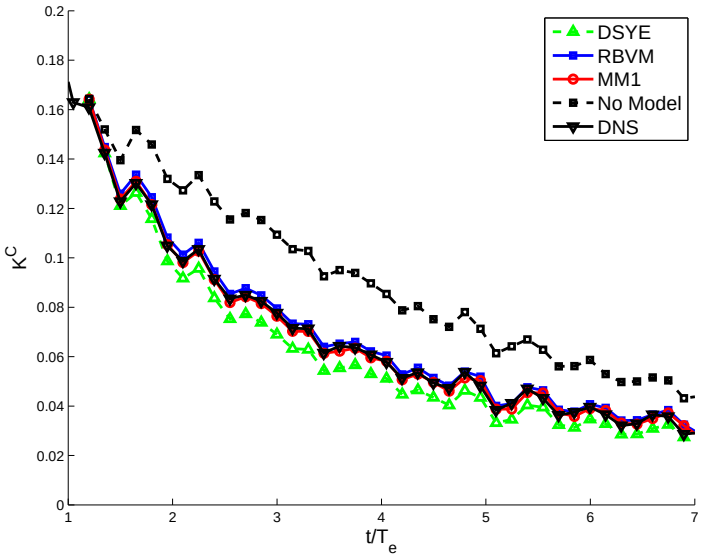

Figure 3.3: Time history of turbulent kinetic energy of the compressible velocity component for the $Re_\lambda = 65.5$ case on a 32^3 grid with $\chi = 0.4$ and $Ma = 0.488$. A comparison of the DSYE, RBVM, MM1, and no model cases.

Figures 3.2 and 3.3 show the turbulent kinetic energy in the incompressible and compressible velocity components, respectively, as a function of time. We observe that the no model case overpredicts these quantities. In Figure 3.2, for the incompressible turbulent kinetic energy, the RBVM model is most accurate followed by the mixed model, followed by the DSYE model which is clearly too dissipative. The RBVM model slightly overpredicts the kinetic energy while the mixed model underpredicts it. The evolution of the compressible component of the kinetic energy is shown in Figure 3.3 and all three LES models perform well. Here the mixed model is the most accurate followed closely by the RBVM model, which slightly overpredicts the kinetic energy. The DSYE model is once again overly dissipative.

This behavior is explained by examining the incompressible and compressible energy spectra at $t/T_e \approx 3.0$ in Figures 3.4 and 3.5 and at $t/T_e \approx 6.0$ in Figures 3.6 and 3.7.

From the figure for the incompressible spectra at $t/T_e \approx 3.0$ (Figure 3.4) we observe that the no-model case displays a pile-up of energy at high wavenumbers. All the LES models are quite accurate at low-to-mid wavenumbers, while the RBVM is the most accurate at high wavenumbers, followed by the mixed model. At $t/T_e \approx 6.0$ (Figure 3.6) the mixed model is the most accurate at the mid-to-high wavenumbers whereas the RBVM model is most accurate at low wavenumbers. In either case the DSYE model is the least accurate.

For the compressible spectra in Figures 3.5 and 3.7 we observe that the energy pile-up in the no-model case is not as large as in the incompressible case thereby indicating that the compressible component of the subgrid model plays a smaller role. All the LES models appear to perform quite well with the RBVM and the mixed models being the most accurate at high wavenumbers. The same conclusions can be drawn for the density and pressure spectra at time $t/T_e \approx 6.0$, shown in Figures 3.8 and 3.9, respectively. The evolution of the root-mean-square (rms) density is shown in Figure 3.10. Once again the DSYE model is observed to lead to smaller rms values while the RBVM and the mixed model are more accurate.

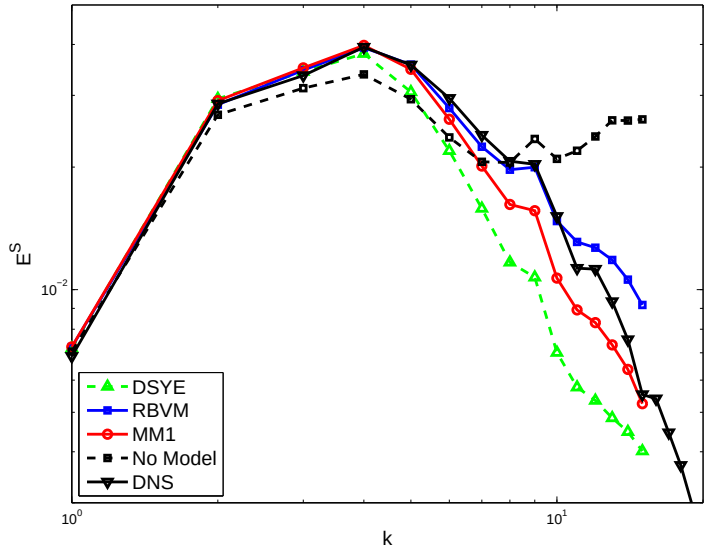

Figure 3.4: Energy spectrum of the incompressible velocity component for the $Re_\lambda = 65.5$ case on a 32^3 grid with $\chi = 0.4$ and $Ma = 0.488$ at $t/T_e \approx 3$. A comparison of the DSYE, RBVM, MM1, and no model cases.

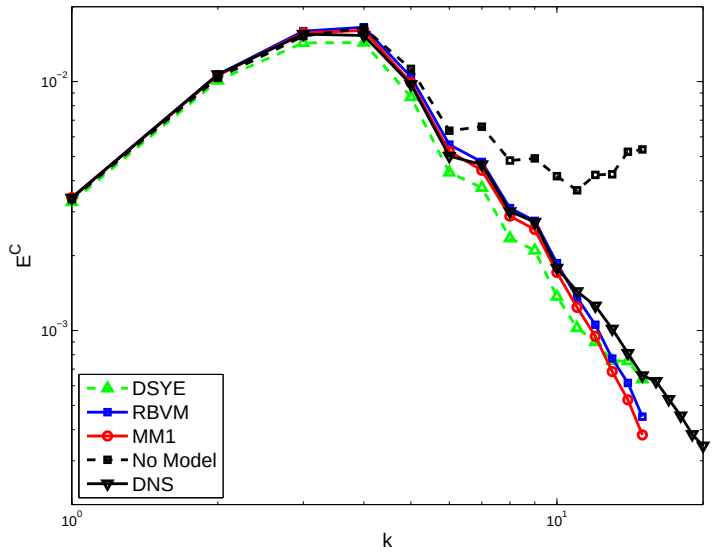

Figure 3.5: Energy spectrum of the compressible velocity component for the $Re_\lambda = 65.5$ case on a 32^3 grid with $\chi = 0.4$ and $Ma = 0.488$ at $t/T_e \approx 3$. A comparison of the DSYE, RBVM, MM1, and no model cases.

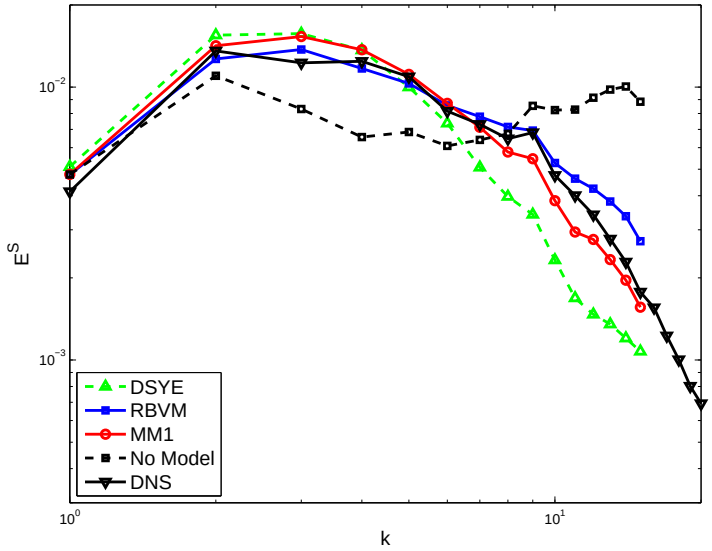

Figure 3.6: Energy spectrum of the incompressible velocity component for the $Re_\lambda = 65.5$ case on a 32^3 grid with $\chi = 0.4$ and $Ma = 0.488$ at $t/T_e \approx 6$. A comparison of the DSYE, RBVM, MM1, and no model cases.

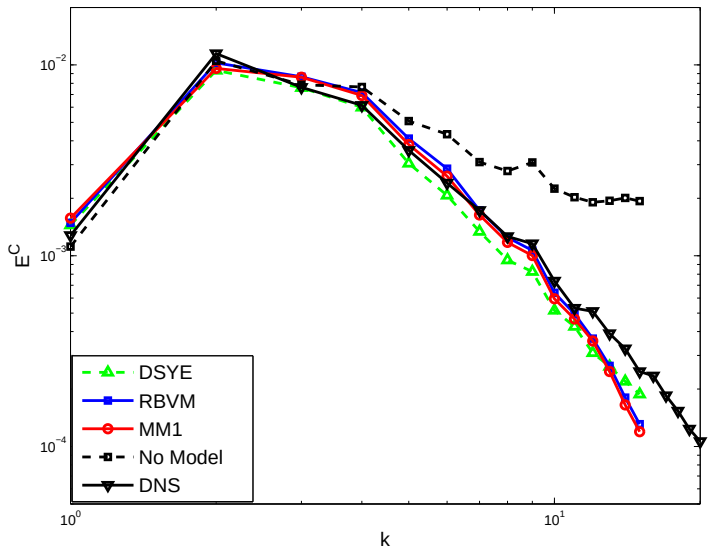

Figure 3.7: Energy spectrum of the compressible velocity component for the $Re_\lambda = 65.5$ case on a 32^3 grid with $\chi = 0.4$ and $Ma = 0.488$ at $t/T_e \approx 6$. A comparison of the DSYE, RBVM, MM1, and no model cases.

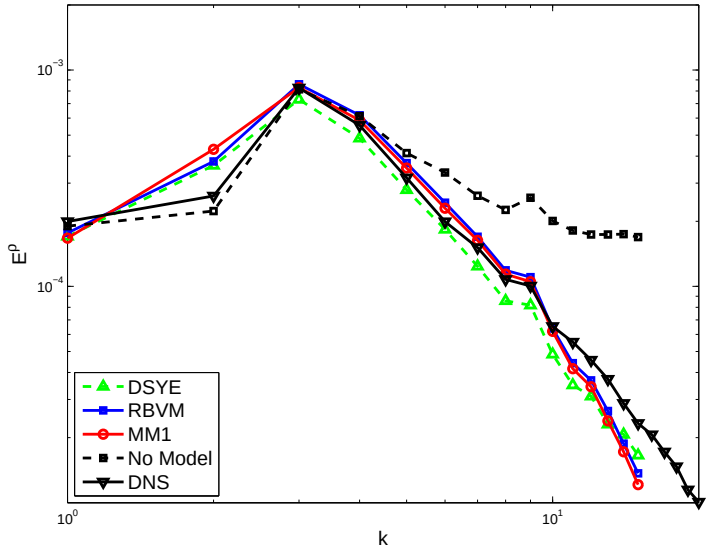

Figure 3.8: Density spectrum for the $Re_\lambda = 65.5$ case on a 32^3 grid with $\chi = 0.4$ and $Ma = 0.488$ at $t/T_e \approx 6$. A comparison of the DSYE, RBVM, MM1, and no model cases.

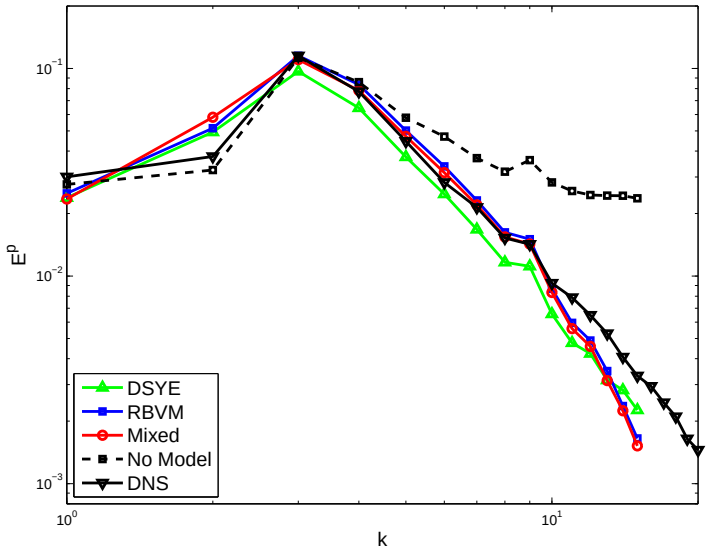

Figure 3.9: Pressure spectrum for the $Re_\lambda = 65.5$ case on a 32^3 grid with $\chi = 0.4$ and $Ma = 0.488$ at $t/T_e \approx 6$. A comparison of the DSYE, RBVM, MM1, and no model cases.

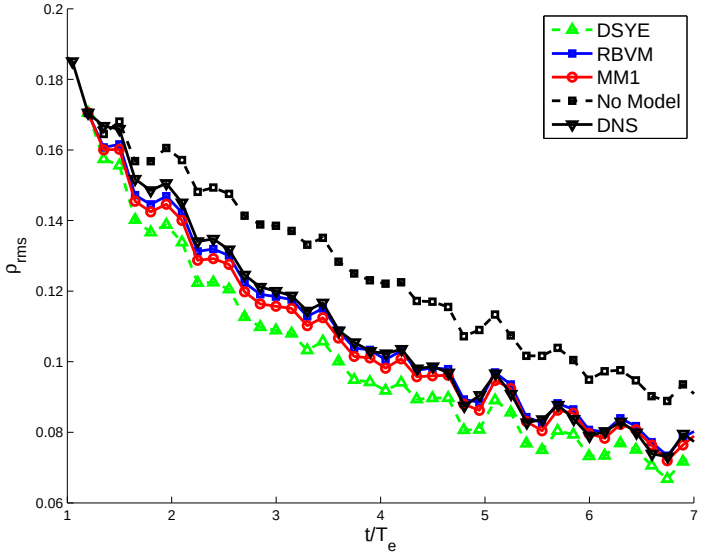

Figure 3.10: Time history of root-mean-square of density for the $Re_\lambda = 65.5$ case on a 32^3 grid with $\chi = 0.4$ and $Ma = 0.488$. A comparison of the DSYE, RBVM, MM1, and no model cases.

We have also performed these simulations with $k^h = 32$ (not shown here). We observe the same trends however the differences between all the models are much smaller.

3.4.2 Study of the effects of varying χ

In this section we examine the effect of varying the initial fraction of the compressible turbulent kinetic energy. In particular we select $\chi = 0.2$ and $\chi = 0.6$ to add to the $\chi = 0.4$ case described in the previous section. The Mach number $Ma = 0.488$ is unchanged.

When χ is small a greater proportion of the total initial kinetic energy is incompressible. As a result a larger contribution from the deviatoric component of the subgrid stress is required. The dynamic Smagorinsky and mixed models respond to this by increasing the value of the model parameters with decreasing values of χ. This is seen in Figure 3.11, where we have plotted value of the deviatoric parameter C_0 as a function of time. We observe that with increasing time all parameters tend to smaller values because of the natural decay in the turbulence intensity. We also note that the value of C_0 for the mixed model is consistently smaller than the

dynamic Smagorinsky model, indicating that the dynamic procedure is accounting for the additional dissipation generated by the RBVM component of the mixed model. With increasing value of χ the ratio of the average value of C_0 for the mixed model to the corresponding value for the dynamic Smagorinsky model appears to decreasing, indicating that for large values of χ the mixed model is tending toward the RBVM model.

For completeness the variation of the other dynamic parameters that is C_1 and Pr_t^{-1} as a function of time is shown in Figures 3.12 and 3.13, respectively. The value of C_1 in the mixed model is selected to be zero as discussed in Section 2.2. The value of Pr_t^{-1} for the mixed model is also zero because the dynamic procedure yields a negative value which is ignored.

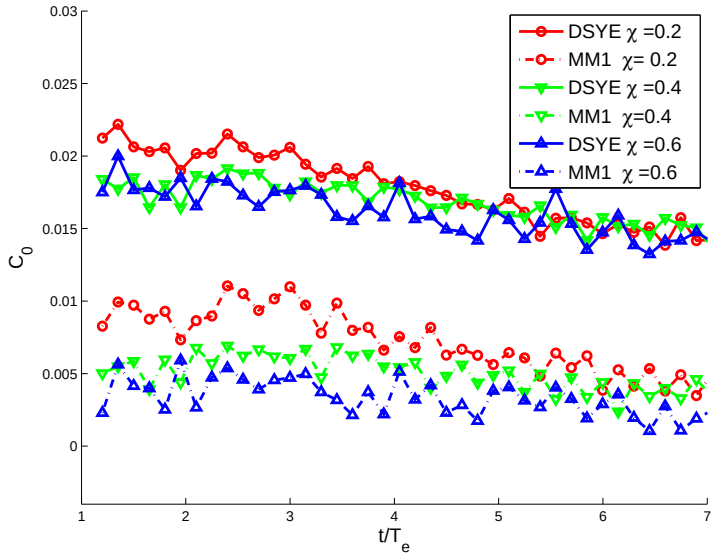

Figure 3.11: Time history of the Smagorinsky coefficient C_0 for the $Re_\lambda = 65.5$ case on a 32^3 grid with $Ma = 0.488$. A comparison of the DSYE and MM1 cases.

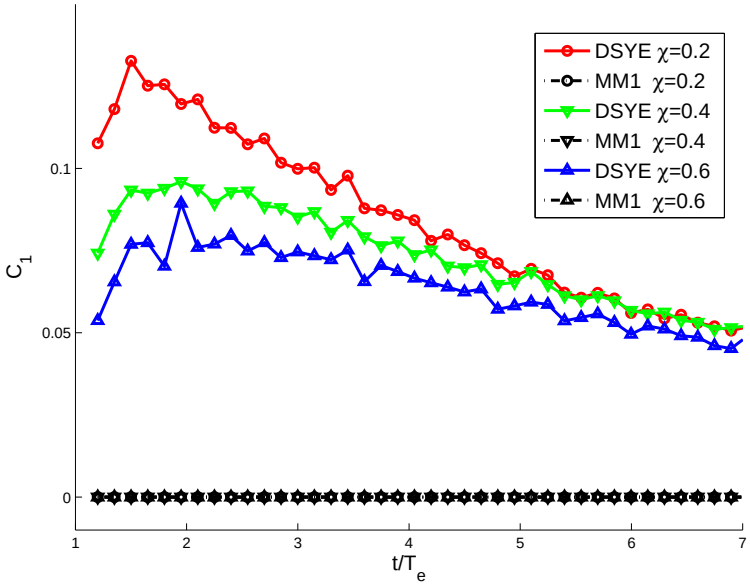

Figure 3.12: Time history of the Smagorinsky coefficient C_1 for the $Re_\lambda = 65.5$ case on a 32^3 grid with $Ma = 0.488$. A comparison of the DSYE and MM1 cases.

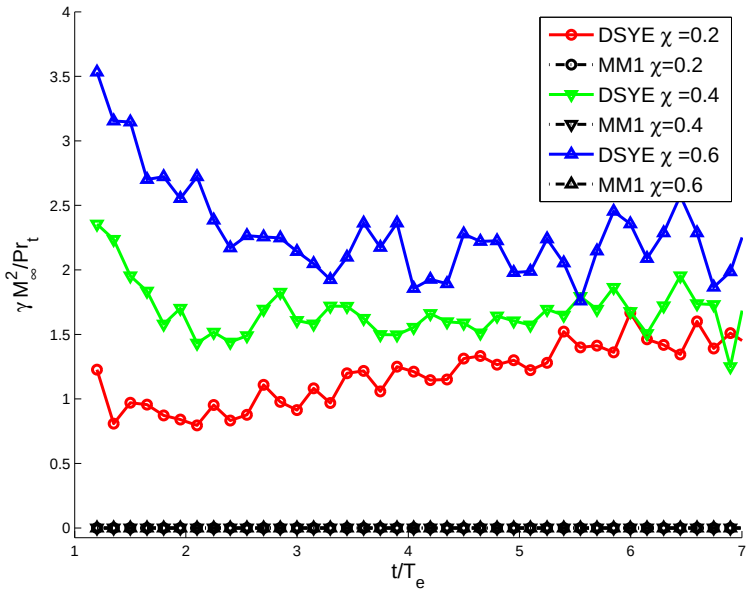

Figure 3.13: Time history of Pr_t for the $Re_\lambda = 65.5$ case on a 32^3 grid with $Ma = 0.488$. A comparison of the DSYE and MM1 cases.

In Figure 3.14 we have plotted the spectrum for the incompressible velocity

component for different models for $\chi = 0.2$ and $t/T_e \approx 6$. We note that RBVM model is the most accurate for low wavenumbers whereas the mixed model is the most accurate for high wavenumbers. The DSYE model is too dissipative. The spectrum for the compressible component is shown in Figure 3.15. All models are very accurate for small wavenumbers whereas the RBVM and the mixed model are slightly more accurate for high wavenumbers.

In Figure 3.16 we have plotted the spectrum for the incompressible velocity component for different models for $\chi = 0.6$ and $t/T_e \approx 6$. We note that RBVM model is the most accurate overall followed by the mixed model. The DSYE model continues to be too dissipative. The spectrum for the compressible component is shown in Figure 3.17. Here all the models are very accurate for the entire range of wavenumbers.

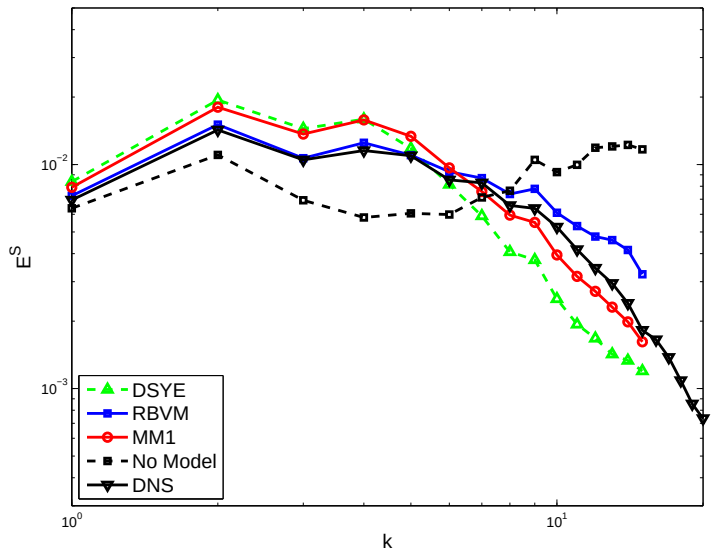

Figure 3.14: Energy spectrum of the incompressible velocity component for the $Re_\lambda = 65.5$ case on a 32^3 grid with $\chi = 0.2$ and $Ma = 0.488$ at $t/T_e \approx 6$. A comparison of the DSYE, RBVM, MM1, and no model cases.

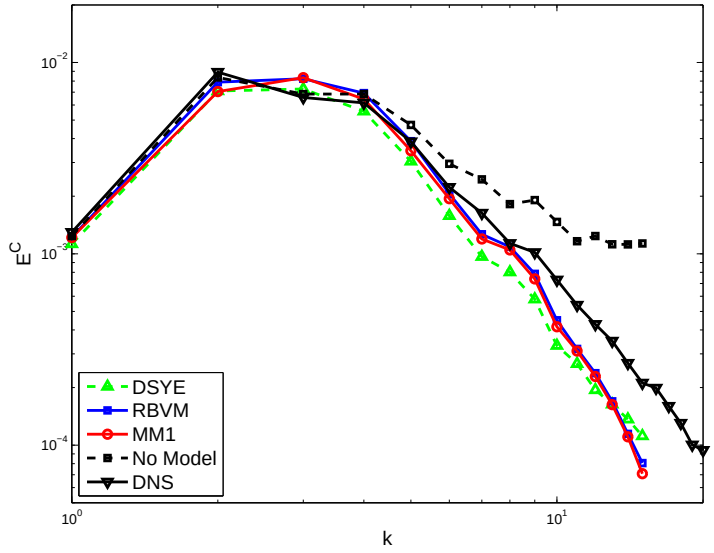

Figure 3.15: Energy spectrum of the compressible velocity component for the $Re_\lambda = 65.5$ case on a 32^3 grid with $\chi = 0.2$ and $Ma = 0.488$ at $t/T_e \approx 6$. A comparison of the DSYE, RBVM, MM1, and no model cases.

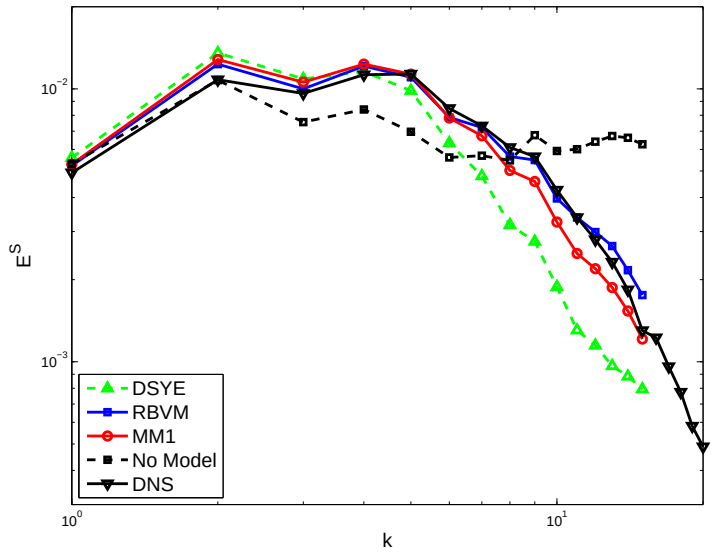

Figure 3.16: Energy spectrum of the incompressible velocity component for the $Re_\lambda = 65.5$ case on a 32^3 grid with $\chi = 0.6$ and $Ma = 0.488$ at $t/T_e \approx 6$. A comparison of the DSYE, RBVM, MM1, and no model cases.

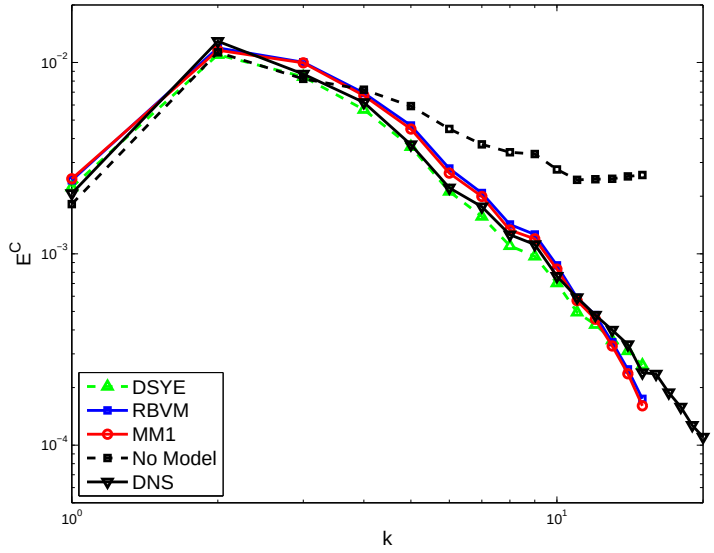

Figure 3.17: Energy spectrum of the compressible velocity component for the $Re_\lambda = 65.5$ case on a 32^3 grid with $\chi = 0.6$ and $Ma = 0.488$ at $t/T_e \approx 6$. A comparison of the DSYE, RBVM, MM1, and no model cases.

3.4.3 Study of the effects of varying Ma

In this section we test the robustness of the LES models with regards to the inherent compressibility of the flow by varying the Mach number. In addition to $Ma = 0.488$, which was considered in Section 3.4.1, we consider $Ma = 0.3$ and $Ma = 0.7$, while fixing $\chi = 0.4$.

In Figure 3.18 we have plotted the spectrum of the incompressible component of the velocity at $t/T_e \approx 6$ for $Ma = 0.3$. At this value of Ma the flow is nearly incompressible. We note that the RBVM and the mixed model are very close to each other and to the exact solution while the DSYE model is inaccurate. In Figure 3.22 we have plotted the variation of the deviatoric parameter C_0, as computed by the dynamic procedure, as a function of time. We observe that for $Ma = 0.3$ this parameter is very small indicating that the mixed model is essentially the same as the RBVM model.

From the plot of the spectrum of the compressible component of kinetic energy at $t/T_e \approx 6$ (see Figure 3.19) we conclude that all the LES models are quite accurate.

In Figure 3.20 we have plotted the spectrum of the incompressible component of the velocity at $t/T_e \approx 6$ for $Ma = 0.7$. At this high Mach number we expect the compressible effects to be more pronounced and we would also expect the formation relatively strong local shocks. From the plot we observe that the RBVM model is most accurate in this case followed by the mixed model. The latter is somewhere between the RBVM and the DSYE model. This may be understood by observing the variation of C_0 for these two models with time (see Figure 3.22). We note that the value of C_0 for the mixed model is higher than it was for $Ma = 0.3$, indicating that its performance will be closer to that of the DSYE model in this case.

From the plot of the spectrum of the compressible component of the velocity we observe that the RBVM and the mixed models are very accurate while the DSYE model underestimates the spectrum.

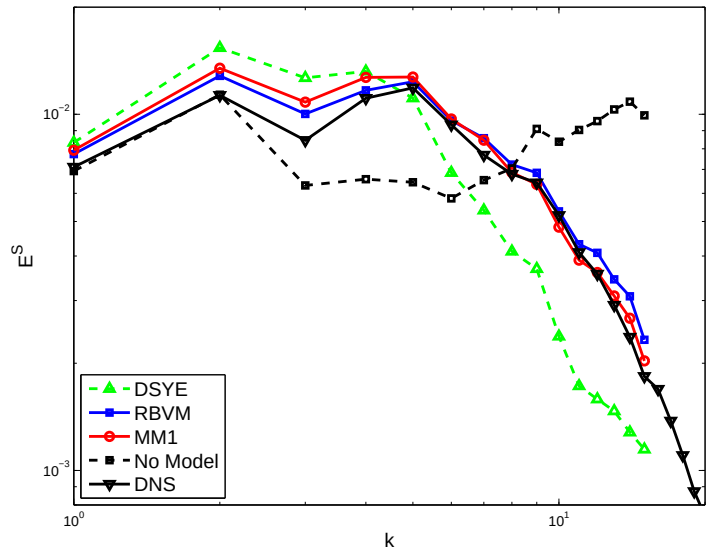

Figure 3.18: Energy spectrum of the incompressible velocity component for the $Re_\lambda = 65.5$ case on a 32^3 grid with $\chi = 0.4$ and $Ma = 0.300$ at $t/T_e \approx 6$. A comparison of the DSYE, RBVM, MM1, and no model cases.

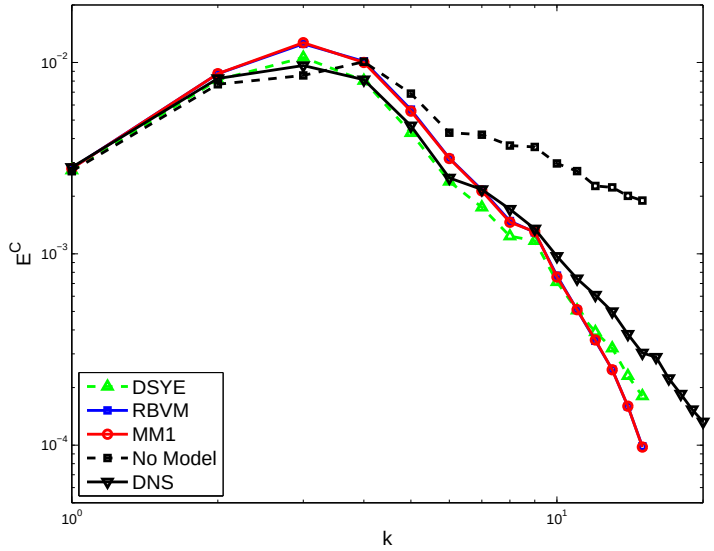

Figure 3.19: **Energy spectrum of the compressible velocity component for the $Re_\lambda = 65.5$ case on a 32^3 grid with $\chi = 0.4$ and $Ma = 0.300$ at $t/T_e \approx 6$. A comparison of the DSYE, RBVM, MM1, and no model cases.**

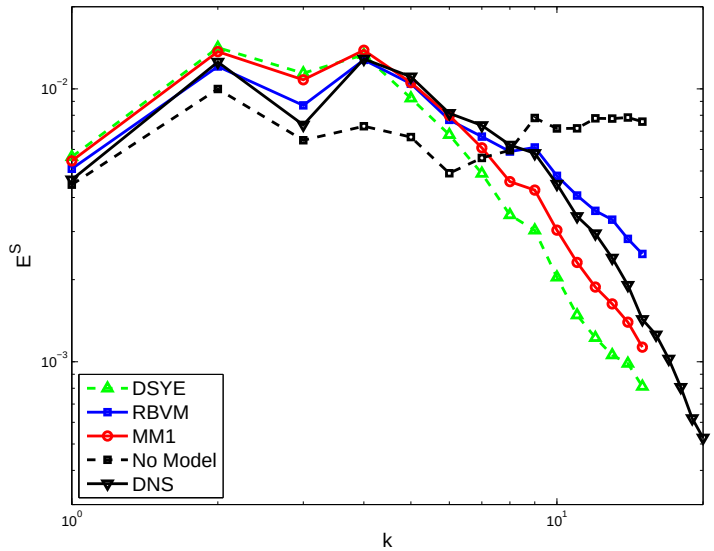

Figure 3.20: **Energy spectrum of the incompressible velocity component for the $Re_\lambda = 65.5$ case on a 32^3 grid with $\chi = 0.4$ and $Ma = 0.700$ at $t/T_e \approx 6$. A comparison of the DSYE, RBVM, MM1, and no model cases.**

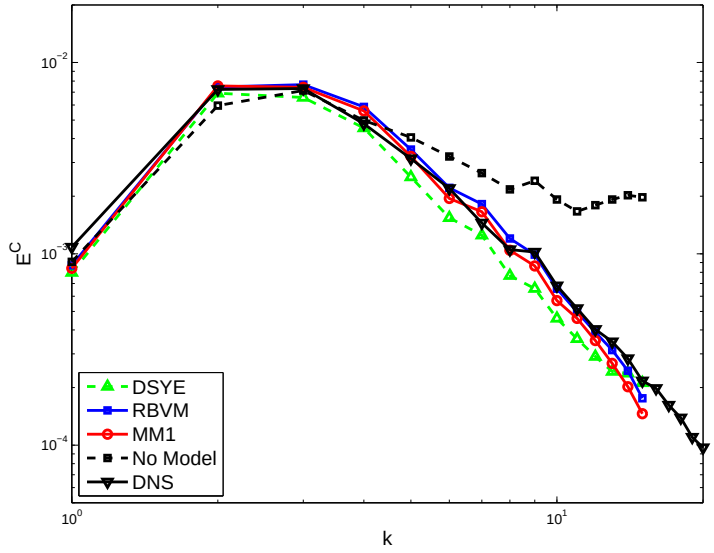

Figure 3.21: **Energy spectrum of the compressible velocity component for the $Re_\lambda = 65.5$ case on a 32^3 grid with $\chi = 0.4$ and $Ma = 0.700$ at $t/T_e \approx 6$. A comparison of the DSYE, RBVM, MM1, and no model cases.**

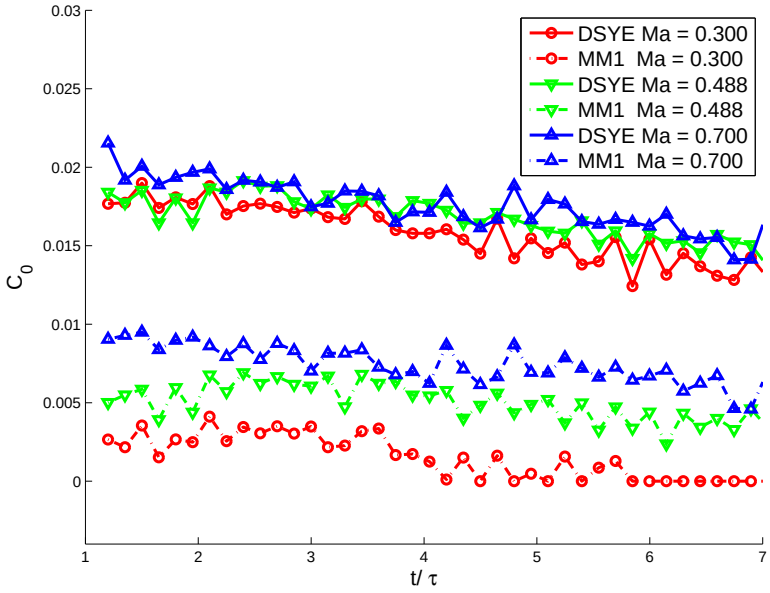

Figure 3.22: **Time history of the Smagorinsky coefficient C_0 for the $Re_\lambda = 65.5$ case on a 32^3 grid with $\chi = 0.4$. A comparison of the DSYE and MM1 cases.**

3.4.4 High Reynolds Number Case

In this section the performance of the LES models at a higher Reynolds number is considered. The DNS was computed using 512^3 modes ($k^h = 256$) in and all other parameters were the same as for the previous run, except the Reynolds number which was set to $Re = 843$. In addition, $\chi = 0.4$ and $Ma = 0.488$ were chosen. For the LES models, which were performed with 32^3 modes ($k^h = 16$), we used the truncated velocity field obtained from the DNS at $t/T_e = 0.92$ as initial condition, where $T_e = 0.667$ is the eddy turn-over time. We compare the performance of the models in the interval $t/T_e = 0.92 - 7.0$, which corresponds to a Taylor micro-scale Reynolds number of $Re_\lambda = 120.95 - 41.97$. We refer to this low Reynolds number test case as $Re_\lambda = 121.0$

For the RBVM and the mixed model, Fourier modes with $k \in (16, 24)$ were used to compute the approximate fine scales.

In Figures 3.23-3.26, we have plotted the Energy spectrum of the incompressible and compressible velocity component at time $t/T_e \approx 3$ and $t/T_e \approx 6$. Once again, for the incompressible velocity component, we observe that the DSYE model is too dissipative. However, the RBVM here is not dissipative enough, and the mixed model is the most accurate, especially at time $t/T_e \approx 6$ in Figure 3.24. In Figure 3.25 and 3.26, for the compressible velocity component, all the LES models are equally accurate; the DSYE model is slightly more dissipative in the middle wavenumber range.

In the examples presented in the previous section, the Reynolds number of the flow was moderate. As a result the cross-stress term was the dominant term, and since the RBVM model captured this term well there was little or no benefit in including the Reynolds stress term via the Smagorinsky model. However, after performing this test at a higher Reynolds number, we can observe the benefit of using the mixed model.

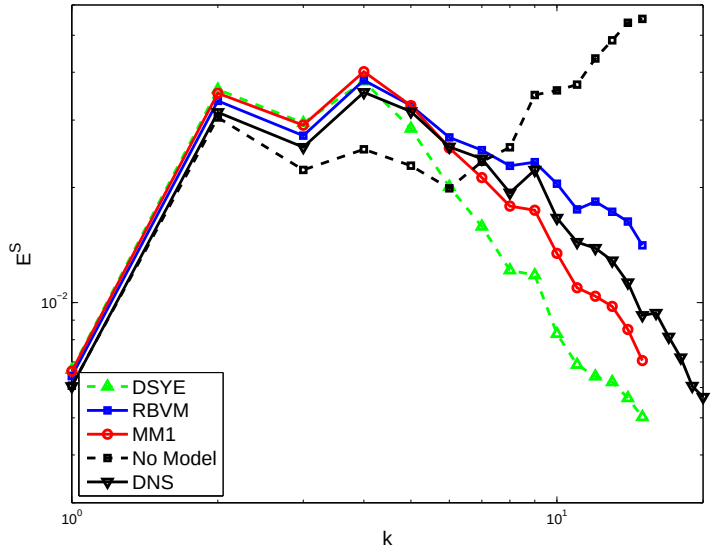

Figure 3.23: Energy spectrum of the incompressible velocity component for the $Re_\lambda = 121.0$ case on a 32^3 grid with $\chi = 0.4$ and $Ma = 0.488$ at $t/T_e \approx 3$. A comparison of the DSYE, RBVM, MM1, and no model cases.

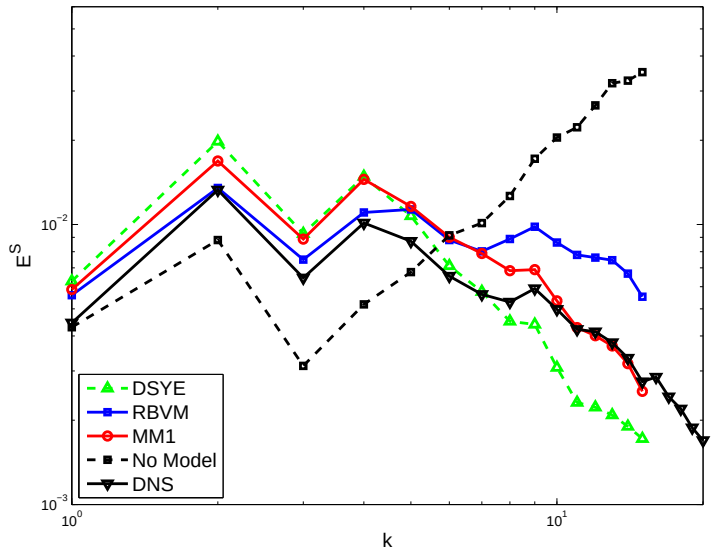

Figure 3.24: Energy spectrum of the incompressible velocity component for the $Re_\lambda = 121.0$ case on a 32^3 grid with $\chi = 0.4$ and $Ma = 0.488$ at $t/T_e \approx 6$. A comparison of the DSYE, RBVM, MM1, and no model cases.

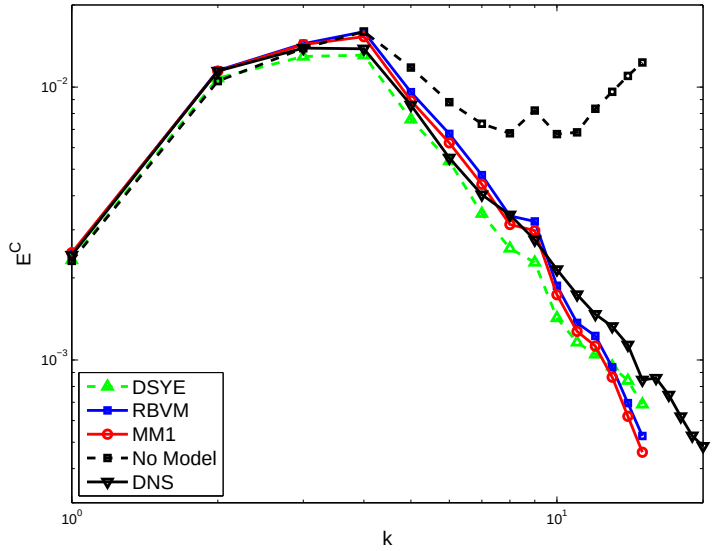

Figure 3.25: Energy spectrum of the compressible velocity component for the $Re_\lambda = 121.0$ case on a 32^3 grid with $\chi = 0.4$ and $Ma = 0.488$ at $t/T_e \approx 3$. A comparison of the DSYE, RBVM, MM1, and no model cases.

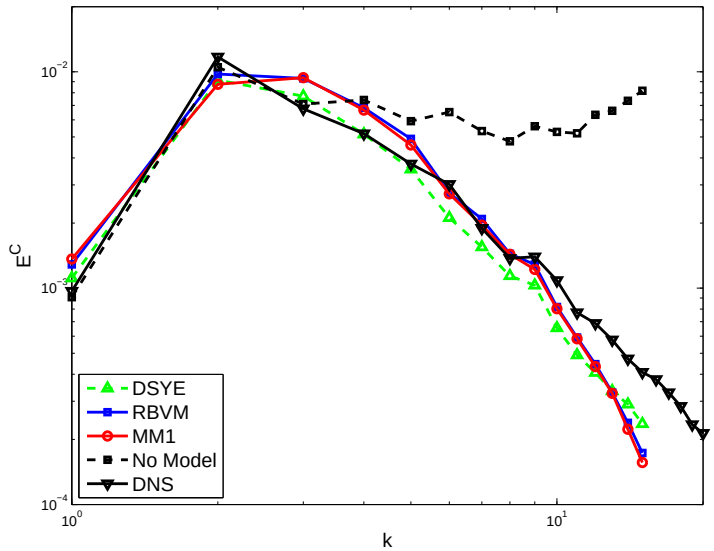

Figure 3.26: Energy spectrum of the compressible velocity component for the $Re_\lambda = 121.0$ case on a 32^3 grid with $\chi = 0.4$ and $Ma = 0.488$ at $t/T_e \approx 6$. A comparison of the DSYE, RBVM, MM1, and no model cases.

We now consider the "convergence" of the LES models by computing the LES solution with 64^3 modes. The solution at $t/\tau \approx 1$ was used as an initial condition for the LES runs which were performed with 64^3 modes ($k^h = 64$). For the RBVM and the mixed model modes with $k \in (64, 96)$ were used to computer the approximate fine scales.

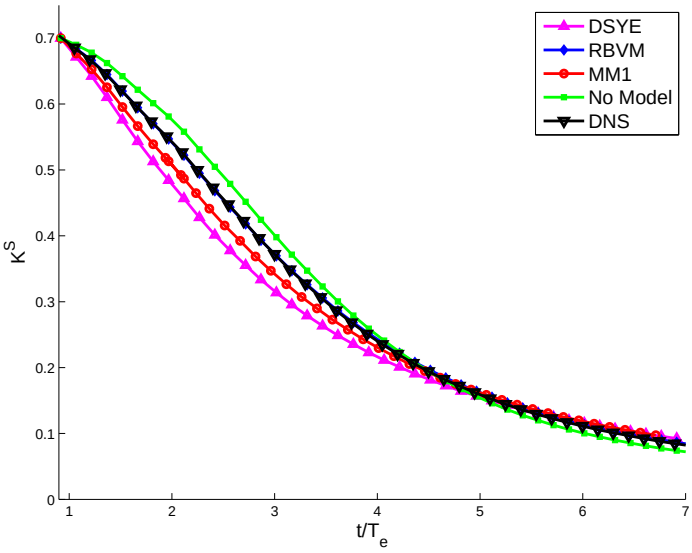

Figure 3.27: Time history of turbulent kinetic energy of the incompressible velocity component for the $Re_\lambda = 121.0$ case on a 64^3 grid with $\chi = 0.4$ and $Ma = 0.488$. A comparison of the DSYE, RBVM, MM1, and no model cases.

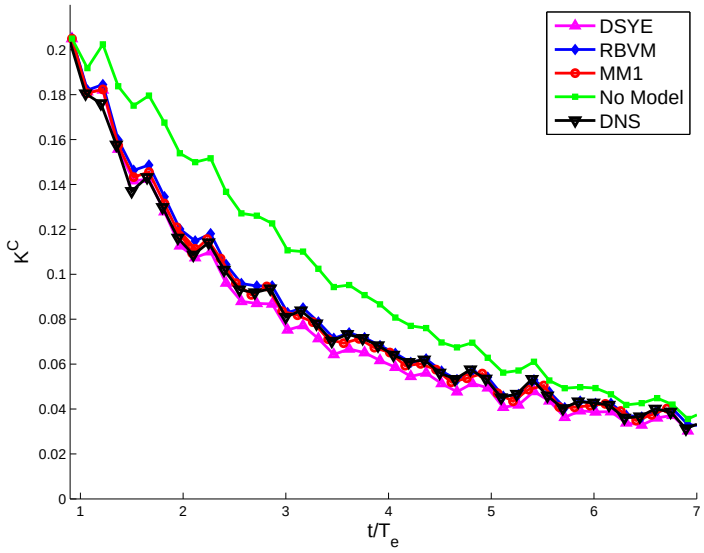

Figure 3.28: Time history of turbulent kinetic energy of the compressible velocity component for the $Re_\lambda = 121.0$ case on a 64^3 grid with $\chi = 0.4$ and $Ma = 0.488$. A comparison of the DSYE, RBVM, MM1, and no model cases.

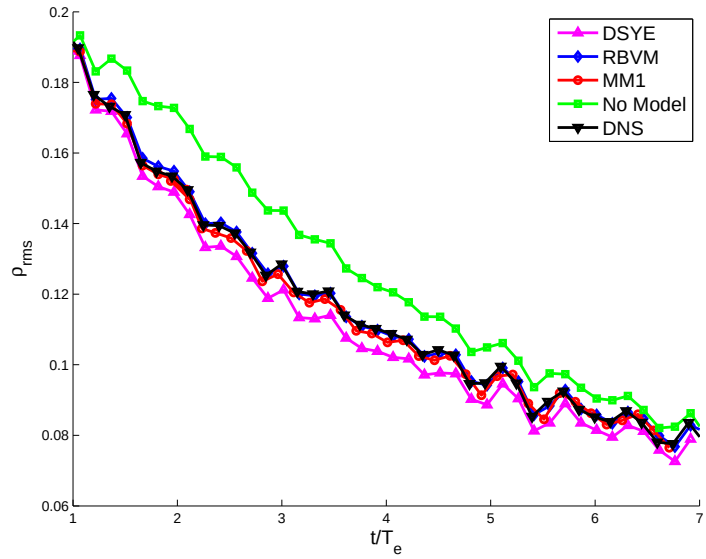

Figure 3.29: Time history of root-mean-square of density for the $Re_\lambda = 121.0$ case on a 64^3 grid with $\chi = 0.4$ and $Ma = 0.488$. A comparison of the DSYE, RBVM, MM1, and no model cases.

In Figures 3.27 - 3.29, we have plotted the evolution of the resolved turbulent

kinetic energies and density rms as a function of time. Once again it is observed that the DSYE model is too dissipative which RBVM and the mixed model works very well. Both the RBVM and mixed model have good agreement with DNS result. In Figures 3.30 - 3.33, the energy spectrum of the incompressible and compressible velocity components are given at $t/T_e \approx 3$ and $t/T_e \approx 6$. Once again we observe that the DSYE model is too dissipative at high wavenumbers for the incompressible velocity component. The RBVM model is very close to DNS. The performance of the mixed model is between the DSYE and RBVM model. For the compressible velocity component, both the RBVM and the mixed models perform very well, while the DSYE model overpredicts the spectrum near the cut-off wavenumber. The spectrum of density and pressure are shown in Figures 3.34 - 3.35. Here all the models are very accurate, however the DSYE model is not as accurate as the RBVM and the mixed model.

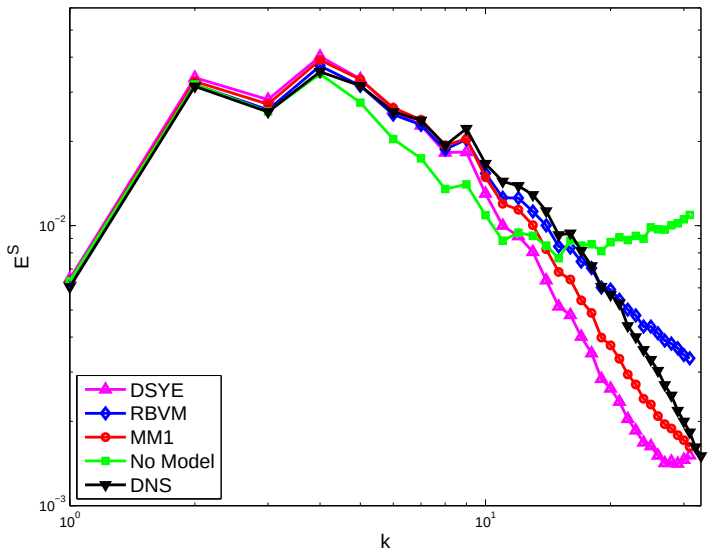

Figure 3.30: Energy spectrum of the incompressible velocity component for the $Re_\lambda = 121.0$ case on a 64^3 grid with $\chi = 0.4$ and $Ma = 0.488$ at $t/T_e \approx 3$. A comparison of the DSYE, RBVM, MM1, and no model cases.

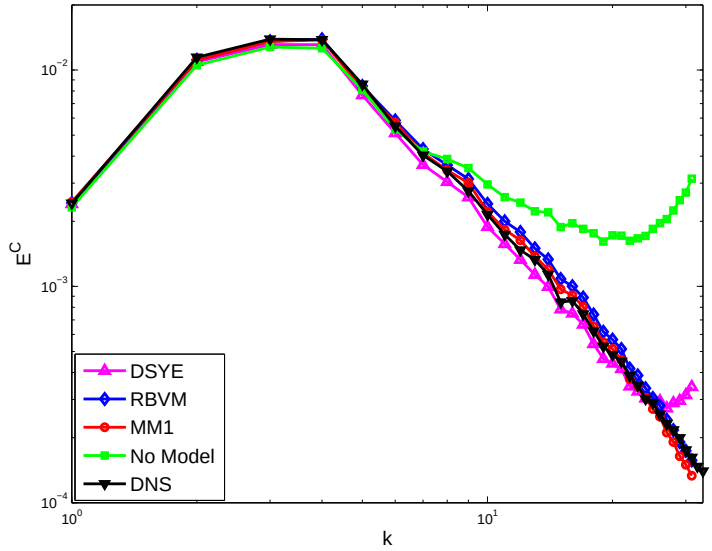

Figure 3.31: Energy spectrum of the compressible velocity component for the $Re_\lambda = 121.0$ case on a 64^3 grid with $\chi = 0.4$ and $Ma = 0.488$ at $t/T_e \approx 3$. A comparison of the DSYE, RBVM, MM1, and no model cases.

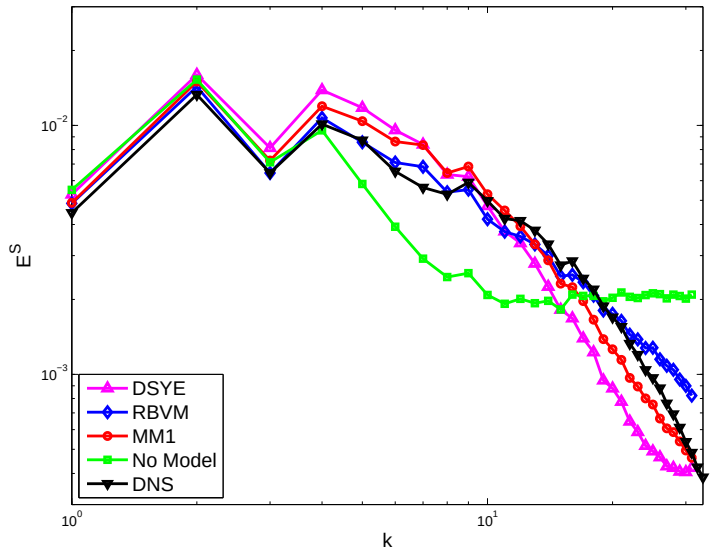

Figure 3.32: Energy spectrum of the incompressible velocity component for the $Re_\lambda = 121.0$ case on a 64^3 grid with $\chi = 0.4$ and $Ma = 0.488$ at $t/T_e \approx 6$. A comparison of the DSYE, RBVM, MM1, and no model cases.

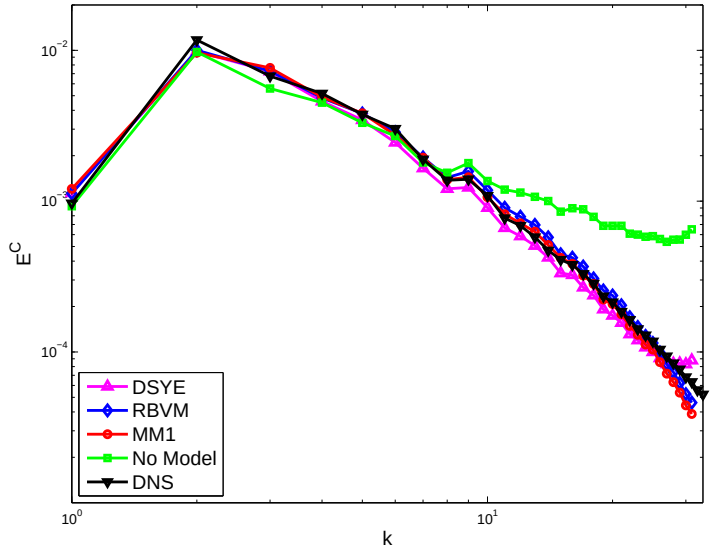

Figure 3.33: Energy spectrum of the compressible velocity component for the $Re_\lambda = 121.0$ case on a 64^3 grid with $\chi = 0.4$ and $Ma = 0.488$ at $t/T_e \approx 6$. A comparison of the DSYE, RBVM, MM1, and no model cases.

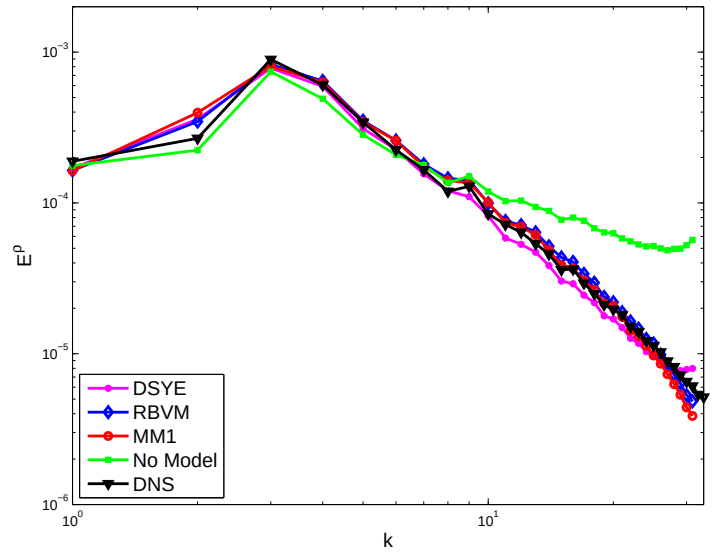

Figure 3.34: Density spectrum for the $Re_\lambda = 121.0$ case on a 64^3 grid with $\chi = 0.4$ and $Ma = 0.488$ at $t/T_e \approx 6$. A comparison of the DSYE, RBVM, MM1, and no model cases.

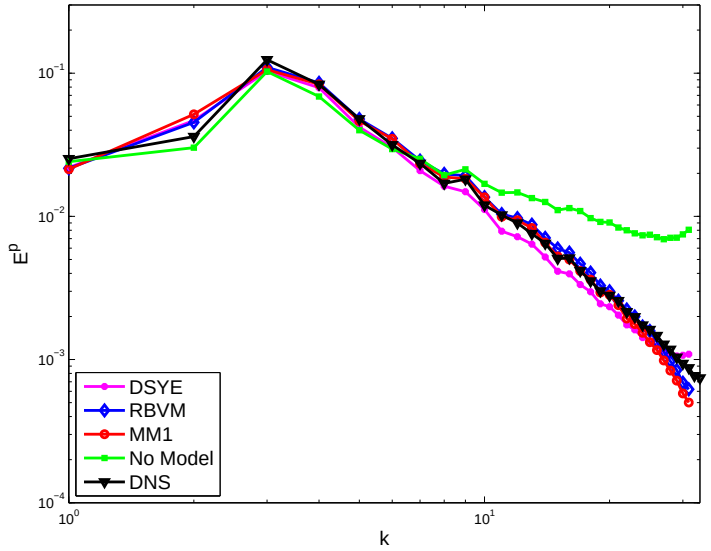

Figure 3.35: Pressure spectrum for the $Re_\lambda = 121.0$ case on a 64^3 grid with $\chi = 0.4$ and $Ma = 0.488$ at $t/T_e \approx 6$. A comparison of the DSYE, RBVM, MM1, and no model cases.

3.4.5 Summary

We have developed and implemented the residual-based variational multiscale (RBVM) model for compressible turbulent flows. Motivated by earlier results for incompressible flows we have also considered a mixed version of this model wherein Smagorinsky, Yoshizawa and eddy-diffusivity terms are added in order to better model the Reynolds stress contributions. Through energy analysis of the mixed model (performed in Chapter 2) we have demonstrated that the Yoshizawa model is redundant because the RBVM model itself introduces a viable Reynolds stress term for the dilatational component of subgrid stresses. In addition, from the dynamic procedure we have found that the eddy-diffusivity term in the energy equation is not required for the mixed RBVM model. As a result the mixed RBVM model contains only one term in addition to the RBVM model. This term models the Reynolds stress component of the deviatoric part of subgrid stresses and is represented by a Smagorinsky-type model.

We have tested the performance of the RBVM, the mixed and the dynamic Smagorinsky-Yoshizawa-eddy diffusivity (DSYE) models in predicting the decay

of compressible, homogeneous, isotropic turbulence in regimes where shocklets are known to exist. We have varied the level of compressibility of the flow by varying the initial proportion of turbulent kinetic energy and by varying the Mach number. In all cases we have found that RBVM and the mixed models are equally accurate and perform significantly better than the DSYE model. We have also found that for the mixed model the variational counterpart of the Germano identity automatically accounts for the dissipation produced by the RBVM terms and produces smaller Smagorinsky parameter when compared to the dynamic Smagorinsky model.

3.5 Numerical Results for the RBEV model

In this section we present results using the RBEV model. The models are tested in decaying homogeneous isotropic turbulent flows which are described in Section 3.4. However, in this section, we just test the cases with $Ma = 0.488$ and $\chi = 0.40$. We still test the models with different Reynolds numbers and different grids (32^3 and 64^3). The RBEV model is compared with dynamic Smagorinsky-Yoshizawa-eddy diffusivity (DSYE) model, and the static Smagorinsky-Yoshizawa-eddy diffusivity (SSYE) model with coefficient $C_s = 0.10$ and $C_s = 0.16$. For all the LES models in this section, $C_\tau = 1.0$ for the stabilization parameter $\boldsymbol{\tau}$. The intent of the results presented in this section is to test the performance of the RBEV model as a stand-alone eddy viscosity model.

3.5.1 Low Reynolds Number Case

In the low Reynolds Numbers case, $Re = 376$ and DNS is performed with 256^3 mesh and time step $dt = 0.001$. For the LES calculations we use the truncated velocity field obtained from the DNS at $t/T_e = 1.2$, where $T_e = 0.667$ as the initial condition. We compare the performance of the models from $t/T_e = 1.2 \sim 7.0$, which corresponds to a Taylor micro-scale Reynolds number of $Re_\lambda = 65.5 \sim 27.4$. Both 32^3 and 64^3 meshes are considered for LES simulation with $dt = 0.005$. We refer this low Reynolds number test case as $Re_\lambda = 65.5$

In Figures 3.36 - 3.42 we present results for the low Reynolds number case on a 32^3 mesh.

In Figure 3.36, the time history of the turbulent kinetic energies (TKE) is plotted for all the models. We observe that overall the RBEV model is the most accurate followed by the static SYE model with $C_s = 0.10$, the DSYE model and then the static SYE model with $C_s = 0.16$. In Figure 3.37, the time history of root-mean-square (RMS) of density and temperature are shown. Both the RBEV and the static SYE model with $C_s = 0.10$ are very close to the DNS result, while the DSYE model and the static SYE model with $C_s = 0.16$ are too dissipative.

In Figure 3.38 we have plotted the spectra of the total TKE at $t/T_e = 3$ and $t/T_e = 6$. We observe that the RBEV and the static SYE(0.10) are the most accurate while the other two models are overly dissipative. This observation also holds for the incompressible spectra shown in Figure 3.39. However, for the compressible spectra we observe that all the models about equally accurate. Figure 3.40 shows the spectrum of density, pressure and temperature at $t/T_e = 6$. Here too, the RBEV and the static SYE(0.10) perform better.

In Figure 3.41, we show the time history of the eddy viscosity of different models at four points given by the coordinates $(0, 0, 0)$, $(L/4, L/4, L/4)$,$(L/2, L/2, L/2)$ and $(0, L/4, L/2)$. We observe that all viscosities vary widely in time but generally decrease with time. The values of the RBEV and the SSYE(0.10) models and of the DSYE and SSYE(0.16) are similar. The same trends are also seen in the values of the average values of viscosities shown in Figure 3.42. These plots explain why the performance of the RBEV and the SSYE(0.10) models and the the DSYE and SSYE(0.16) models is similar. They also explain why the results for the latter are more dissipative.

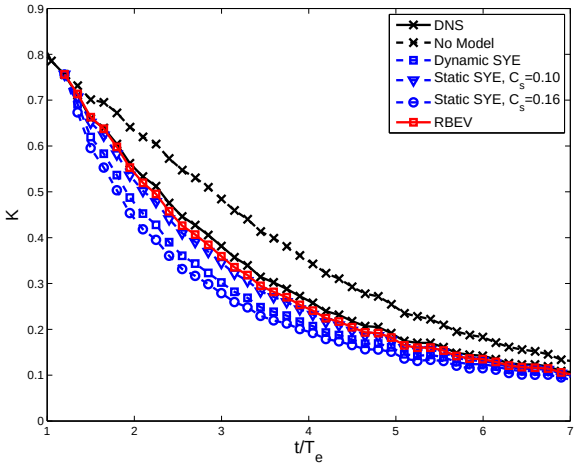

(a) total velocity

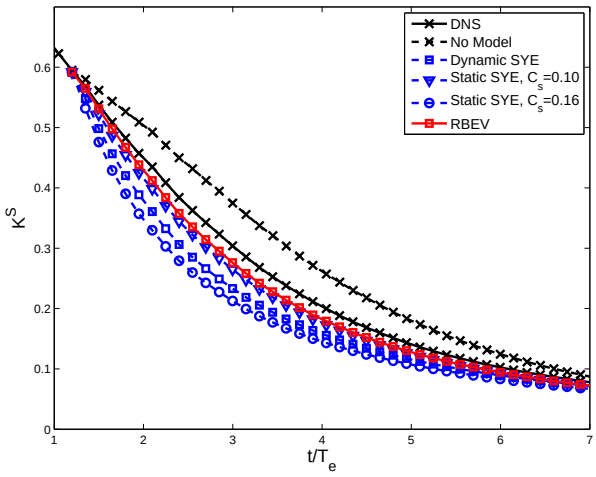

(b) solenoidal velocity

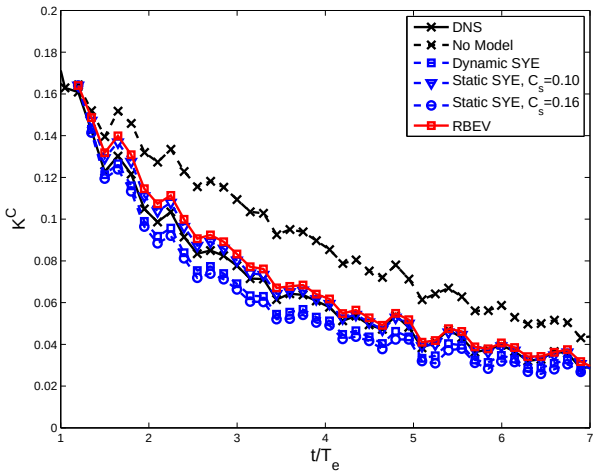

(c) dilatational velocity

Figure 3.36: Time history of turbulent kinetic energy for the $Re_\lambda = 65.5$ case on a 32^3 grid. A comparison of the dynamic and static SYE, RBEV, and no model cases.

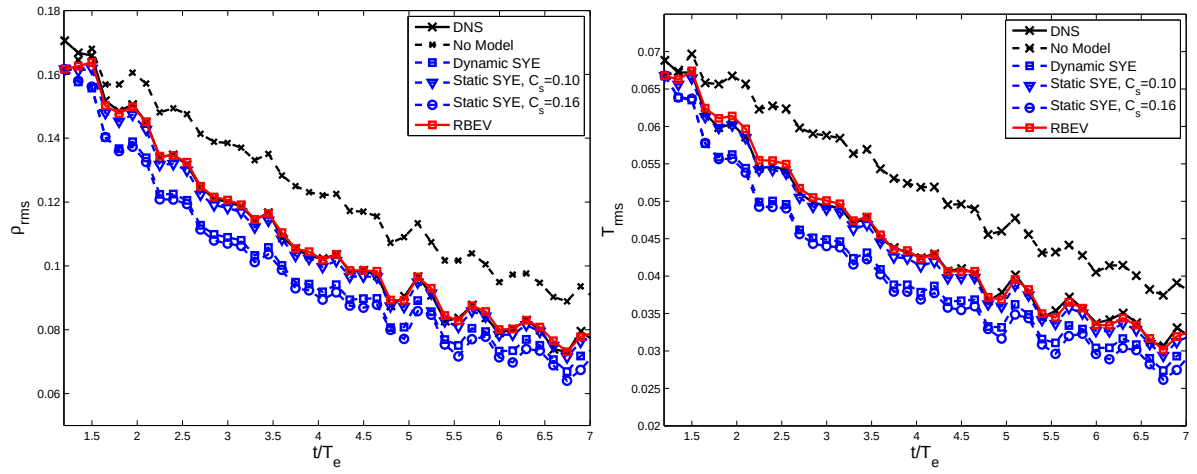

(a) density (b) temperature

Figure 3.37: Time history of root-mean-square of density and temperature for the $Re_\lambda = 65.5$ case on a 32^3 grid. A comparison of the dynamic and static SYE, RBEV, and no model cases.

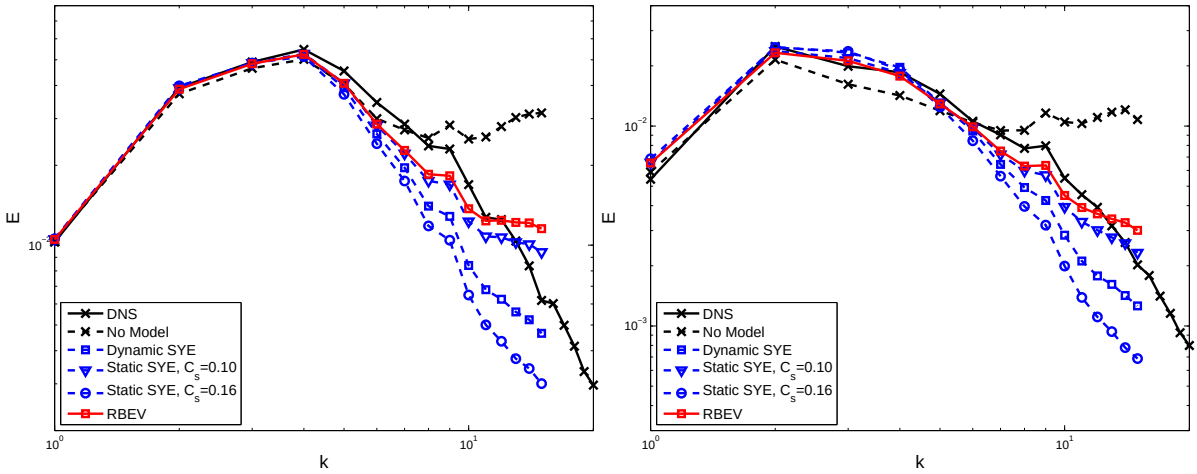

(a) total velocity, $t/T_e = 3$ (b) total velocity, $t/T_e = 6$

Figure 3.38: Energy spectrum of the total velocity for the $Re_\lambda = 65.5$ case on a 32^3 grid. A comparison of the dynamic and static SYE, RBEV, and no model cases.

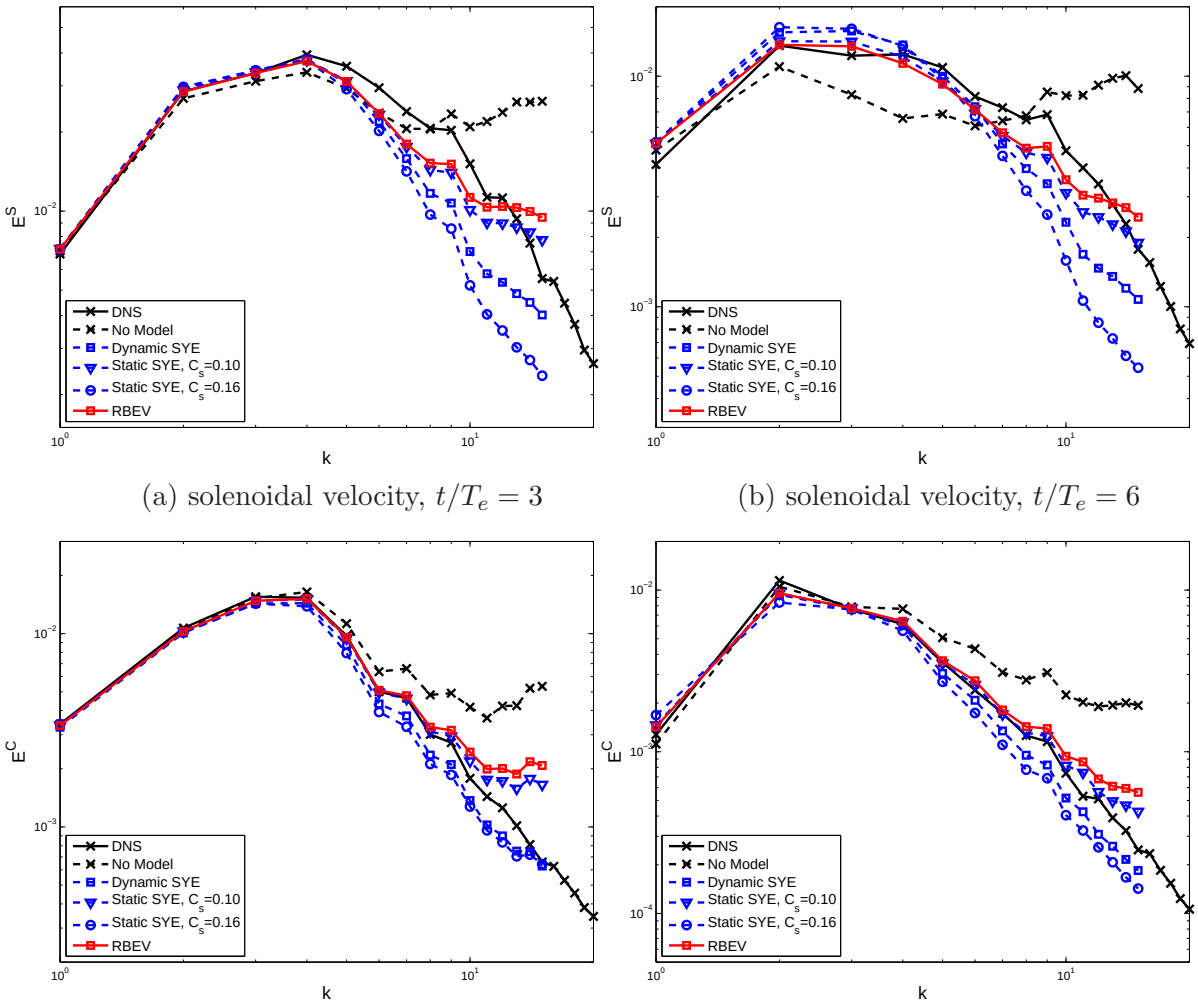

(a) solenoidal velocity, $t/T_e = 3$

(b) solenoidal velocity, $t/T_e = 6$

(c) dilatational velocity, $t/T_e = 3$

(d) dilatational velocity, $t/T_e = 6$

Figure 3.39: Energy spectrum of solenoidal and dilatational velocity for the $Re_\lambda = 65.5$ case on a 32^3 grid. A comparison of the dynamic and static SYE, RBEV, and no model cases.

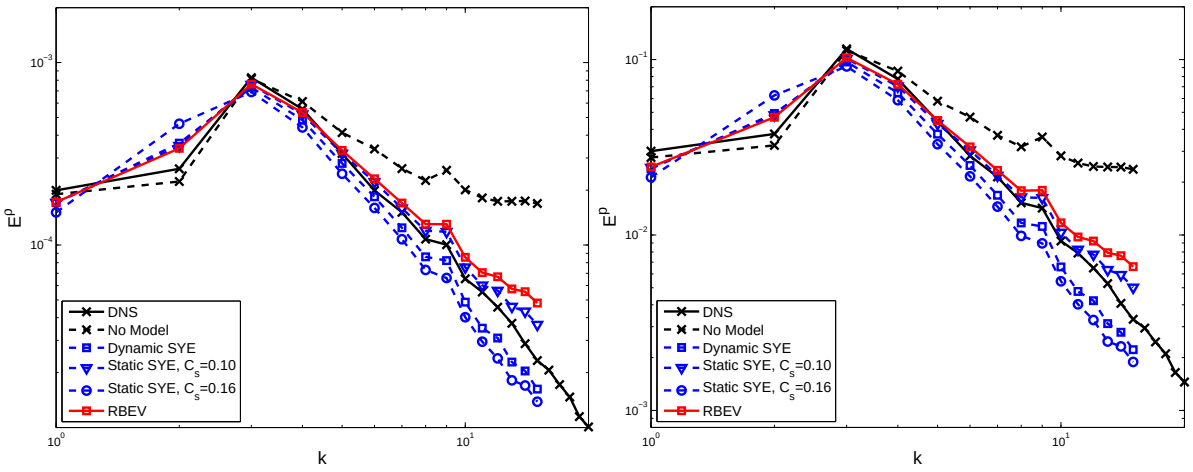

(a) density, $t/T_e = 6$

(b) pressure, $t/T_e = 6$

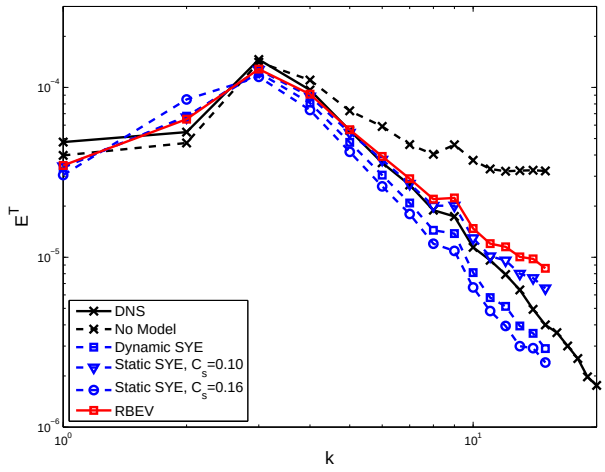

(c) temperature, $t/T_e = 6$

Figure 3.40: Spectrum of density, pressure and temperature for the $Re_\lambda = 65.5$ case on a 32^3 grid. A comparison of the dynamic and static SYE, RBEV, and no model cases.

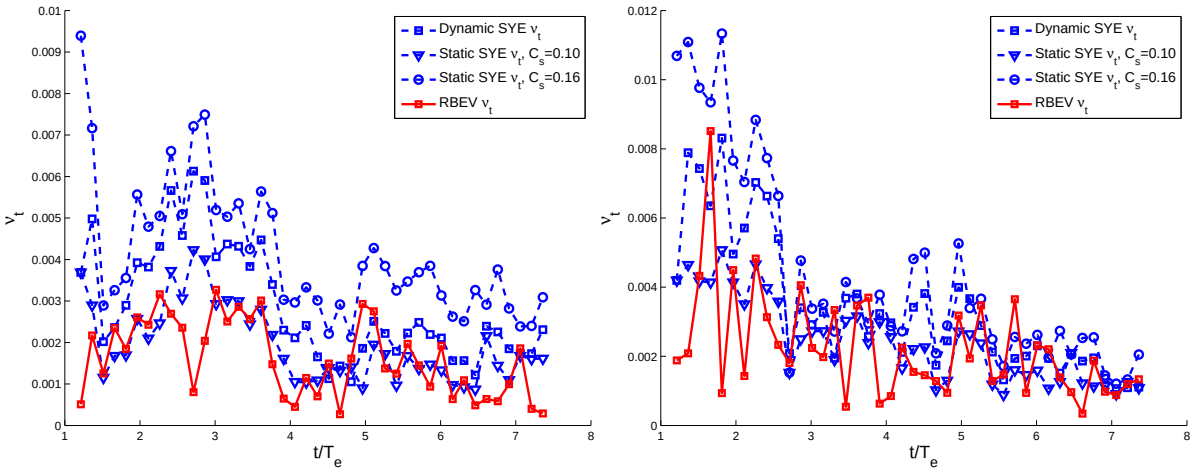

(a) point $(0, 0, 0)$ (b) point $(L/4, L/4, L/4)$

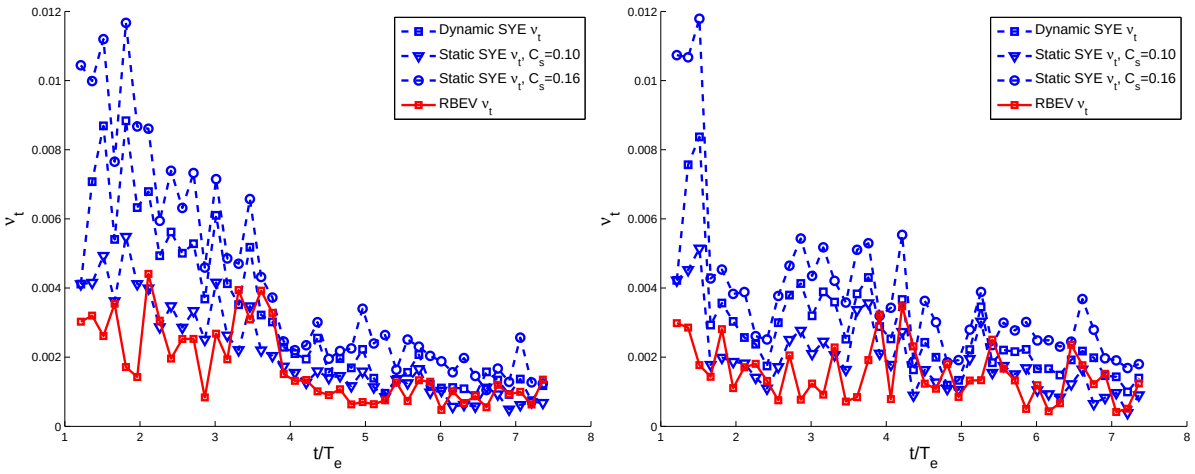

(c) point $(L/2, L/2, L/2)$ (d) point $(0, L/4, L/2)$

Figure 3.41: Time history of eddy viscosity for the $Re_\lambda = 65.5$ case on a 32^3 grid. A comparison of the dynamic and static SYE and RBEV cases.

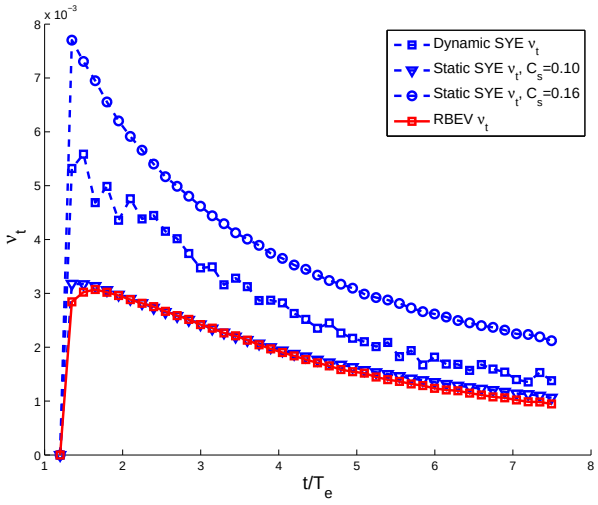

Figure 3.42: Time history of average eddy viscosity for the $Re_\lambda = 65.5$ case on a 32^3 grid. A comparison of the dynamic and static SYE and RBEV cases.

We now consider the same problem but on a fine mesh of 64^3 modes. In Figure 3.43 we have plotted the evolution of kinetic energies as a function of time. We now observe that the RBEV, DSYE, and SSYE(0.10) models are all very accurate while the SSYE(0.16) model is less so. The same observations hold for the time-history of the RMS of density and temperature shown in Figure 3.44.

In the spectra of the total velocity (Figure 3.45) and incompressible velocity (Figure 3.46(a) and (b)), RBEV is most accurate followed by DSYE and SSYE(0.1), and then SSYE(0.16). For the compressible velocity spectra (shown in Figure 3.46(c) and (d)), the DSYE and the SSYE(0.1) are the most accurate followed by the RBEV and the SSYE(0.16) models. The spectra for density, temperature and pressure (Figure 3.47) all show the same trends.

The average eddy viscosity as a function of time for all the models is shown in Figure 3.48. We observe that the values for the DSYE and SSYE(0.1) is very close, while that of SSYE(0.16) is higher and that of RBEV is smaller. This explains why the RBEV is the least dissipative, followed by the DSYE and SSYE(0.1), and then the SSYE(0.16) models.

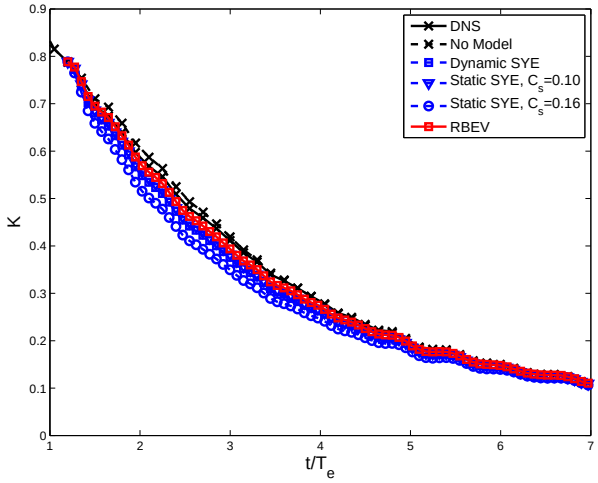

(a) total velocity

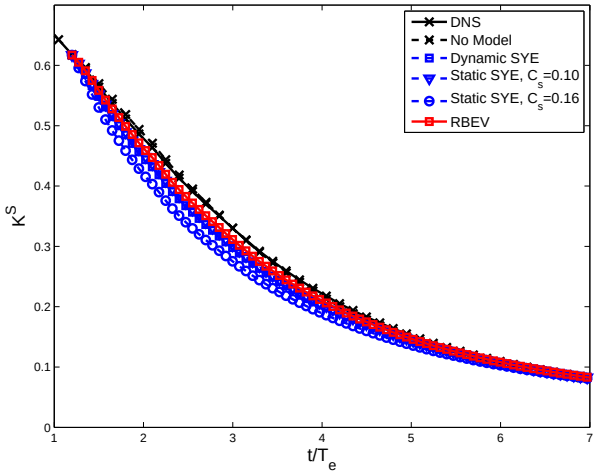

(b) solenoidal velocity

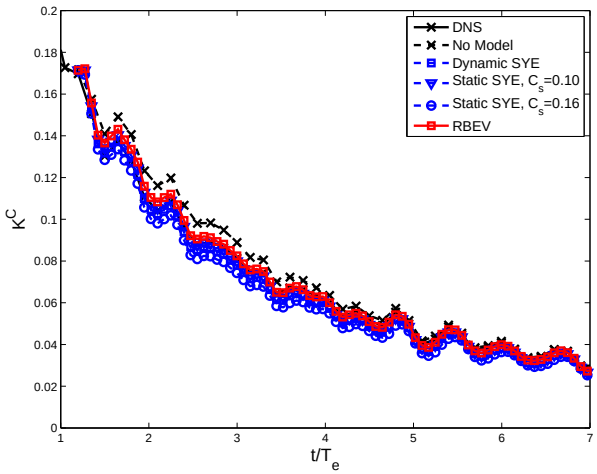

(c) dilatational velocity

Figure 3.43: Time history of turbulent kinetic energy for the $Re_\lambda = 65.5$ case on a 64^3 grid. A comparison of the dynamic and static SYE, RBEV, and no model cases.

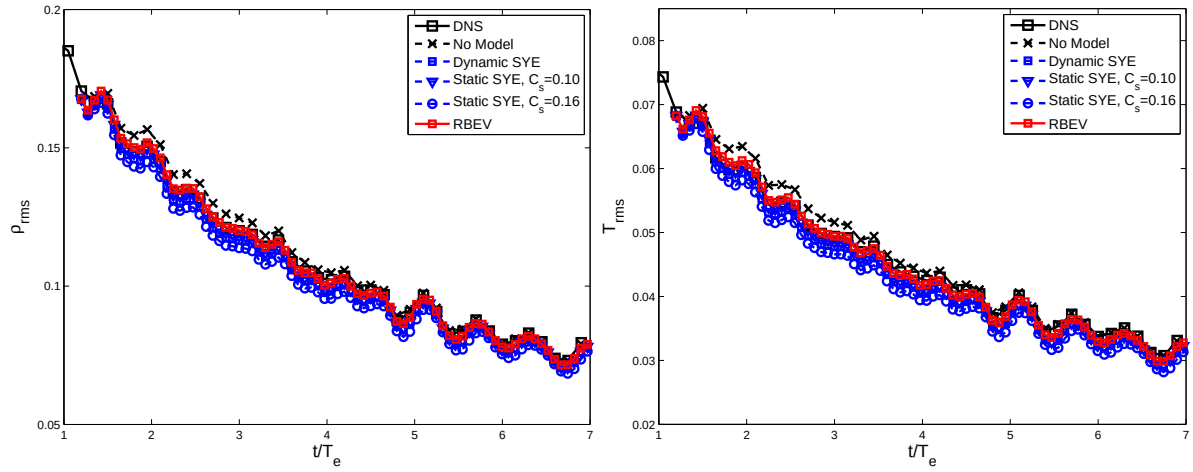

(a) density (b) temperature

Figure 3.44: Time history of root-mean-square of density and temperature for the $Re_\lambda = 65.5$ case on a 64^3 grid. A comparison of the dynamic and static SYE, RBEV, and no model cases.

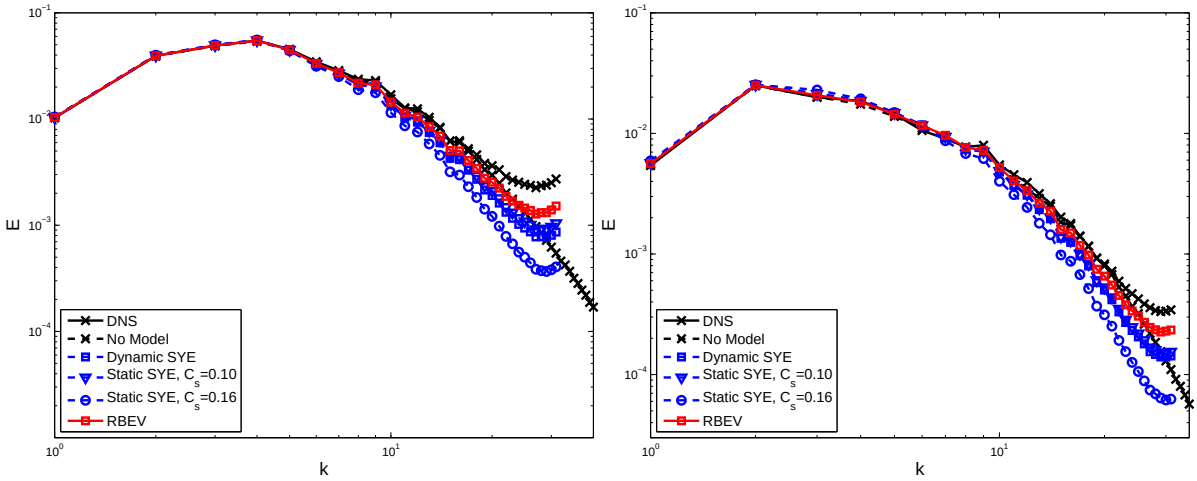

(a) total velocity, $t/T_e = 3$ (b) total velocity, $t/T_e = 6$

Figure 3.45: Energy spectrum of the total velocity for the $Re_\lambda = 65.5$ case on a 64^3 grid. A comparison of the dynamic and static SYE, RBEV, and no model cases.

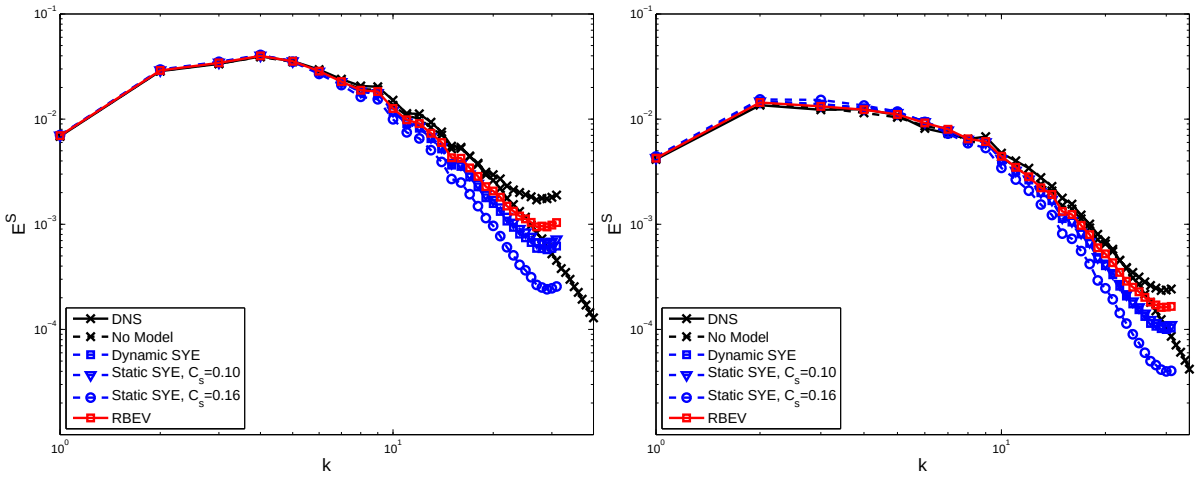

(a) solenoidal velocity, $t/T_e = 3$ (b) solenoidal velocity, $t/T_e = 6$

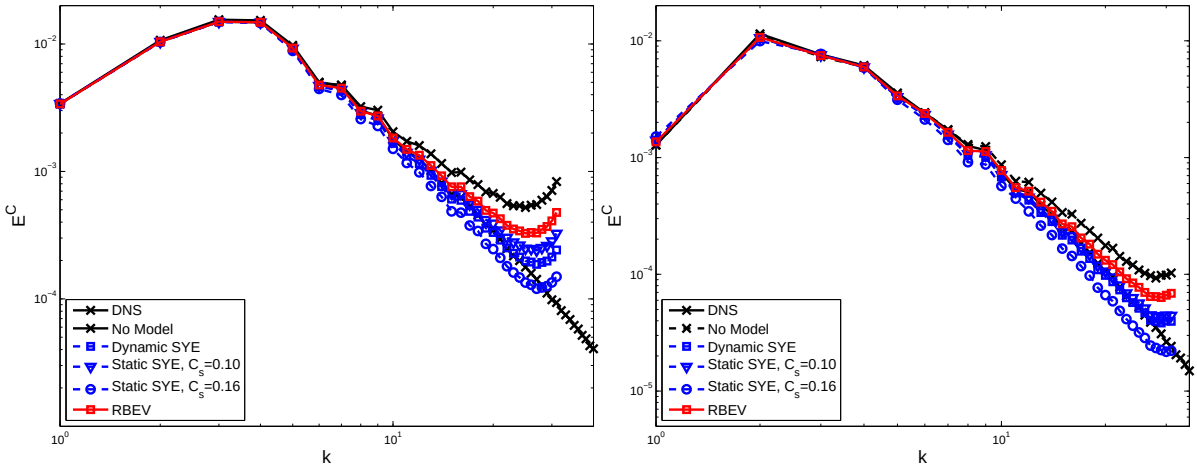

(c) dilatational velocity, $t/T_e = 3$ (d) dilatational velocity, $t/T_e = 6$

Figure 3.46: Energy spectrum of solenoidal and dilatational velocity for the $Re_\lambda = 65.5$ case on a 64^3 grid. A comparison of the dynamic and static SYE, RBEV, and no model cases.

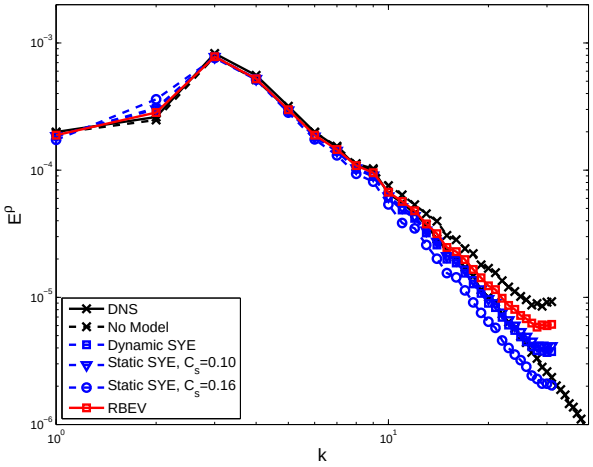

(a) density, $t/T_e = 6$

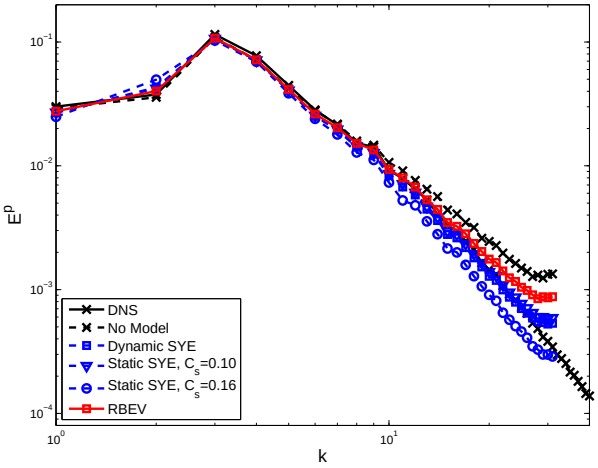

(b) pressure, $t/T_e = 6$

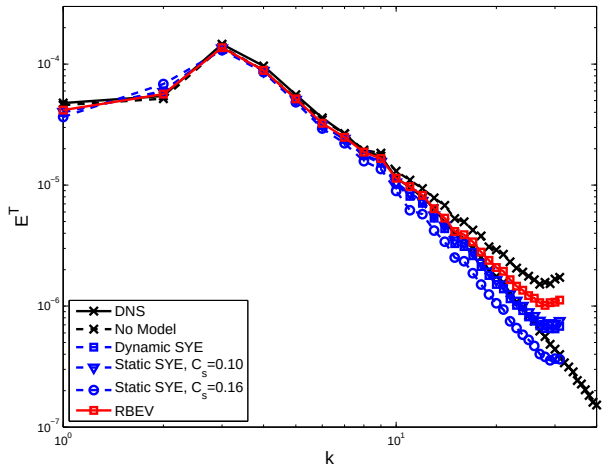

(c) temperature, $t/T_e = 6$

Figure 3.47: Spectrum of density, pressure and temperature for the $Re_\lambda = 65.5$ case on a 64^3 grid. A comparison of the dynamic and static SYE, RBEV, and no model cases.

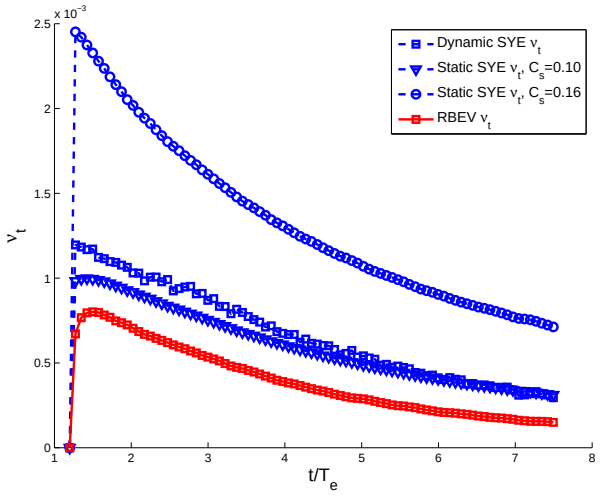

Figure 3.48: Time history of average eddy viscosity for the $Re_\lambda = 65.5$ case on a 64^3 grid. A comparison of the dynamic and static SYE and RBEV cases.

3.5.2 High Reynolds Number Case

In the high Reynolds Numbers case, $Re = 843.79$. For the LES calculations we use the truncated velocity field obtained from the DNS at $t/T_e = 1.05$, where $T_e = 0.667$ at the initial condition. For the DNS, the mesh is 512^3 with $dt = 0.0005$. We compare the performance of the models from $t/T_e = 1.05 \sim 7.0$, which corresponds to a Taylor micro-scale Reynolds number of $Re_\lambda = 117.1 \sim 40.9$. Both 32^3 and 64^3 meshes are considered for LES simulation with $dt = 0.005$. We refer this test case as $Re_\lambda = 117.1$. Figures 3.49 - 3.60 contain the plots for this case.

First we consider the results for the 32^3 case. The plots for the variation of turbulent kinetic energies and RMS values (Figures 3.49 and 3.50, respectively) indicate that RBEV model and the SSYE(0.10) model are the equally accurate followed by the DSYE and SSYE(0.16) models.

The spectra for the total kinetic energy (Figure 3.51) and the incompressible kinetic energy (Figure 3.52(a) and (b)) reveal that the RBEV and the SSYE(0.10) models are the most accurate followed by the DSYE and the SSYE(0.16) models.

In the spectra for the compressible kinetic energy (Figure 3.52(c) and (d)), no LES model is particularly good. The DSYE and the SSYE(0.16) models are too dissipative with the RBEV and the SSYE(0.10) models are not dissipative enough.

In the spectra of the density, pressure and temperature (Figure 3.53), we observe that the RBEV and SSYE(0.10) models are once the most accurate. However, now they behave differently: while the RBEV model underpredicts at large wavenumber, the SSYE(0.10) model overpredicts.

Figure 3.54 shows the spatial average of eddy viscosity as function of time. The RBEV and the SSYE(0.10) models, and the DSYE and the SSYE(0.16) have similar values, which would explain their similar performances.

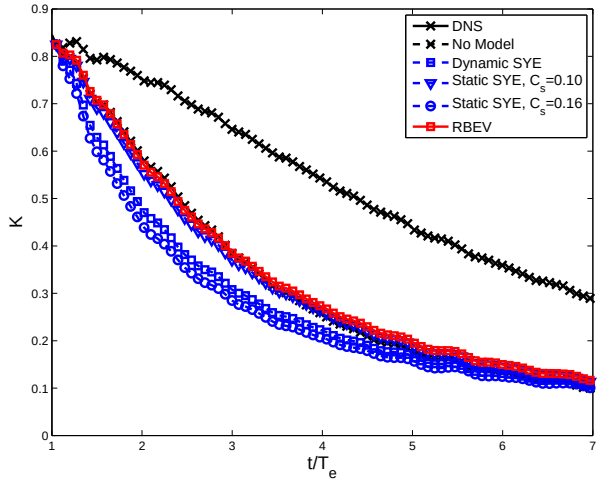

(a) total velocity

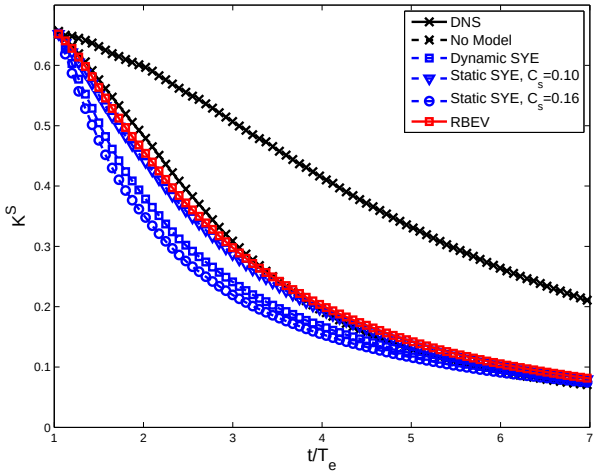

(b) solenoidal velocity

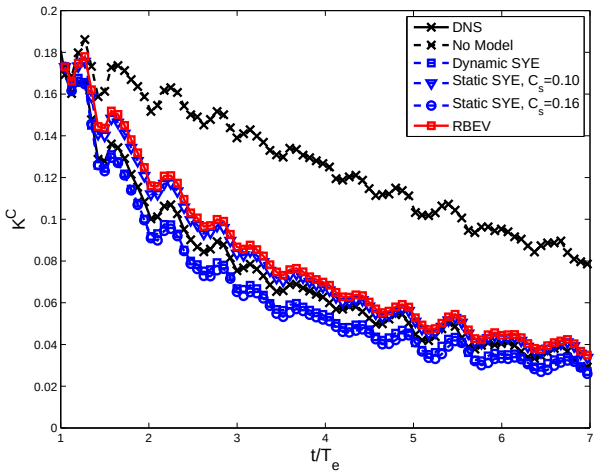

(c) dilatational velocity

Figure 3.49: Time history of turbulent kinetic energy for the $Re_\lambda = 117.1$ case on a 32^3 grid. A comparison of the dynamic and static SYE, RBEV, and no model cases.

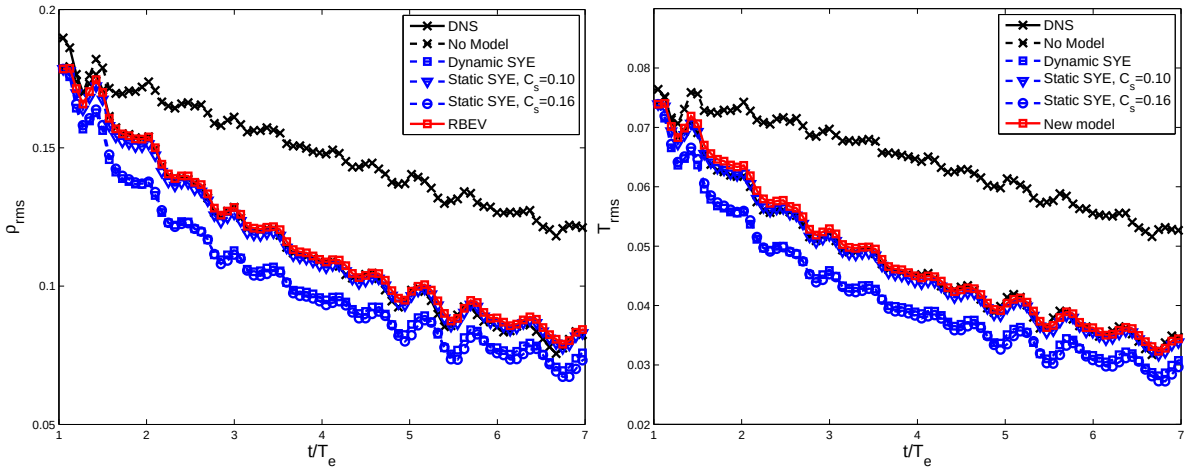

(a) density (b) temperature

Figure 3.50: Time history of root-mean-square of density and temperature for the $Re_\lambda = 117.1$ case on a 32^3 grid. A comparison of the dynamic and static SYE, RBEV, and no model cases.

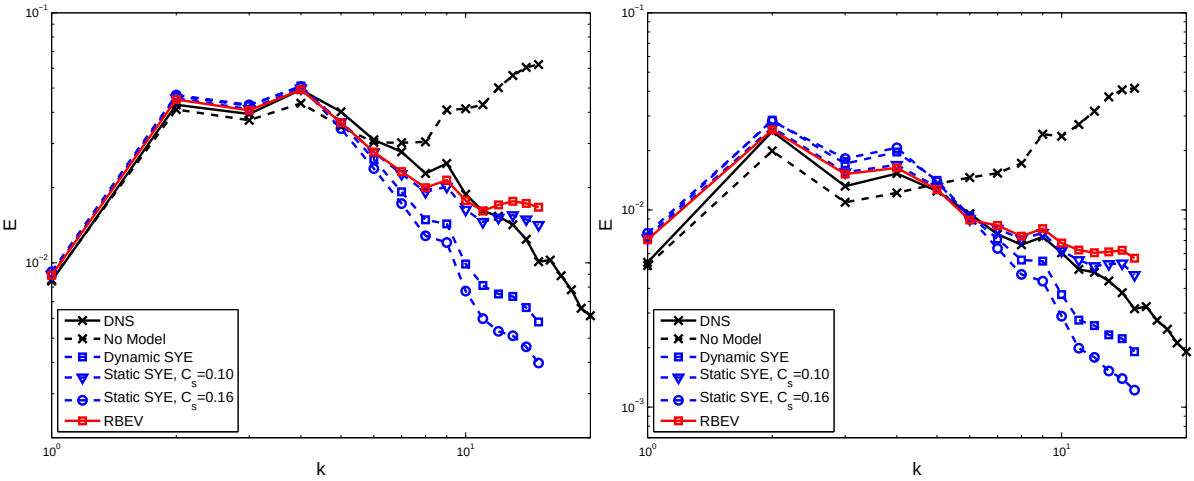

(a) total velocity, $t/T_e = 3$ (b) total velocity, $t/T_e = 6$

Figure 3.51: Energy spectrum of the total velocity for the $Re_\lambda = 117.1$ case on a 32^3 grid. A comparison of the dynamic and static SYE, RBEV, and no model cases.

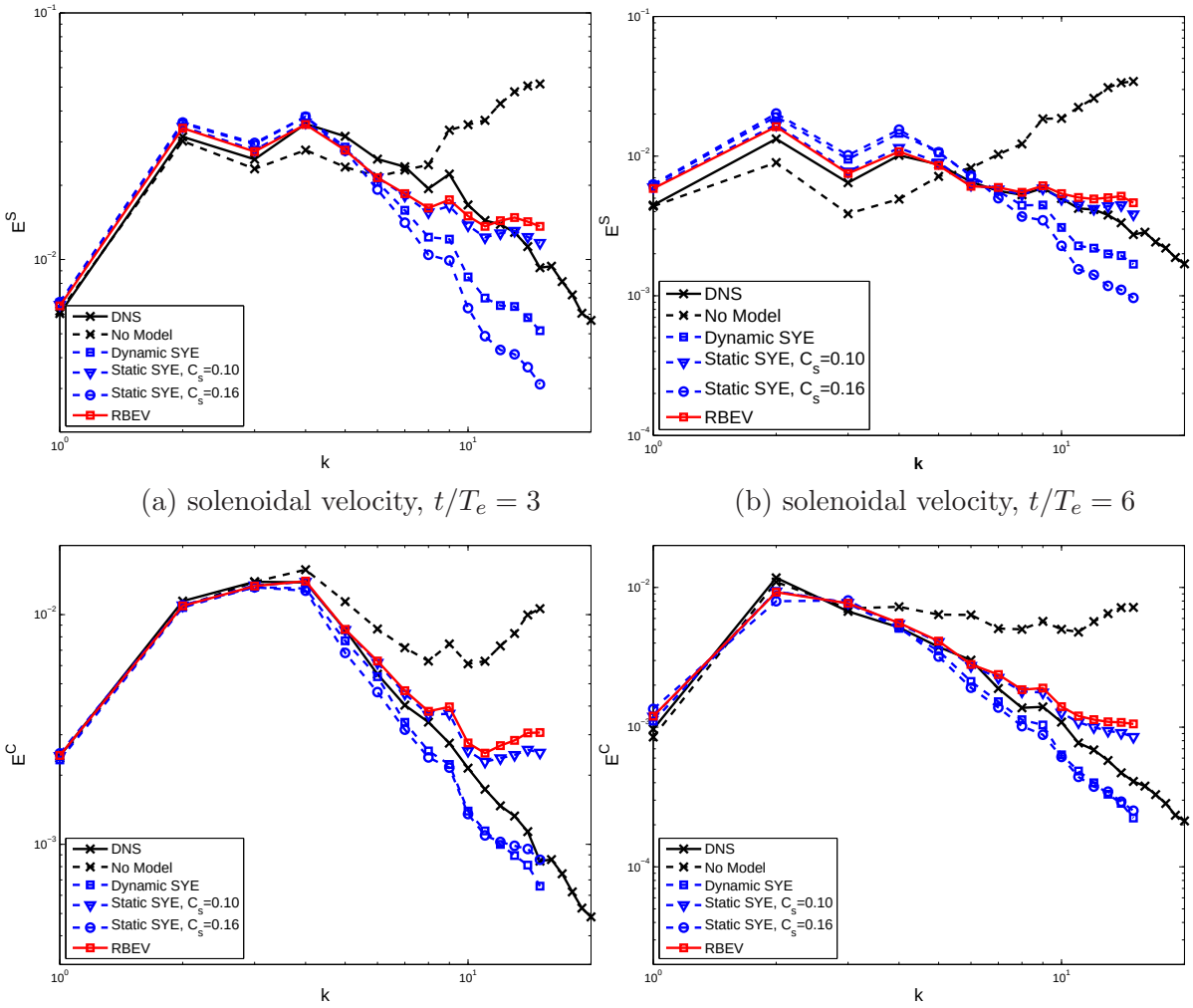

(a) solenoidal velocity, $t/T_e = 3$

(b) solenoidal velocity, $t/T_e = 6$

(c) dilatational velocity, $t/T_e = 3$

(d) dilatational velocity, $t/T_e = 6$

Figure 3.52: Energy spectrum of solenoidal and dilatational velocity for the $Re_\lambda = 117.1$ case on a 32^3 grid. A comparison of the dynamic and static SYE, RBEV, and no model cases.

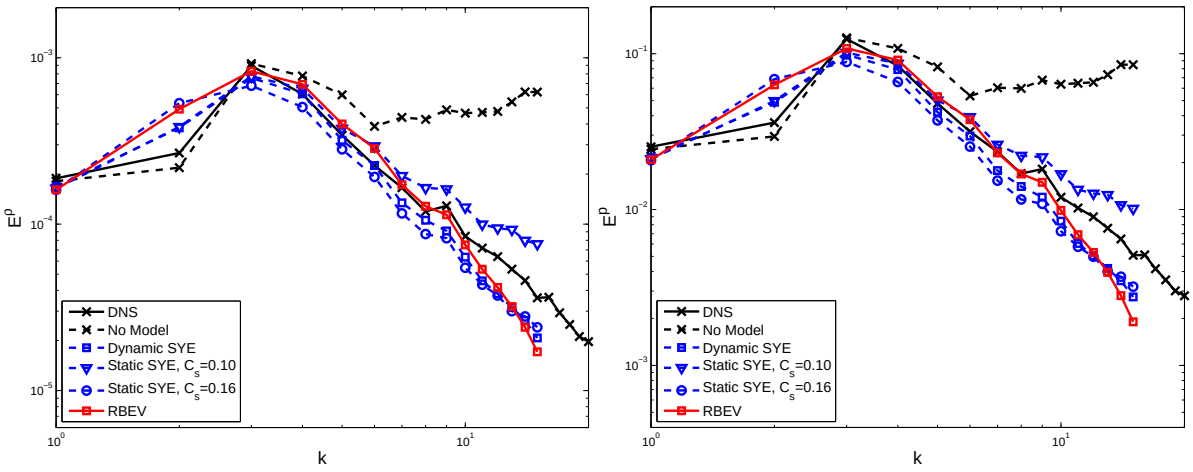

(a) density, $t/T_e = 6$

(b) pressure, $t/T_e = 6$

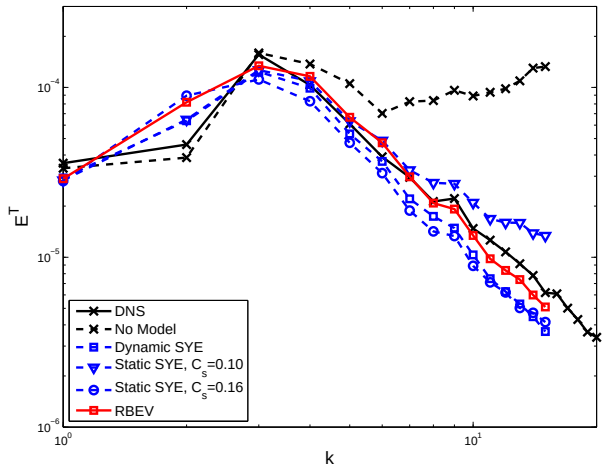

(c) temperature, $t/T_e = 6$

Figure 3.53: Spectrum of density, pressure and temperature for the $Re_\lambda = 117.1$ case on a 32^3 grid. A comparison of the dynamic and static SYE, RBEV, and no model cases.

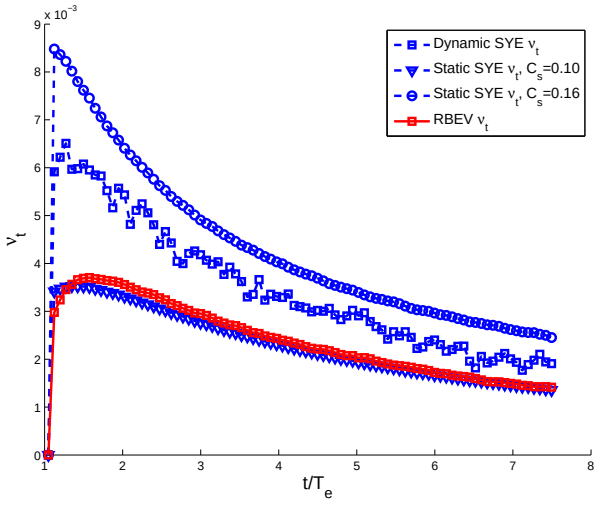

Figure 3.54: Time history of average eddy viscosity for the $Re_\lambda = 117.1$ case on a 32^3 grid. A comparison of the dynamic and static SYE and RBEV cases.

Figures 3.55 - 3.60 are the results for high Reynolds number, $Re_\lambda = 117.1$ case, on a 64^3 mesh.

In Figure 3.55 we have plotted the evolution of kinetic energies as a function of time. For the total and incompressible component, we observe that the RBEV is the most accurate followed by DSYE and SSYE(0.1), and then SSYE(0.16). For the compressible component the same trend is seen even though all models appear to perform well. The same trend is observed in the evolution of rms values of density and temperature (see Figure 3.56).

In the plots for the spectra for the total and incompressible kinetic energy we observe that the RBEV model is the most accurate followed by SSYE(0.10), DSYE, and SSYE(0.16) (see Figures 3.57 and 3.58). In the spectra of the compressible kinetic energy we observe that the DSYE is most accurate, followed by the SSYE(0.10) model, the RBEV model and the SSYE(0.16) model. In this case the SSYE(0.10) and RBEV models are not dissipative enough while the SSYE(0.16) is too dissipative. The same trends are seen in the spectra for the density, pressure

and temperature(see Figure 3.59).

These results are explained by looking at the variation of the average eddy viscosity of all models (see Figure 3.60). We observe that the SSYE(0.16) has the largest viscosity, followed by the DSYE, the SSYE(0.10) and the RBEV models.

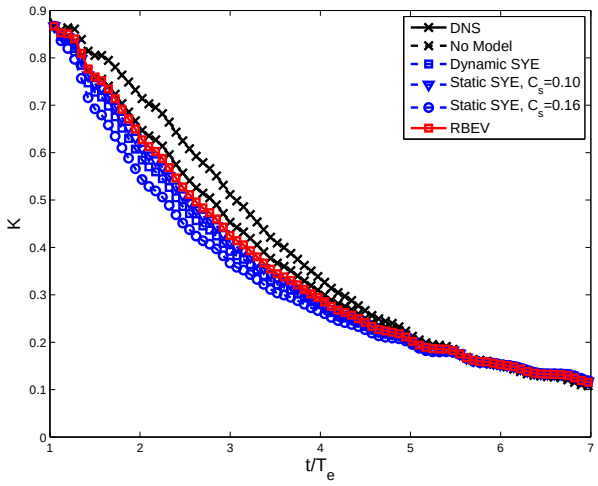

(a) total velocity

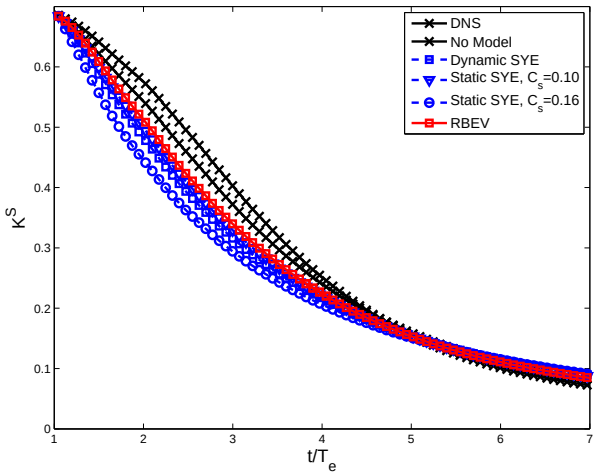

(b) solenoidal velocity

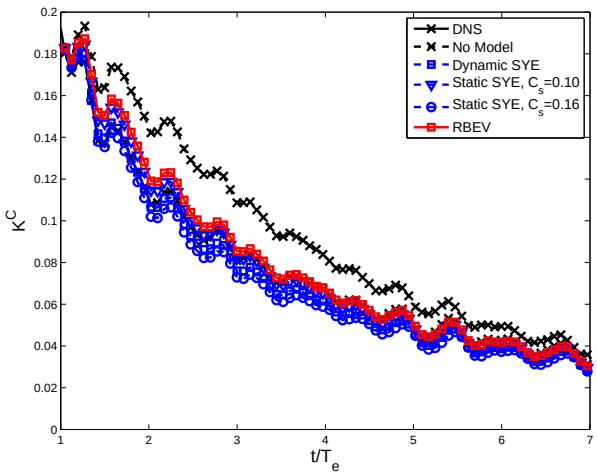

(c) dilatational velocity

Figure 3.55: Time history of turbulent kinetic energy for the $Re_\lambda = 117.1$ case on a 64^3 grid. A comparison of the dynamic and static SYE, RBEV, and no model cases.

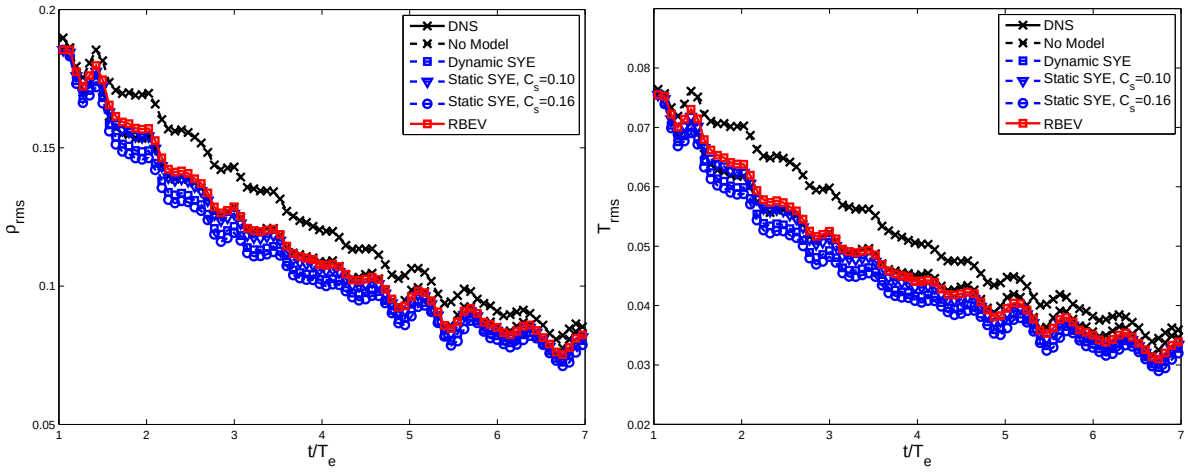

(a) density (b) temperature

Figure 3.56: Time history of root-mean-square of density and temperature for the $Re_\lambda = 117.1$ case on a 64^3 grid. A comparison of the dynamic and static SYE, RBEV, and no model cases.

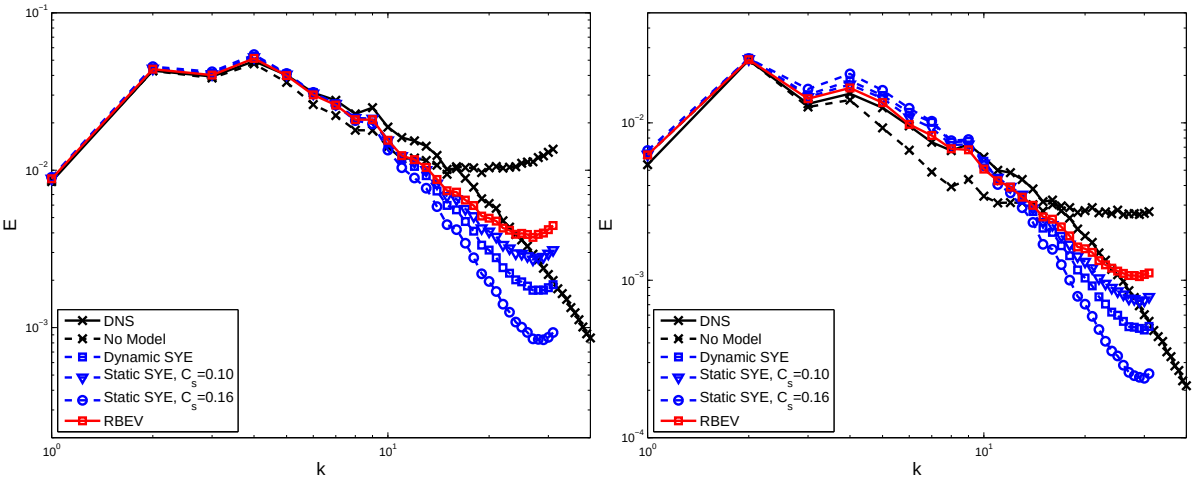

(a) total velocity, $t/T_e = 3$ (b) total velocity, $t/T_e = 6$

Figure 3.57: Energy spectrum of the total velocity for the $Re_\lambda = 117.1$ case on a 64^3 grid. A comparison of the dynamic and static SYE, RBEV, and no model cases.

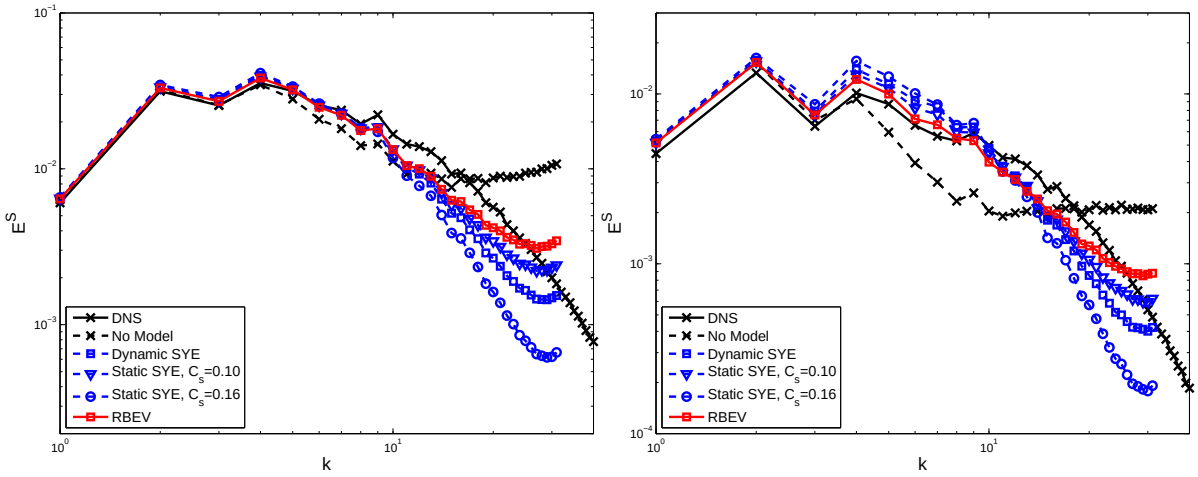

(a) solenoidal velocity, $t/T_e = 3$

(b) solenoidal velocity, $t/T_e = 6$

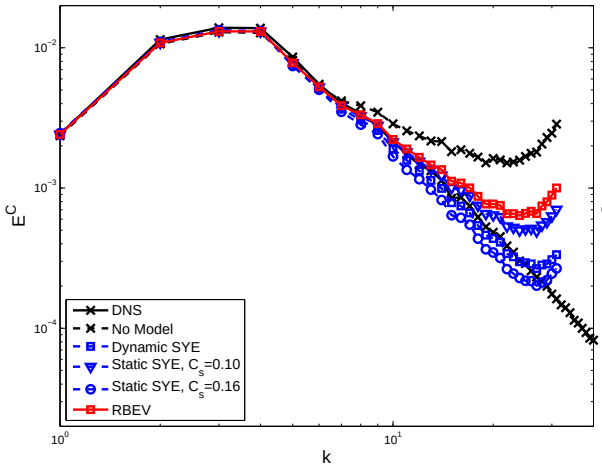

(c) dilatational velocity, $t/T_e = 3$

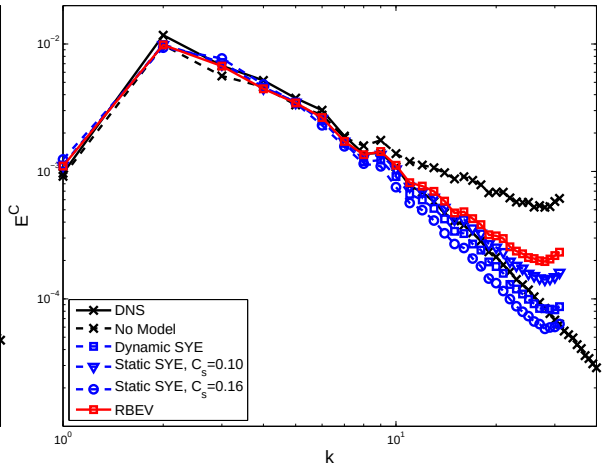

(d) dilatational velocity, $t/T_e = 6$

Figure 3.58: Energy spectrum of solenoidal and dilatational velocity for the $Re_\lambda = 117.1$ case on a 64^3 grid. A comparison of the dynamic and static SYE, RBEV, and no model cases.

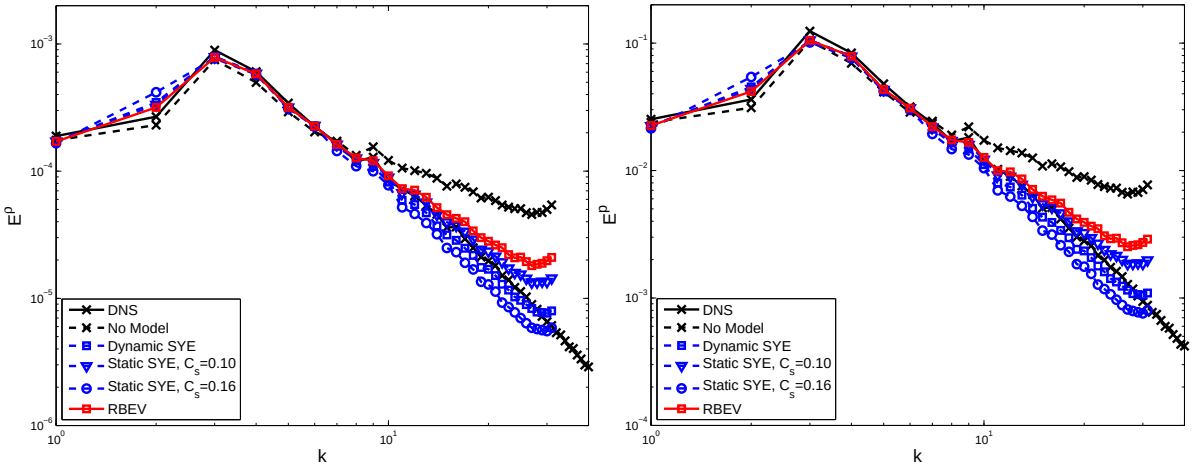

(a) density, $t/T_e = 6$

(b) pressure, $t/T_e = 6$

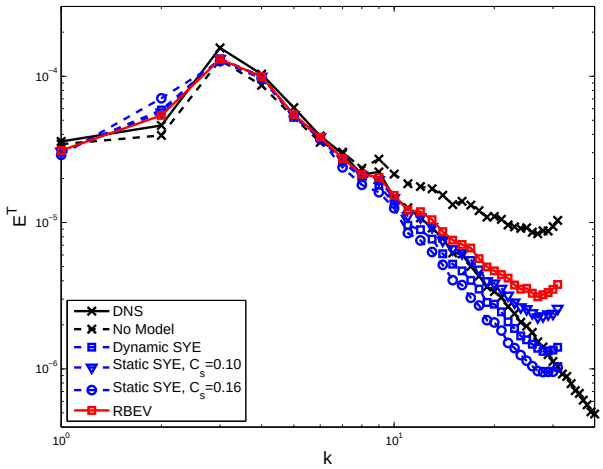

(c) temperature, $t/T_e = 6$

Figure 3.59: Spectrum of density, pressure and temperature for the $Re_\lambda = 117.1$ case on a 64^3 grid. A comparison of the dynamic and static SYE, RBEV, and no model cases.

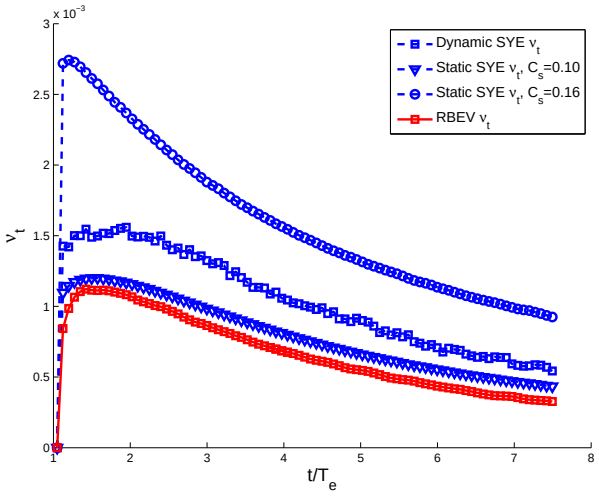

Figure 3.60: Time history of average eddy viscosity for the $Re_\lambda = 117.1$ case on a 64^3 grid. A comparison of the dynamic and static SYE and RBEV cases.

3.6 Numerical Results for the MM2 Model

In this section we present the results of the purely residual-based mixed model (MM2). The models are tested in the same decaying homogeneous isotropic turbulent flows as that for the RBEV model in the previous section. The MM2 model is compared with the RBVM model, the RBEV model and the DSYE model. We remind the reader that the MM2 model is an additive combination of the RBVM and RBEV models. We test the models with different Reynolds numbers and different grids (32^3 and 64^3). For all the LES models in this section, $C_\tau = 1.0$ in the definition for the stabilization parameter $\boldsymbol{\tau}$.

3.6.1 Low Reynolds Number Case

The parameters for this flow are the same as the low Reynolds number case described in the previous section.

In Figures 3.61 - 3.66 we present results for the low Reynolds number case on a 32^3 mesh. In Figure 3.61, the time history of the turbulent kinetic energies is plotted

for all the models. For the total and incompressible component, we observe that the RBVM model is the most accurate followed by the RBEV and MM2 models, and then the DSYE model. For the compressible component, the RBVM model is the most accurate followed by MM2 and RBEV, and then DSYE. In Figure 3.62, the time history of RMS of density and temperature are shown. Both the RBEV and RBVM models are very close to the DNS result, followed by the MM2 model. The DSYE model is too dissipative.

In Figure 3.63, we have plotted the spectra of the total TKE at $t/T_e = 3$ and $t/T_e = 6$. We observe that RBVM mode is the most accurate while the MM2 model is slightly more dissipative and the RBEV model displays a slight pile-up on energy at large wavenumbers. DSYE is the least accurate and is too dissipative. This observation also holds for the incompressible spectra shown in Figure 3.64(a) and (b). However, for the compressible spectra in Figure 3.64(c) and (d), we observe that the RBEV model and the DSYE model are better than the RBVM and MM2 models. The last two are too dissipative.

Figure 3.65 shows the spectra of density, pressure and temperature at $t/T_e = 6$. For the density and pressure, the RBEV model and the DSYE model are more accurate than the RBVM and MM2 models. The latter two are too dissipative. For the temperature, the RBVM model is the best, followed the RBEV model and the DSYE model. The MM2 model is still too dissipative.

The average values of viscosities as a function of time are shown in Figure 3.66. We observe that the eddy viscosity from the RBEV component in the mixed model is smaller than that in the pure RBEV model. This is because the RBVM component in mixed model also adds some dissipation to the simulation, so the effect of eddy viscosity from RBEV component is reduced. It shows that the RBEV model behaves like a dynamic model, as it adjusts to the overall dissipation in the system.

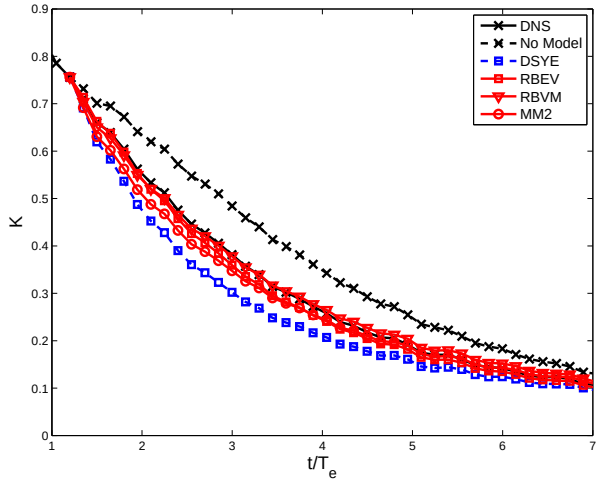

(a) total velocity

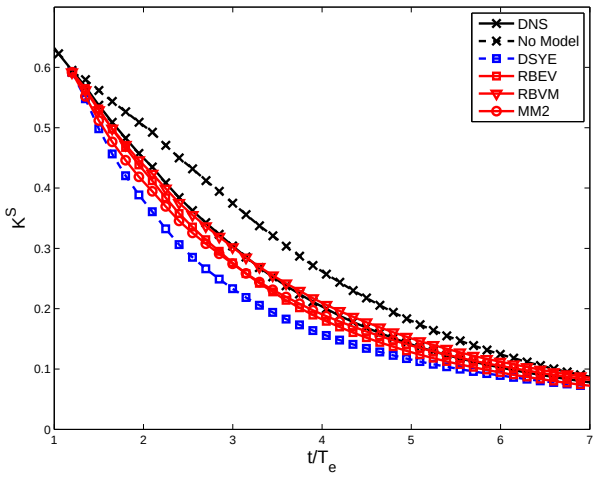

(b) solenoidal velocity

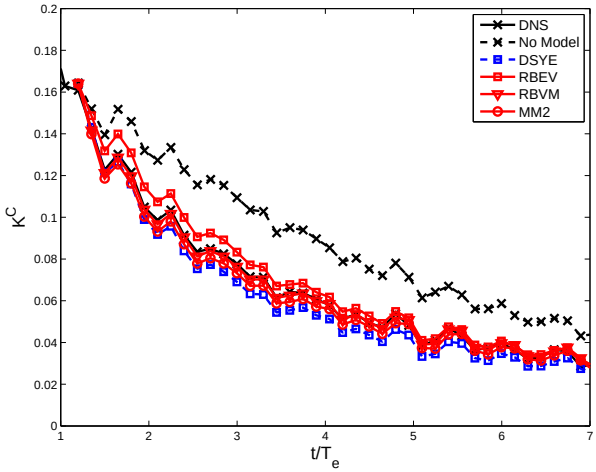

(c) dilatational velocity

Figure 3.61: Time history of turbulent kinetic energy for the $Re_\lambda = 65.5$ case on a 64^3 grid. A comparison of the dynamic SYE, RBEV, RBVM, MM2 and no model cases.

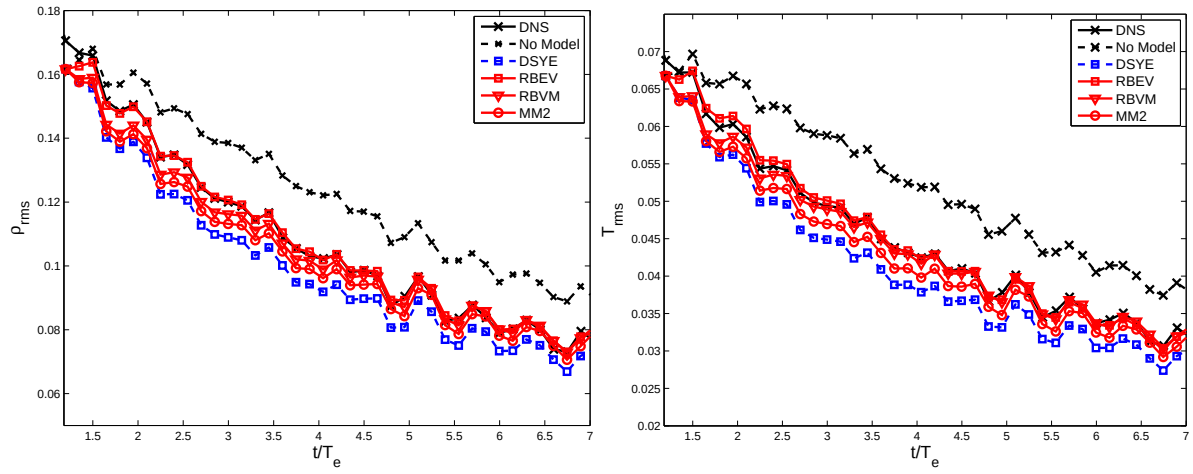

(a) density (b) temperature

Figure 3.62: Time history of root-mean-square of density and temperature for the $Re_\lambda = 65.5$ case on a 64^3 grid. A comparison of the dynamic SYE, RBEV, RBVM, MM2 and no model cases.

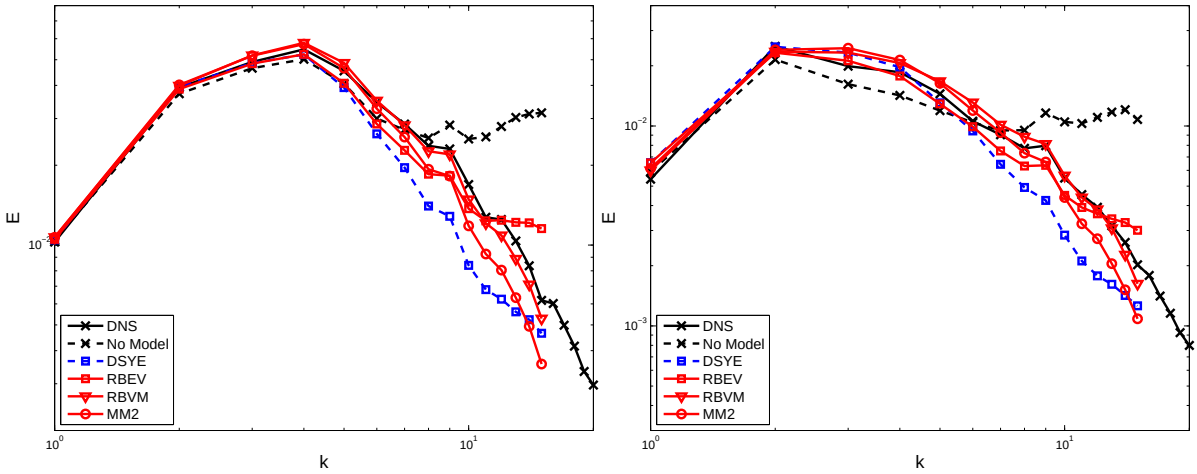

(a) total velocity, $t/T_e = 3$ (b) total velocity, $t/T_e = 6$

Figure 3.63: Energy spectrum of the total velocity for the $Re_\lambda = 65.5$ case on a 64^3 grid. A comparison of the dynamic SYE, RBEV, RBVM, MM2 and no model cases.

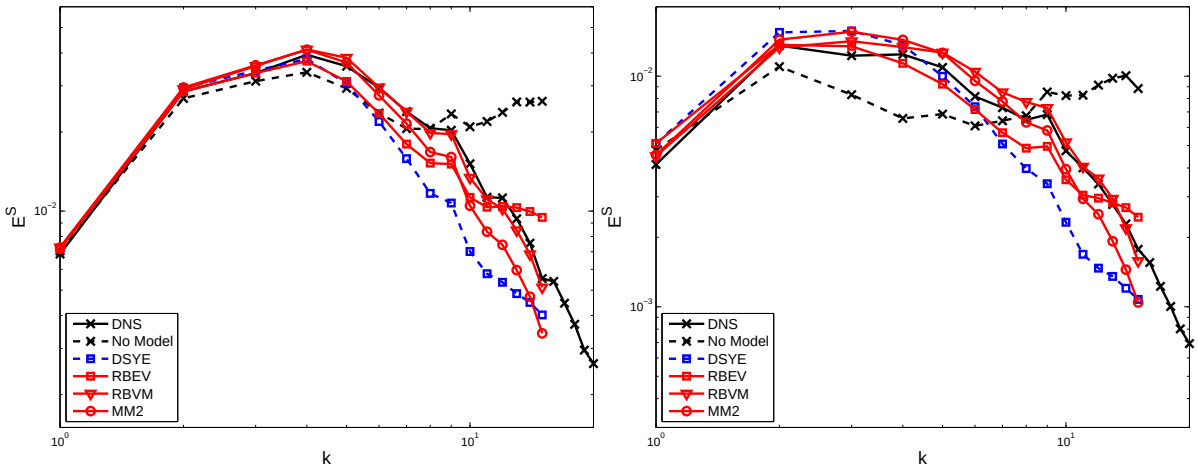

(a) solenoidal velocity, $t/T_e = 3$

(b) solenoidal velocity, $t/T_e = 6$

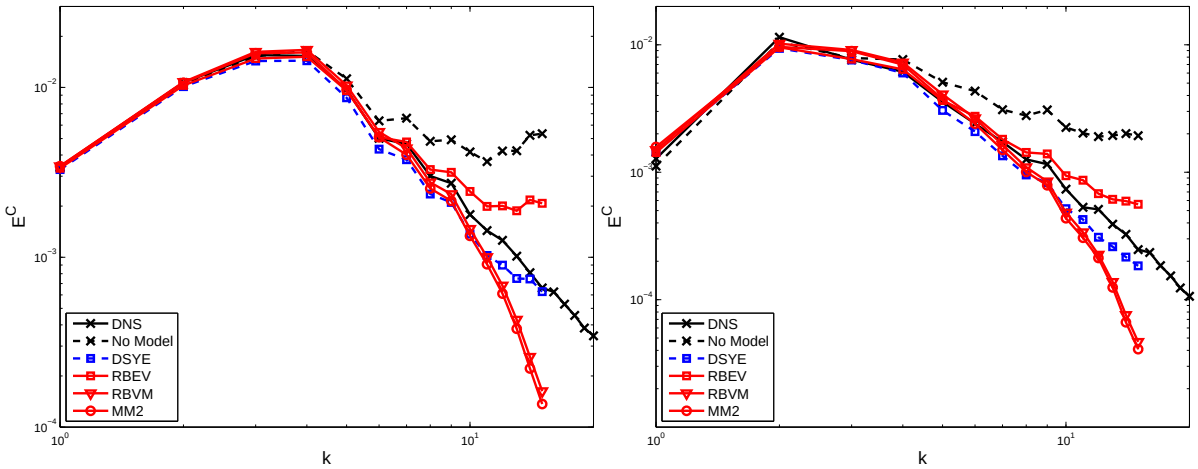

(c) dilatational velocity, $t/T_e = 3$

(d) dilatational velocity, $t/T_e = 6$

Figure 3.64: Energy spectrum of solenoidal and dilatational velocity for the $Re_\lambda = 65.5$ case on a 64^3 grid. A comparison of the dynamic SYE, RBEV, RBVM, MM2 and no model cases.

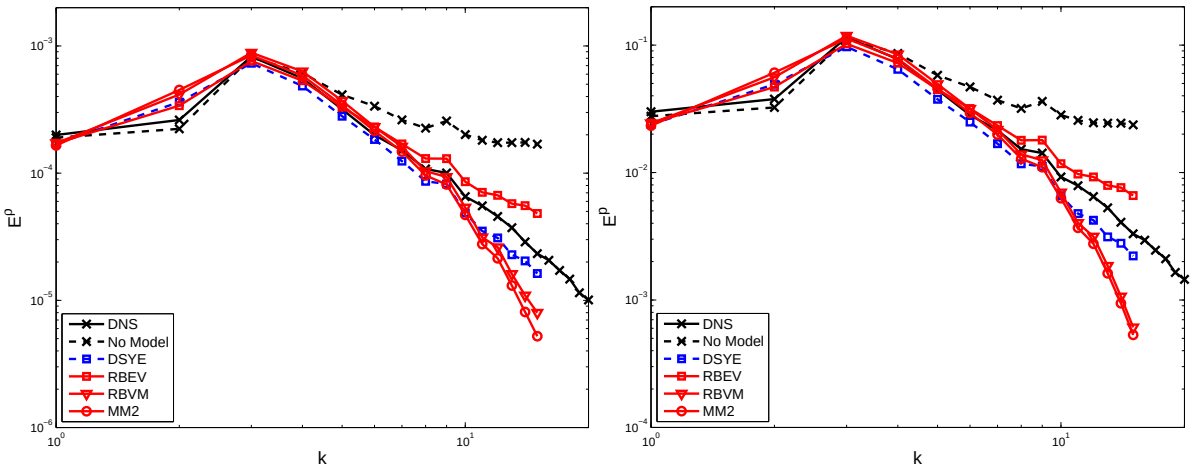

(a) density, $t/T_e = 6$ (b) pressure, $t/T_e = 6$

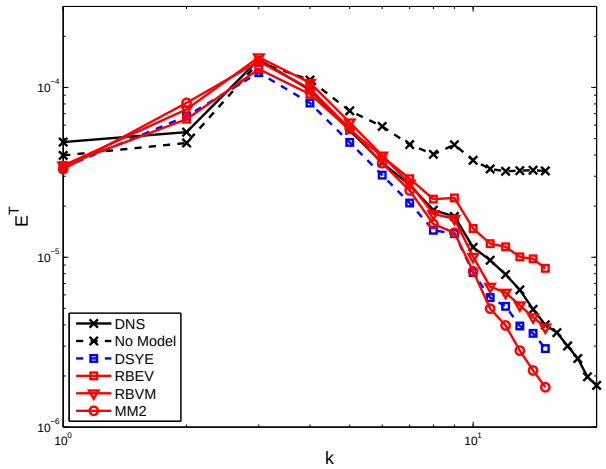

(c) temperature, $t/T_e = 6$

Figure 3.65: Spectrum of density, pressure and temperature for the $Re_\lambda = 65.5$ case on a 64^3 grid. A comparison of the dynamic SYE, RBEV, RBVM, MM2 and no model cases.

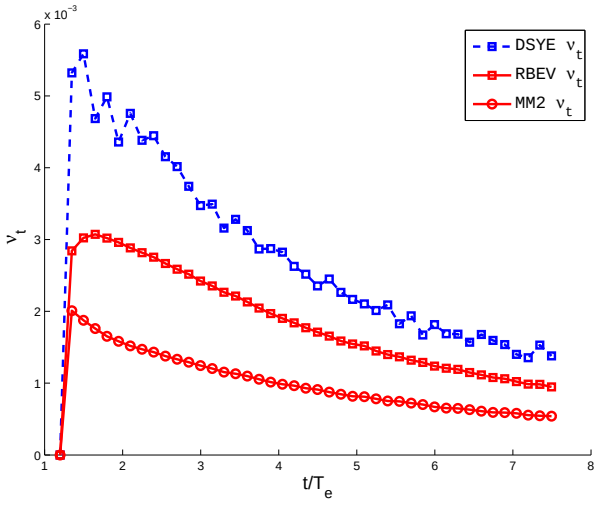

Figure 3.66: Time history of average eddy viscosity for the $Re_\lambda = 65.5$ case on a 64^3 grid. A comparison of the dynamic SYE, RBEV, MM2 cases.

We now consider the same problem but on a finer mesh of 64^3 modes. In Figures 3.67 - 3.72 we present the results for this test.

In Figure 3.67, the time history of the turbulent kinetic energies is plotted for all the models. We now observe that the RBEV, RBVM, and MM2 models are all very accurate while the DSYE model is less so. The same observations hold for the time-history of the RMS of density and temperature shown in Figure 3.68.

In the spectra of the total velocity (Figure 3.69) and incompressible velocity (Figure 3.70(a) and (b)), the RBVM and the MM2 models are most accurate followed by the RBEV model. The DSYE model is a little dissipative. For the compressible velocity spectra (shown in Figure 3.70(c) and (d)), the DSYE model is the most accurate followed by the RBEV model. The RBVM and MM2 models are slightly overly dissipative in the high wavenumber range. The spectra for density, temperature and pressure (Figure 3.71) all show the same trends.

The average values of viscosities as a function of time is shown in Figure 3.72. We still observe that the eddy viscosity of RBEV component in the mixed model is smaller than that in the pure RBEV model. Once again this points to the apparent

"dynamic" nature of this model.

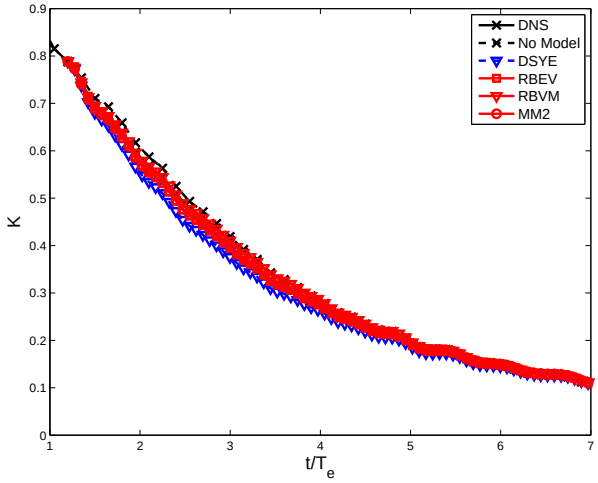

(a) total velocity

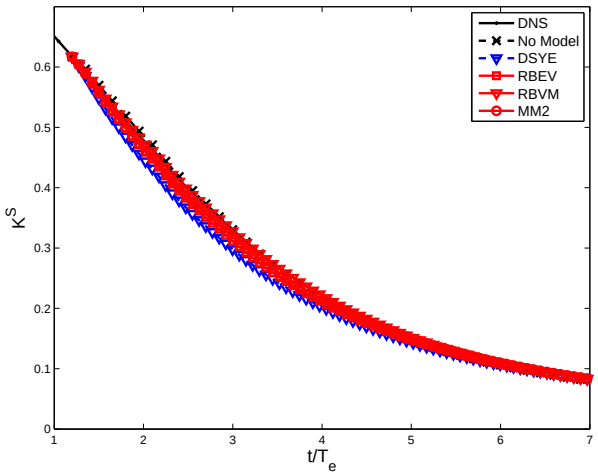

(b) solenoidal velocity

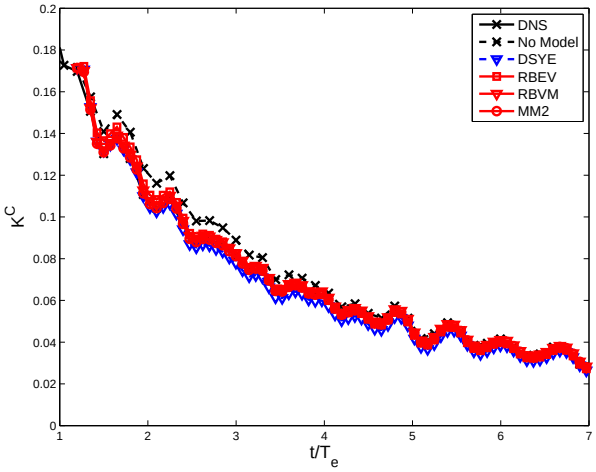

(c) dilatational velocity

Figure 3.67: Time history of turbulent kinetic energy for the $Re_\lambda = 65.5$ case on a 64^3 grid. A comparison of the dynamic SYE, RBEV, RBVM, MM2 and no model cases.

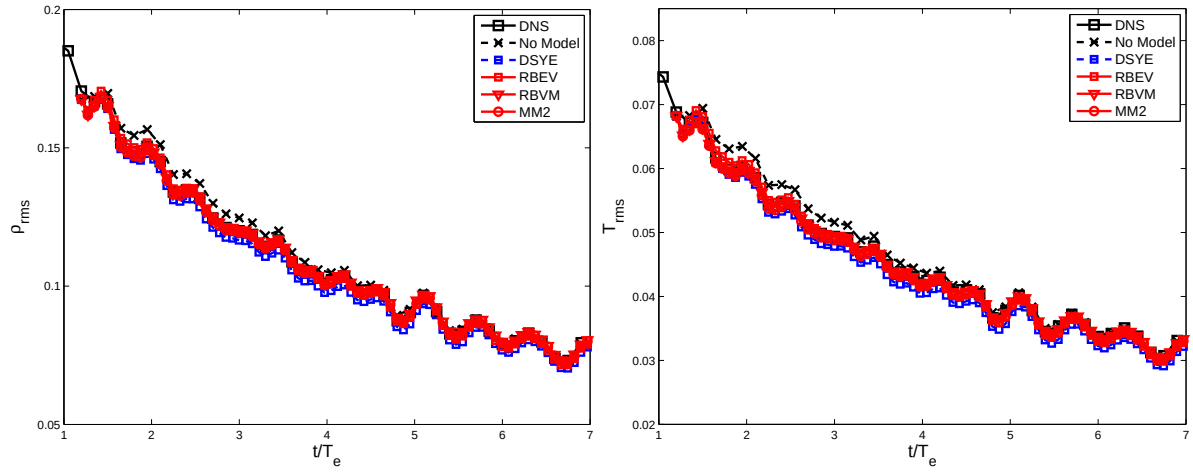

(a) density (b) temperature

Figure 3.68: Time history of root-mean-square of density and temperature for the $Re_\lambda = 65.5$ case on a 64^3 grid. A comparison of the dynamic SYE, RBEV, RBVM, MM2 and no model cases.

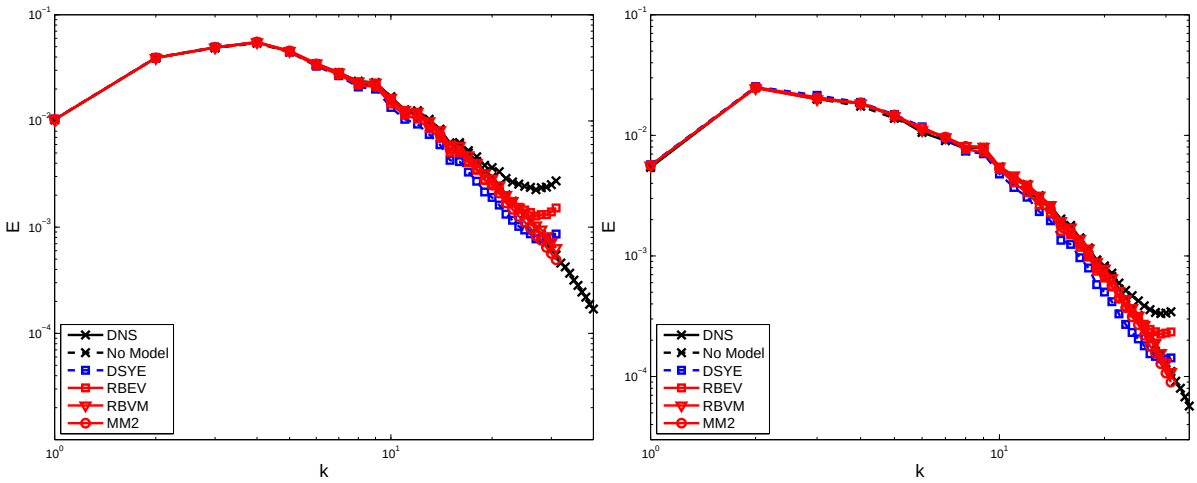

(a) total velocity, $t/T_e = 3$ (b) total velocity, $t/T_e = 6$

Figure 3.69: Energy spectrum of the total velocity for the $Re_\lambda = 65.5$ case on a 64^3 grid. A comparison of the dynamic SYE, RBEV, RBVM, MM2 and no model cases.

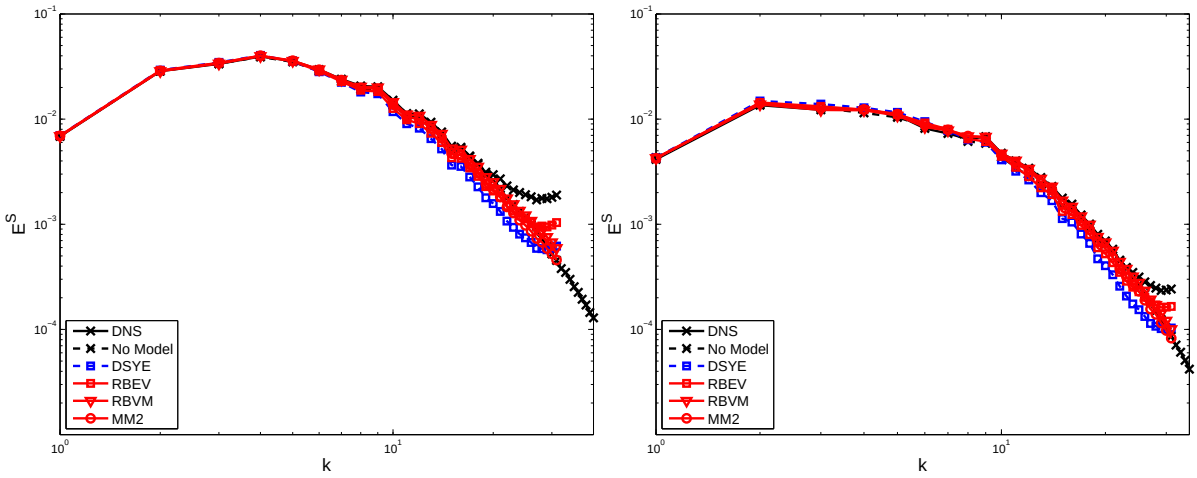

(a) solenoidal velocity, $t/T_e = 3$

(b) solenoidal velocity, $t/T_e = 6$

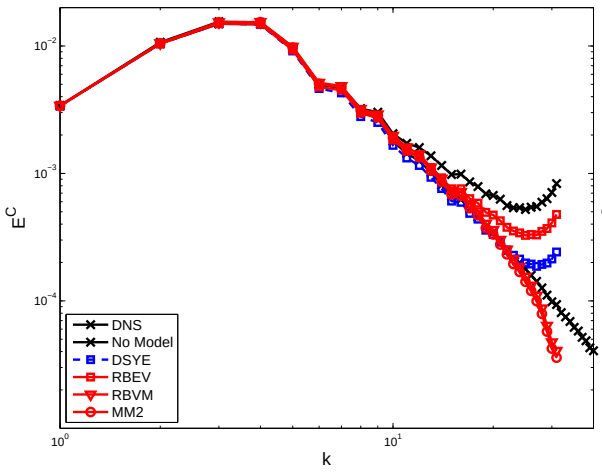

(c) dilatational velocity, $t/T_e = 3$

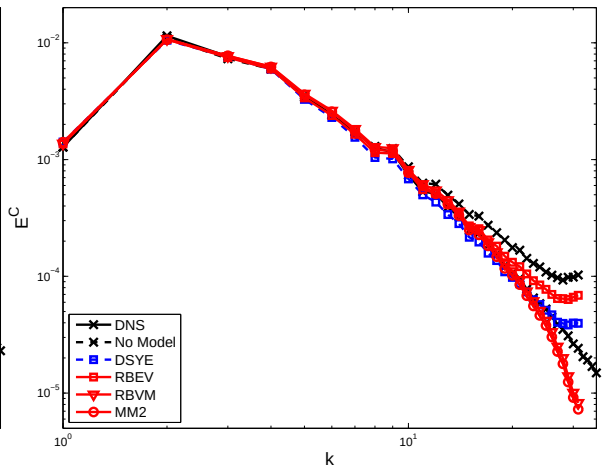

(d) dilatational velocity, $t/T_e = 6$

Figure 3.70: Energy spectrum of solenoidal and dilatational velocity for the $Re_\lambda = 65.5$ case on a 64^3 grid. A comparison of the dynamic SYE, RBEV, RBVM, MM2 and no model cases.

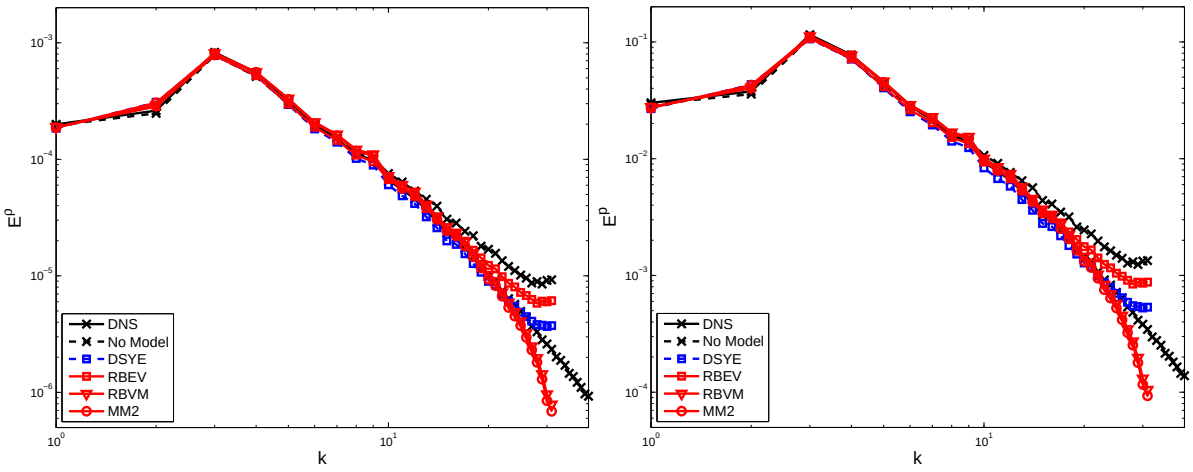

(a) density, $t/T_e = 6$ (b) pressure, $t/T_e = 6$

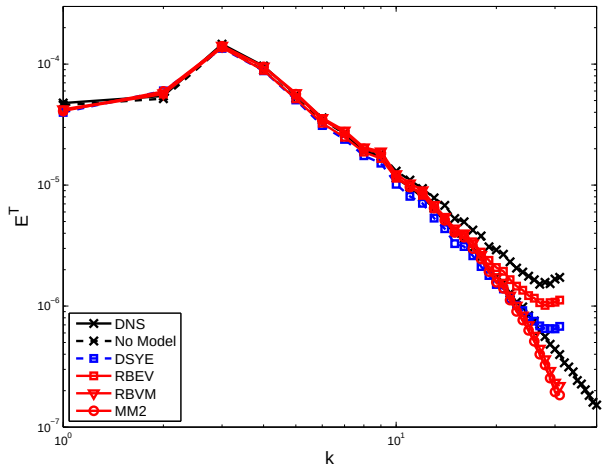

(c) temperature, $t/T_e = 6$

Figure 3.71: Spectrum of density, pressure and temperature for the $Re_\lambda = 65.5$ case on a 64^3 grid. A comparison of the dynamic SYE, RBEV, RBVM, MM2 and no model cases.

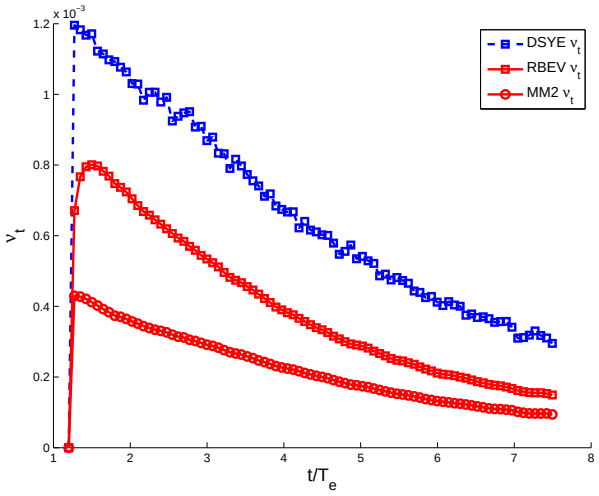

Figure 3.72: Time history of average eddy viscosity for the $Re_\lambda = 65.5$ case on a 64^3 grid. A comparison of the dynamic SYE, RBEV, MM2 cases.

3.6.2 High Reynolds Number Case

In the high Reynolds numbers case, the simulation conditions are the same as in the high Reynolds number case presented in Section 3.6.2. Figures 3.73 - 3.84 contain the plots for this case.

First we consider the results for the 32^3 mesh. In Figure 3.73, we have plotted the evolution of kinetic energies as a function of time. For the total and incompressible component, we observe that the RBVM model is the most accurate followed by the MM2 and RBEV models, and then the DSYE model. For the compressible component, the RBVM and MM2 models are the best, followed by the RBEV and DSYE model.

Figure 3.74 shows the evolution of rms values of density and temperature. The RBEV model is the most accurate for density followed by the RBVM and MM2 models. For temperature, the RBEV and RBVM models are the most accurate followed by the MM2 model. DSYE is too dissipative for both density and temperature.

In the plots for the spectra for the total and incompressible kinetic energy we

observe that the RBVM model is the most accurate followed by MM2, RBEV, and then DSYE (see Figures 3.75 and 3.76). In the spectra of the compressible kinetic energy we observe that the DSYE is most accurate, followed by RBEV model, then the RBVM and MM2 models. In this case the RBEV models is not dissipative enough while the RBVM and MM2 models are too dissipative.

In the spectra for the density, pressure and temperature (Figure 3.77), the RBVM model is the best for the density, followed by the DSYE model. The RBEV model is not dissipative enough and the MM2 model is too dissipative. For pressure, RBEV and DSYE are the most accurate, while the RBVM and MM2 models are too dissipative. For the temperature, the MM2 model is the best followed by the DSYE model while the RBEV and RBVM models are not dissipative enough.

The average values of viscosities as a function of time are shown in Figure 3.78. We still observe that the eddy viscosity of RBEV component in the mixed model is smaller than that in the pure RBEV model, highlighting the "dynamic" nature of this model. We also observe that the turbulent viscosities for all models are larger than those for the low Reynolds number case shown in Figure 3.66.

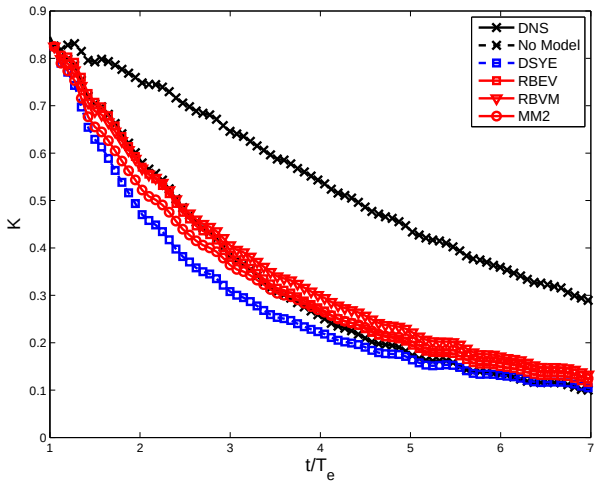

(a) total velocity

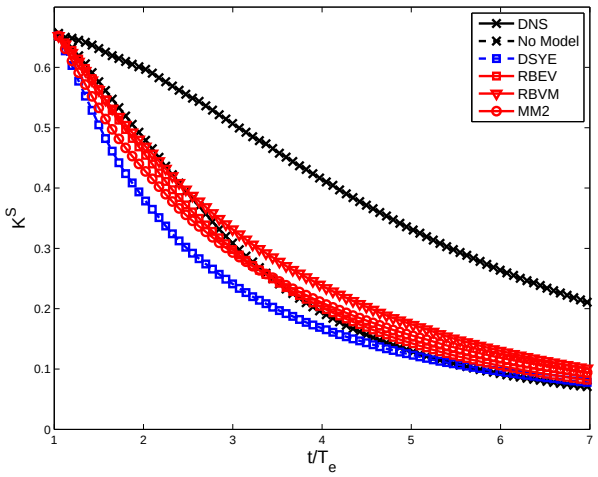

(b) solenoidal velocity

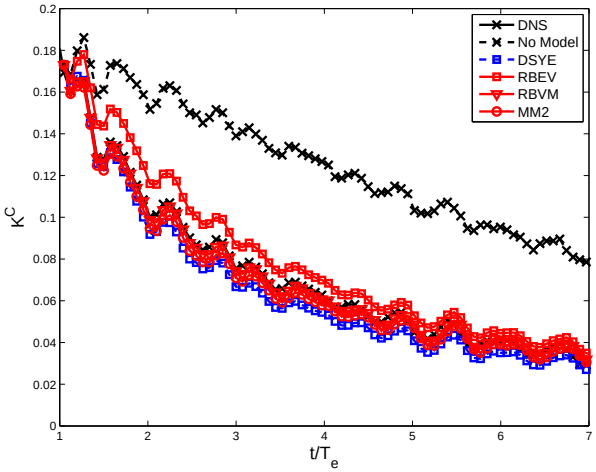

(c) dilatational velocity

Figure 3.73: Time history of turbulent kinetic energy for the $Re_\lambda = 117.1$ case on a 32^3 grid. A comparison of the dynamic SYE, RBEV, RBVM, MM2 and no model cases.

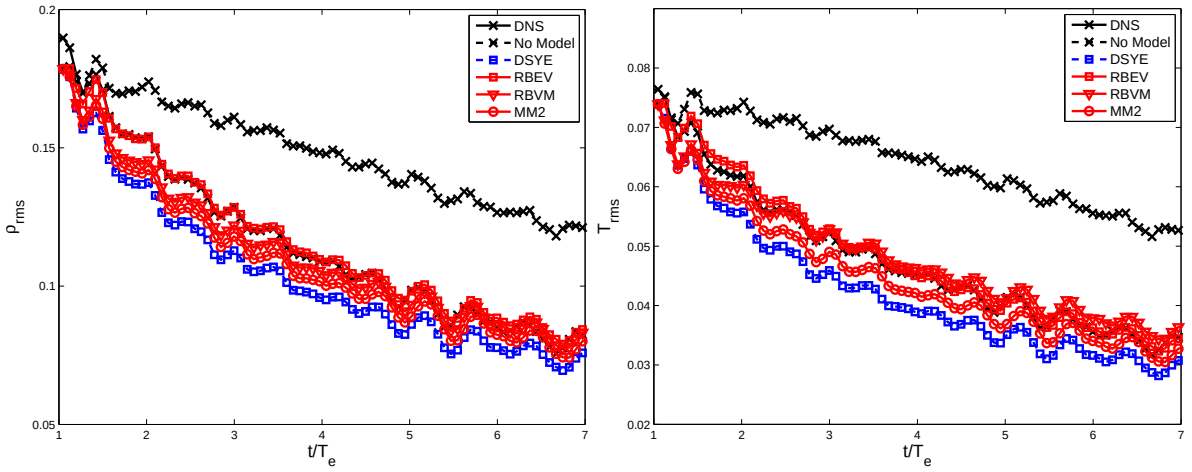

(a) density (b) temperature

Figure 3.74: Time history of root-mean-square of density and temperature for the $Re_\lambda = 117.1$ case on a 32^3 grid. A comparison of the dynamic SYE, RBEV, RBVM, MM2 and no model cases.

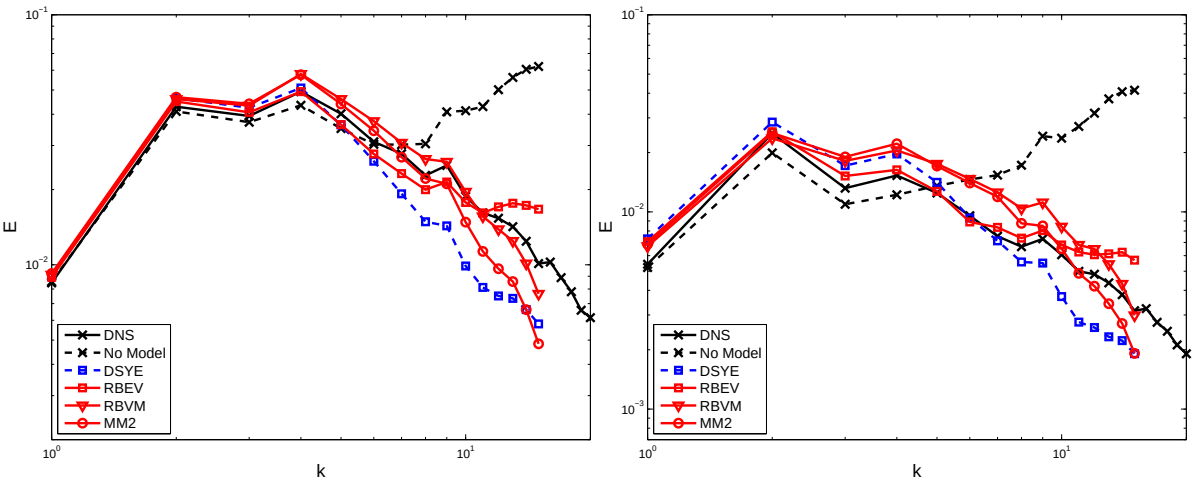

(a) total velocity, $t/T_e = 3$ (b) total velocity, $t/T_e = 6$

Figure 3.75: Energy spectrum of the total velocity for the $Re_\lambda = 117.1$ case on a 32^3 grid. A comparison of the dynamic SYE, RBEV, RBVM, MM2 and no model cases.

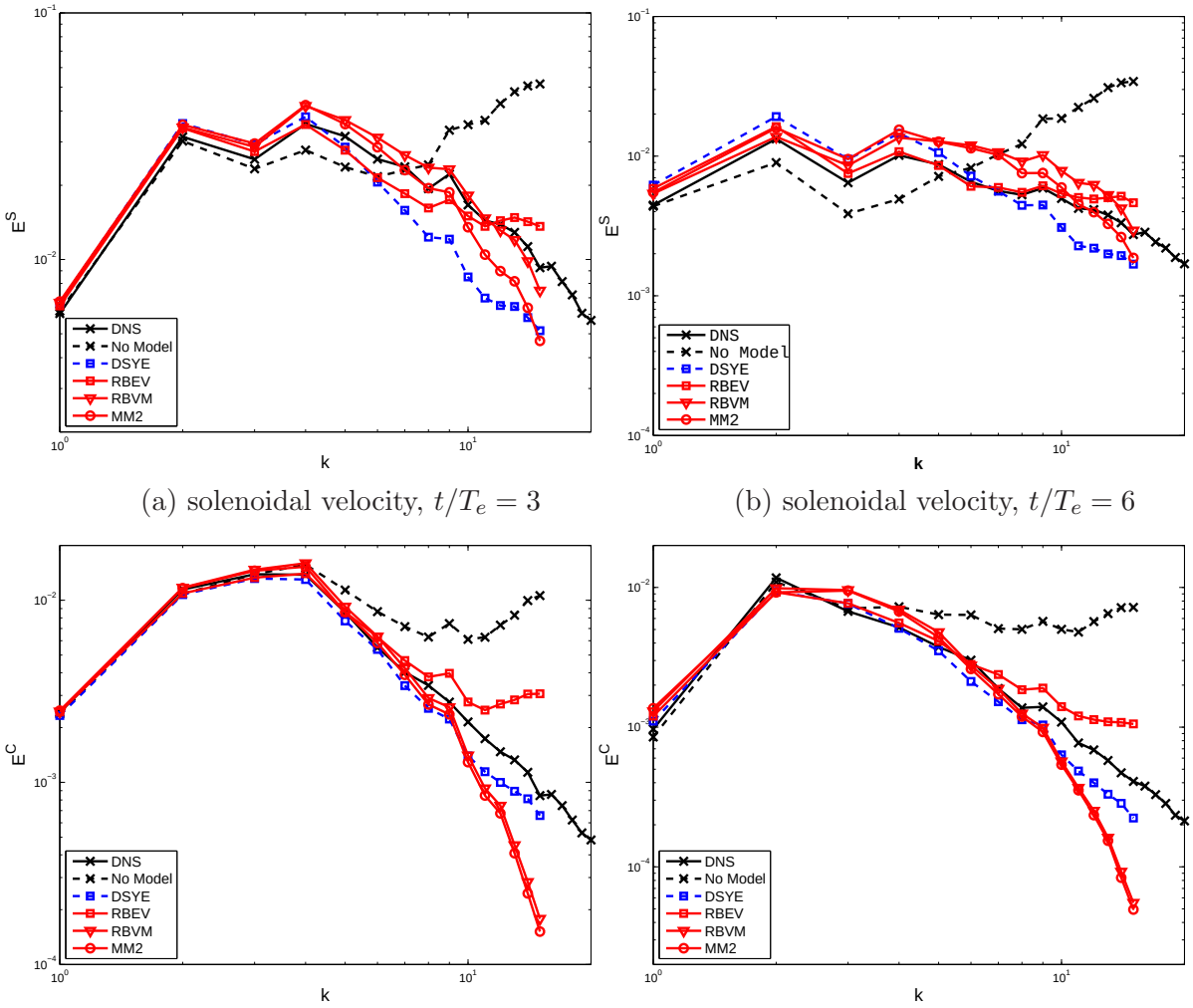

(a) solenoidal velocity, $t/T_e = 3$

(b) solenoidal velocity, $t/T_e = 6$

(c) dilatational velocity, $t/T_e = 3$

(d) dilatational velocity, $t/T_e = 6$

Figure 3.76: Energy spectrum of solenoidal and dilatational velocity for the $Re_\lambda = 117.1$ case on a 32^3 grid. A comparison of the dynamic SYE, RBEV, RBVM, MM2 and no model cases.

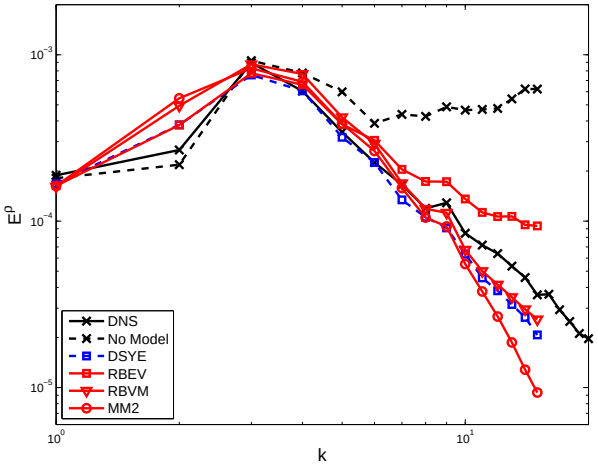

(a) density, $t/T_e = 6$

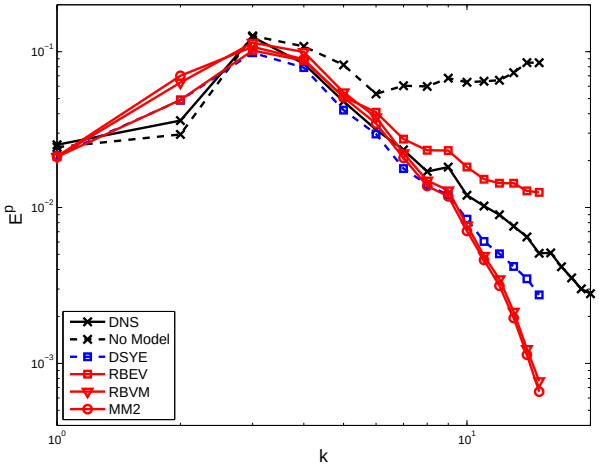

(b) pressure, $t/T_e = 6$

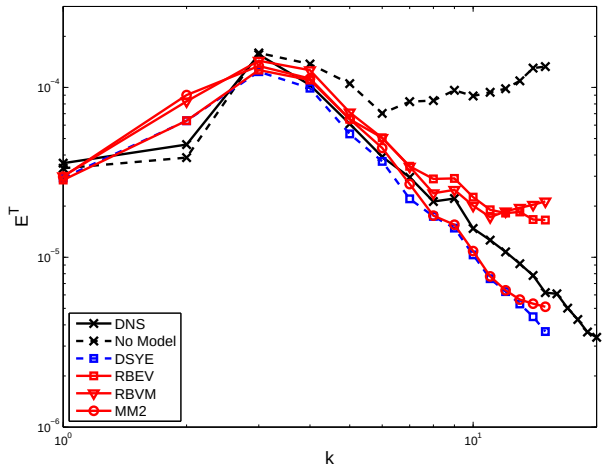

(c) temperature, $t/T_e = 6$

Figure 3.77: Spectrum of density, pressure and temperature for the $Re_\lambda = 117.1$ case on a 32^3 grid. A comparison of the dynamic SYE, RBEV, RBVM, MM2 and no model cases.

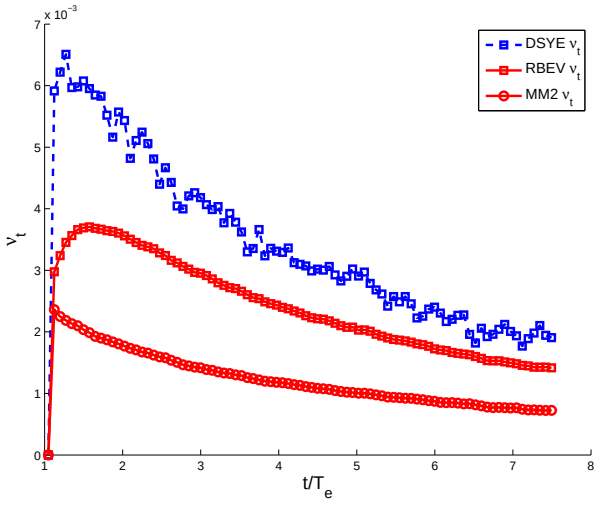

Figure 3.78: Time history of average eddy viscosity for the $Re_\lambda = 117.1$ case on a 32^3 grid. A comparison of the dynamic SYE, RBEV, MM2 cases.

In Figures 3.79 - 3.84 we plot the results for high Reynolds number case on a finer, 64^3 mesh.

In Figure 3.79 we have plotted the evolution of kinetic energies as a function of time. For the total and incompressible component, we observe that the RBEV, RBVM and MM2 models are very accurate while the DSYE model is slightly dissipative. We note that the MM2 model dissipates slightly more energy than what is required while the RBEV is not dissipative enough. For the compressible component, the RBVM and MM2 models are very accurate followed by the RBEV and DSYE models. The same trend is observed in the evolution of rms values of density and temperature (see Figure 3.80).

In the plots for the spectra for the total and incompressible kinetic energy, we observe that the RBVM model is the most accurate followed by the MM2, and RBEV models (see Figures 3.81 and 3.82), while the DSYE model is too dissipative. In the spectra of the compressible kinetic energy we observe that the DSYE is most accurate, followed by the RBEV model, then the RBVM and the MM2 models. In this case the RBEV models is not dissipative enough while the RBVM and MM2

models are too dissipative. The same trends are seen in the spectra for the density, pressure (see Figure 3.83). For temperature, the DSYE is most accurate, followed by the RBVM and MM2 models, and then RBEV model.

The average values of viscosities as a function of time are shown in Figure 3.84. Once again the DSYE is the largest followed by the pure RBEV and then the RBEV component of the MM2 model.

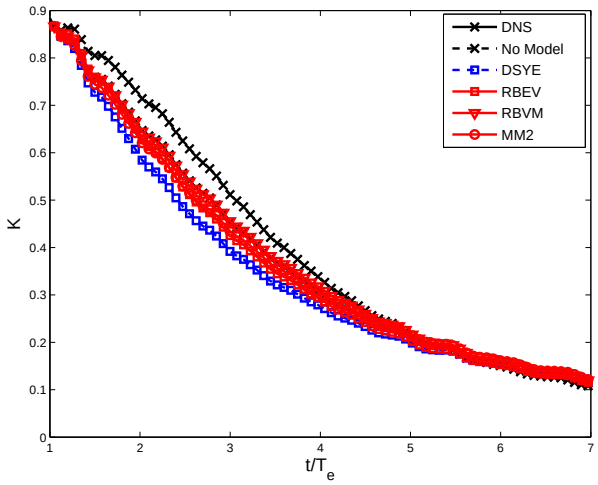

(a) total velocity

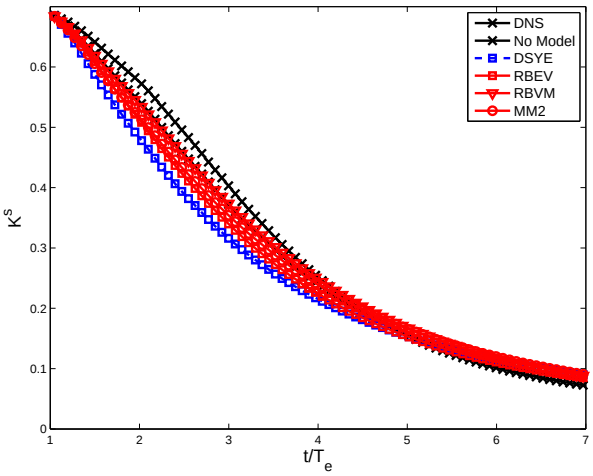

(b) solenoidal velocity

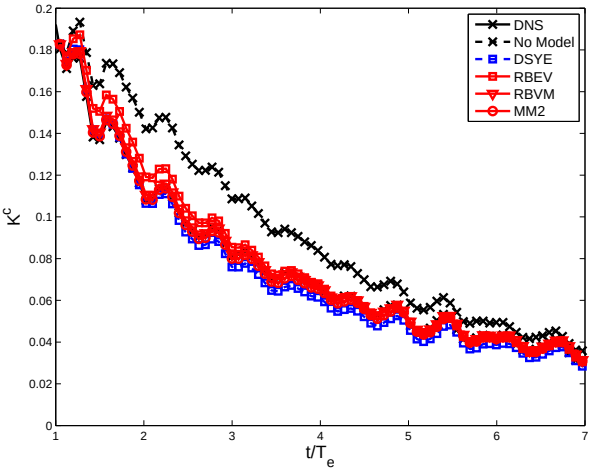

(c) dilatational velocity

Figure 3.79: Time history of turbulent kinetic energy for the $Re_\lambda = 117.1$ case on a 64^3 grid. A comparison of the dynamic SYE, RBEV, RBVM, MM2 and no model cases.

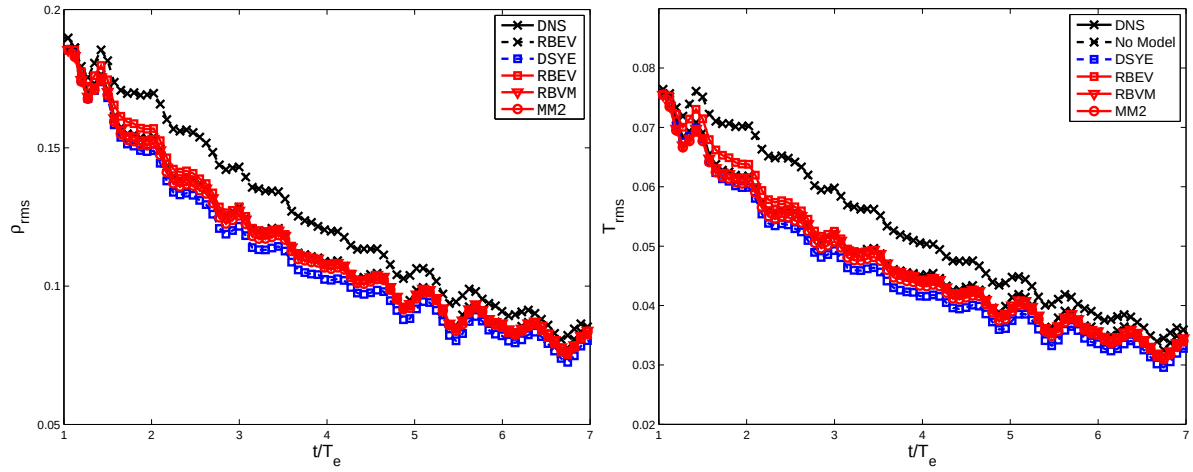

(a) density (b) temperature

Figure 3.80: Time history of root-mean-square of density and temperature for the $Re_\lambda = 117.1$ case on a 64^3 grid. A comparison of the dynamic SYE, RBEV, RBVM, MM2 and no model cases.

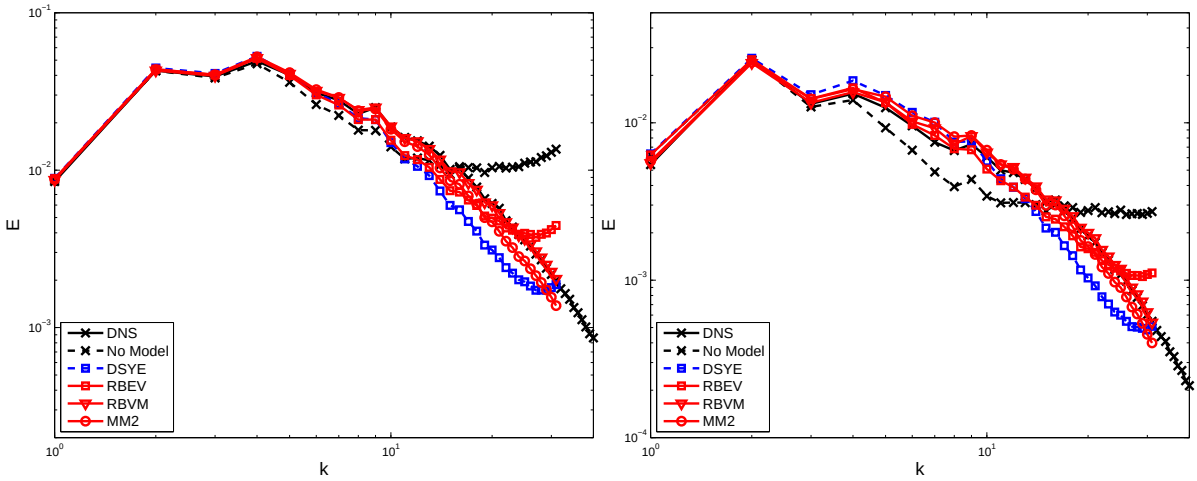

(a) total velocity, $t/T_e = 3$ (b) total velocity, $t/T_e = 6$

Figure 3.81: Energy spectrum of the total velocity for the $Re_\lambda = 117.1$ case on a 64^3 grid. A comparison of the dynamic SYE, RBEV, RBVM, MM2 and no model cases.

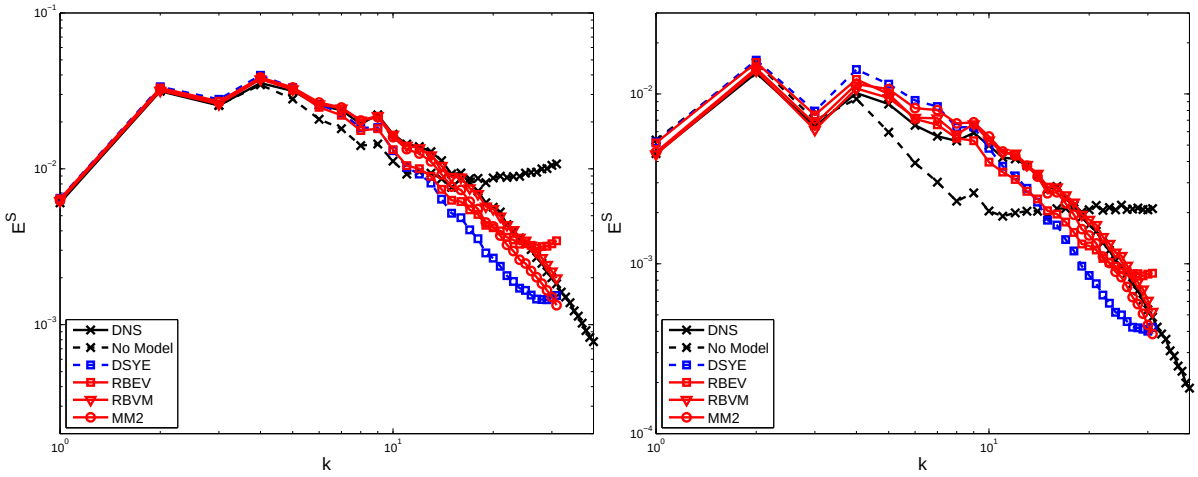

(a) solenoidal velocity, $t/T_e = 3$

(b) solenoidal velocity, $t/T_e = 6$

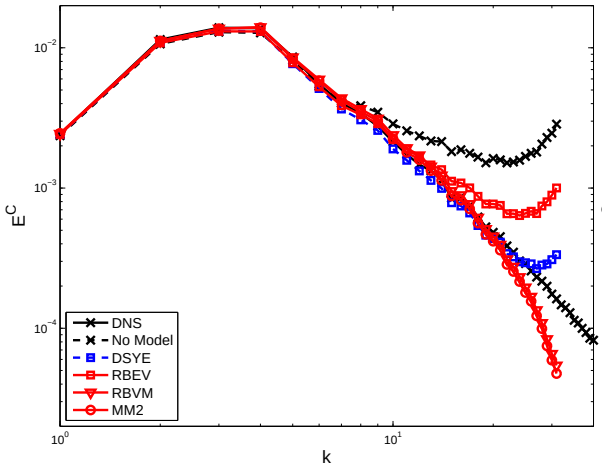

(c) dilatational velocity, $t/T_e = 3$

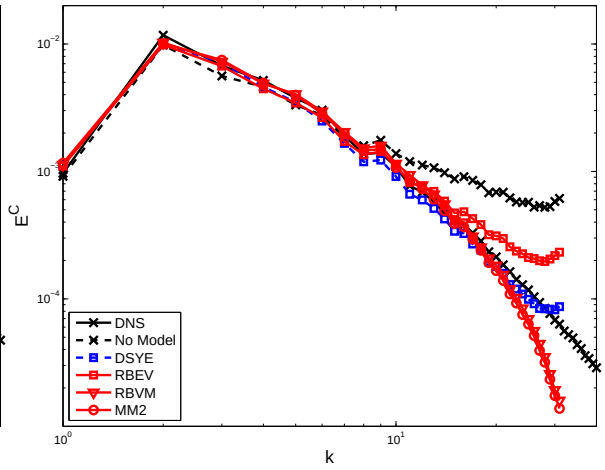

(d) dilatational velocity, $t/T_e = 6$

Figure 3.82: Energy spectrum of solenoidal and dilatational velocity for the $Re_\lambda = 117.1$ case on a 64^3 grid. A comparison of the dynamic SYE, RBEV, RBVM, MM2 and no model cases.

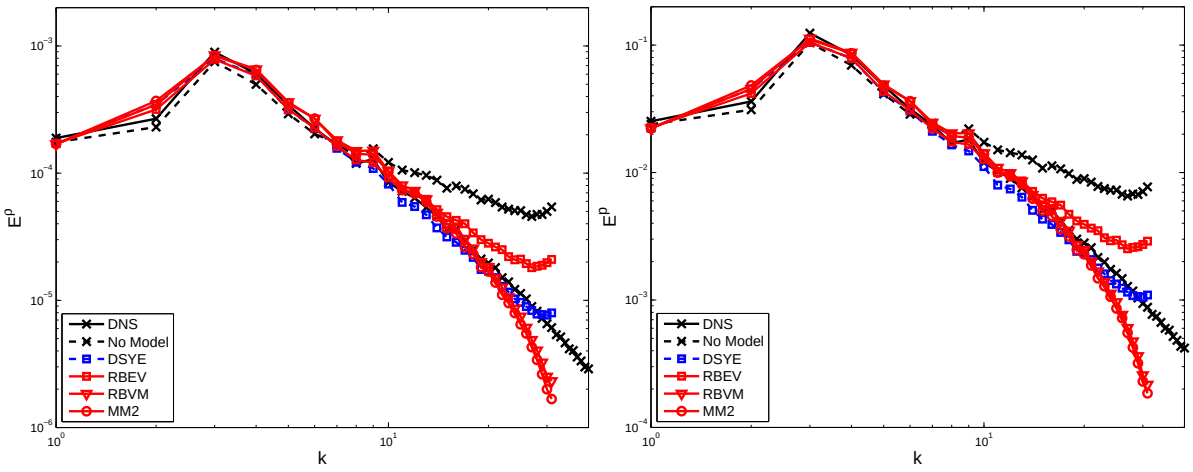

(a) density, $t/T_e = 6$ (b) pressure, $t/T_e = 6$

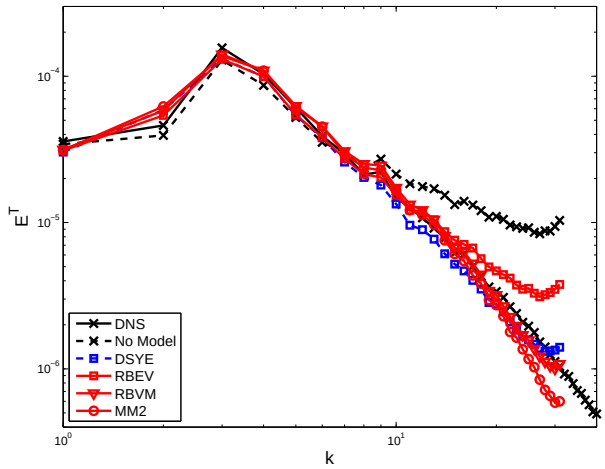

(c) temperature, $t/T_e = 6$

Figure 3.83: Spectrum of density, pressure and temperature for the $Re_\lambda = 117.1$ case on a 64^3 grid. A comparison of the dynamic SYE, RBEV, RBVM, MM2 and no model cases.

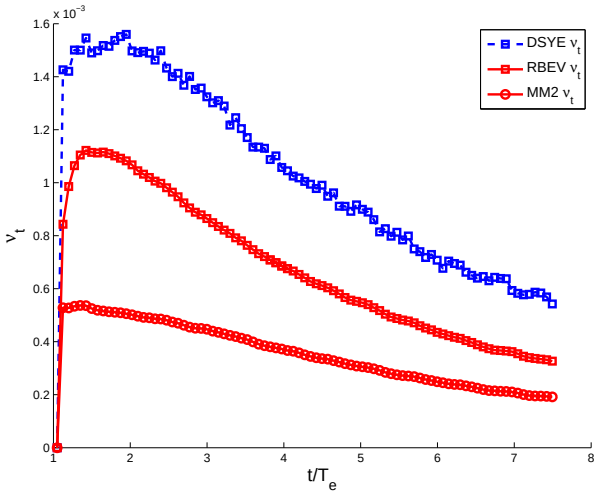

Figure 3.84: Time history of average eddy viscosity for the $Re_\lambda = 117.1$ case on a 64^3 grid. A comparison of the dynamic SYE, RBEV, MM2 cases.

3.7 The RBEV and MM2 Models with $C_\tau = 0.5$

In previous sections, we tested the RBEV and the MM2 models with $C_\tau = 1.0$. In this section, we set $C_\tau = 0.5$ and test the performance of the LES models. In particular, the Low Reynolds number case $Re_\lambda = 65.5$, and the high Reynolds number case $Re_\lambda = 117.1$ are tested on a 32^3 mesh. The other simulation parameters are the same as in the previous section.

3.7.1 Low Reynolds Number Case

In Figures 3.85 - 3.89 we present results for the low Reynolds number case on a 32^3 mesh.

In Figure 3.85, the time history of the turbulent kinetic energies is plotted for all the models. For the total and incompressible component, we observe that the RBEV, RBVM and MM2 models are very accurate while the DSYE model is too dissipative. For the compressible component, the RBVM and the MM2 models are very accurate, while the RBEV model is not dissipative enough and the DSYE model is too dissipative. The same trend is observed in the evolution of rms values

of density and temperature (see Figure 3.86).

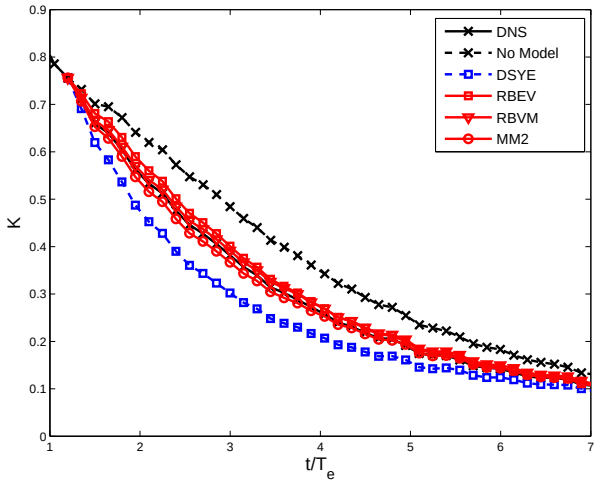

(a) total velocity

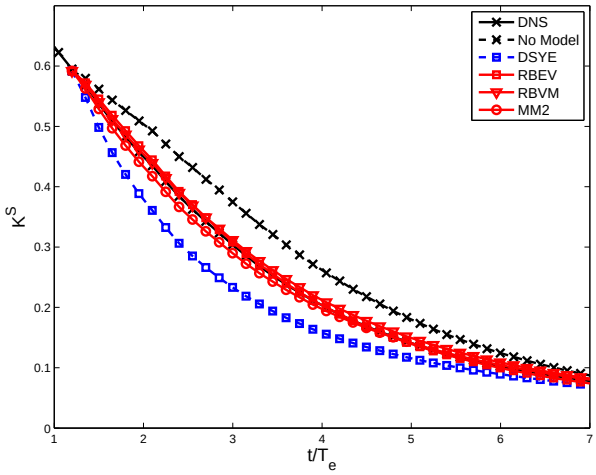

(b) solenoidal velocity

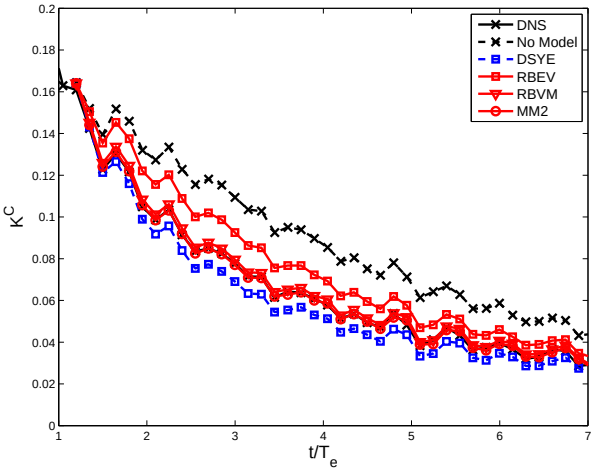

(c) dilatational velocity

Figure 3.85: Time history of turbulent kinetic energy for the $Re_\lambda = 65.5$ case on a 32^3 grid. A comparison of the dynamic SYE, RBEV, RBVM, MM2 and no model cases, with $C_\tau = 0.5$.

In Figures 3.87 - 3.88, we have plotted the spectra of the turbulent kinetic energies at $t/T_e = 3$ and $t/T_e = 6$. We observe that for the total and incompressible component, the MM2 model is very accurate, followed by the RBVM model and the RBEV model, while the DSYE model is the least. For the compressible spectra

we observe that the RBVM, MM2 and DSYE models are about equally accurate, while the RBEV model is not dissipative enough. Figure 3.89 shows the spectrum of density, pressure and temperature at $t/T_e = 6$. The RBVM, MM2 and DSYE models are about equally accurate, while the RBEV model is not dissipative enough.

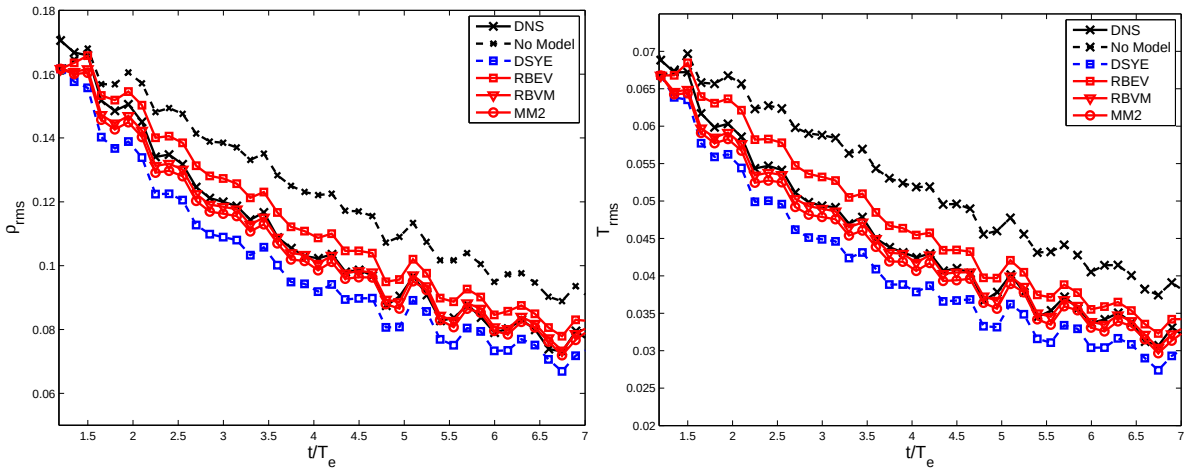

(a) density (b) temperature

Figure 3.86: Time history of root-mean-square of density and temperature for the $Re_\lambda = 65.5$ case on a 32^3 grid. A comparison of the dynamic SYE, RBEV, RBVM, MM2 and no model cases, with $C_\tau = 0.5$.

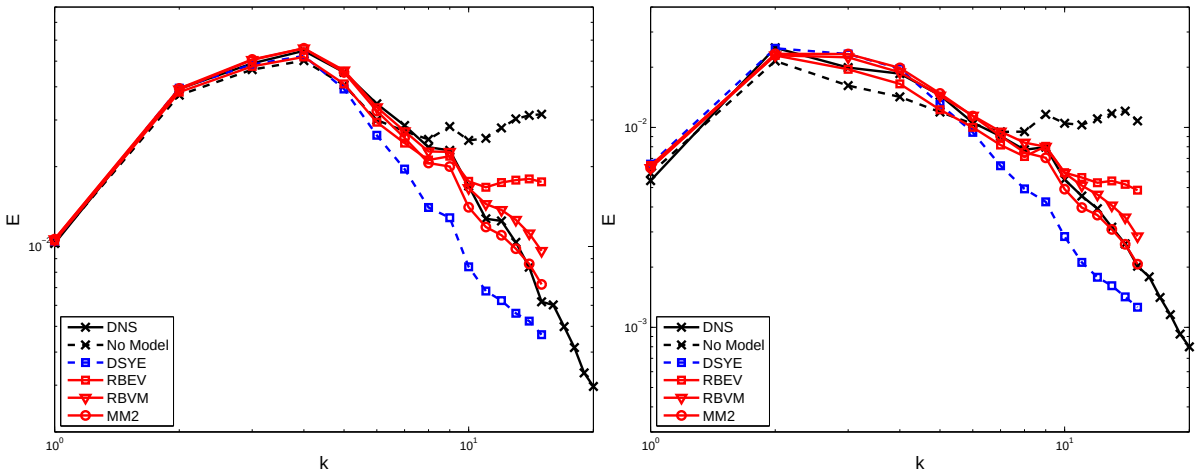

(a) total velocity, $t/T_e = 3$ (b) total velocity, $t/T_e = 6$

Figure 3.87: Energy spectrum of the total velocity for the $Re_\lambda = 65.5$ case on a 32^3 grid. A comparison of the dynamic SYE, RBEV, RBVM, MM2 and no model cases, with $C_\tau = 0.5$.

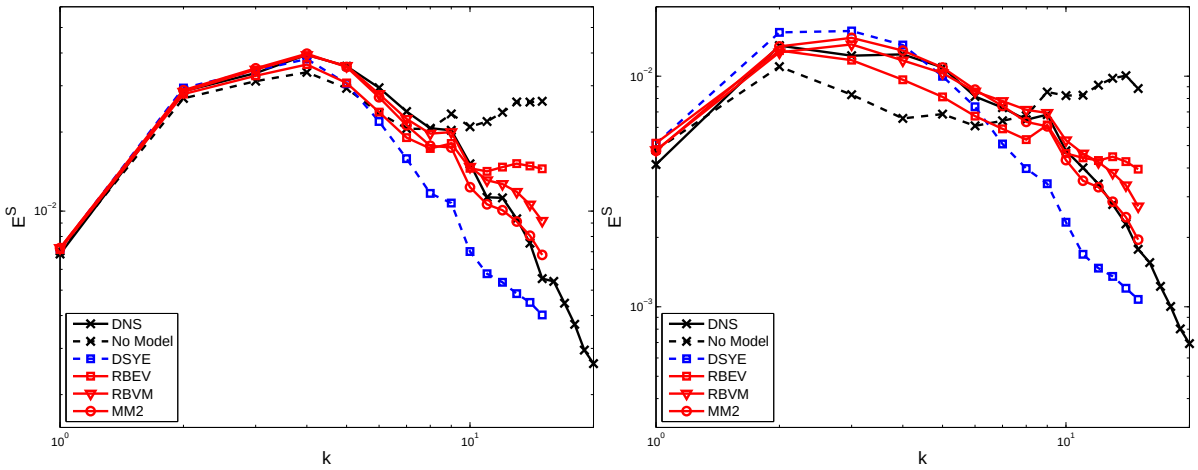

(a) solenoidal velocity, $t/T_e = 3$ (b) solenoidal velocity, $t/T_e = 6$

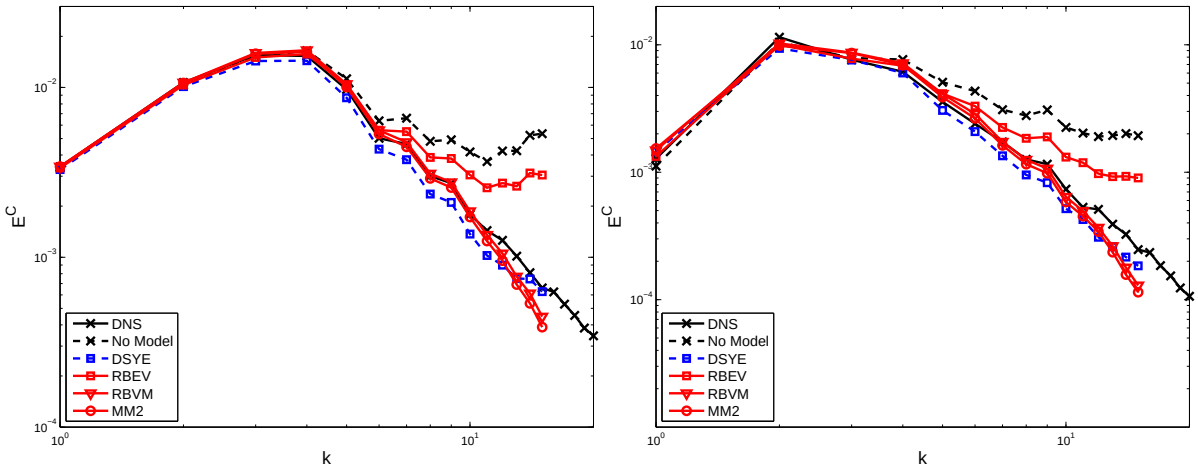

(c) dilatational velocity, $t/T_e = 3$ (d) dilatational velocity, $t/T_e = 6$

Figure 3.88: Energy spectrum of solenoidal and dilatational velocity for the $Re_\lambda = 65.5$ case on a 32^3 grid. A comparison of the dynamic SYE, RBEV, RBVM, MM2 and no model cases, with $C_\tau = 0.5$.

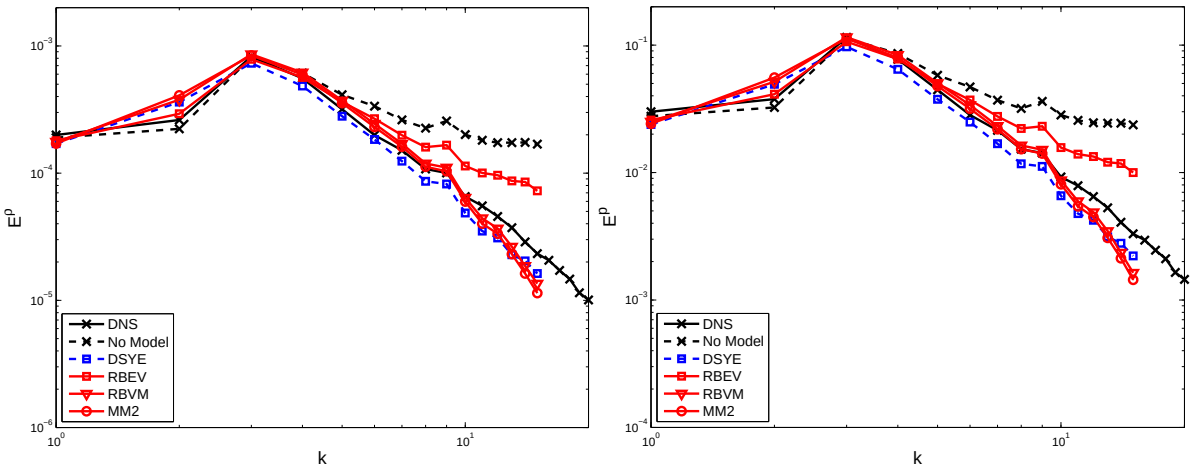

(a) density, $t/T_e = 6$

(b) pressure, $t/T_e = 6$

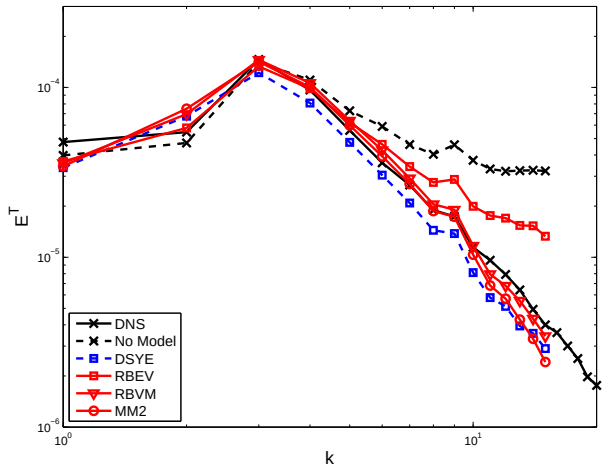

(c) temperature, $t/T_e = 6$

Figure 3.89: Spectrum of density, pressure and temperature for the $Re_\lambda = 65.5$ case on a 32^3 grid. A comparison of the dynamic SYE, RBEV, RBVM, MM2 and no model cases, with $C_\tau = 0.5$.

3.7.2 High Reynolds Number Case

In Figures 3.90 - 3.94 we present the results for the high Reynolds number case on a 32^3 mesh.

In Figure 3.90, the time history of the turbulent kinetic energies is plotted for all the models. For the total and incompressible component, we observe that the MM2 models is the most accurate followed by the RBVM and RBEV models,

and then the DSYE model . For the compressible component the RBVM and MM2 model are very accurate, while the RBEV model is not dissipative enough and the DSYE model is slightly overly dissipative. The same trend is observed in the evolution of rms values of density and temperature (see Figure 3.86).

In Figures 3.87 - 3.88, we have plotted the spectra of the turbulent kinetic energies at $t/T_e = 3$ and $t/T_e = 6$. We observe that for the total and incompressible component, the MM2 model is the most accurate, followed by the RBVM model, and then the RBEV and DSYE model. The RBEV model is not dissipative enough while the DSYE model is too dissipative. For the compressible spectra we observe that the RBVM, MM2 and DSYE models are about equally accurate, while the RBEV model is not dissipative enough. Figure 3.89 shows the spectrum of density, pressure and temperature at $t/T_e = 6$. For the density and pressure, the RBVM, MM2 and DSYE models are about equally accurate, while the RBEV model is not dissipative enough. For the temperature, the MM2 model is the most accurate, followed by the RBVM and DSYE model, while the RBEV model is not dissipative enough.

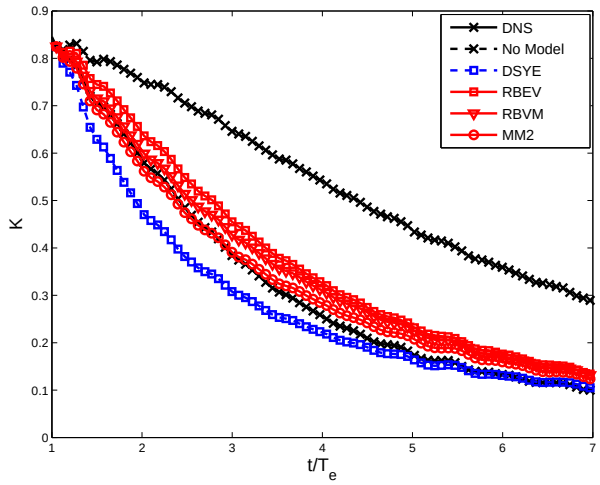

(a) total velocity

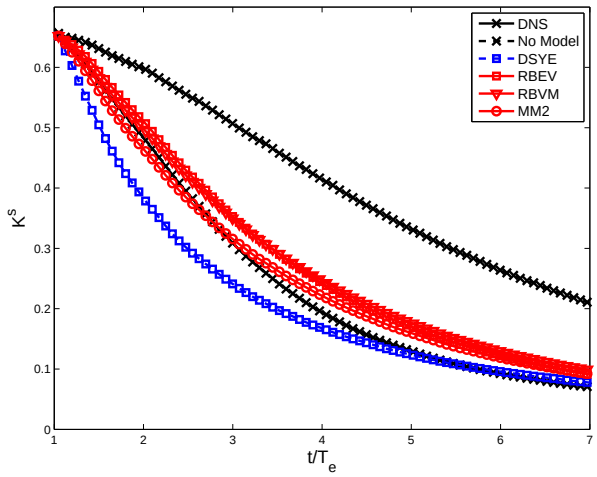

(b) solenoidal velocity

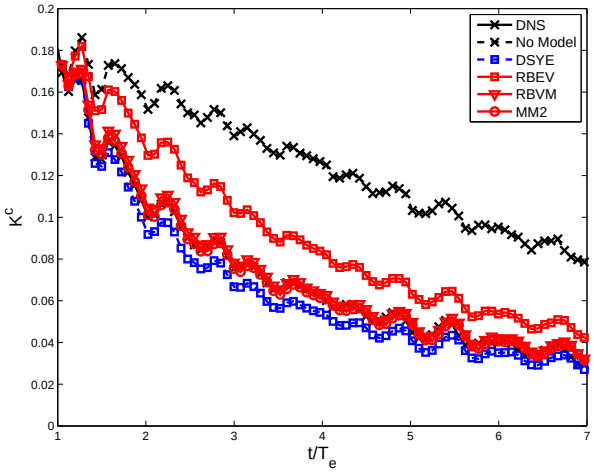

(c) dilatational velocity

Figure 3.90: Time history of turbulent kinetic energy for the $Re_\lambda = 117.1$ case on a 32^3 grid. A comparison of the dynamic SYE, RBEV, RBVM, MM2 and no model cases, with $C_\tau = 0.5$.

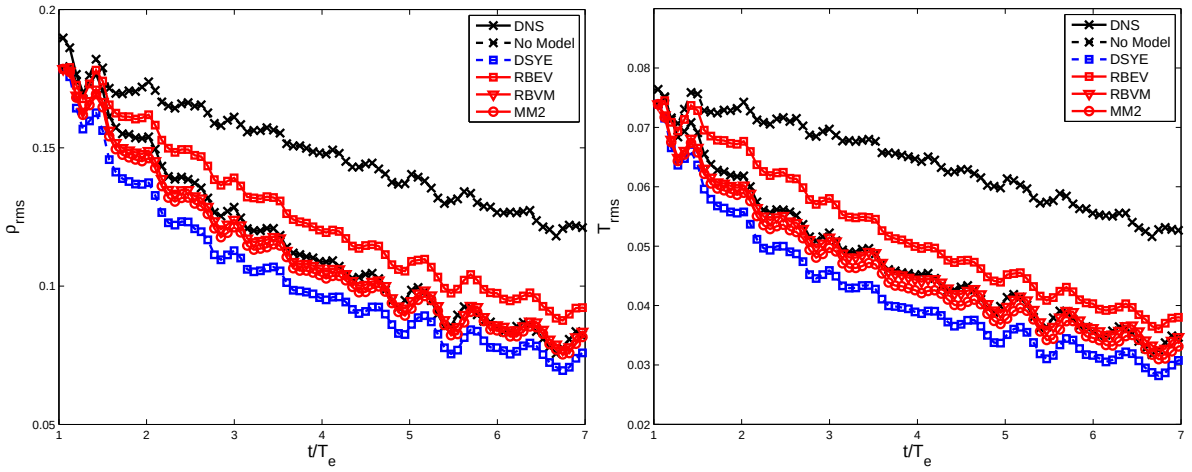

(a) density (b) temperature

Figure 3.91: Time history of root-mean-square of density and temperature for the $Re_\lambda = 117.1$ case on a 32^3 grid. A comparison of the dynamic SYE, RBEV, RBVM, MM2 and no model cases, with $C_\tau = 0.5$.

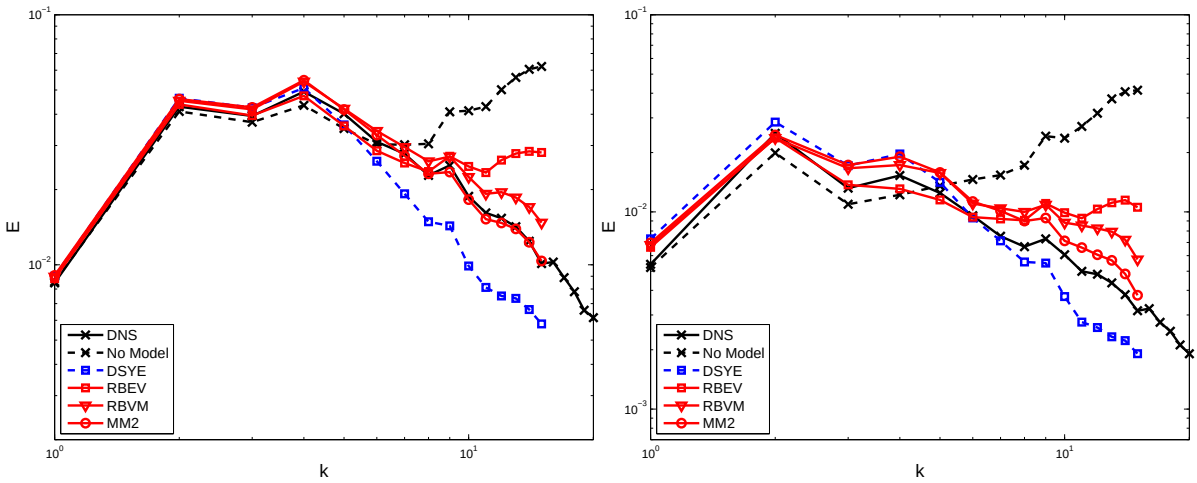

(a) total velocity, $t/T_e = 3$ (b) total velocity, $t/T_e = 6$

Figure 3.92: Energy spectrum of the total velocity for the $Re_\lambda = 117.1$ case on a 32^3 grid. A comparison of the dynamic SYE, RBEV, RBVM, MM2 and no model cases, with $C_\tau = 0.5$.

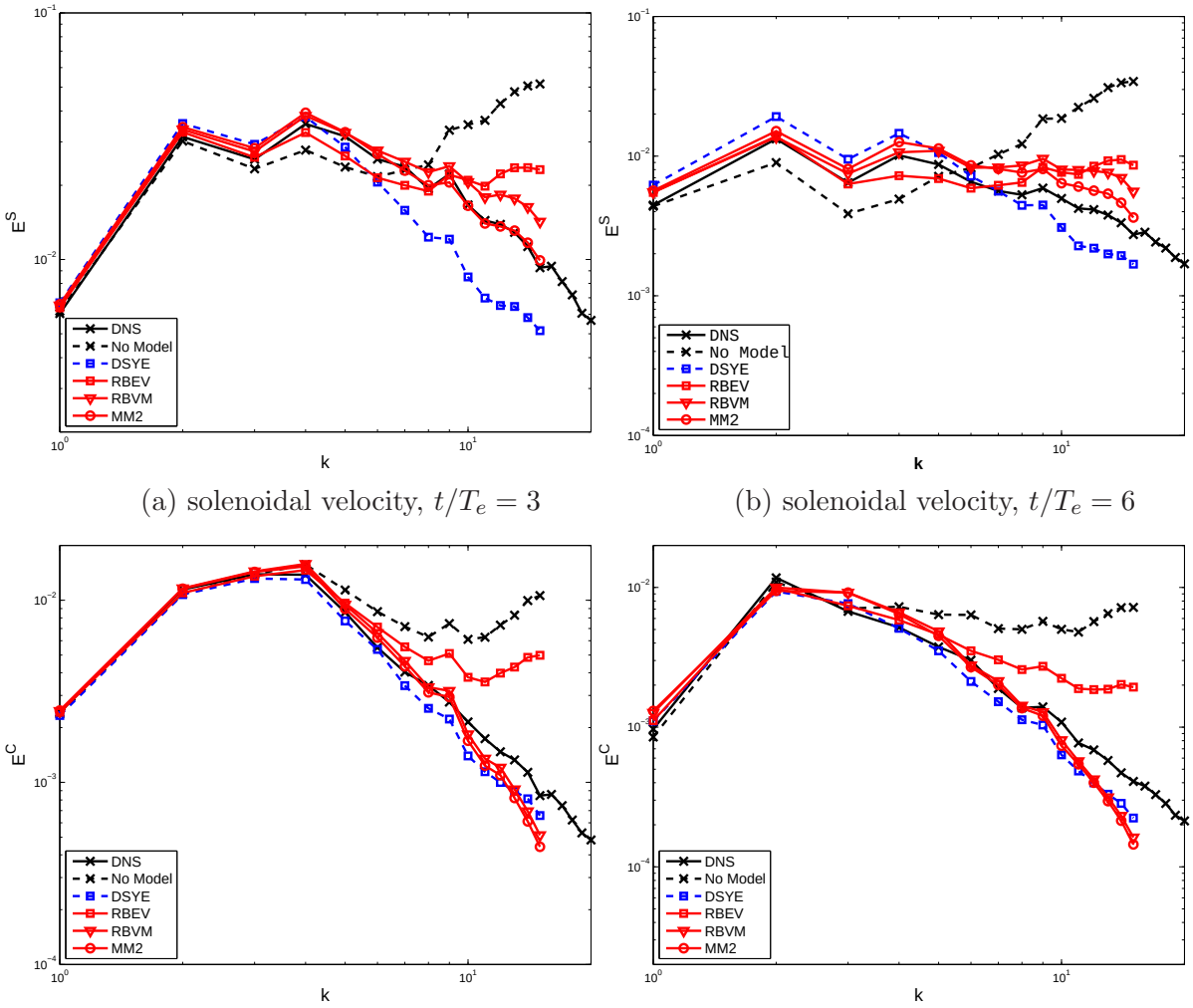

(a) solenoidal velocity, $t/T_e = 3$

(b) solenoidal velocity, $t/T_e = 6$

(c) dilatational velocity, $t/T_e = 3$

(d) dilatational velocity, $t/T_e = 6$

Figure 3.93: Energy spectrum of solenoidal and dilatational velocity for the $Re_\lambda = 117.1$ case on a 32^3 grid. A comparison of the dynamic SYE, RBEV, RBVM, MM2 and no model cases, with $C_\tau = 0.5$.

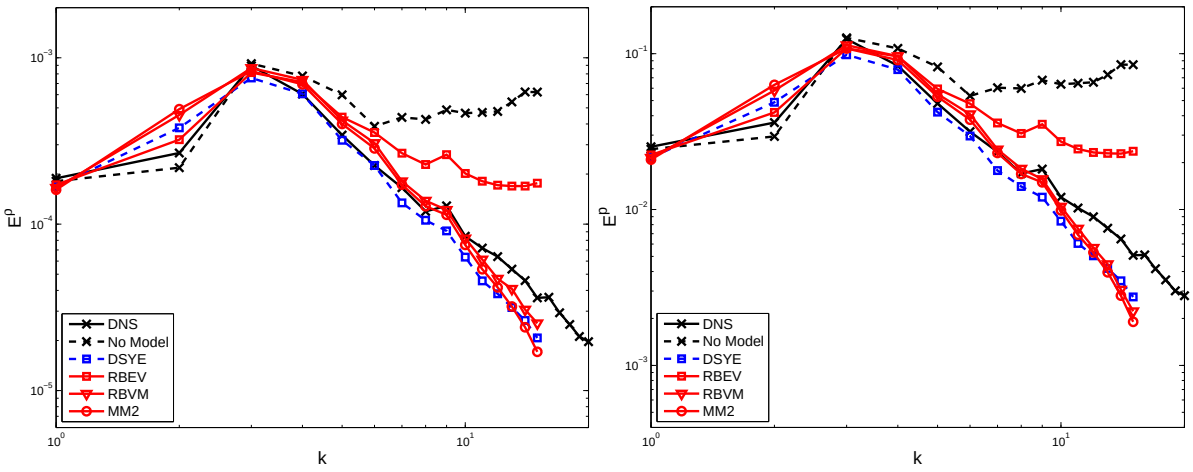

(a) density, $t/T_e = 6$

(b) pressure, $t/T_e = 6$

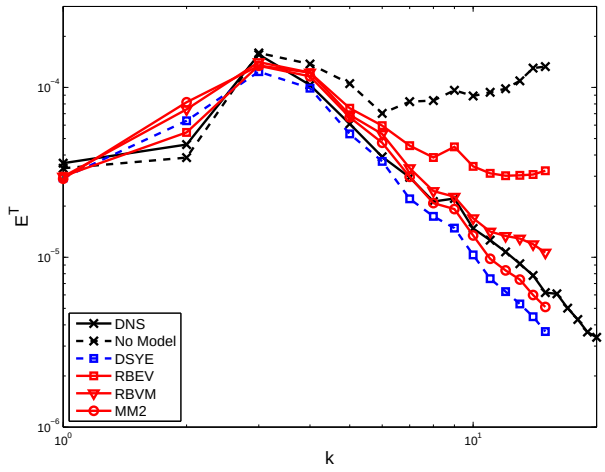

(c) temperature, $t/T_e = 6$

Figure 3.94: Spectrum of density, pressure and temperature for the $Re_\lambda = 117.1$ case on a 32^3 grid. A comparison of the dynamic SYE, RBEV, RBVM, MM2 and no model cases, with $C_\tau = 0.5$.

3.8 Chapter Summary

In this chapter, we have implemented four residual-based LES models for the compressible turbulent flows within a Fourier-spectral method. They are

- the residual-based variational multiscale (RBVM) model
- the mixed model (MM1) based on the RBVM and the DSYE models
- the residual-based eddy viscosity (RBEV) model
- the purely residual-based mixed model (MM2), which is a combination of the RBVM and the RBEV models

We tested the performance of these LES models in predicting the decay of compressible, homogeneous, isotropic turbulence in regimes where shocklets are known to exist. The LES models are tested with Taylor micro-scale Reynolds numbers of $Re_\lambda \approx 65$ and $Re_\lambda \approx 120$ on 32^3 and 64^3 grids.

First, we compared the performance of the RBVM, the DSYE and the mixed model (MM1) models. We varied the level of compressibility of the flow by varying the initial proportion of compressible turbulent kinetic energy and by varying the Mach number. In all cases we found that the RBVM and MM1 models are generally more accurate and perform significantly better than the DSYE model. We also found that for the MM1 model the variational counterpart of the Germano identity automatically accounts for the dissipation produced by the RBVM terms and produces smaller Smagorinsky parameter when compared to the dynamic Smagorinsky model.

Second, we compared the RBEV model with the static SYE (0.1 and 0.16) and the DSYE model. The goal here was to compare the performance of the newly proposed RBEV model with other popular eddy viscosity models. We found that the RBEV model, which does not require the dynamic calculation of a parameter, outperformed the DSYE model.

Third we have examined the performance of the new purely residual-based mixed model (MM2). We have found that with the parameter $C_\tau = 1.0$ it yields results that are overly dissipative, specially for the compressible quantities of interest. However, it still outperforms the DSYE model (but not the RBVM model). With $C_\tau = 0.5$ the mixed model (MM2) is the most accurate model.

Our recommendation is therefore to use purely residual based mixed model (MM2) with $C_\tau = 0.5$. This model is accurate, easy too implement, as it involves no dynamic procedure, and consistent, in that it vanished when the residual of the coarse scales is small.

CHAPTER 4
Residual-Based Models Applied to Incompressible Turbulent Channel Flow

4.1 Introduction

The residual-based eddy viscosity (RBEV) model and the purely residual-based mixed model (MM2) have been applied to the decay of compressible homogeneous isotropic turbulence (HIT) in Chapter 3. Results show that the RBEV model and the MM2 model match the DNS results well and better than the dynamic Smagorinsky-Yoshizawa-eddy diffusivity (DSYE) model and static Smagorinsky-Yoshizawa-eddy diffusivity (SSYE) model with the coefficient $C_s = 0.16$. In contrast to HIT, most flows in nature are bounded by one or more solid surfaces. Fully developed channel flow is one of the simplest bounded flows and is a good test case for new LES models. The residual-based variational multiscale (RBVM) model and the mixed model (MM1) based on RBVM have been applied to incompressible turbulent channel flow by Wang and Oberai. In this Chapter, we apply the RBEV model and the MM2 model to the incompressible fully developed turbulent channel flow with the finite element method (FEM). We do this for two reasons: (1) to test the performance of these models for wall bounded flows and (2) to implement these models in a finite element code, so that they can then be applied to modeling flows in complex geometric configurations.

The layout of this chapter is as follows. In Section 4.1, we specialize the weak form of the models developed in Chapter 2 to the finite element method. The precise definition of the unresolved scales and the stabilization parameters $\boldsymbol{\tau}$ is also provided. In Section 4.2, the fully developed channel flow is introduced to understand some important concepts and behavior of these turbulent flows. In section 4.3, we apply the RBEV model and the MM2 model to study the fully developed channel flow and compare their performance with each other as well as the RBVM model and the dynamic Smagorinsky model. Conclusions are drawn in

Section 4.5.

4.2 Residual-based models

In Chapter 2, we have introduced and developed the residual-based eddy viscosity model (RBEV) and the purely residual-based mixed model (MM2). In this chapter we apply these LES models to incompressible turbulent channel flow by using the finite element method.

4.2.1 Weak form for FEM

The weak form of the RBEV and MM2 models for incompressible flows is given by Equation (2.58) in Chapter 2. It is repeated here for convenience:

Find $\boldsymbol{U}^h \in \mathcal{V}^h$, such that

$$A\big(\boldsymbol{W}^h, \boldsymbol{U}^h + b_1\boldsymbol{U}'\big) + \big(\nabla \boldsymbol{w}^h, 2\nu_t \boldsymbol{S}^h\big) = (\boldsymbol{W}^h, \boldsymbol{F}) \quad \forall \boldsymbol{W}^h \in \mathcal{V}^h. \tag{4.1}$$

where $\boldsymbol{U^h} = [\boldsymbol{u}^h, p^h]^T$ are the unknowns with $\boldsymbol{F} = [\boldsymbol{f},\ 0]^T$, and $\boldsymbol{S}^h$ is the rate of strain. Further, $\nu_t = \bar{C}h|\boldsymbol{u}'|$ is the eddy viscosity of the RBEV model. The semi-linear form $A(\cdot,\cdot)$ in the incompressible case is given by,

$$\begin{aligned} A(\boldsymbol{W}, \boldsymbol{U}) \quad \equiv \quad & (\boldsymbol{w}, \boldsymbol{u}_{,t}) - (\nabla \boldsymbol{w}, \boldsymbol{u} \otimes \boldsymbol{u}) \\ & - (\nabla \cdot \boldsymbol{w}, p) + 2\nu(\nabla^S \boldsymbol{w}, \nabla^S \boldsymbol{u}) + (q, \nabla \cdot \boldsymbol{u}), \end{aligned} \tag{4.2}$$

and the fine scale solution is expressed in terms of the coarse scale residual as

$$\boldsymbol{U}' \approx -\mathbb{P}'\boldsymbol{\tau}(\boldsymbol{U}^h)\ \mathbb{P}'^T \mathcal{R}(\boldsymbol{U}^h). \tag{4.3}$$

We note that in Equation (4.1) b_1 is a parameter. By changing the values of b_1 and $\bar{C}$, Equation (4.1) represents different models. When $b_1 = \bar{C} = 0$, we arrive at DNS. When $b_1 = 0$ and $\bar{C} = 0.0740$, we arrive at the RBEV model. When $b_1 = 1$ and $\bar{C} = 0$, we arrive at the RBVM model. When $b_1 = 1$ and $\bar{C} = 0.0740$, we arrive at the MM2 model.

After using Equation (4.3) in (4.1) we recognize that the fine scale variables appear in all linear and non-linear terms of $A(\cdot,\cdot)$. We retain all the nonlinear terms. However, for the linear terms, following [15] we ignore the time derivative and the viscous terms $(\boldsymbol{w}^h, \boldsymbol{u}'_{,t}) = 0$ and $2\nu(\nabla^S \boldsymbol{w}^h, \nabla^S \boldsymbol{u}') = 0$ to arrive at:

The mixed model (MM2) is given as: Find $\boldsymbol{U}^h \in \mathcal{V}^h$, such that

$$\begin{aligned} & A(\boldsymbol{W}^h, \boldsymbol{U}^h) - b_1(\nabla \boldsymbol{w}^h, \boldsymbol{u}^h \otimes \boldsymbol{u}' + \boldsymbol{u}' \otimes \boldsymbol{u}^h + \boldsymbol{u}' \otimes \boldsymbol{u}') \\ - \quad & b_1(\nabla \cdot q^h, \boldsymbol{u}') - (\nabla \cdot \boldsymbol{w}^h, p') + \left(\nabla \boldsymbol{w}^h, 2\nu_t \boldsymbol{S}^h\right) = (\boldsymbol{w}^h, \boldsymbol{f}). \end{aligned} \tag{4.4}$$

In the equation above there should be a parameter b_1 in front of the p' term. However, we have replaced this with 1 because without this term, the finite element is unstable while using the same interpolation functions for $\boldsymbol{u}^h$ and p^h. So we need this term for all models. We note that Equation (4.4) includes all the models tested in this chapter, except the dynamic Smagorinsky model, which is described in [36]. In particular,

- With $b_1 = 0$ and $\bar{C} = 0$, we arrive at DNS, just with stabilization for pressure.
- With $b_1 = 1$ and $\bar{C} = 0$, we arrive at the RBVM model.
- With $b_1 = 0$ and $\bar{C} = 0.0740$, we arrive at the RBEV model.
- With $b_1 = 1$ and $\bar{C} = 0.0740$, we arrive at the mixed model (MM2).

4.2.2 Unresolved scales and stabilization parameter $\boldsymbol{\tau}$

In Equation (4.4) the unresolved scales $\boldsymbol{U}'$ is depend upon stabilization parameter $\boldsymbol{\tau}$ and the coarse scale residual $\mathcal{R}(\boldsymbol{U}^h)$. With $\boldsymbol{\tau}$ and $\mathcal{R}(\boldsymbol{U}^h)$, the fine scale velocity and pressure are written as

$$\boldsymbol{u}' = -\tau_M \boldsymbol{r}_M(\boldsymbol{u}^h, p^h), \tag{4.5}$$

$$p' = -\tau_C r_C(\boldsymbol{u}^h). \tag{4.6}$$

where $\boldsymbol{\tau} = \mathtt{diag}(\tau_M, \tau_M, \tau_M, \tau_C)$ is diagonal matrix, and following [15] the $\mathbb{P}'$ and $\mathbb{P}'^T$ operators are replaced with the identity. The stabilization parameters for velocity

τ_M and pressure τ_C are defined as:

$$\tau_M = \frac{1}{\sqrt{(2C_1/\Delta t)^2 + u_i g_{ij} u_j + C_2 \nu^2 g_{ij} g_{ij}}}, \tag{4.7}$$

$$\tau_C = \frac{1}{8C_1} \frac{1}{\tau_M tr(g_{ij})}. \tag{4.8}$$

The constant C_1 is obtained by considering the local gradient in element space-time coordinate systems [37], and we will study the effect of different C_1 value in the following sections. The positive constant C_2, which is derived from an element-wise inverse estimate [38], is independent of the grid size, and in this chapter $C_2 = 36$ is fixed. The tensor $g_{ij} = \xi_{k,i}\xi_{k,j}$ is the covariant metric tensor, where $\xi_{i,j} = \partial\xi_i/\partial x_j$. The stabilization parameter τ_M comes from the asymptotic scaling arguments in [39] which are developed within stabilized finite methods [40, 41].

The coarse scale residual $\mathcal{R} = [\boldsymbol{r}_M(\boldsymbol{u}^h, p^h), r_C(\boldsymbol{u}^h)]^T$ is given by

$$\boldsymbol{r}_M(\boldsymbol{u}^h, p^h) = \boldsymbol{u}^h_{,t} + \nabla \cdot (\boldsymbol{u}^h \otimes \boldsymbol{u}^h) + \nabla p^h - \nu \nabla^2 \boldsymbol{u}^h - \boldsymbol{f}, \tag{4.9}$$

$$r_C(\boldsymbol{u}^h) = \nabla \cdot \boldsymbol{u}^h. \tag{4.10}$$

For more discussions about this fine-scale approximation, the reader is referred to [15].

4.3 Turbulent Channel Flow

In contrast to the homogeneous isotropic turbulence which is discussed in the previous chapter, most flows in nature are bounded by one or more solid surfaces, for example, a typical flow goes through pipes or ducts. In this thesis, we consider one of the simplest of bounded flows: fully developed channel flow. In channel flows, the mean velocity vector is parallel to the wall.

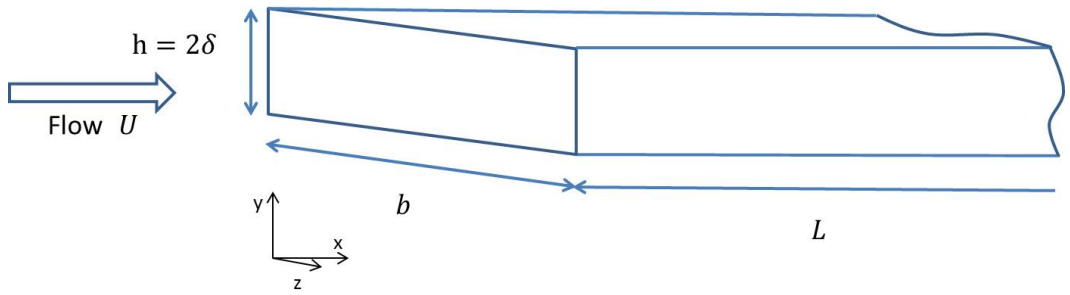

Figure 4.1: Sketch of channel flow.

Figure 4.1 is a sketch of a typical channel flow. Turbulent flow goes through a rectangular channel. The height of the channel is $h = 2\delta$, the length L and the width b. The x direction is determined by the mean flow direction, which is called streamwise direction, y is the wall normal direction. The third direction, z is called spanwise direction.

The Reynolds number used to characterize the flow is

$$Re = (2\delta)\overline{U}/\nu, \tag{4.11}$$

where $\overline{U}$ is the bulk velocity

$$\overline{U} = \frac{1}{\delta}\int_0^\delta \langle U\rangle dy, \tag{4.12}$$

or

$$Re_0 = \delta U_0/\nu, \tag{4.13}$$

where $U_0 = \langle U\rangle_{y=\delta}$ is the centerline velocity.

In a fully developed flow, with large $L \gg \delta$ and $b \gg \delta$, the flow is statistically independent of x and z. The velocities in the three coordinate directions are $\boldsymbol{U} = (U, V, W)$ with fluctuations $\boldsymbol{u} = (u, v, w)$. The flow is considered as statistically stationary. In the average velocity $\langle \boldsymbol{U}\rangle = (\langle U\rangle, \langle V\rangle, \langle W\rangle)$, where the angular

brackets denote the average operator in directions and time, $\langle V \rangle$ and $\langle W \rangle$ are zero and $\langle U \rangle$ depends only on the wall normal direction. Experiments also confirm the natural expectation that the flow is statistically symmetric about the mid-plane $y = \delta$. The flow could be driven by the pressure gradient or body force. The pressure gradient or body force is balanced by the surface force due to the wall shear stress.

4.3.1 Wall shear stress

We assume the flow is driven by the pressure gradient and there is no body force. Using the average operator on the continuity equation of NS equation, we get the mean continuity equation,

$$\langle U_{i,i} \rangle = 0, \tag{4.14}$$

with $\boldsymbol{u} = \boldsymbol{U} - \langle \boldsymbol{U} \rangle$, we also get,

$$u_{i,i} = 0, \tag{4.15}$$

which means both the average velocity and the fluctuation velocity satisfy the continuity equation.

Using the average operator on the momentum equations, we get the mean-momentum equations,

$$\langle U_j \rangle \langle U_i \rangle_{,j} + \frac{1}{\rho} \langle p \rangle_{,i} - \nu \langle U_i \rangle_{,jj} + \langle u_i u_j \rangle_{,j} = 0. \tag{4.16}$$

The y direction mean-momentum equation is

$$0 = \frac{d}{dy} \langle v^2 \rangle + \frac{1}{\rho} \frac{\partial \langle p \rangle}{\partial y}, \tag{4.17}$$

with the boundary condition $\langle v^2 \rangle_{y=0} = 0$, integrates on y to

$$\langle v^2 \rangle + \langle p \rangle / \rho = p_w(x)/\rho, \tag{4.18}$$

where $p_w = \langle p(x, 0, 0) \rangle$ is the mean pressure on the bottom wall. As $\langle v^2 \rangle$ is inde-

pendent of x, the mean pressure gradient in x direction is uniform:

$$\frac{\partial\langle p\rangle}{\partial x} = \frac{dp_w}{dx}. \tag{4.19}$$

The x direction mean-momentum equation is

$$0 = \nu\frac{d^2\langle U\rangle}{dy^2} - \frac{d}{dy}\langle uv\rangle - \frac{1}{\rho}\frac{\partial\langle p\rangle}{\partial x}, \tag{4.20}$$

and it can be rewritten as

$$\frac{d\tau}{dy} = \frac{dp_w}{dx}, \tag{4.21}$$

where $\tau(y)$ is the total shear stress

$$\tau = \rho\nu\frac{d\langle U\rangle}{dy} - \rho\langle uv\rangle. \tag{4.22}$$

For this flow there is no mean acceleration, so in Equation (4.21), **the mean pressure gradient in streamwise direction is balanced by the shear-stress gradient in the wall normal direction**.

Since τ is a function only of y, and p_w is a function only of x (because p_w in defined only on the wall), so in Equation (4.21), both $d\tau/dy$ and dp_w/dx are constant. The solutions for $\tau(y)$ and dp_w/dx can be written in terms of *the wall shear stress*

$$\tau_w = \tau(0). \tag{4.23}$$

Because $\tau(y)$ is antisymmetric about the mid-plane, so $\tau(\delta)$ is zero, and at the top wall the stress is $\tau(2\delta) = -\tau_w$. Hence, the solution to Equation (4.21) is

$$\tau(y) = \tau_w(1 - \frac{y}{\delta}), \tag{4.24}$$

and

$$-\frac{dp_w}{dx} = \frac{\tau_w}{\delta}. \tag{4.25}$$

The total shear stress $\tau(y)$ in Equation 4.22 is the sum of the viscous stress

$\rho\nu d\langle U\rangle/dy$ and the Reynolds stress $-\rho\langle uv\rangle$. At the wall all the Reynolds stresses are zero because the boundary condition $\boldsymbol{U}(\boldsymbol{x},t)=0$. As a result, the wall shear stress is entirely due to the viscous contribution, so the *wall shear stress* is

$$\tau_w = \rho\nu(\frac{d\langle U\rangle}{dy})_{y=0}. \tag{4.26}$$

4.3.2 Wall units

With the wall shear stress τ_w, viscosity ν and density ρ, we define the viscous scales, which are the appropriate scales for the near wall region. These are the *friction velocity*

$$u_\tau = \sqrt{\frac{\tau_w}{\rho}}, \tag{4.27}$$

and the *viscous length-scale*

$$\delta_\nu = \nu\sqrt{\frac{\rho}{\tau_w}} = \frac{\nu}{u_\tau}. \tag{4.28}$$

and the *friction Reynolds number* based on the viscous scales is defined by

$$Re_\tau = \frac{u_\tau\delta}{\nu} = \frac{\delta}{\delta_\nu}. \tag{4.29}$$

The distance from the wall measured in viscous lengths is denoted by

$$y^+ = \frac{y}{\delta_\nu} = \frac{u_\tau y}{\nu}, \tag{4.30}$$

similarly, in streamwise and spanwise direction

$$x^+ = \frac{x}{\delta_\nu} = \frac{u_\tau x}{\nu}, \tag{4.31}$$

$$z^+ = \frac{z}{\delta_\nu} = \frac{u_\tau z}{\nu}. \tag{4.32}$$

The velocity in wall unit $u^+(y^+)$ defined by

$$u^+ = \langle U\rangle/u_\tau. \tag{4.33}$$

These variables are expressed in *wall units*.

4.3.3 Law of the wall and regions and layers near the wall

A fully developed channel flow is completely specified by ρ, ν, δ and dp/dx. As u_τ is a function of ρ, δ and dp/dx, in a fully developed channel flow, it can also be completely specified by ρ, ν, δ and u_τ. Two independent non-dimensional parameters can be formed together with y, and they are y/δ and $Re_\tau = u_\tau\delta/\nu$. Since $Re_\tau = (y/\delta_\nu)/(y/\delta)$ so the mean velocity $\langle U\rangle$ can be written as

$$\langle U\rangle = u_\tau F(\frac{y}{\delta_\nu}, \frac{y}{\delta}), \tag{4.34}$$

where F is a universal non-dimensional function.

The mean velocity gradient is an important parameter in channel flows, because the viscous stress and the turbulent production are both determined by $\mathtt{d}\langle U\rangle/\mathtt{d}y$. So we to solve $\mathtt{d}\langle U\rangle/\mathtt{d}y$ instead of $\langle U\rangle$, and we can write

$$\frac{d\langle U\rangle}{dy} = \frac{u_\tau}{y}\Phi(\frac{y}{\delta_\nu}, \frac{y}{\delta}), \tag{4.35}$$

where Φ is an other universal non-dimensional function.

It is found that at high Reynolds number, when $y/\delta \ll 1$, there is an region where the mean velocity is only determined by the viscous scales, and independent of δ. This region is called *inner layer*. In the inner layer,

$$\frac{d\langle U\rangle}{dy} = \frac{u_\tau}{y}\Phi_1(\frac{y}{\delta_\nu}), \tag{4.36}$$

where

$$\Phi_1(\frac{y}{\delta_\nu}) = \lim_{y/\delta\ll 1}\Phi(\frac{y}{\delta_\nu}, \frac{y}{\delta}). \tag{4.37}$$

With the velocity in wall unit $u^+(y^+)$ defined by $u^+ = \langle U\rangle/u_\tau$, Equation (4.36) can be written as

$$\frac{du^+}{dy^+} = \frac{1}{y^+}\Phi(y^+). \tag{4.38}$$

Equation (4.38) shows that the velocity in wall unit u^+ is only a function of the wall unit y^+, and independent of u_τ. This is the *law of the wall*:

$$u^+ = F_w(y^+), \tag{4.39}$$

where

$$F_w(y^+) = \int_0^{y^+} \frac{1}{y^+}\Phi_1(y^+)\mathtt{y}^+. \tag{4.40}$$

The region with $y^+ < 50$, is called the *viscous wall region*, where the viscous contribution to the shear stress is important. When $y^+ < 5$ within viscous wall region, it is the *viscous sublayer*, where the Reynolds shear stress is negligible. One important conclusion for this layer is $F_w(y^+) = y^+$ and this leads to $u^+ = y^+$.

When $y^+ > 30, y/\delta < 0.3$, the viscosity can be neglect, and it is found that $\Phi_1 = 1/\kappa$, where κ is a constant. Then u^+ is solved as

$$u^+ = \frac{1}{\kappa}\mathtt{ln}y^+ + B, \tag{4.41}$$

where $B = 5.2$ is a constant, and $\kappa = 0.41$ is the Von Kármán constant. This is the *log law* for $y^+ > 30$, and this region is called the *log-law region*. Figure 4.2 (cited from [3].) shows that four different Reynolds numbers cases all match the log law very well when $y^+ > 30$.

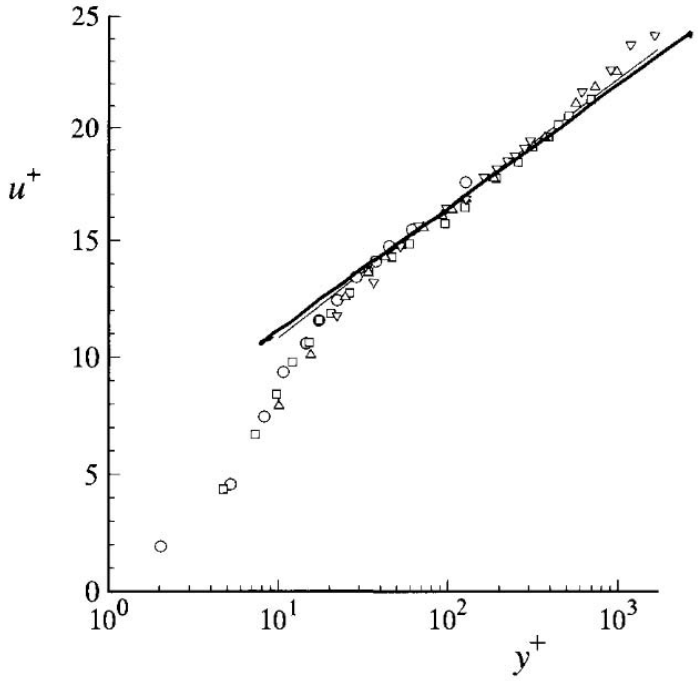

Figure 4.2: Mean velocity profiles in fully developed turbulent channel flow measured by Wei and Willmarth (1989): ◯, $Re_0 = 2,970$; □, $Re_0 = 14,914$; △, $Re_0 = 22,776$; ▽, $Re_0 = 39,582$; the solid line represent the log-law.

Here is a summary of the regions and layers that describe the near-wall flows.

When $y/\delta < 0.1$, we are in the *inner layer*, and in this layer, $\langle U \rangle$ determined by u_τ and y^+, independent of U_0 and δ. When $y^+ > 50$ and $y/\delta \leq 1$, we are in the *outer layer*, and in this layer direct effects of viscosity on $\langle U \rangle$ are negligible. The region between inner and outer layers is the *overlap region* with $y^+ > 50$ and $y/\delta < 0.1$.

In the inner layer, when $y^+ < 50$ we are in the *viscous wall region*, and in this region, the viscous contribution to the shear stress is significant. Especially when $y^+ < 5$ in the viscous wall region, we are in the *viscous sublayer*. In this layer, the Reynolds shear stress is negligible compared with the viscous stress, and $U^+ = y^+$. When $y^+ > 30$ and $y/\delta < 0.3$, we are in the *Log-law region*, where $u^+ = \frac{1}{\kappa}\mathtt{ln}y^+ + B$.

The region between the viscous sublayer and the log-law region is the *buffer layer* with $5 < y^+ < 30$. As the Reynolds number Re of the flow increases with δ changing, the fraction of the channel occupied by the viscous wall region decreases, since δ_ν/δ varies as Re^{-1}.

4.4 Numerical Simulation

All the LES models including the RBEV model , the RBVM model, dynamic Smagorinsky model and the mixed model (MM2) are tested for turbulent channel flow. The computation domain is shown in Figure 4.3 and the dimensions in streamwise, wall-normal, and spanwise directions of the computational domain are $L_x = 2\pi$, $L_y = 2h = 2$, and $L_z = 2\pi/3$. We impose periodic boundary condition to in the in streamwise and spanwise directions. It means the real dimensions in streamwise and spanwise directions are infinity. Channel flow with $Re_\tau = 395$ and $Re_\tau = 590$ are tested. The friction Reynolds number is defined as $Re_\tau = u_\tau h/\nu$, where $u_\tau$is the friction velocity, $h = 1$ is the channel half-width and ν is the kinematic viscosity.

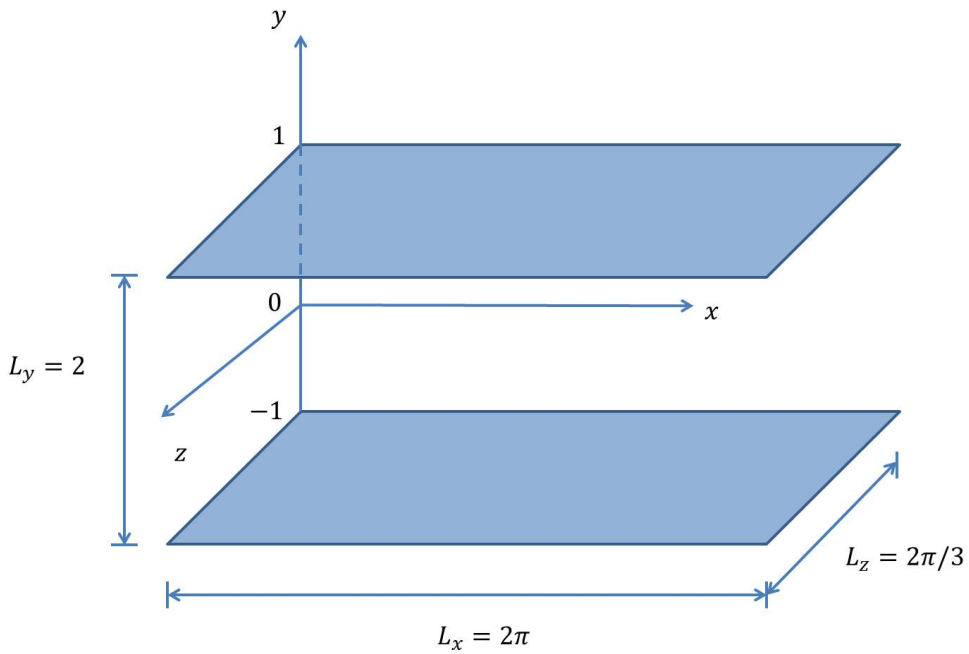

Figure 4.3: Computational domain for LES of turbulent channel flow.

The flow is driven by a constant body force in the streamwise direction. For the boundary condition, no-slip boundary conditions are applied to the upper and lower walls and periodic boundary conditions are applied in the streamwise and spanwise directions. For the initial condition, we we follow the following procedure.

The simulation starts from an initial condition with zero initial pressure and a parabolic velocity profile with random perturbations in the streamwise direction. When the flow is determined to have reached a statistically stationary state, this stage is terminated. During this stage the flow transforms from a "parabolic" flow to a real channel turbulent flow. We use the velocity field at the end of this stage as initial condition for all LES models. For every model, the simulation is further evolved till a statistically stationary state is obtained. this takes about 60 flow-through times. Statistics are then collected for the next 120 flow through times. The generalized-α method [42] is used for discretization in time.

The parabolic velocity with random perturbations is given as

$$[U, V, W] = [1.5 * (1 - y^2) + 0.4 * (r - 0.5), 0, 0], \tag{4.42}$$

where y is the wall-normal coordinate and r is random variable in the range $(-1, 1)$.

The simulations were performed using 32^3 and 64^3 finite elements. For both meshes, we employ C0-continuous trilinear basis functions. The mesh is uniform along the x and z directions and nonuniform along the wall normal direction. The resolution in the wall normal direction is much finer at the wall in order to resolve the boundary layer. Grid points in the y direction are clustered near the wall by the following function:

$$y_i = \frac{1}{b} tanh\big(\xi_i tanh^{-1}(b)\big), \tag{4.43}$$

where ξ_i is a set of uniformly spaced points in the interval $[-1, 1]$. The coefficient b is a parameter that controls the strength of the clustering. The value of b is chosen such that for the first point in the all-normal direction $y^+ < 1$. Thus the first plane of grid points off the wall is within the viscous sublayer. Figure 4.4 shows the 33^3 mesh.

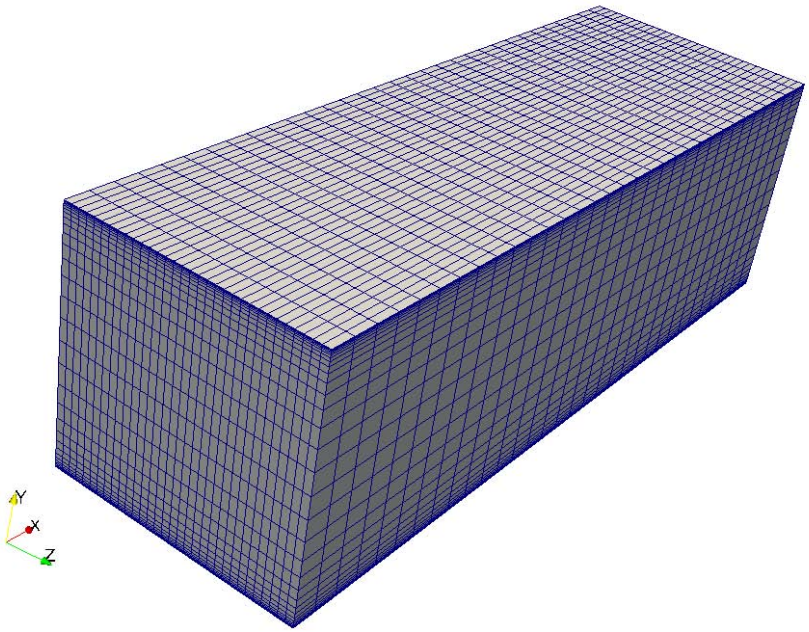

Figure 4.4: 32^3 mesh for turbulent channel flow.

Table 4.1: Physical parameters for the channel flow problem.

Re_τ Nom.	Re_τ Actual	ν	f_b	ρ	dt
395	392.24	$14.8384e-5$	$33.87522076-4$	1.0	0.05 and 0.025
590	585.88	$6.6508514e-5$	$15.18351427e-4$	1.0	0.025

Table 4.2: Numerical parameters for the channel flow problem.

Re_τ Nom.	$N_x \times N_y \times N_z$	$\triangle x^+$	$\triangle y^+_{min}$	$\triangle y^+_{max}$	$\triangle z^+$	dt^+
395	$32 \times 32 \times 32$	77.4	1.31	67.9	25.8	1.15 and 0.57
395	$64 \times 64 \times 64$	38.8	0.47	19.4	12.9	1.15 and 0.57
590	$64 \times 64 \times 64$	57.9	0.71	28.9	19.3	0.57

We perform the LES with a mesh of 32^3 and 64^3 finite elements, and compare the performance of all the LES models with DNS results of [43]. The DNS results were computed using a Chebychev-tau formulation in the wall normal direction and

a Fourier representation in the streamwise and spanwise directions, on a mesh of $256 \times 193 \times 192$. Thus the DNS has 264 times as many points for 32^2 case and 35 times as many points for the 64^3 case. The new LES models are also compared to SUPG stablized dynamic Smagorinsky model [36]. The physical and numerical parameters we used are listed in Tables 4.1 and 4.2, respectively.

In the following subsections, we will first discuss the channel flow with $Re_\tau = 395$ and then the channel flow with $Re_\tau = 590$.

4.4.1 $Re_\tau = 395$

In this subsection we consider the performance of the RBEV, RBVM and MM2 models and also examine the effect of two important numerical parameters dt and the constant C_1 that appears in the definition of τ_m (see Equation (4.7)).

4.4.1.1 RBEV

Figure 4.5 - 4.9 are the results for the RBEV model on a 32^3 mesh with $dt = 0.050$ and $C_1 = 3$. Figure 4.5 compares average streamwise velocities of different models. It shows that the no model test underpredicts the average velocity, while the Smagorinsky model overestimates the average velocity. The same conclusion can be drawn from the semi-log plot for u^+ in Figure 4.6 presented in wall coordinates. In this plot we have also plotted the analytical solutions $u^+ = y^+$ and $u^+ = 1/\kappa \ln y^+ + B$, where $\kappa = 0.41$ and $B = 5.5$. We note that the DNS data matches these analytical solutions well, as does the RBEV model. The no model test underpredicts the velocity, while the Smagorinsky model overestimates the velocity.

Figure 4.7 compares the average pressures. Big oscillations are observed for the for no model case, while the Smagorinsky model also overestimates the average pressure. The RBEV model matches the DNS solution most accurately.

In Figure 4.8, we compare the fluctuations computed by the LES models with their DNS counterparts. We note that all models overpredict the streamwise fluctuations u_{rms} in (a) though the RBEV model is marginally more accurate than the others. For the wall normal fluctuations, v_{rms} in (b), the RBEV model is the most accurate in the near wall region while the dynamic Smagorinsky model is the most

accurate in the center of the channel. For the spanwise fluctuations, w_{rms} in (c), the dynamic Smagorinsky model is more accurate than RBEV model, and both of them overpredict the vlaue.

In Figure 4.9, the average values of the eddy viscosity, the stabilization parameter and the residual of the momentum equation are shown. In (a), the eddy viscosity is near to zero close the wall and grows within the channel. It is remarkable that it achieves this behavior without an explicit dynamic approach. We attribute this behavior to the fact that RBEV model is inherently dynamic in that it is based on the residual of the coarse scales which automatically vanishes in well-resolved regions of the flow. In (b), the stabilization τ starts from almost 0 at the wall and quickly reaches a constant value in the channel. In (c), the residual is reduced when a small distance from the wall and then grows quickly for a very short distance. Then it begins to reduce, and reaches the lowest point at the middle of the channel.

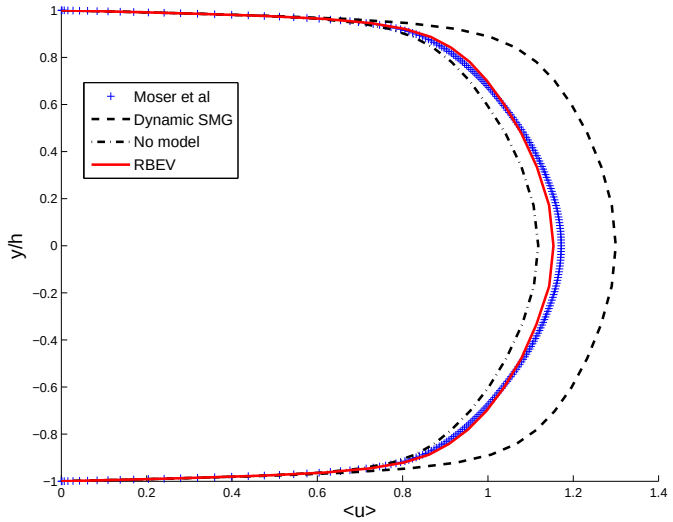

Figure 4.5: Average streamwise velocity for the $Re_\tau = 395$ case on a 32^3 mesh with $dt = 0.050$ and $C_1 = 3$. A comparison of the Dynamic Smagorinsky, RBEV and no model cases.

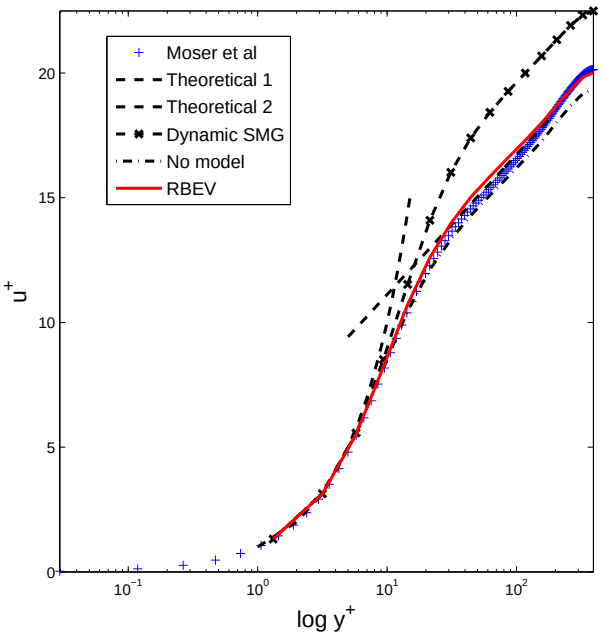

Figure 4.6: **Average streamwise velocity in wall coordinates for the $Re_\tau = 395$ case on a 32^3 mesh with $dt = 0.050$ and $C_1 = 3$. A comparison of the Dynamic Smagorinsky, RBEV and no model cases.**

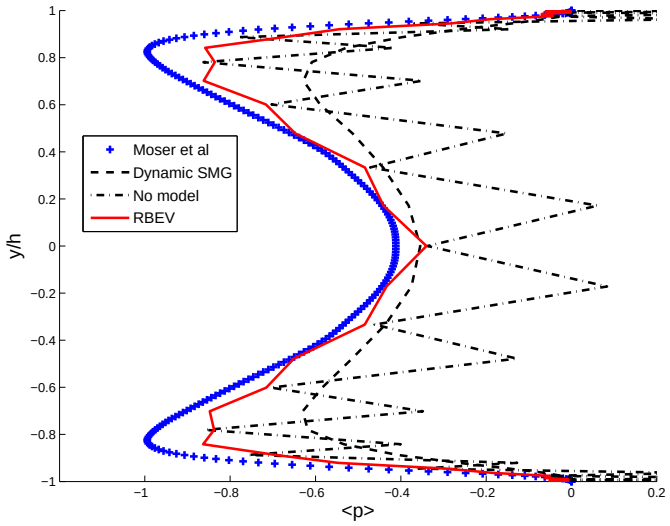

Figure 4.7: **Average pressure for the $Re_\tau = 395$ case on a 32^3 mesh with $dt = 0.050$ and $C_1 = 3$. A comparison of the Dynamic Smagorinsky, RBEV and no model cases.**

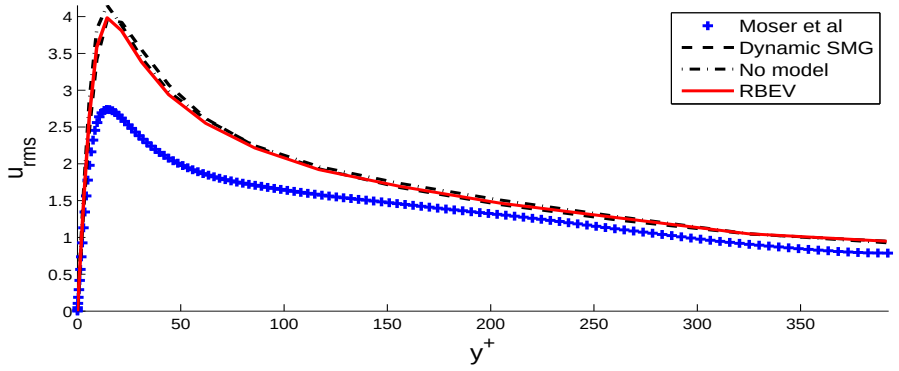

(a) RMS of velocity fluctuations in streamwise direction

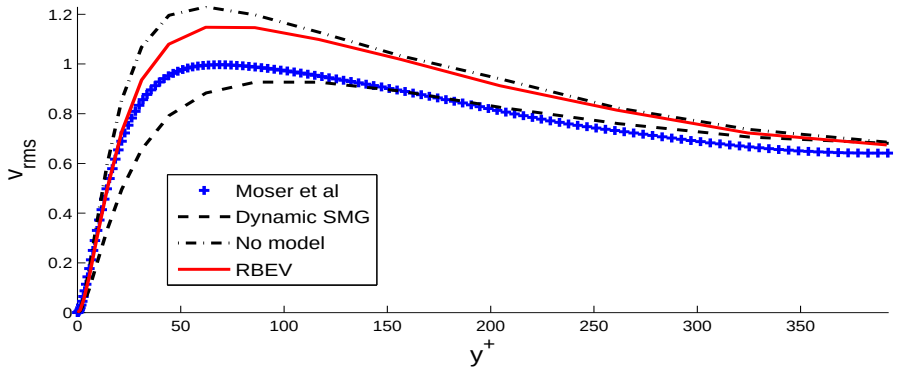

(b) RMS of velocity fluctuations in wall normal direction

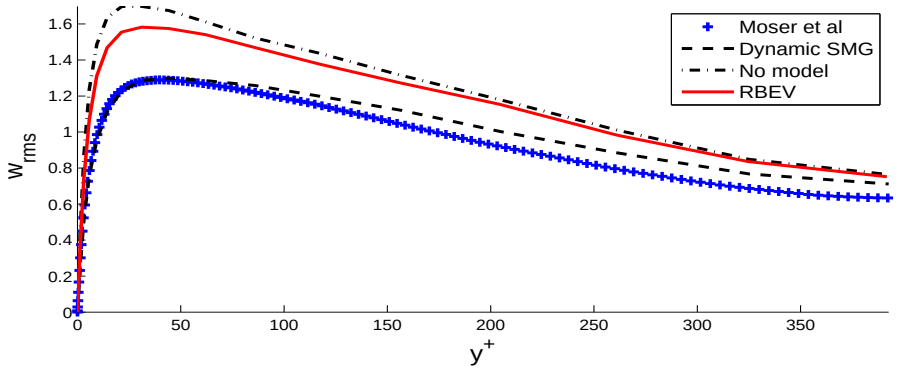

(c) RMS of velocity fluctuations in spanwise direction

Figure 4.8: RMS of velocity fluctuations in wall coordinates for the $Re_\tau = 395$ case on a 32^3 mesh with $dt = 0.050$ and $C_1 = 3$. A comparison of the Dynamic Smagorinsky, RBEV and no model cases.

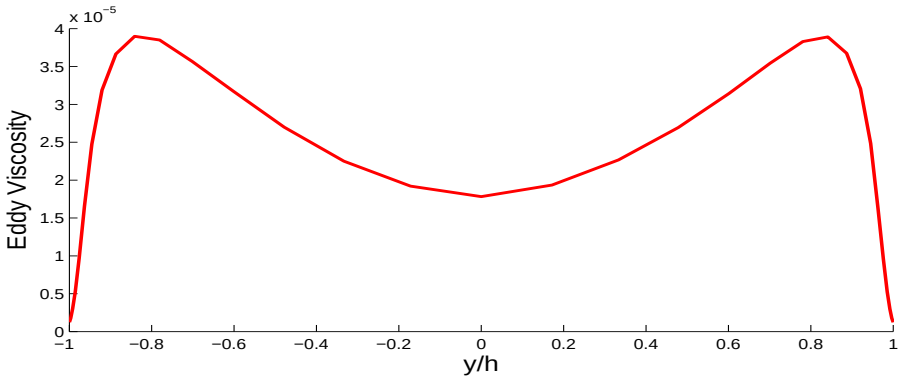

(a) eddy viscosity

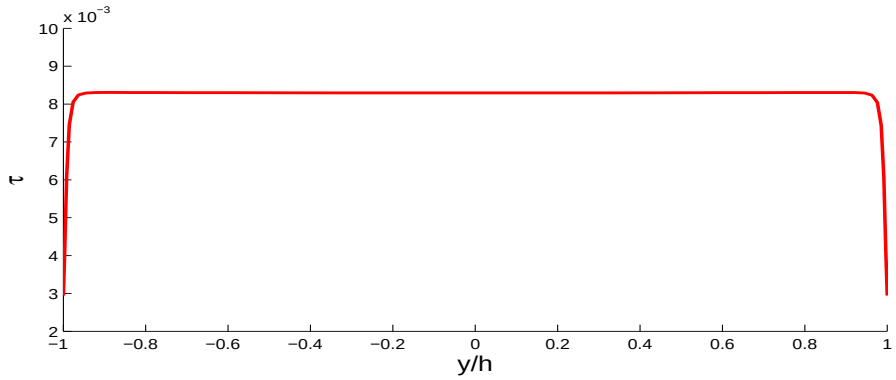

(b) stabilization parameter τ_m

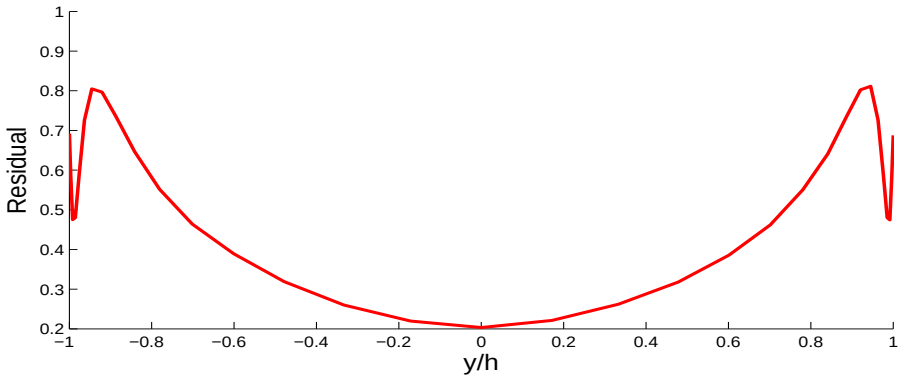

(c) Residual of the momentum equation

Figure 4.9: Average value of the eddy viscosity, stabilization parameter and residual of the momentum equation for the $Re_\tau = 395$ case on a 32^3 mesh with $dt = 0.050$ and $C_1 = 3$. Values for RBEV model.

Mesh and time-step refinement

In the section, we study the effects of varying the time step and grid refinement for the RBEV model with $Re_\tau = 395$. We consider $dt = 0.025$ and $dt = 0.050$ and meshes of 32 and 64 elements which leads to four cases. The parameter $C_1 = 3$ for all cases.

Figure 4.10 compares average streamwise velocities of different models.. All the RBEV models match the DNS solution very accurately, and some convergence with grid refinement is observed. The same conclusion can be drawn from the semi-log plot for u^+ in Figure 4.11 presented in wall coordinates.

For the average pressure profile in Figure 4.12, the results on the 64^3 mesh are better than on the 32^3 mesh. They are closer to the DNS result and are smoother.

In Figure 4.13, we compare the fluctuations computed by the LES models with their DNS counterparts. We note that though all RBEV tests overpredict the streamwise fluctuations u_{rms} near wall region in (a), the RBEV results on the 64^3 mesh are more accurate than the ones on a 32^3 mesh. The RBEV results on the 64^3 mesh also match DNS very well when $y^+ > 100$. For the v_{rms} in (b), all RBEV tests overpredict in near wall region. The RBEV results on the 64^3 mesh are slightly more accurate than the ones on the 32^3 mesh. For the spanwise fluctuations, w_{rms} in (c),the improvement in going from the coarse to the fine mesh is significant.

In Figure 4.9, the average values of the eddy viscosity, the stabilization parameter and the residual of the momentum equation are shown. In (a), we observe that the RB eddy viscosity reduces with refinement in space and time. In that sense it displays a "dynamic" behavior. We note that the stabilization parameter in (b) appears to depend strongly on the time step and not the mesh size in most of the domain. It is basically equal to $dt/(2C_1)$ in this region. Close to the wall the mesh size is small enough so that this is not the case. Remarkably the coarse scale residual (c) is about the same for all cases. This indicates that even with the 64^3 mesh the simulation is far from being fully resolved, and that the models still play an important role.

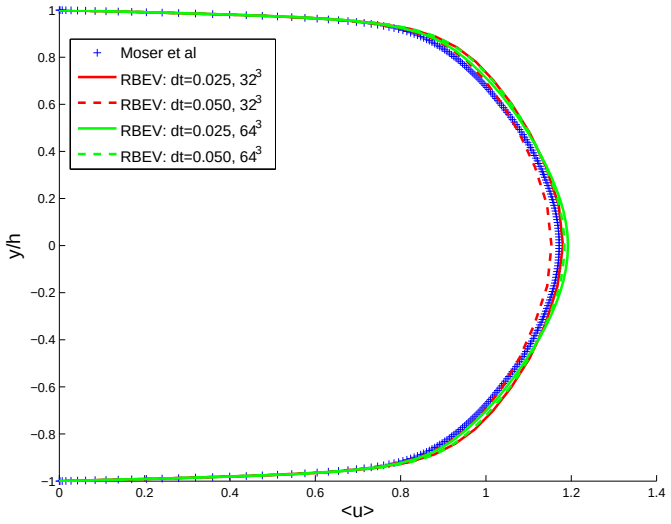

Figure 4.10: Average streamwise velocity for the $Re_\tau = 395$ case wtih $C_1 = 3$. A comparison of the RBEV model on 32^3 and 64^3 meshes with $dt = 0.025$ and $dt = 0.050$.

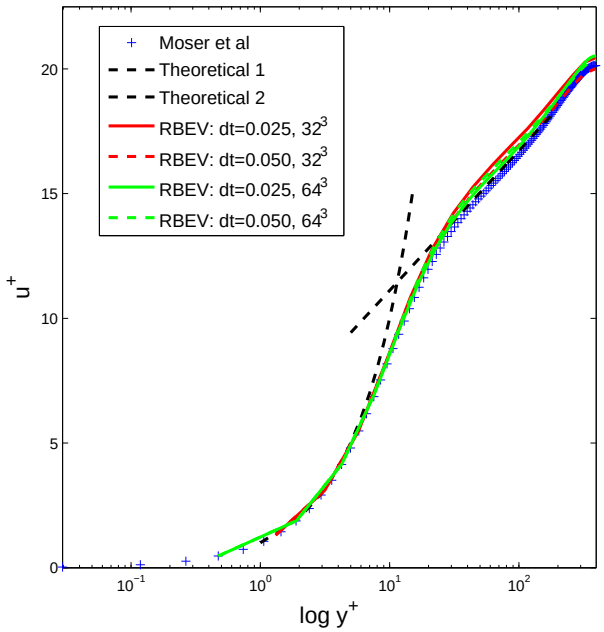

Figure 4.11: Average streamwise velocity in wall coordinates for the $Re_\tau = 395$ case wtih $C_1 = 3$. A comparison of the RBEV model on 32^3 and 64^3 meshes with $dt = 0.025$ and $dt = 0.050$.

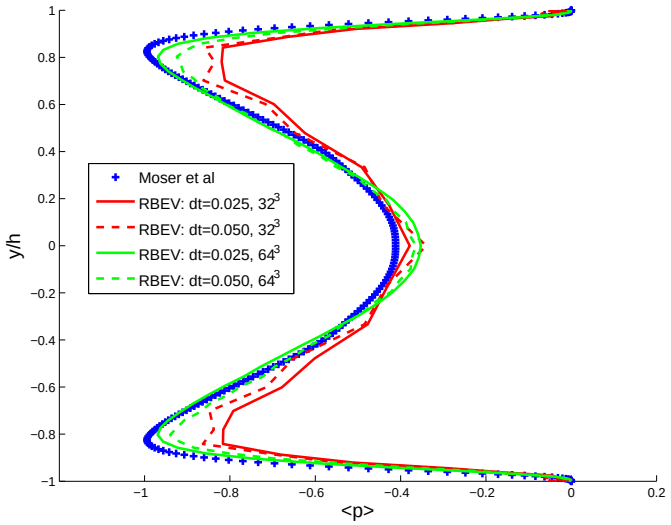

Figure 4.12: Average pressure for for the $Re_\tau = 395$ case wtih $C_1 = 3$. A comparison of the RBEV model on 32^3 and 64^3 meshes with $dt = 0.025$ and $dt = 0.050$.

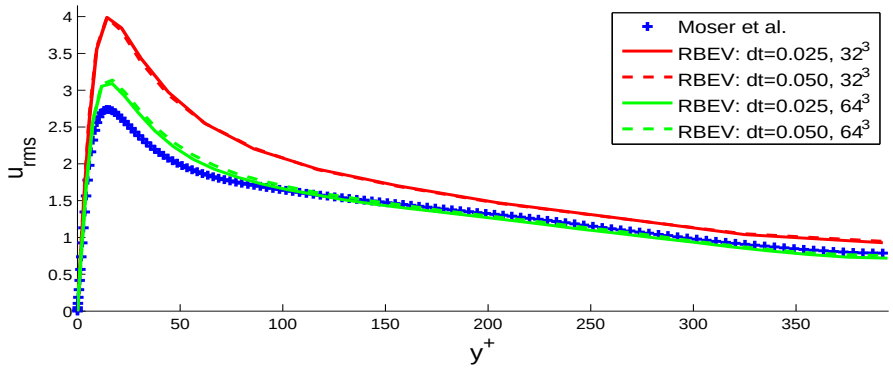

(a) RMS of velocity fluctuations in streamwise direction

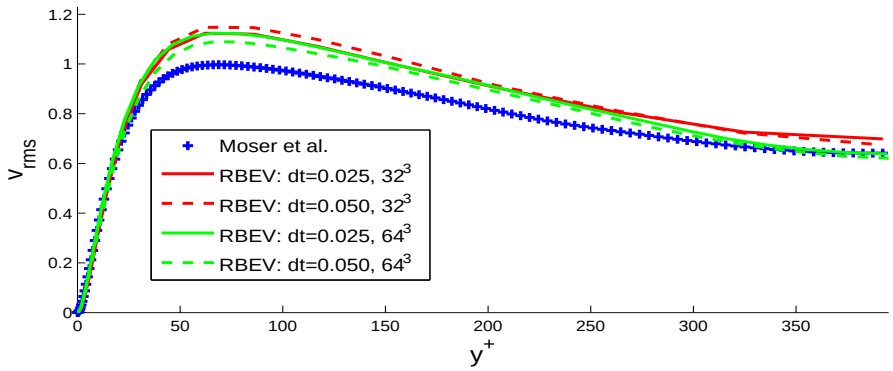

(b) RMS of velocity fluctuations in wall normal direction

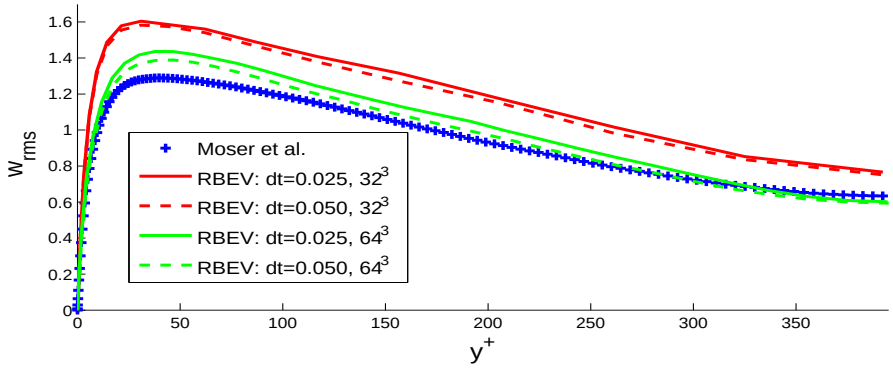

(c) RMS of velocity fluctuations in spanwise direction

Figure 4.13: RMS of velocity fluctuations in wall coordinates for the $Re_\tau = 395$ case wtih $C_1 = 3$. A comparison of the RBEV model on 32^3 and 64^3 meshes with $dt = 0.025$ and $dt = 0.050$.

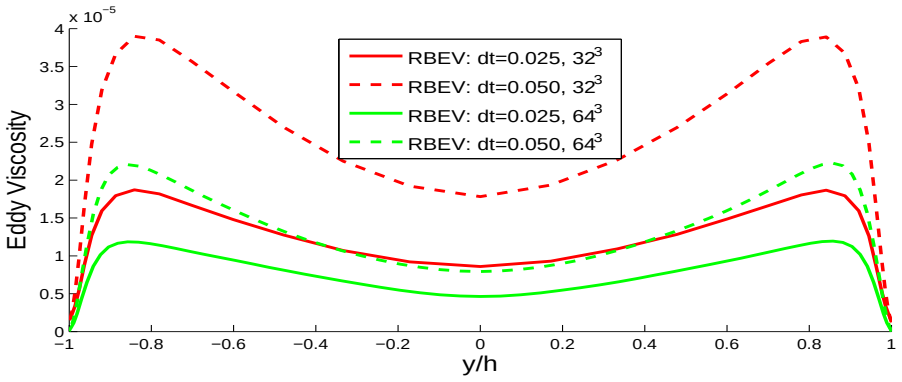

(a) eddy viscosity

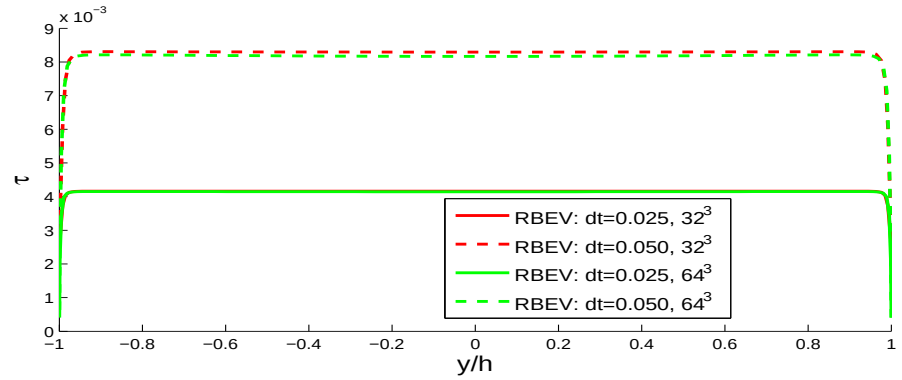

(b) stabilization parameter τ_m

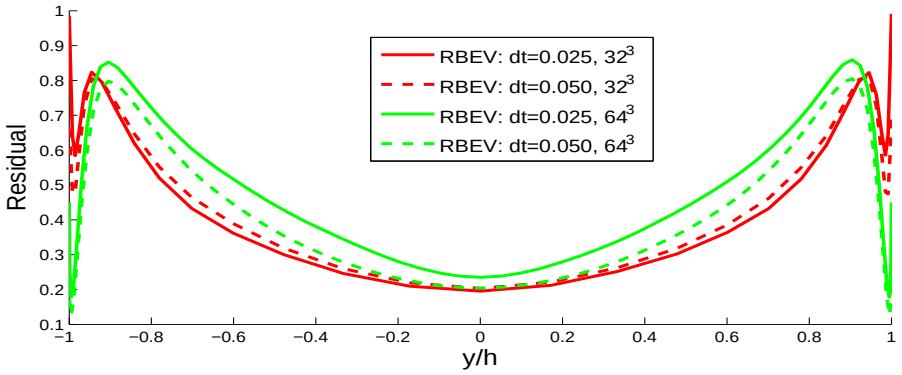

(c) Residual of the momentum equation

Figure 4.14: Average value of the eddy viscosity, stabilization parameter and residual of the momentum equation for the $Re_\tau = 395$ case wtih $C_1 = 3$. A comparison of the RBEV model on 32^3 and 64^3 meshes with $dt = 0.025$ and $dt = 0.050$.

Effect of varying C_1

In the section, we examine the effect of varying C_1 with $dt = 0.050$.

In Figures 4.15 - 4.19 we present the results for the RBEV model on the 32^2 mesh.

Figure 4.15 compares average streamwise velocities. We observe that the RBEV model with $C_1 = 2$ and $C_1 = 3$ matches the DNS solution very accurately. The RBEV models with $C_1 = 12$ and $C_1 = 72$ underpredicts the average velocity, while the RBEV model with $C_1 = 1$ overestimates the average velocity. The same conclusion can be drawn from the semi-log plot for u^+ in Figure 4.16 presented in wall coordinates. The reason for this behavior is tied to the expression for the stabilization parameter τ_m. We note that the viscosity is proportional to τ_m through the expression for $\boldsymbol{u}'$. Also, for the parameters considered in this problem, in most of the domain, $\tau_m \sim dt/(2C_1)$. Thus as C_1 is increased the turbulent viscosity decreases (see Figure 4.19) and as a result the mean velocity also decreases.

In the average pressure profile in Figure 4.17, the RBEV model with $C_1 = 3$ matches the DNS solution most accurately. The RBEV model with $C_1 = 1$ and $C_1 = 2$ overestimate the average pressure. We observe that oscillations becomes bigger if C_1 is bigger. Once again this may be attributed to the reduction in the turbulent viscosity with increasing C_1.

In Figure 4.18, we compare the fluctuations computed by the LES models with their DNS counterparts. We note that all RBEV tests overpredict the streamwise fluctuations u_{rms} near wall region in (a). For the v_{rms} in (b), the RBEV models with $C_1 = 2$ and $C_1 = 3$ are the most accurate in the near wall region $y^+ < 50$, while the RBEV models with $C_1 = 12$ and $C_1 = 72$ overpredict in near wall region and the RBEV model with $C_1 = 1$ underpredicts. For the w_{rms} in (c), the RBEV model with $C_1 = 1$ is most accurate. All the other RBEV results overpredict this fluctuation.

In Figure 4.19, the average values of the eddy viscosity, the stabilization parameter and the residual of the momentum equation are shown. In (a), we observe that the eddy viscosity decreases as C_1 is increased. This is attributed to the de-

crease in the stabilization parameter shown in (b). The residual in (c) is about the same for all cases.

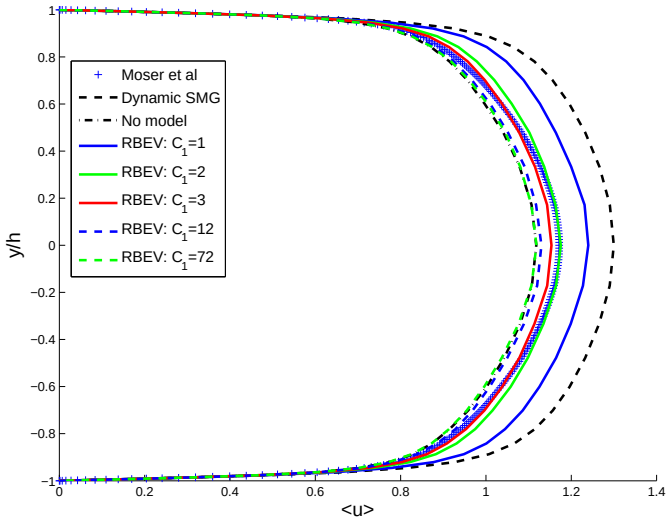

Figure 4.15: Average streamwise velocity for the $Re_\tau = 395$ case on a 32^3 mesh with $dt = 0.050$. A comparison of the RBEV model with $C_1 = 1, 2, 3, 12, 72$.

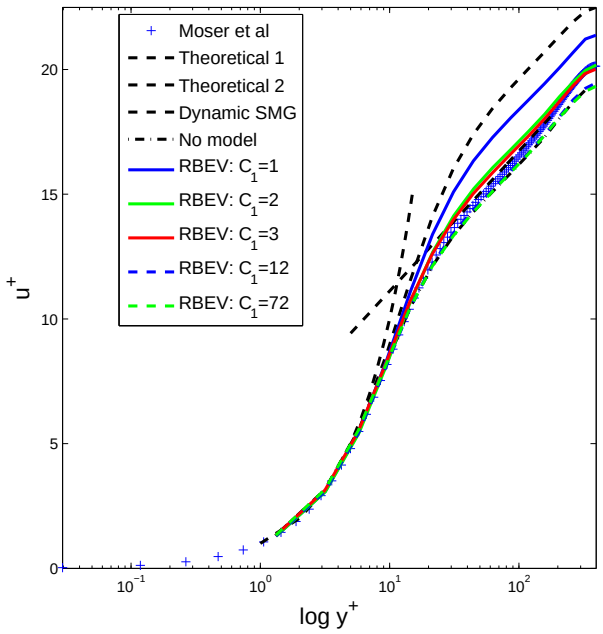

Figure 4.16: Average streamwise velocity in wall coordinatesfor the $Re_\tau = 395$ case on a 32^3 mesh with $dt = 0.050$. A comparison of the RBEV model with $C_1 = 1, 2, 3, 12, 72$.

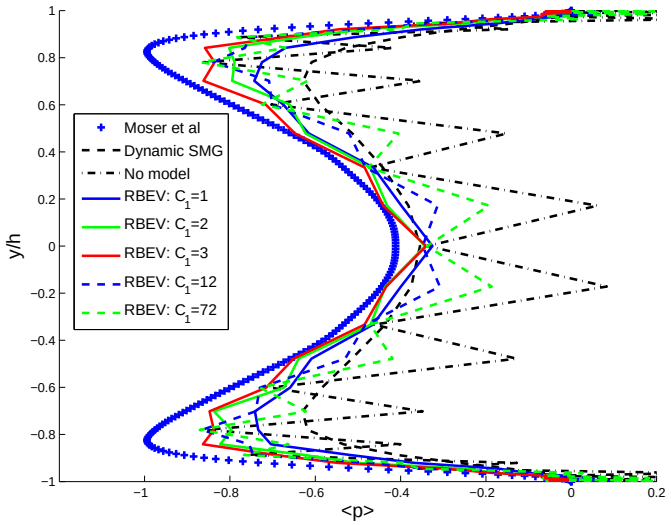

Figure 4.17: Average pressure for the $Re_\tau = 395$ case on a 32^3 mesh with $dt = 0.050$. A comparison of the RBEV model with $C_1 = 1, 2, 3, 12, 72$.

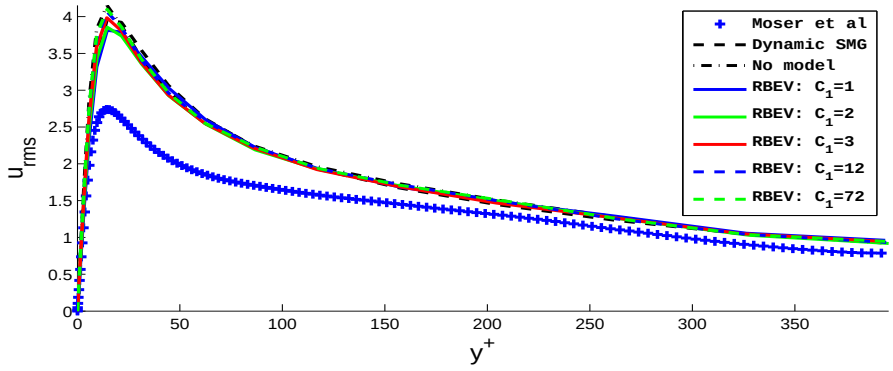

(a) RMS of velocity fluctuations in streamwise direction

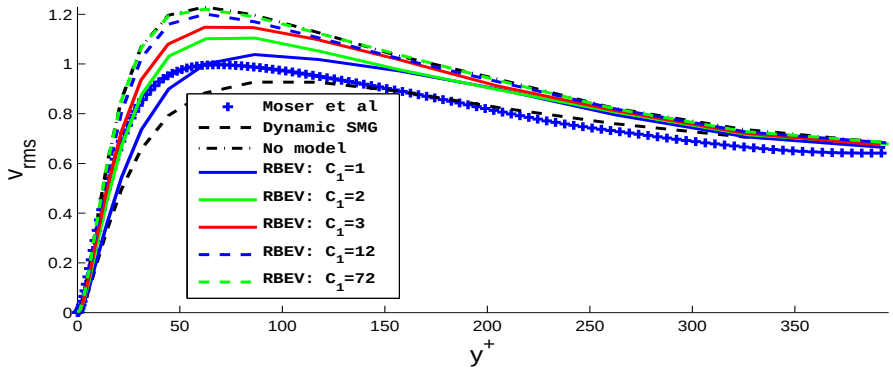

(b) RMS of velocity fluctuations in wall normal direction

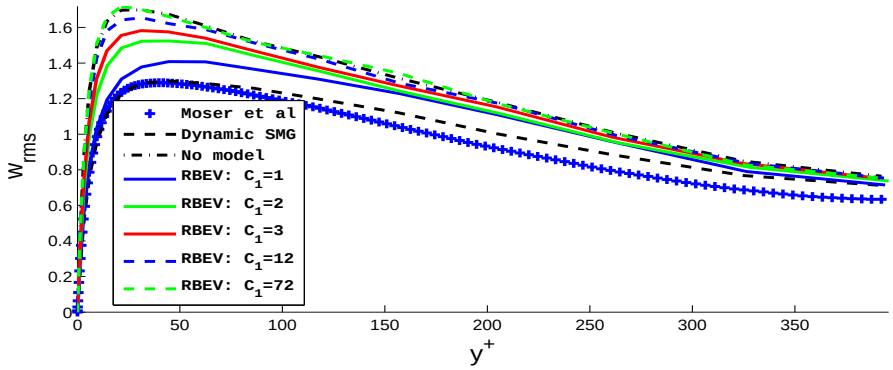

(c) RMS of velocity fluctuations in spanwise direction

Figure 4.18: RMS of velocity fluctuations in wall coordinates for the $Re_\tau = 395$ case on a 32^3 mesh with $dt = 0.050$. A comparison of the RBEV model with $C_1 = 1, 2, 3, 12, 72$.

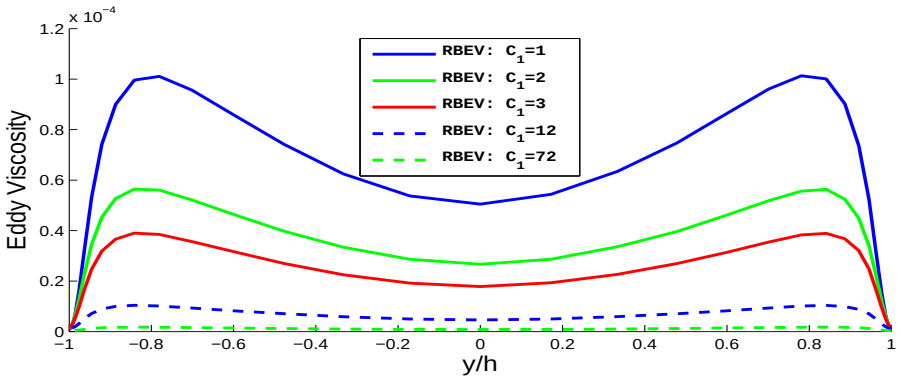

(a) eddy viscosity

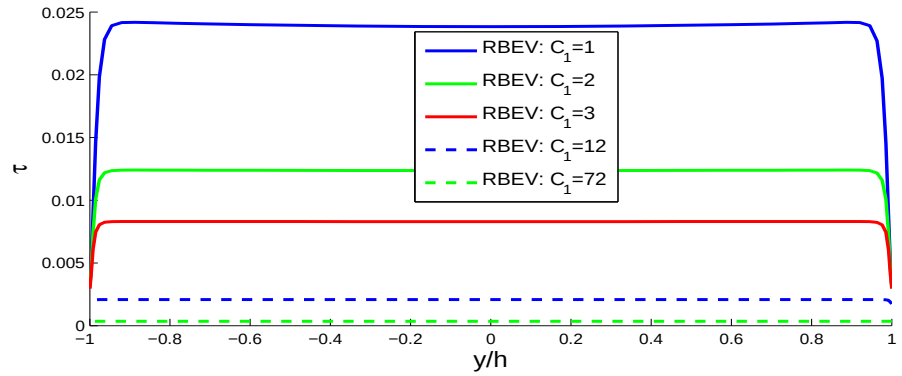

(b) stabilization parameter τ_m

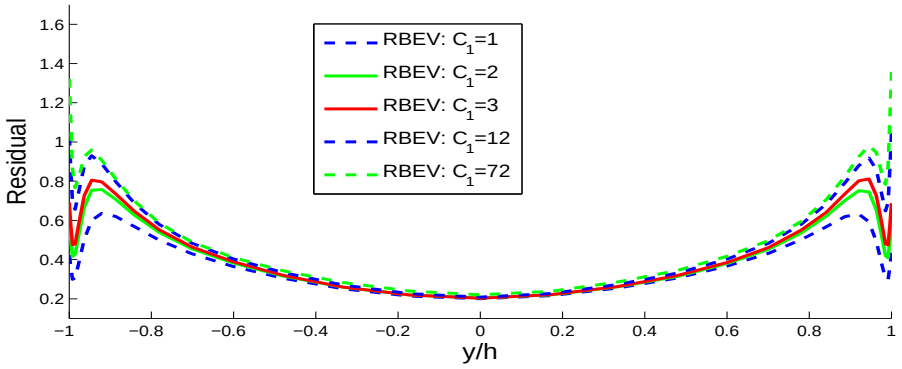

(c) Residual of the momentum equation

Figure 4.19: Average value of the eddy viscosity, stabilization parameter and residual of the momentum equation for the $Re_\tau = 395$ case on a 32^3 mesh with $dt = 0.050$. A comparison of the RBEV model with $C_1 = 1, 2, 3, 12, 72$.

For the 32^3 mesh it might be concluded that the values of $C_1 = 2, 3$ produced the most accurate results. We now test whether this hold for the 64^3 mesh. The results are shown in Figures 4.20 - 4.24.

Figure 4.20 compares average streamwise velocities for different values of C_1. We observed that the RBEV model with $C_1 = 3$ matches the DNS solution very accurately. It shows that the RBEV model with $C_1 = 6$ and $C_1 = 12$ slightly underpredicts the average velocity, while the RBEV model with $C_1 = 1$ overestimates the average velocity. The same conclusion can be drawn from the semi-log plot for u^+ in Figure 4.21 presented in wall coordinates. This behavior is consistent with the values of the turbulent viscosities shown in Figure 4.24.

In the average pressure profile presented in Figure 4.22 we observe that the larger values of C_1 produce more accurate results. However, the results for $C_1 = 3$, though not the most accurate, is still acceptable. The result for $C_1 = 1$ is clearly wrong and needs to be explored some more.

In Figure 4.23, we compare the fluctuations computed by the LES models with their DNS counterparts. The RBEV model with $C_1 = 1$ is clearly incorrect. All the other RBEV models overpredict the streamwise fluctuations u_{rms} near wall region in (a), but are very accurate near the center of the channel. For the v_{rms} in (b), the RBEV model with $C_1 = 3$ is the most accurate in the near wall region $y^+ < 50$. When $y^+ > 70$, the dynamic Smagorinsky model is most accurate. For the w_{rms} in (c), the dynamic Smagorinsky model is most accurate, followed by the RBEV model with $C_1 = 3$.

In Figure 4.24, the average values of the eddy viscosity, the stabilization parameter and the residual of the momentum equation are shown. The RBEV model with $C_1 = 1$ performs unusually. If we ignore this case, in (a), we observe that the eddy viscosity decreases as C_1 is increased. The same conclusion can be drawn from the stabilization parameter in (b). The residual in (c) is about the same for all cases.

In summary, for the 64^3 case also we conclude that the value of $C_1 = 3$ provides the most accurate results.

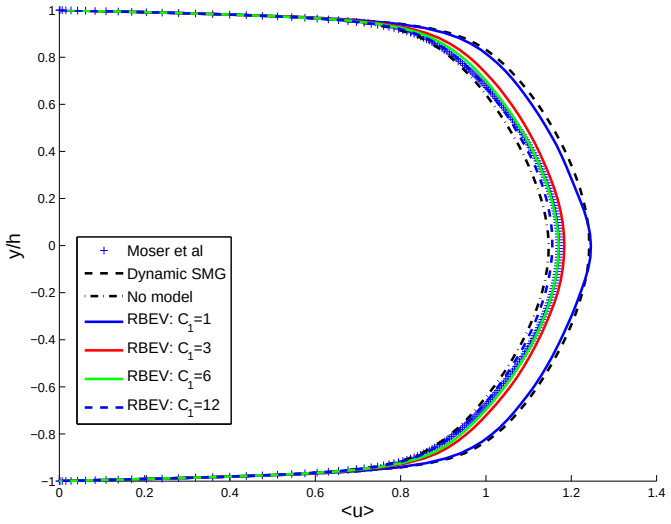

Figure 4.20: Average streamwise velocity for the $Re_\tau = 395$ case on a 64^3 mesh with $dt = 0.050$. A comparison of the RBEV model with $C_1 = 1, 3, 6, 12$.

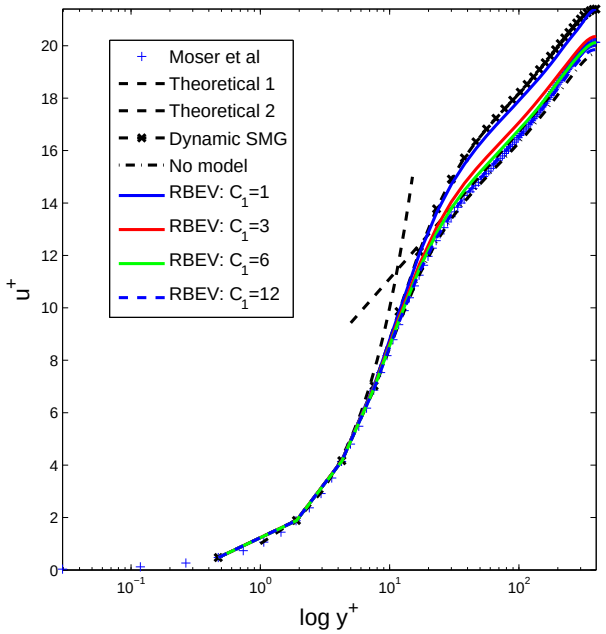

Figure 4.21: Average streamwise velocity in wall coordinates for the $Re_\tau = 395$ case on a 64^3 mesh with $dt = 0.050$. A comparison of the RBEV model with $C_1 = 1, 3, 6, 12$.

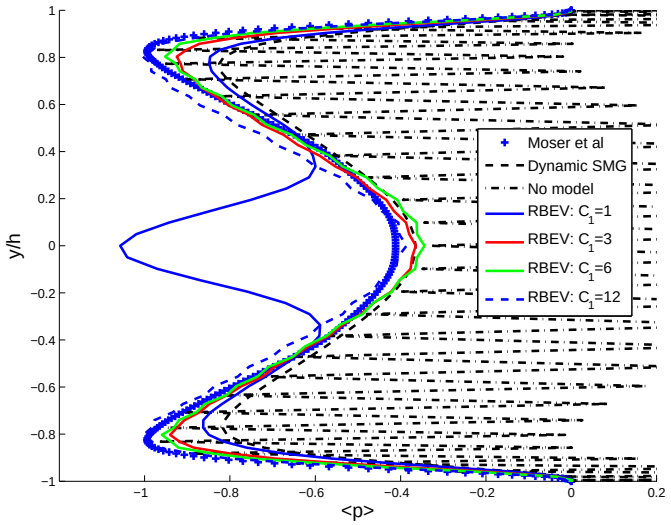

Figure 4.22: Average pressure for the $Re_\tau = 395$ case on a 64^3 mesh with $dt = 0.050$. A comparison of the RBEV model with $C_1 = 1, 3, 6, 12$.

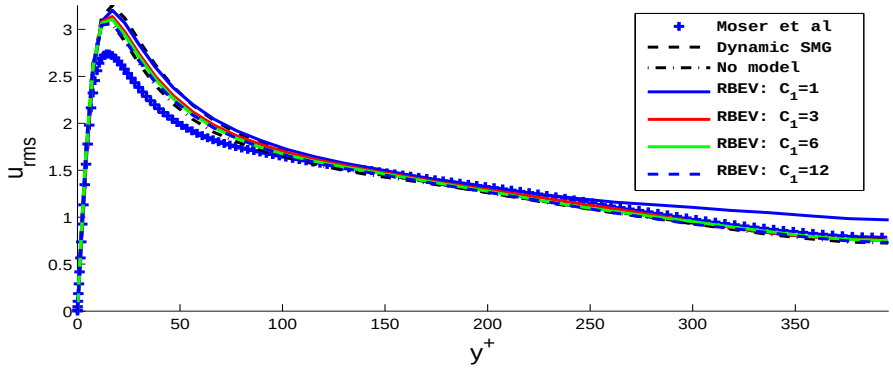

(a) RMS of velocity fluctuations in streamwise direction

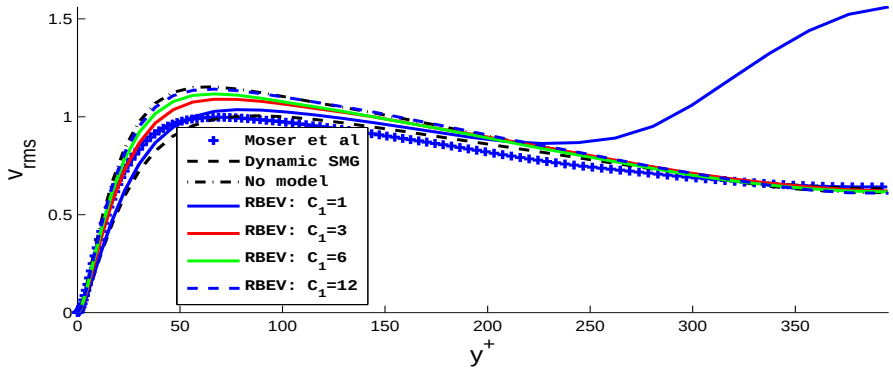

(b) RMS of velocity fluctuations in wall normal direction

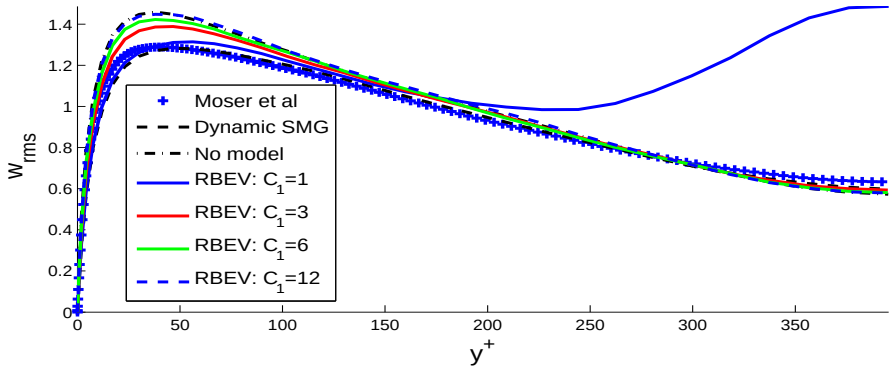

(c) RMS of velocity fluctuations in spanwise direction

Figure 4.23: RMS of velocity fluctuations in wall coordinates for the $Re_\tau = 395$ case on a 64^3 mesh with $dt = 0.050$. A comparison of the RBEV model with $C_1 = 1, 3, 6, 12$.

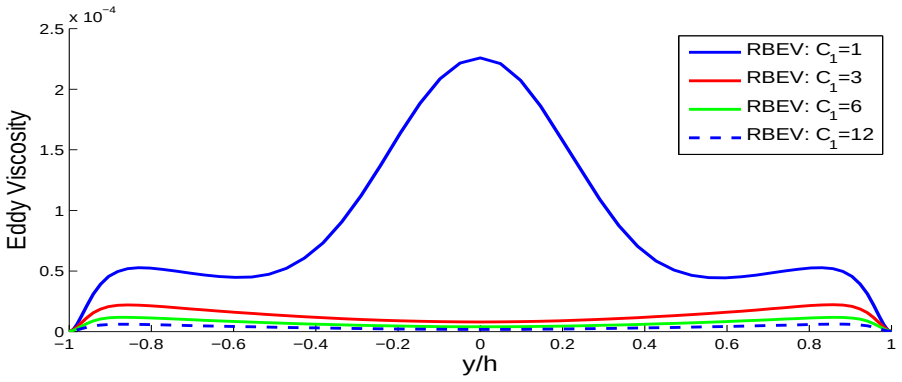

(a) eddy viscosity

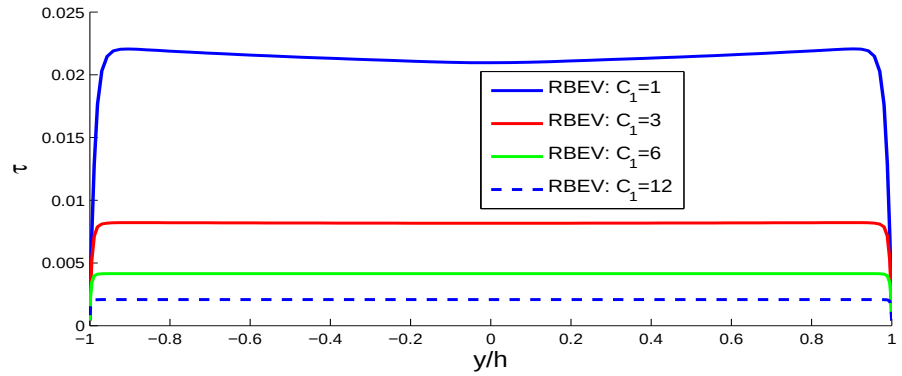

(b) stabilization parameter τ_m

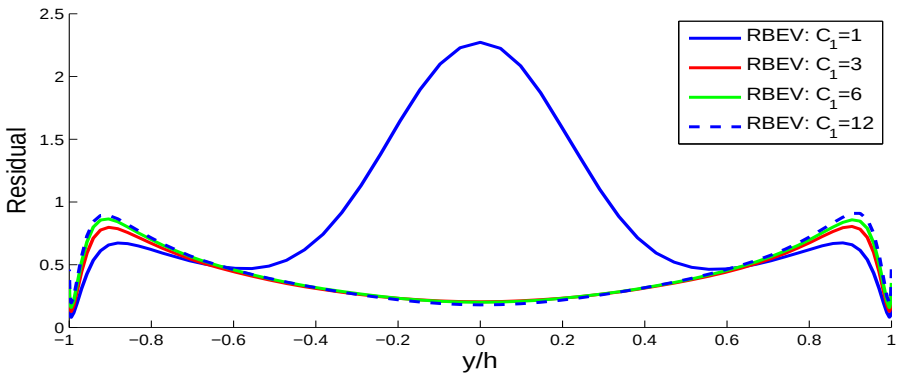

(c) Residual of the momentum equation

Figure 4.24: Average value of the eddy viscosity, stabilization parameter and residual of the momentum equation for the $Re_\tau = 395$ case on a 64^3 mesh with $dt = 0.050$. A comparison of the RBEV model with $C_1 = 1, 3, 6, 12$.

4.4.1.2 MM2

In this section we present results for the purely residual-based mixed model (MM2). First we consider its performance on the 32^3 mesh with $C_1 = 3$ and $dt = 0.05$. Not surprisingly, we find what with this value of C_1 this model is too viscous and leads to an over-prediction of the mean velocity. This is explained by recognizing that with this value of C_1 the RBEV model by itself produced enough viscosity so as to yield an accurate mean velocity. In the MM2 model we are adding to it the viscous contribution from the RBVM model, which clearly means that the resulting model will be too viscous.

Thereafter, we set $C_1 = 12$ and test the performance of this method on a 32^3 and a 64^3 mesh with $dt = 0.0050$ units. With this value of C_1 it performs very well and is competitive with the RBEV model with $C_1 = 3$.

In Figures 4.25 - 4.29 we present results on the 32^3 mesh with $C_1 = 3$.

In Figure 4.25 compares average streamwise velocities of different models. The RBEV model matches the DNS most accurately. The RBVM and the MM2 models overestimate the average velocity and they are very close to each other. All the residual-based models are more accurate than the dynamic Smagorinsky model. The same conclusion can be drawn from the semi-log plot for u^+ in Figure 4.26 presented in wall coordinates. Figure 4.27 compares the average pressure. The RBVM model and the MM2 model overestimate the pressure profile. The pressure profile from the RBVM model and the MM2 model are smoother than the RBEV model. All the residual-based models are more accurate than the dynamic Smagorinsky model.

In Figure 4.28, we compare the fluctuations computed by the LES models with their DNS counterparts. We note that all models overpredict the streamwise fluctuations u_{rms} in (a), though the RBEV model is marginally more accurate than the others. For the wall normal fluctuations, v_{rms} in (b), the RBVM model and the MM2 model are more accurate than the RBEV model in the whole channel, and both of them are more accurate than dynamic Smagorinsky model around the channel center. For the spanwise fluctuations, w_{rms} in (c), the RBVM model and

the MM2 model are more accurate than the RBEV model, and both of them are also more accurate dynamic Smagorinsky model near the channel center. In the near wall region, the dynamic Smagorinsky model is most accurate, followed by the MM2 model and the RBVM model, then the RBEV model.

In Figure 4.29, the average values of the eddy viscosity, the stabilization parameter and the residual of the momentum equation are shown. In (a), the eddy viscosity in the MM2 model is smaller than that in the pure RBEV model. This is reasonable because in the MM2 model the RBVM component also contributes to the dissipation. So the contribution from of the RBEV component is reduced dynamically. In (b), the stabilization parameter τ is the same for both these models. Finally, in (c), we observe that the residual from the MM2 model is smaller than that for RBEV model, which is the reason why the eddy viscosity in MM2 model is smaller than that of the pure RBEV model.

In summary we note that while the MM2 model produces reasonable results with $C_1 = 3$, it is not as good as the RBEV model alone. In general is too viscous. This may be corrected by using a large value of C_1, as shown in the next set of results.

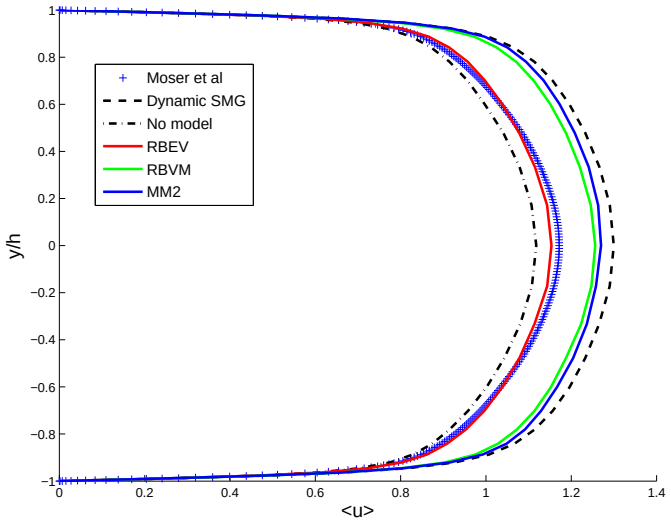

Figure 4.25: Average streamwise velocity for the $Re_\tau = 395$ case on a 32^3 mesh with $dt = 0.050$ and $C_1 = 3$. A comparison of the RBEV, RBVM, and MM2 cases.

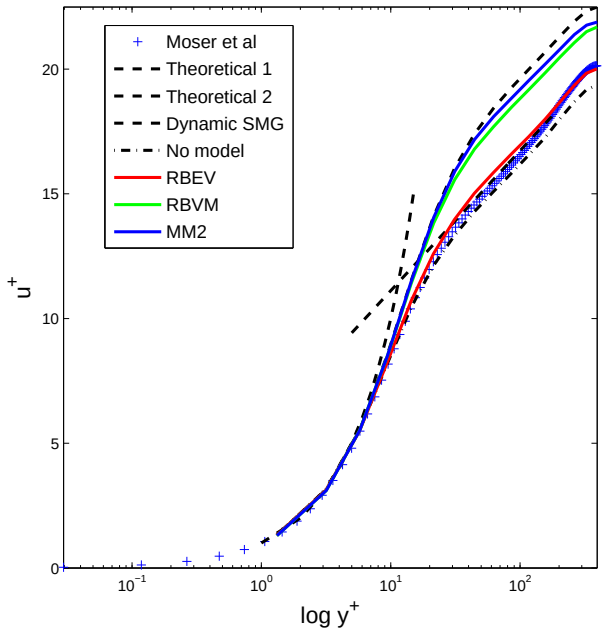

Figure 4.26: Average streamwise velocity in wall coordinates for the $Re_\tau = 395$ case on a 32^3 mesh with $dt = 0.050$ and $C_1 = 3$. A comparison of the RBEV, RBVM, and MM2 cases.

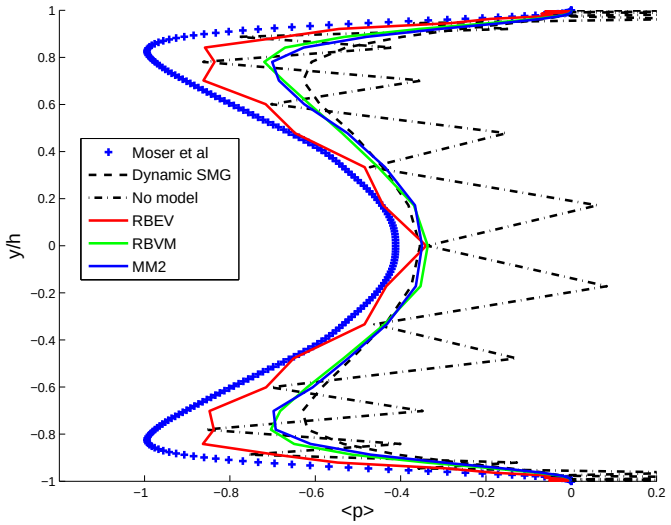

Figure 4.27: Average pressure for the $Re_\tau = 395$ case on a 32^3 mesh with $dt = 0.050$ and $C_1 = 3$. A comparison of the RBEV, RBVM, and MM2 cases.

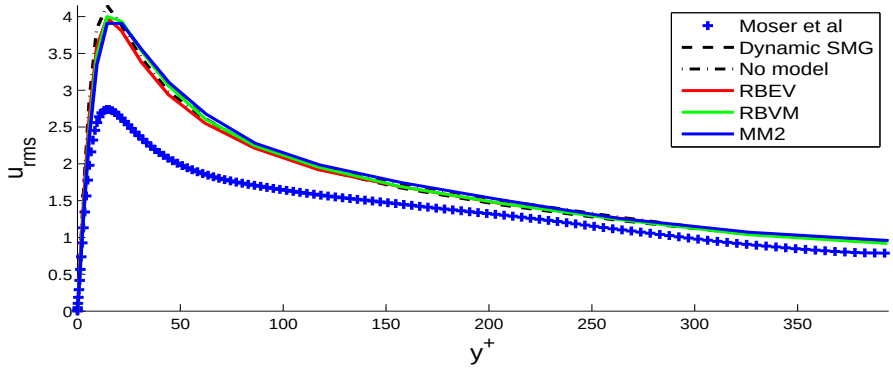

(a) RMS of velocity fluctuations in streamwise direction

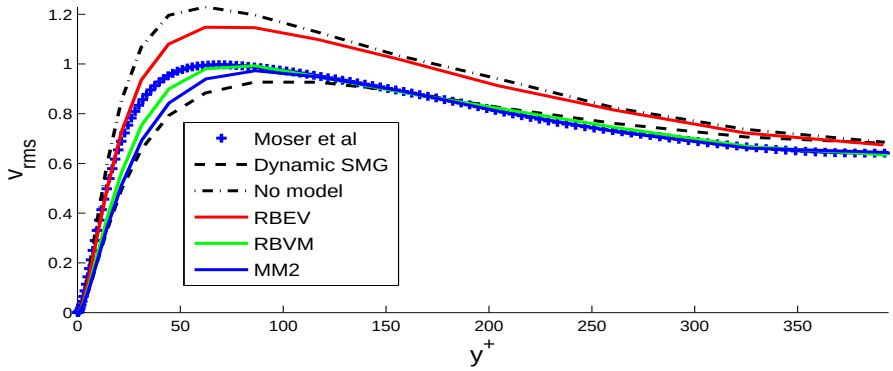

(b) RMS of velocity fluctuations in wall normal direction

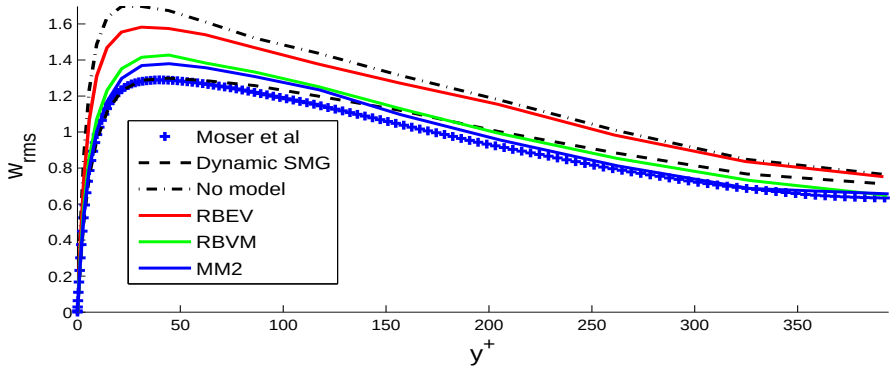

(c) RMS of velocity fluctuations in spanwise direction

Figure 4.28: RMS of velocity fluctuations in wall coordinates for the $Re_\tau = 395$ case on a 32^3 mesh with $dt = 0.050$ and $C_1 = 3$. A comparison of the RBEV, RBVM, and MM2 cases.

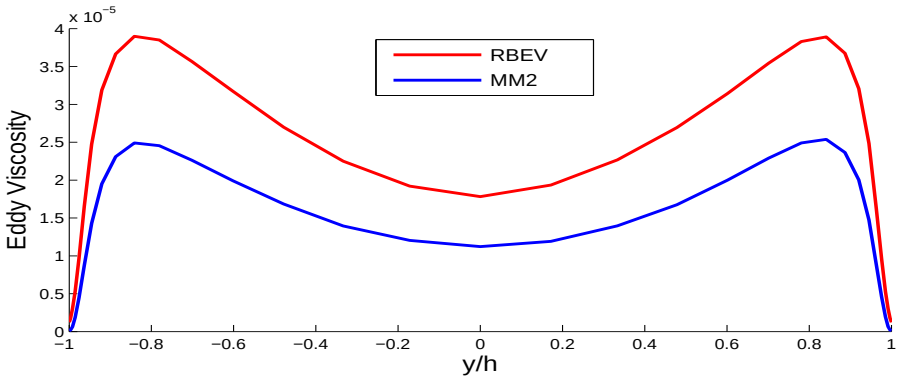

(a) eddy viscosity

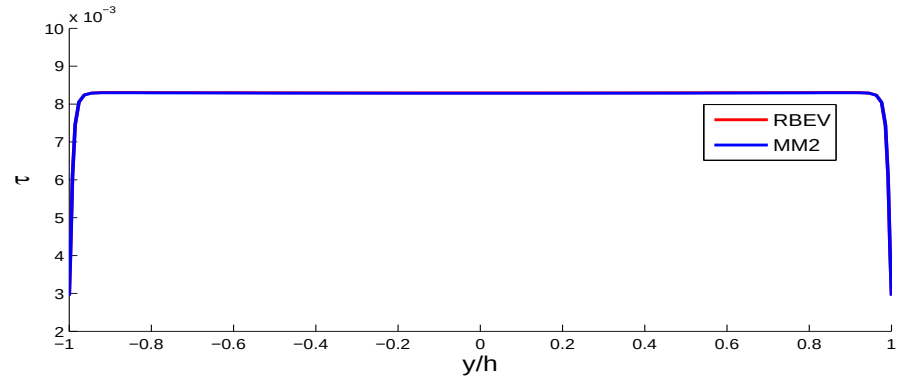

(b) stabilization parameter τ_m

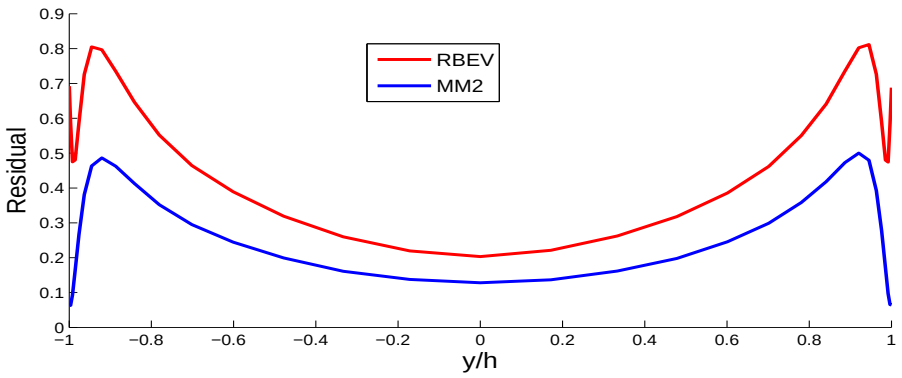

(c) Residual of the momentum equation

Figure 4.29: Average value of the eddy viscosity, stabilization parameter and residual of the momentum equation for the $Re_\tau = 395$ case on a 32^3 mesh with $dt = 0.050$ and $C_1 = 3$. A comparison of the RBEV, and MM2 cases.

In Figures 4.30 - 4.34, we plot the results for LES models on a 32^3 mesh with $dt = 0.050$ and $C_1 = 12$.

Figure 4.30 compares average streamwise velocities of different models. The RBVM model and the MM2 model match DNS most accurately. The RBEV model underpredicts the profile. The same conclusion can be drawn from the semi-log plot for u^+ in Figure 4.31 presented in wall coordinates. Figure 4.31 compares the average pressure. All of the three models have the similar performance while the RBEV model has some oscillations.

In Figure 4.33, we compare the fluctuations computed by the LES models with their DNS counterparts. We note that all the models overpredict the streamwise fluctuations u_{rms} in (a) though the MM2 model is marginally more accurate than the others. For the wall normal fluctuations, v_{rms} in (b), the MM2 model and the RBVM model are more accurate than the RBEV model. In the near wall region, all the three models are more accurate than the dynamic Smagorinsky model. At the center of the channel, the MM2 model and the RBVM model also match the DNS results very accurately. For the spanwise fluctuations, w_{rms} in (c), the MM2 model and the RBVM model are more accurate than the RBEV model. Overall the dynamic Smagorinsky model is the most accurate.

In Figure 4.34, the average values of the eddy viscosity, the stabilization parameter and the residual of the momentum equation are shown. In (a), the eddy viscosity in the MM2 model is smaller than that in the pure RBEV model. In (b), the stabilization parameter τ are the same. In (c), the residual from the MM2 model is smaller than that from the RBEV model, which also accounts for the smaller eddy viscosity observed in (a).

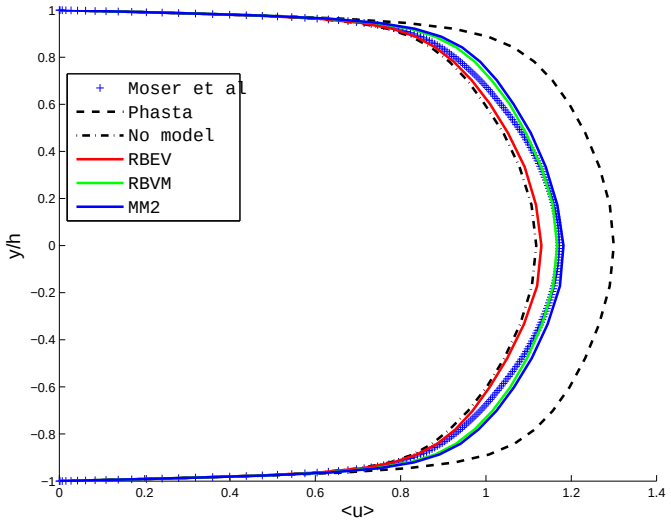

Figure 4.30: Average streamwise velocity for the $Re_\tau = 395$ case on a 32^3 mesh with $dt = 0.050$ and $C_1 = 12$. A comparison of the RBEV, RBVM, and MM2 cases.

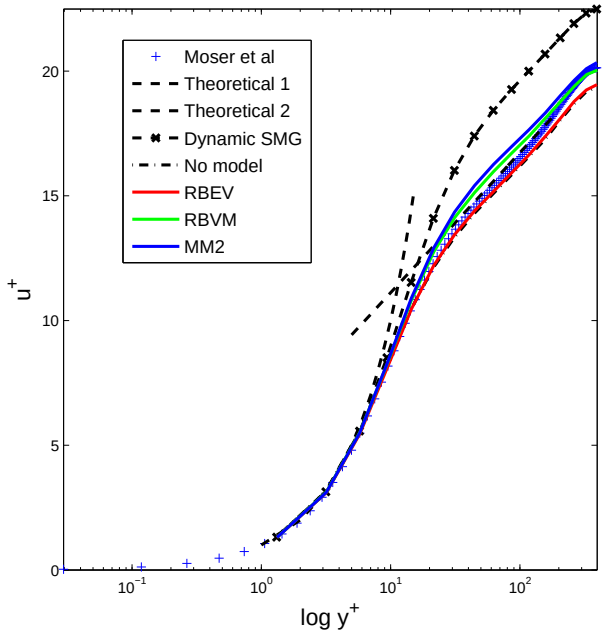

Figure 4.31: Average streamwise velocity in wall coordinates for the $Re_\tau = 395$ case on a 32^3 mesh with $dt = 0.050$ and $C_1 = 12$. A comparison of the RBEV, RBVM, and MM2 cases.

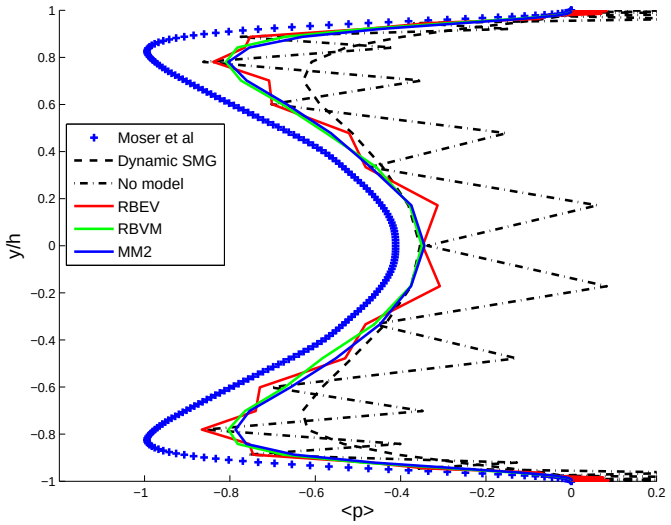

Figure 4.32: Average pressure for the $Re_\tau = 395$ case on a 32^3 mesh with $dt = 0.050$ and $C_1 = 12$. A comparison of the RBEV, RBVM, and MM2 cases.

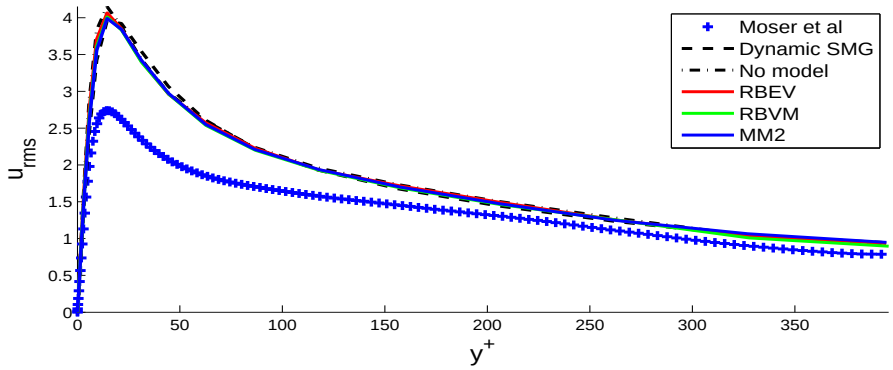

(a) RMS of velocity fluctuations in streamwise direction

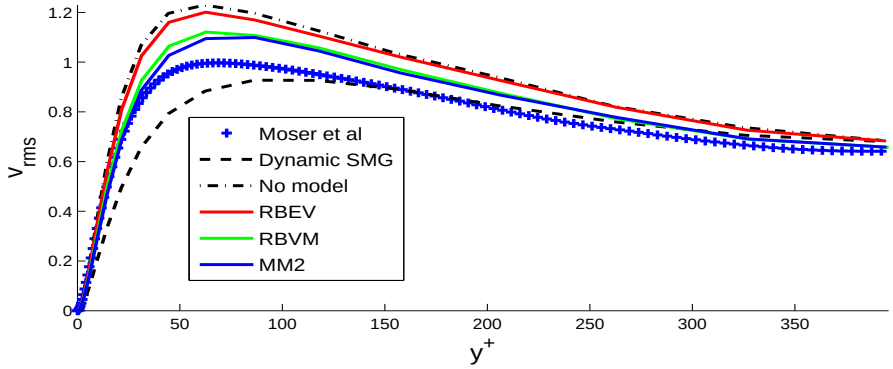

(b) RMS of velocity fluctuations in wall normal direction

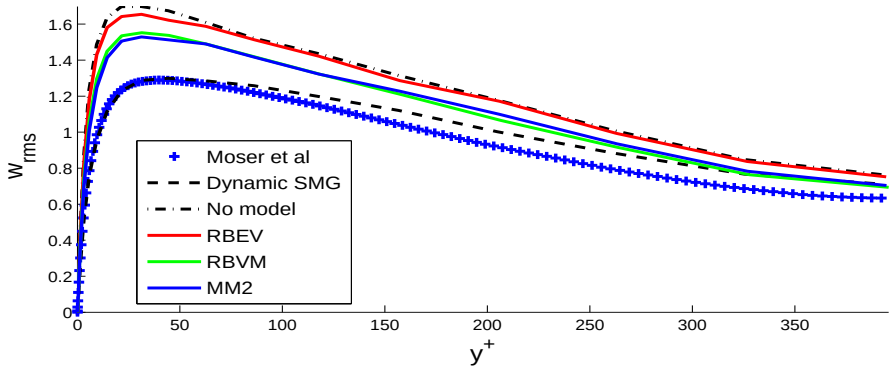

(c) RMS of velocity fluctuations in spanwise direction

Figure 4.33: RMS of velocity fluctuations in wall coordinates for the $Re_\tau = 395$ case on a 32^3 mesh with $dt = 0.050$ and $C_1 = 12$. A comparison of the RBEV, RBVM, and MM2 cases.

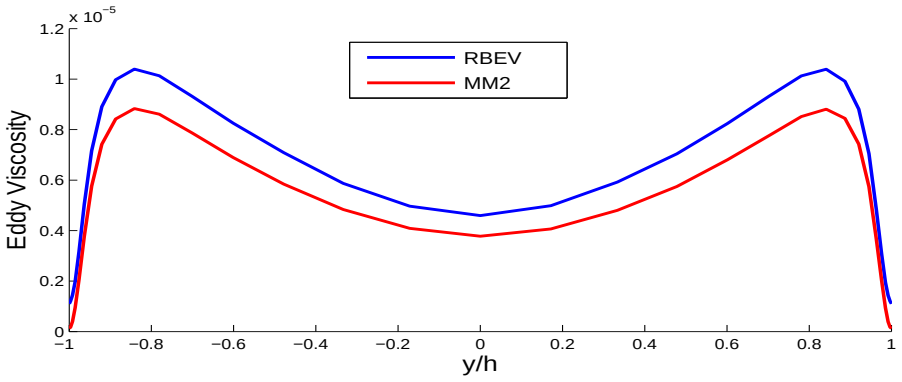

(a) eddy viscosity

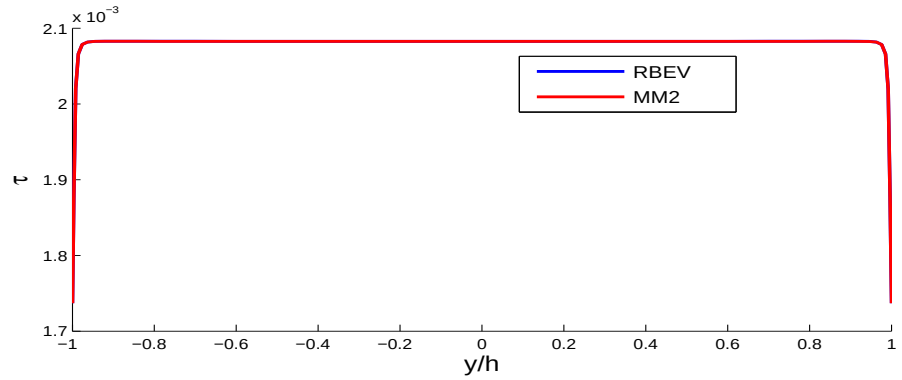

(b) stabilization parameter τ_m

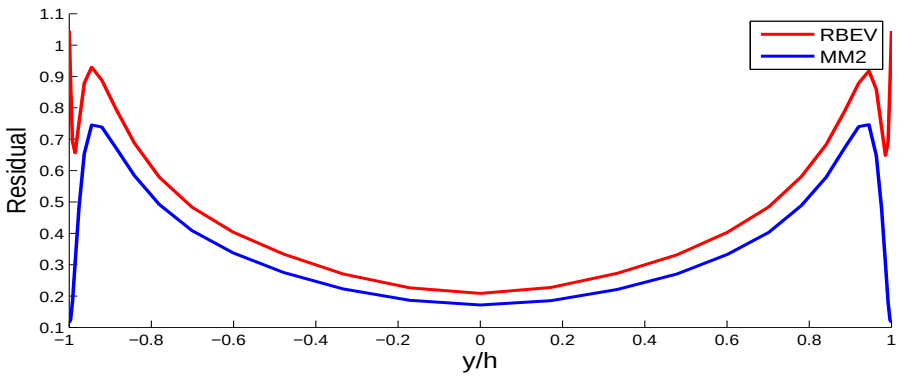

(c) Residual of the momentum equation

Figure 4.34: Average value of the eddy viscosity, stabilization parameter and residual of the momentum equation for the $Re_\tau = 395$ case on a 32^3 mesh with $dt = 0.050$ and $C_1 = 12$. A comparison of the RBEV, and MM2 cases.

From the result on the 32^3 mesh we conclude that for the RBVM and MM2 models the value of $C_1 = 12$ produces the most accurate results. We now consider this value for the 64^3 mesh. In Figures 4.35 - 4.39 we plot the results for LES models on a 64^3 mesh with $dt = 0.050$ and $C_1 = 12$.

Figure 4.35 compares average streamwise velocities of different models. We observe that all the residual-based models are very accurate. The RBEV underestimates the velocity profile while the RBVM and MM2 models over estimate it slightly. The same conclusion can be drawn from the semi-log plot for u^+ in Figure 4.36 presented in wall coordinates. Figure 4.37 compares the average pressure. All of the three residual-based models have the similar performance while the RBEV model has some oscillations. Further, the RBEV model matches DNS most accurately where the profile has a turn-over point while the RBVM and mixed model are more accurate when pressure profile is more straight. All of them are more accurate than the dynamic Smagorinsky model.

In Figure 4.38, we compare the fluctuations computed by the LES models with their DNS counterparts. We note that all models overpredict the streamwise fluctuations u_{rms} in (a) though the RBEV model is marginally more accurate than the others. For the wall normal fluctuations, v_{rms} in (b), the MM2 and RBVM models are more accurate than the RBEV model. In the near wall region, all three residual-based models are more accurate than dynamic Smagorinsky model which underpredicts the fluctuations. For the spanwise fluctuations, w_{rms} in (c), the MM2 model and the RBVM model are more accurate than the RBEV model. Near the center of the channel, all three residual-based models slightly underpredict the fluctuations. The dynamic Smagorinsky model is the most accurate. .

In Figure 4.39, the average values of the eddy viscosity, the stabilization parameter and the residual of the momentum equation are shown. In (a), the eddy viscosity in the MM2 model is smaller than in the pure RBEV model. In (b), we observe that the stabilization parameter τ are the same for these models. In (c), we note that the residual from the MM2 model is smaller than that from the RBEV model leading to the difference in the eddy viscosity for these models.

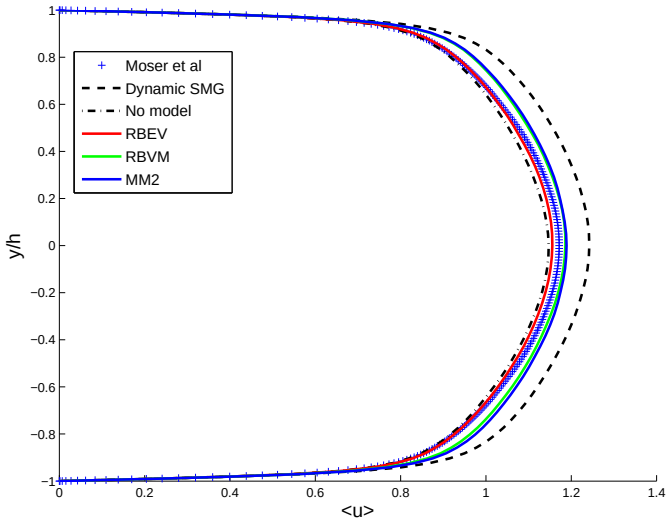

Figure 4.35: Average streamwise velocity for the $Re_\tau = 395$ case on a 64^3 mesh with $dt = 0.050$ and $C_1 = 12$. A comparison of the RBEV, RBVM, and MM2 cases.

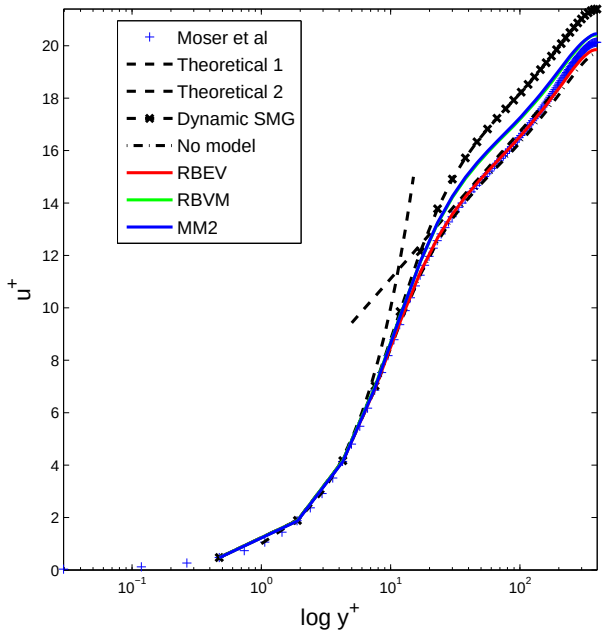

Figure 4.36: Average streamwise velocity in wall coordinates for the $Re_\tau = 395$ case on a 64^3 mesh with $dt = 0.050$ and $C_1 = 12$. A comparison of the RBEV, RBVM, and MM2 cases.

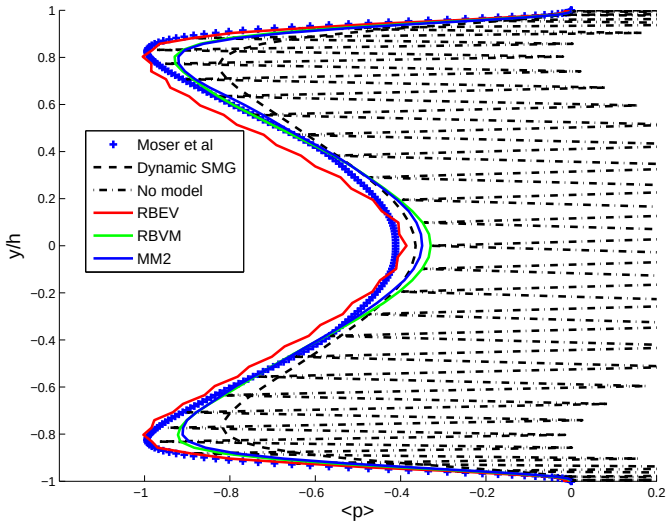

Figure 4.37: Average pressure for the $Re_\tau = 395$ case on a 64^3 mesh with $dt = 0.050$ and $C_1 = 12$. A comparison of the RBEV, RBVM, and MM2 cases.

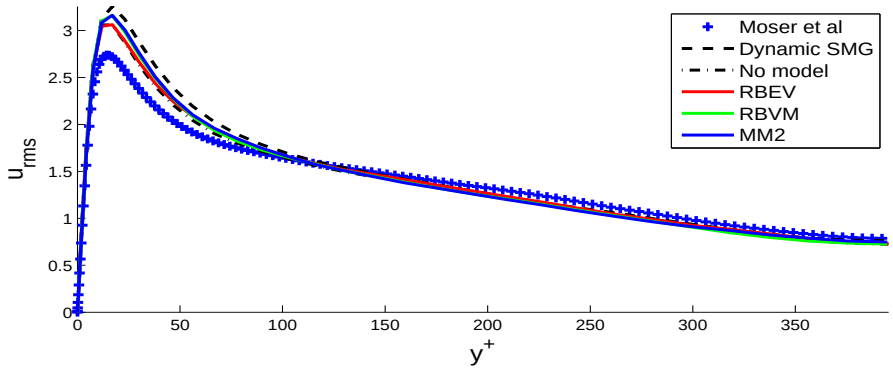

(a) RMS of velocity fluctuations in streamwise direction

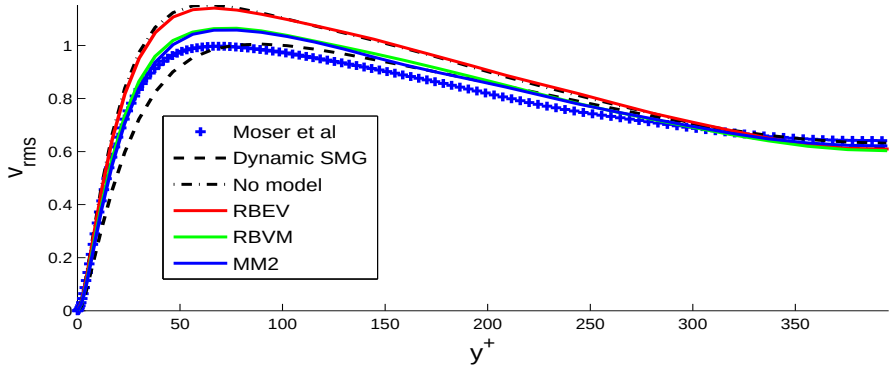

(b) RMS of velocity fluctuations in wall normal direction

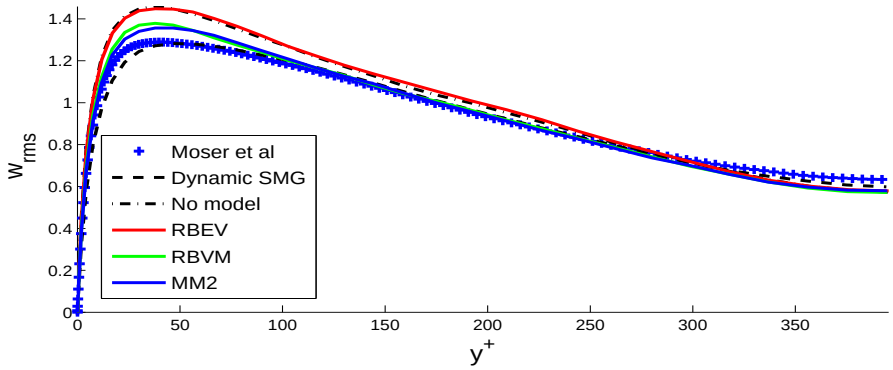

(c) RMS of velocity fluctuations in spanwise direction

Figure 4.38: RMS of velocity fluctuations in wall coordinates for the $Re_\tau = 395$ case on a 64^3 mesh with $dt = 0.050$ and $C_1 = 12$. A comparison of the RBEV, RBVM, and MM2 cases.

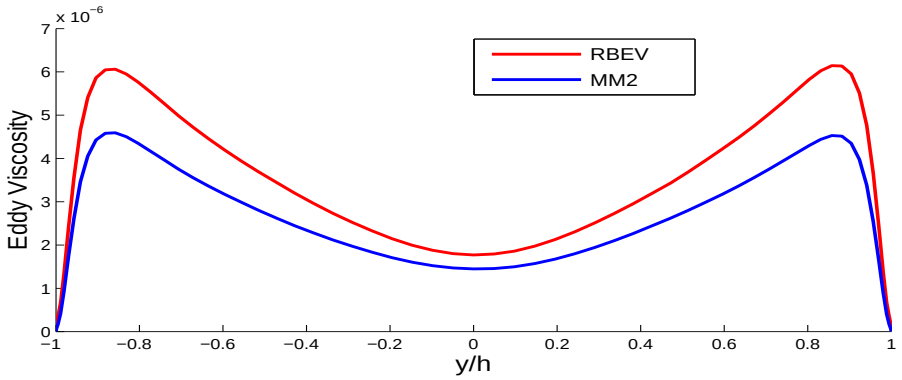

(a) eddy viscosity

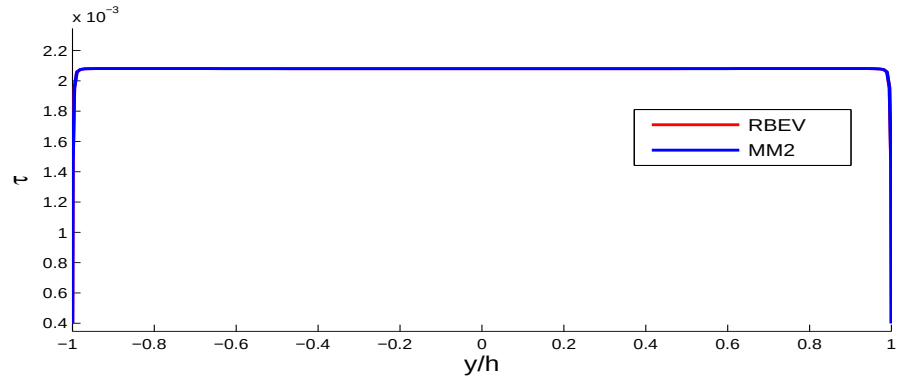

(b) stabilization parameter τ_m

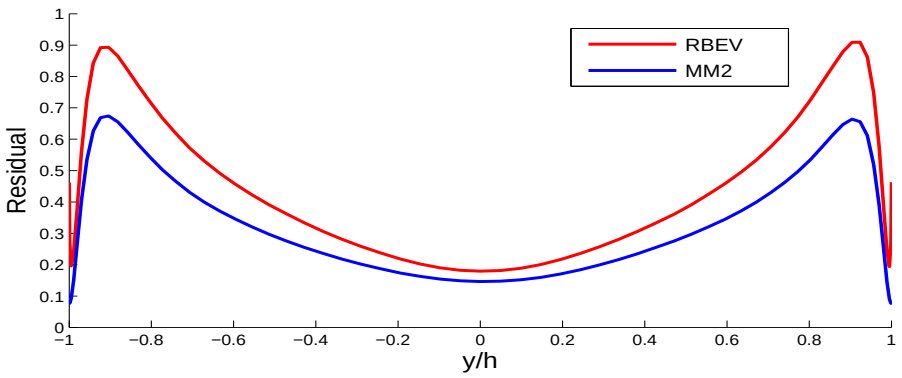

(c) Residual of the momentum equation

Figure 4.39: Average value of the eddy viscosity, stabilization parameter and residual of the momentum equation for the $Re_\tau = 395$ case on a 64^3 mesh with $dt = 0.050$ and $C_1 = 12$. A comparison of the RBEV, and MM2 cases.

4.4.2 $Re_\tau = 590$

In this section we test the LES models at a higher Reynolds number of $Re_\tau = 590$. We only consider the 64^3 element mesh. First we consider the performance of the RBEV model with $C_1 = 3$, which provided the best results for the lower Reynolds number case. We note that it continues to be very accurate at the higher Reynolds number. Thereafter we examine the performance of the MM2 model at $C_1 = 12$, and observe that it too continues to be accurate at the higher Reynolds number.

4.4.2.1 RBEV

In Figures 4.40 - 4.44 we plot the results for the RBEV model with $Re = 590$ on a 64^3 grid with $dt = 0.025$ and different value of $C_1 = 1, 3, 12$.

Figure 4.40 compares results for the average streamwise velocity profile. The RBEV model with $C_1 = 3$ matches the DNS most accurately. The RBEV model with $C_1 = 12$ slightly underpredicts and the RBEV model with $C_1 = 1$ slightly overpredicts the average velocity. The same trends are observed in the semi-log plot for u^+ in Figure 4.41 presented in wall coordinates. Figure 4.40 compares the average pressure. The RBEV models with $C_1 = 3$ and $C_1 = 12$ match the DNS most accurately while the RBEV model with $C_1 = 1$ slightly overpredicts the average pressure.

In Figure 4.43, we compare the fluctuations computed by the LES models with their DNS counterparts. We note that all models overpredict the streamwise fluctuations u_{rms} in (a). For the wall normal fluctuations, v_{rms} in (b), the RBVM model with $C_1 = 1$ is more accurate than the others. Near the center of the channel, all three models are very good. The same conclusion can be drawn for the spanwise fluctuations, w_{rms} in (c).

In Figure 4.44, the average values of the eddy viscosity, the stabilization parameter and the residual of the momentum equation are shown. Once again we observe that as C_1 increases the eddy viscosity and the stabilization parameter decrease, while the residual remain relatively unchanged.

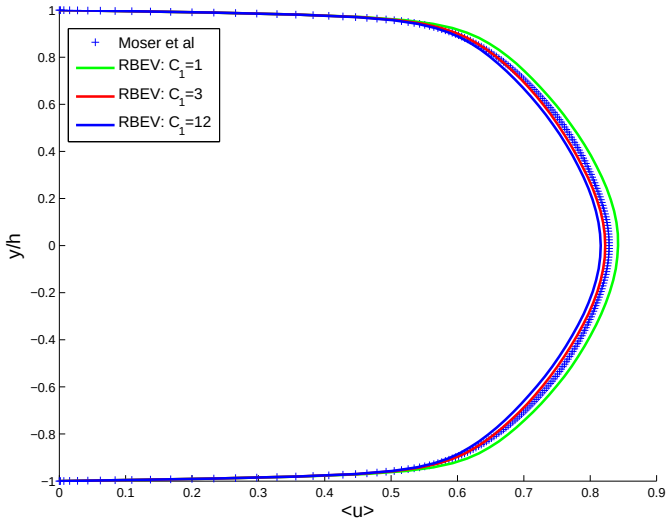

Figure 4.40: Average streamwise velocity for the $Re_\tau = 590$ case on a 64^3 mesh with $dt = 0.025$. A comparison of $C_1 = 1, 3, 12$ for the RBEV model.

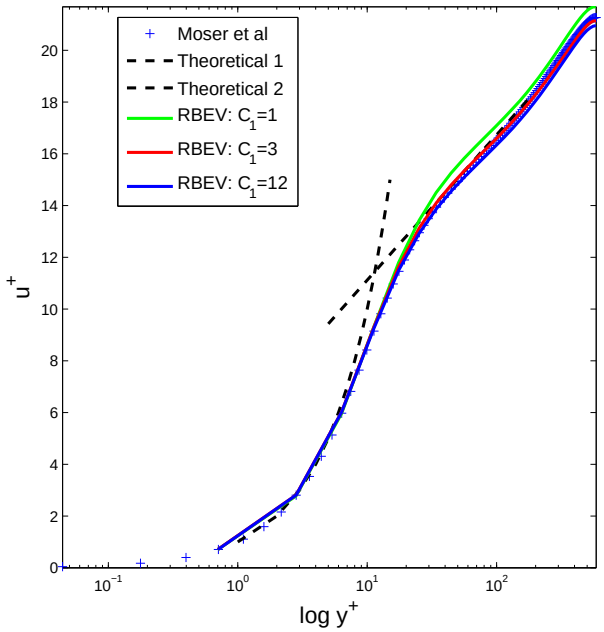

Figure 4.41: Average streamwise velocity in wall coordinates for the $Re_\tau = 590$ case on a 64^3 mesh with $dt = 0.025$. A comparison of $C_1 = 1, 3, 12$ for the RBEV model.

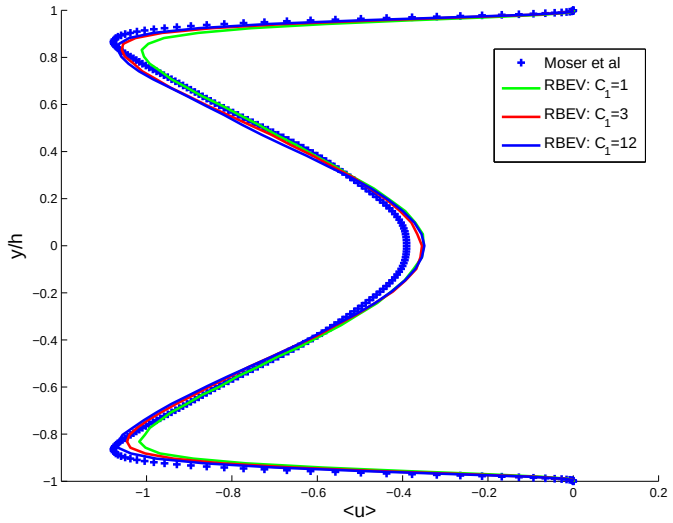

Figure 4.42: Average pressure for the $Re_\tau = 590$ case on a 64^3 mesh with $dt = 0.025$. A comparison of $C_1 = 1, 3, 12$ for the RBEV model.

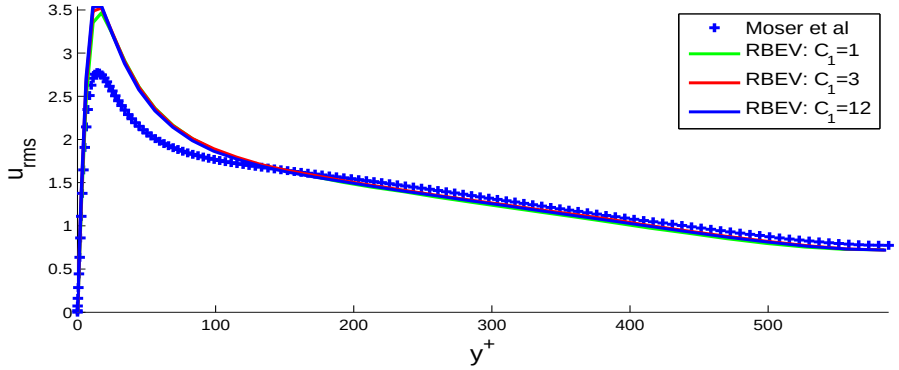

(a) RMS of velocity fluctuations in streamwise direction

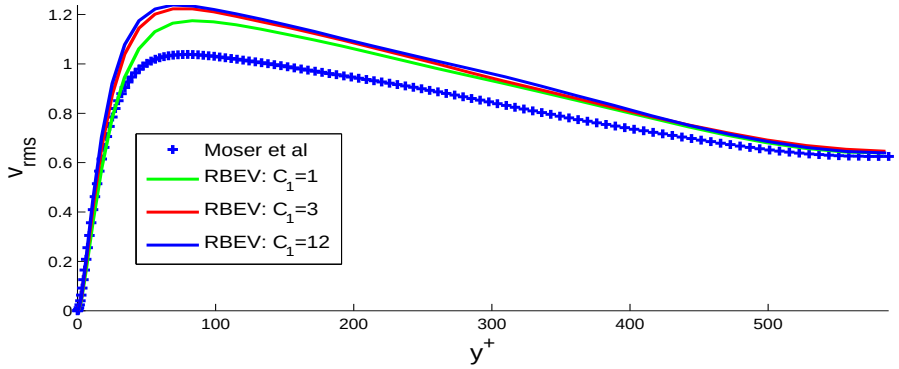

(b) RMS of velocity fluctuations in wall normal direction

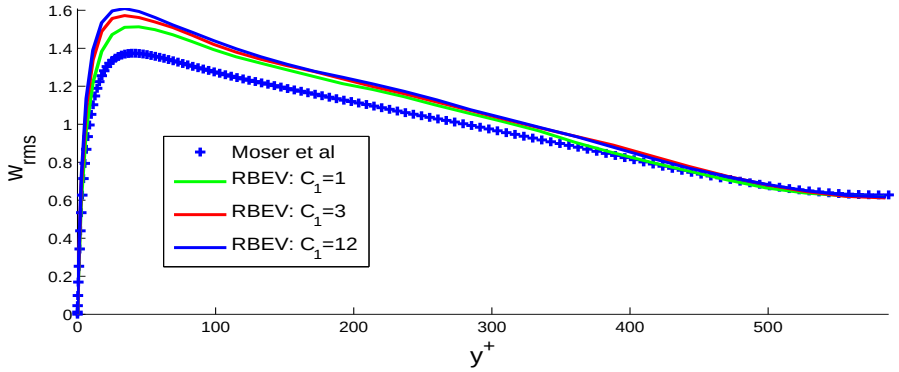

(c) RMS of velocity fluctuations in spanwise direction

Figure 4.43: RMS of velocity fluctuations in wall coordinates for the $Re_\tau = 590$ case on a 64^3 element mesh with $dt = 0.025$. A comparison of $C_1 = 1, 3, 12$ for the RBEV model.

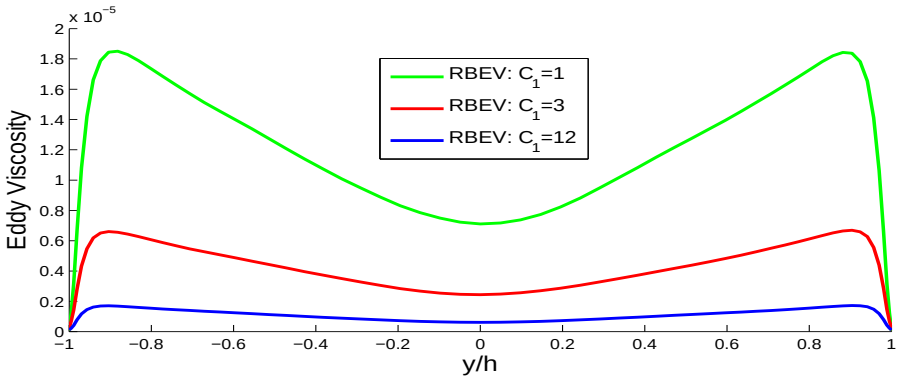

(a) eddy viscosity

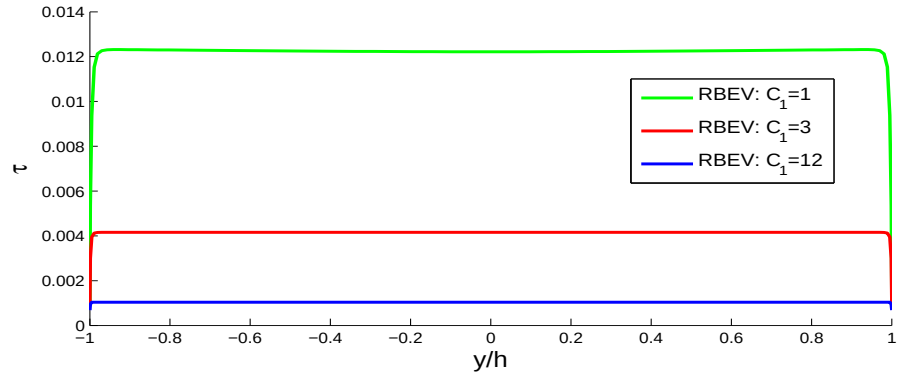

(b) stabilization parameter τ_m

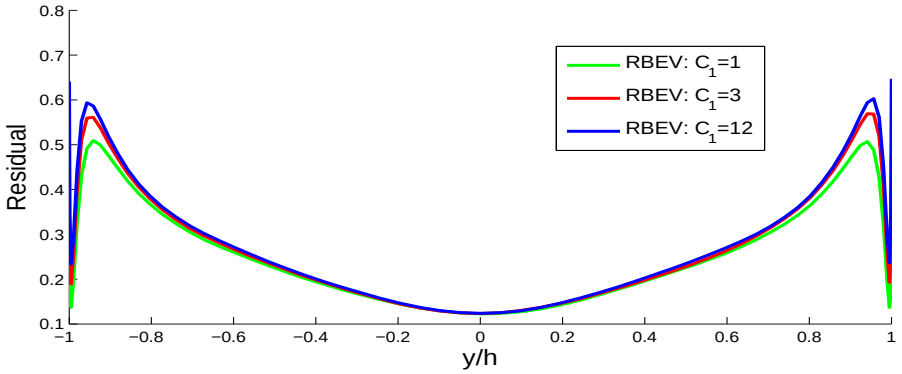

(c) Residual of the momentum equation

Figure 4.44: Average value of the eddy viscosity, stabilization parameter and residual of the momentum equation for the $Re_\tau = 590$ case on a 64^3 element mesh with $dt = 0.025$. A comparison of $C_1 = 1, 3, 12$ for the RBEV model.

4.4.2.2 MM2

In this subsection, we apply the MM2 model to the high Reynolds number case on a 64^3 grid with $dt = 0.025$. We compare the performance of the MM2 model with the RBEV model and the RBVM model with $C_1 = 12$.

In Figures 4.45 - 4.49 we plot the results for LES models on a 64^3 grid with $dt = 0.050$ and $C_1 = 12$.

Figure 4.45 compares results for the average streamwise velocity profile. The RBVM model and the MM2 model match DNS solution very accurately. The RBEV model slightly underpredicts the average velocity. The same trends are seen in the semi-log plot for u^+ in Figure 4.46 presented in wall coordinates. In Figure 4.47 we compare the average pressure and conclude that the RBEV model is the most accurate.

In Figure 4.48, we compare the fluctuations computed by the LES models with their DNS counterparts. We note that all the models are quite accurate. For the streamwise fluctuations the results are very similar, while for the spanwise and wall-normal fluctuations the RBVM and RBEV models are more accurate.

In Figure 4.49, the average values of the eddy viscosity, the stabilization parameter and the residual of the momentum equation are shown. We observe that the eddy viscosity of the MM2 model is smaller than that of the RBEV model, and that this difference can be attributed to the smaller value of residual for the former.

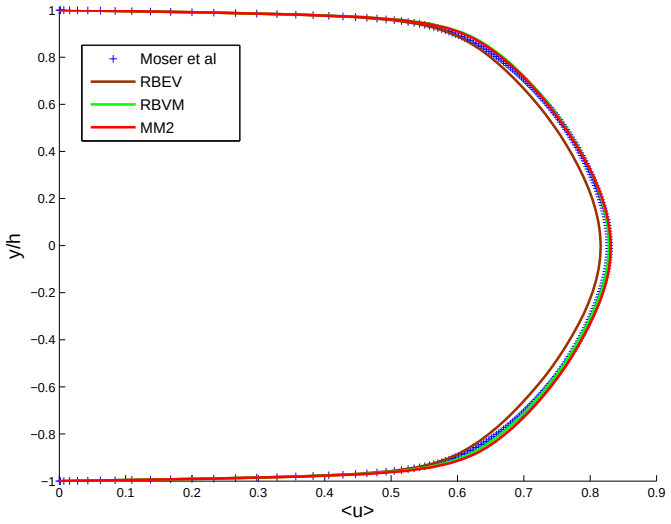

Figure 4.45: Average streamwise velocity for the $Re_\tau = 590$ case on a 64^3 mesh with $dt = 0.025$ and $C_1 = 12$. A comparison of the RBEV, RBVM, and MM2 cases.

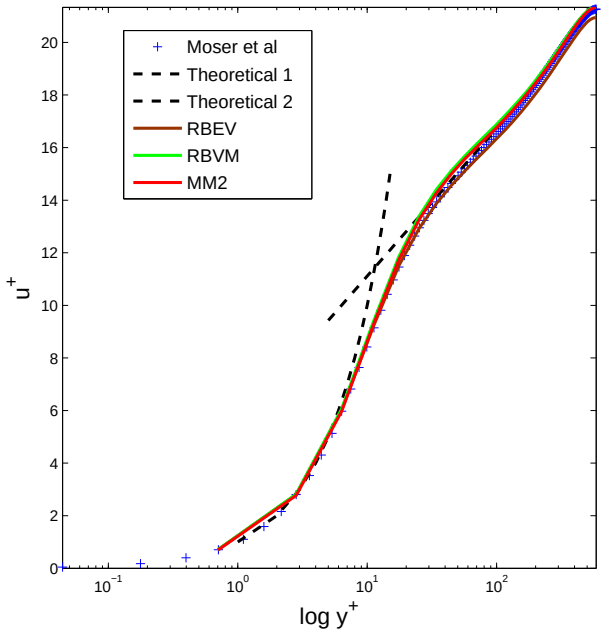

Figure 4.46: Average streamwise velocity in wall coordinates for the $Re_\tau = 590$ case on a 64^3 mesh with $dt = 0.025$ and $C_1 = 12$. A comparison of the RBEV, RBVM, and MM2 cases.

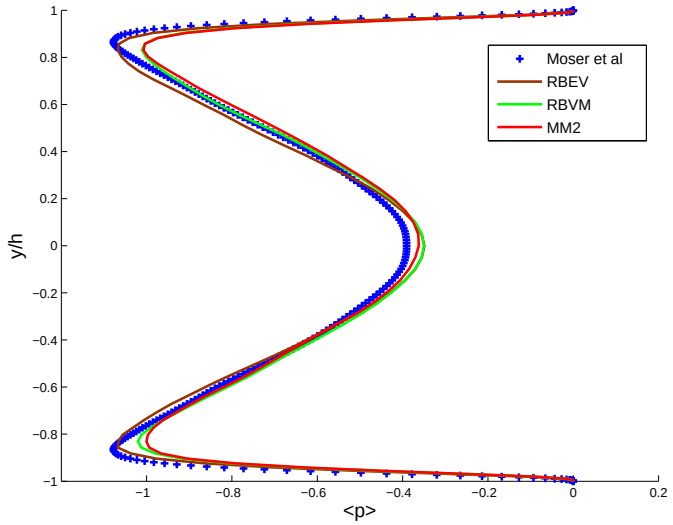

Figure 4.47: Average pressure for the $Re_\tau = 590$ case on a 64^3 mesh with $dt = 0.025$ and $C_1 = 12$. A comparison of the RBEV, RBVM, and MM2 cases.

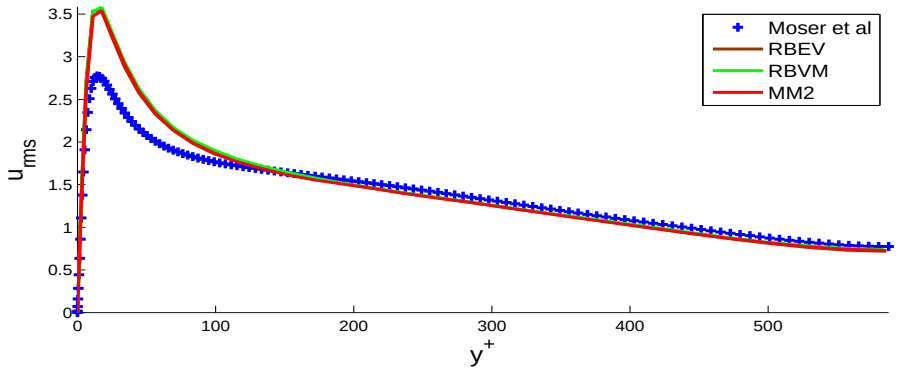

(a) RMS of velocity fluctuations in streamwise direction

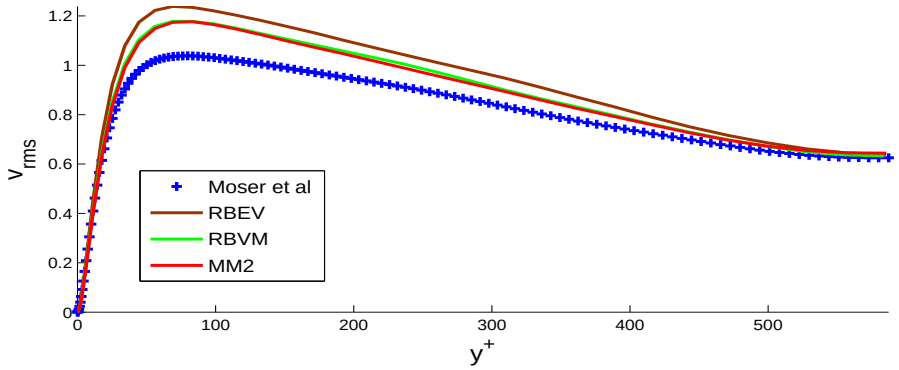

(b) RMS of velocity fluctuations in wall normal direction

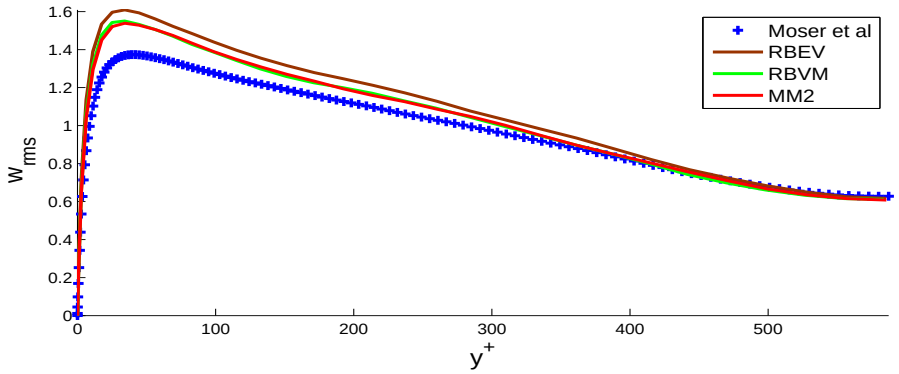

(c) RMS of velocity fluctuations in spanwise direction

Figure 4.48: RMS of velocity fluctuations in wall coordinates for the $Re_\tau = 590$ case on a 64^3 element mesh with $dt = 0.025$ and $C_1 = 12$. A comparison of the RBEV, RBVM, and MM2 cases.

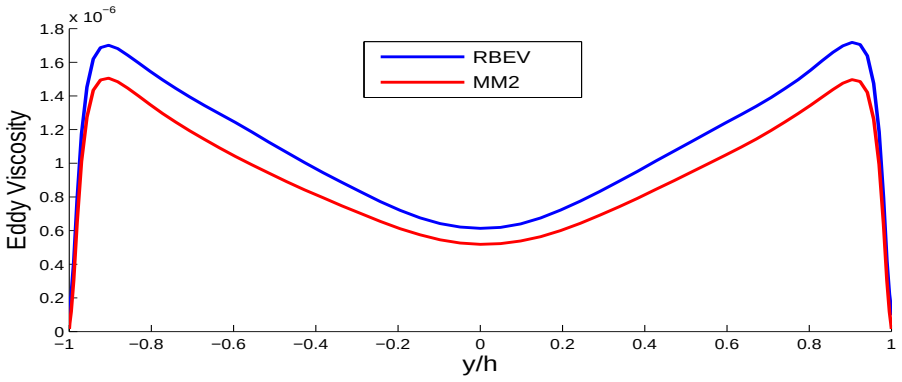

(a) eddy viscosity

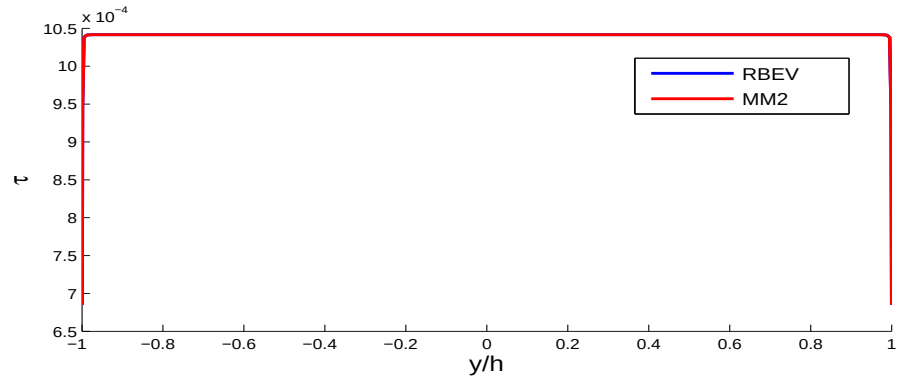

(b) stabilization parameter τ_m

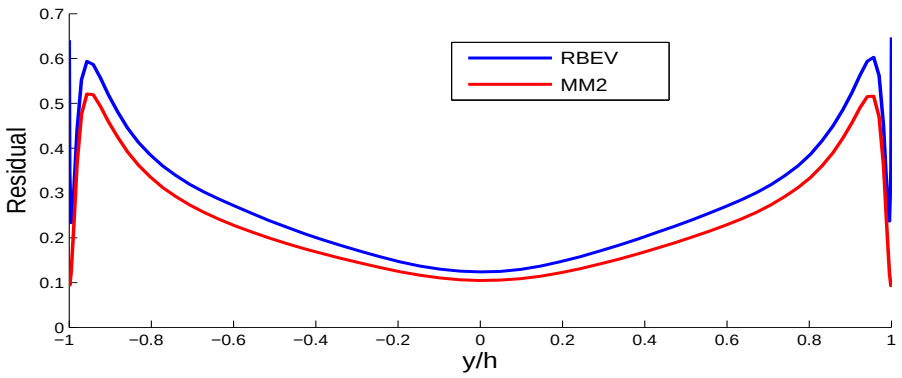

(c) Residual of the momentum equation

Figure 4.49: Average value of the eddy viscosity, stabilization parameter and residual of the momentum equation for the $Re_\tau = 590$ case on a 64^3 element mesh with $dt = 0.025$ and $C_1 = 12$. A comparison of the RBEV, and MM2 cases.

4.5 Chapter summary

In this chapter, we have implemented two residual-based LES models for incompressible turbulent flows within the finite element method. They are

- the residual-based eddy viscosity (RBEV) model
- the purely residual-based mixed model (MM2), which is a combination of the RBVM and the RBEV models

We tested the performance of these LES models in predicting fully developed turbulent channel flows. The LES models are tested on problems with friction Reynolds numbers $Re_\tau = 390, 590$ on 32^3 and 64^3 grids.

First, we compared the performance of the RBEV and the dynamic Smagorinsky models. We found that the RBEV model is generally more accurate and performs significantly better than the dynamic Smagorinsky model. We also note that the performance of the RBEV model strongly depends on the value of C_1, which is a parameter within the stabilization parameter τ_m. With $C_1 = 3$, the RBEV model matches the DNS result very accurately for the average streamwise velocity and the average pressure. We observe that the eddy viscosity of the RBEV model is near to zero close the wall and grows within the channel. It is remarkable that it achieves this behavior without an explicit dynamic approach. We attribute this behavior to the fact that RBEV model is inherently dynamic in that it is based on the residual of the coarse scales which automatically vanishes in well-resolved regions of the flow. We also observed that the eddy viscosity reduces with refinement in space and time. In that sense it displays a "dynamic" behavior. The RBEV model is more accurate and much easier to implement than the dynamic Smagorinsky model, and it is found to be robust by examining the dependence of its performance on grid size, the constant in the stabilization parameter, and the Reynolds number. We conclude that the RBEV model represents a viable strategy for wall bounded flows.

Thereafter we examined the performance of the new purely residual-based mixed model (MM2). We observed that the MM2 model with $C_1 = 12$ performs

very accurately. It is competitive with the RBEV model with $C_1 = 3$ and is more accurate than dynamic Smagorinsky model. We also found that for the MM2 model the eddy viscosity of the RBEV term automatically accounts for the dissipation produced by the RBVM terms and produces smaller eddy viscosity when compared to the purely RBEV model. Since there is no dynamic evaluation of parameters within this model, it is much easier to implement than the mixed model (MM1) based on the RBVM and the dynamic Smagorinsky models. The performance of the MM2 model is found to be robust by examining its dependence on grid sizes, the constant C_1 in the stabilization parameter, and the Reynolds number.

Our recommendation is therefore to use the residual-based eddy viscosity (RBEV) model with $C_1 = 3$ and the purely residual based mixed model (MM2) with $C_1 = 12$ within finite element method. These models are accurate, easy to implement, as they involve no dynamic procedure, and are consistent, in that the eddy viscosity vanishes when the residual of the coarse scales is small.

CHAPTER 5
Conclusion

In this thesis we have developed and implemented several residual-based large eddy simulation models for compressible and incompressible turbulent flows. Within this framework our main accomplishments are:

(1) We have extended the residual-based variational multiscale formulation (RBVM) to compressible turbulent flows. New definition of stabilization parameter τ is proposed for compressible turbulent flows. We have tested the performance of the RBVM model in predicting the decay of compressible, homogeneous, isotropic turbulence (HIT) in regimes where shocklets are known to exist within Fourier-spectral method. We varied the level of compressibility of the flow by varying the initial proportion of compressible turbulent kinetic energy and by varying the Mach number. In all cases we found that the RBVM model is generally more accurate and performs better than the popular dynamic Smagorinsky-Yoshizawa-eddy-diffusivity (DSYE) model.

(2) We have proposed and implemented a mixed model (MM1) based on the RBVM and DSYE models. In the MM1 model, the RBVM terms account for cross stresses while the DSYE terms account for Reynolds stresses. The MM1 model is tested on the same compressible HIT as the RBVM model with varying the level of compressibility of the flow. We have found that the MM1 model is generally more accurate than the DSYE model. For low Reynolds number the MM1 model is somewhat less accurate than the RBVM model, while for high Reynolds number it is more accurate than the RBVM model. This is to be expected because Reynolds stresses are important in high Reynolds number turbulent flows.

(3) We have developed and tested a new residual-based eddy viscosity model (RBEV) that uses the RBVM formulation. In the RBEV model, the eddy viscosity

is defined as $\nu_t \sim h|\boldsymbol{u}'|$, where h is the grid size and $\boldsymbol{u}'$ is the fine scales velocity fluctuation. The RBEV model is inherently dynamic because it is based on the residual of the coarse scales which automatically vanishes in well-resolved regions of the flow. In this way, the RBEV model requires no dynamic calculation of a parameter, so it is much easier to implement than the dynamic Smagorinsky type models.

The RBEV model is tested on the same compressible HIT as the RBVM and MM1 models. We observed that the RBEV model is more accurate than the DSYE model for the incompressible velocity component, while for the compressible velocity component it is not dissipative enough. Compared to the DSYE model, the RBEV model achieves similar accuracy but without a dynamic evlautation of parameters.

The RBEV model is also tested on the incompressible fully developed turbulent channel flows within finite element method. The RBEV model is observed to be more accurate and much easier to implement than dynamic Smagorinsky model. We also observed that the eddy viscosity of the RBEV model is near to zero close to the wall and grows within the channel. It is remarkable that it achieves this behavior without an explicit dynamic approach. By examining the dependence of the performance of this model on grid (spatial and temporal) size, constants that appear within the stabilization parameter and the Reynolds number, the RBEV model is found to be robust and it represents a viable strategy for simulating wall bounded flows.

(4) Motivated by the MM1 model and the RBEV model above, we developed and implemented a purely residual based mixed model (MM2) based on the RBVM and RBEV models. In the MM2 model, the RBVM terms account for cross stresses while the RBEV terms account for Reynolds stresses. The MM2 model is inherently dynamic but does not involve the dynamic calculation of parameters, so it is much easier to implement than the MM1 model.

The MM2 model is tested for the compressible HIT and it is observed to be more accurate than the DSYE model. For low Reynolds number the MM2 model is slightly less accurate than RBVM the model, while for high Reynolds number it is

more accurate than the RBVM model.

The MM2 model is also tested for the same incompressible channel turbulent flows as the RBEV model. For a different set of constant values in the definition of stabilization parameter the MM2 model is as accurate as the RBEV model, and is more accurate than the dynamic Smagorinsky model. We also found that for the MM2 model the eddy viscosity of the RBEV term automatically accounts for the dissipation produced by the RBVM terms and produces smaller eddy viscosity when compared to the pure RBEV model. The MM2 model is much easier to implement than the MM1 model. By testing this model for a range of problem parameters we conclude that it is robust, and it represents a viable strategy for simulating wall bounded flows.

For future work, the RBVM, the RBEV and the MM2 models will be applied to other problems, including flows with complex geometries and flows at very large scales. These models will also be extended to magnetohydrodynamics (MHD) or related areas.

REFERENCES

[1] J. P. Richter, *The notebooks of Leonardo da Vinci.* New York: Dover Publications, 1970.

[2] O. Reynolds, "An experimental investigation of the circumstances which determine whether the motion of water shall be direct or sinuous, and the law of resistance in parallel channels," *Philosph. Trans. Roy. Soc. London*, vol. 174, pp. 935–982, 1883.

[3] S. B. Pope, *Turbulent flows.* Cambridge, UK: Cambridge University Press, 2000.

[4] J. L. Lumley, *Turbulence and turbulence modeling, research trends in fluid dynamics.* Woodbury, NY: API Press, 1996.

[5] A. N. Kolmogorov, "1941a: Dissipation of energy in locally isotropic turbulence," *Doklady Akademiia Nauk SSSR*, vol. 30, pp. 301–305, 1941.

[6] A. N. Kolmogorov, "1941b: The local structure of turbulence in incompressible viscous uid for very large Reynolds numbers," *Doklady Akademiia Nauk SSSR*, vol. 31, pp. 538–540, 1941.

[7] A. N. Kolmogorov, "The equations of turbulent motion in an incompressible fluid," *Izvestia Acad. Sci., USSR*, vol. Phys. 6, pp. 56–58, 1942.

[8] J. Smagorinsky, "General circulation experiments with the primitive equations. I. the basic experiment," *Mon. Weather Rev.*, vol. 91, pp. 99–164, 1963.

[9] A. Yoshizawa, "Statistical theory for compressible turbulent shear flows, with the application to subgrid modeling," *Phys. Fluids*, vol. 29, pp. 2152–2164, 2000.

[10] P. Moin, K. Squires, W. Cabot, and S. Lee, "A dynamic subgrid-scale model for compressible turbulence and scalar transport," *Phys. Fluids A: Fluid*, vol. 3, pp. 2746–2757, 1991.

[11] J. Bardina, J. H. Ferziger, and W. C. Reynolds, "Improved subgrid-scale models for large-eddy simulation," in *Amer. Inst. of Aeronautics and Astronautics, Fluid and Plasma Dynamics Conf. 13th*, vol. 1, Snowmass, CO, 1980, pp. 14–16.

[12] R. A. Clark, J. H. Ferziger, and W. C. Reynolds, " Evaluation of subgrid-scale models using an accurately simulated turbulent flow," *J. Fluid Mech*, vol. 91, pp. 1–16, 1979.

[13] A. Favre, " Equations des gaz turbulents compressibles," *J. Mecanique*, vol. 4, pp. 361–390, 1965.

[14] T. J. R. Hughes, L. Mazzei, and K. E. Jansen, "Large Eddy Simulation and the Variational Multiscale Method," *Comput. Vis. Sci.*, vol. 3, pp. 47–59, 2000.

[15] Y. Bazilevs, V. M. Calo, J. A. Cottrell, T. J. R. Hughes, A. Reali, and G. Scovazzi, "Variational multiscale residual-based turbulence modeling for large eddy simulation of incompressible flows," *Comput. Methods Appl. Mech. Eng.*, vol. 197, no. 1-4, pp. 173–201, 2007.

[16] R. Codina, "Stabilized finite element approximation of transient incompressible flows using orthogonal subscales," *Comput. Methods Appl. Mech. Eng.*, vol. 191, no. 39-40, pp. 4295–4321, 2002.

[17] P. Gamnitzer, V. Gravemeier, and W. A. Wall, "Time-dependent subgrid scales in residual-based large eddy simulation of turbulent channel flow," *Comput. Methods Appl. Mech. Eng.*, vol. 199, no. 13-16, pp. 819–827, 2010.

[18] Z. Wang and A. A. Oberai, "Spectral analysis of the dissipation of the residual-based variational multiscale method," *Comput. Methods Appl. Mech. Eng.*, vol. 199, no. 13-16, pp. 810–818, 2010.

[19] Z. Wang and A. A. Oberai, "A mixed large eddy simulation model based on the residual-based variational multiscale formulation," *Phys. Fluids*, vol. 22, pp. 075 107:1–9, 2010.

[20] T. J. R. Hughes and G. Sangalli, "Variational multiscale analysis: the fine-scale green's function, projection, optimization, localization, and stabilized methods," *SIAM J. Numerical Anal.*, vol. 45(2), pp. 539–557, 2007.

[21] A. A. Oberai, J. Liu, D. Sondak, and T. J. R. Hughes, "A residual-based eddy viscosity model for the les of turbulent flows," *Comput. Methods Appl. Mech. Eng.*, submitted.

[22] D. Sondak and A. A. Oberai, "LES models for incompressible magnetohydrodynamics derived from the variational multiscale formulation," *Phys. Plasmas*, submitted.

[23] A. A. Oberai and J. Wanderer, "Variational formulation of the Germano identity for the Navier–Stokes equations," *J. Turbulence*, vol. 6, no. 7, pp. 1–17, 2005.

[24] A. A. Oberai and J. Wanderer, "A dynamic multiscale viscosity method for the spectral approximation of conservation laws," *Comput. Methods Appl. Mech. Eng.*, vol. 195, no. 13-16, pp. 1778–1792, 2006.

[25] C. G. Speziale, G. Erlebacher, T. A. Zang, and M. Y. Hussaini, "The subgrid-scale modeling of compressible turbulence," *Phys. Fluids*, vol. 31, pp. 940–942, 1988.

[26] S. Liu, C. Meneveau, and J. Katz, "On the properties of similarity subgrid-scale models as deduced from measurements in a turbulent jet," *J. Fluid Mech.*, vol. 275(-1), pp. 83–119, 1994.

[27] B. Vreman, B. Geurts, and H. Kuerten, " Subgrid-modeling in LES of compressible flow," *Appl. Sci. Res.*, vol. 54, pp. 191–203, 1995.

[28] A. Leonard and G. S. Winckelmans, "A tensor-diffusivity subgrid model for large-eddy simulation," in *Proc. Isaac Newton Institute Symposium / ERCOFTAC Workshop.* Norwell, MA: Kluwer Academic Publishers, 1999, pp. 12–14.

[29] G. S. Winckelmans, A. A. Wray, O. V. Vasilyev, and H. Jeanmart, "Explicit-filtering large-eddy simulation using the tensor-diffusivity model supplemented by a dynamic Smagorinsky term," *Phys. Fluids*, vol. 13, pp. 1385–1403, 2001.

[30] D. K. Lilly, " A proposed modification of the Germano subgrid-scale closure method," *Phys. Fluids*, vol. A 4 (3), pp. 633–635, 1992.

[31] G. Hauke, "Simple stabilizing matrices for the computation of compressible flows in primitive variables," *Comput. Methods Appl. Mech. Eng.*, vol. 190, no. 51-52, pp. 6881–6893, 2001.

[32] W. Hwang and J. K. Eaton, "Creating homogeneous and isotropic turbulence without a mean flow," *Exp. Fluids*, vol. 36, pp. 444–454, 2004.

[33] R. Samtaney, D. I. Pullin, and B. Kosović, "Direct numerical simulation of decaying compressible turbulence and shocklet statistics," *Phys. Fluids*, vol. 13(5), pp. 1415–1430, 2001.

[34] C. Canuto, M. Y. Hussaini, A. Quarteroni, and T. A. Zang, *Spectral methods in fluid dynamics.* New York City, NY: Springer, 1988.

[35] J. Liu and A. A. Oberai, "The residual-based variational multiscale formulation for the large eddy simulation of compressible flows," *Comput. Methods Appl. Mech. Eng.*, vol. accepted, 2012.

[36] M. Germano, U. Piomelli, P. Moin, and W. H. Cabot, "A dynamic subgridscale eddy viscosity model," *Phys. Fluids*, vol. A 3, pp. 1760–1765, 1991.

[37] F. Shakib, *Finite element analysis of the compressible Euler and Navier-Stokes equations.* Stanford, CA: Stanford University, 1989.

[38] C. Johnson, *Numerical solution of partial differential equations by the finite element method*. Cambridge, UK: Cambridge University Press, 1987.

[39] G. I. Barenblatt, *Scaling, self-similarity, and intermediate asymptotics: dimensional analysis and intermediate asymptotics*. Cambridge, UK: Cambridge University Press, 1987.

[40] T. J. R. Hughes and M. Mallet, "A new finite element formulation for computational fluid dynamics: III. The generalized streamline operator for multidimensional advective-diffusive systems," *Comput. Methods Appl. Mech. Eng.*, vol. 58(3), pp. 305–328, 1986.

[41] F. Shakib, T. J. R. Hughes, and Z. Johan, "A new finite element formulation for computational fluid dynamics: X. The compressible Euler and Navier-Stokes equations," *Comput. Methods Appl. Mech. Eng.*, vol. 89(1-3), pp. 141–219, 1991.

[42] K. E. Jansen, C. H. Whiting, and C. M. Hulbert, "Generalized- α method for integrating the filtered Navier-Stokes equations with a stabilized finite element method," *Comput. Methods Appl. Mech. Eng.*, vol. 190(3), pp. 305–319, 2000.

[43] R. D. Moser, J. Kim, and N. N. Mansour, "Direct numerical simulation of turbulent channel flow up to $Re_\tau = 590$," *Phys. Fluids*, vol. 11, pp. 943–945, 1999.